University of Antwerp

Faculty of Science
Department of Physics

$\mathcal{O}(\mathcal{N})$ numerical methods for investigating graphene heterostructures and moiré patterns

---

$\mathcal{O}(\mathcal{N})$ numerieke methoden voor onderzoek naar grafen heterostructuren en moiré patronen

Thesis submitted for the degree of
Doctor in Science: Physics
at the University of Antwerp to be defended by
Miša Anđelković

Promotors
Prof. Dr. François M. Peeters
Dr. Lucian Covaci

Antwerp, December 2019

Members of the jury

Chairman

Prof. Dr. Jacques Tempere, University of Antwerp, Belgium

Promotors

Prof. Dr. François M. Peeters, University of Antwerp, Belgium
Dr. Lucian Covaci, University of Antwerp, Belgium

Members

Prof. Dr. Pierre Van Mechelen, University of Antwerp, Belgium
Prof. Dr. Tatiana G. Rappoport, Federal University of Rio de Janeiro, Brasil
Prof. Dr. Lino da Costa Pereira, KU Leuven, Belgium
Prof. Dr. Vincent Meunier, Rensselaer Polytechnice Institute, USA

Contact

Miša Anđelković
misa.s.andelkovic@gmail.com

Nataši,
za sve strpljenje i podršku

Acknowledgements

"No man is an island."
— Devotions Upon Emergent Occasions,
John Donne

There are many people without whose support and help the completion of this thesis would not be possible. I would like to take this opportunity to thank them.

First and foremost, I would like to express my deep gratitude to my research supervisors and mentors, Prof. François Peeters, for his invaluable research ideas and positive criticism of this research work, and Dr. Lucian Covaci for his patient guidance and encouragement, for countless discussions, and his willingness to help no matter what the problem was. I am very grateful to them for having the opportunity to work with our colleagues from experimental groups. I thank Dr. Jinhai Mao and Dr. Yuhang Jiang from the research group of Prof. Eva Andrei (Rutgers University), and Thomas Lane from the research group of Prof. Vladimir Fal'ko (the University of Manchester) for invaluable insight into their experimental and theoretical work. My special appreciation goes to Simão M. João, Prof. João M. V. P. Lopes, Prof. Tatiana Rappoport, and Prof. Aires Ferreira for numerous discussions and the collaboration on the KITE project.

I am indebted to all the members of the jury for their critical view on my thesis and insightful suggestions on how to improve it.

I thank Prof. Milan Tadić and Prof. Vladimir Arsoski for being inspiring and supportive during the final days of my undergraduate studies. Their academic pursuits encouraged me to start with mine. I am very grateful to Prof. Milorad Milošević for invaluable discussions and his efforts in helping me to improve my work.

I thank all my friends and colleagues in Antwerp. Special thanks

to Dean, Slaviša, Željko, Marko, Longlong, Samira, Sara, Rebeca, Víctor, Ben, Matthias, Amir, Hossein, Nikolas and Alfredo who notably contributed to this research, both scientifically and personally. I am very grateful for your friendliness and for making the time in Antwerp something to remember.

To my lifelong friends from Serbia who supported me on this journey, Milena, Miloš, Milica, Nenad, Kića, Ogi, Kaća, Marjan, Nataša, Marko, Rade, Ilija, Nadežda, Paja and Dule I am forever grateful.

Hvala mojoj familiji i prijateljima, porodicama Luković, Milanović, Milić, Stevanović, Stojanović, Kaličanin, Milojević i Stefanović.

Neizmerno sam zahvalan porodici Nestorović, a posebno Nikoli, Mileni i Radi, što su Natašu, mene, i naš odlazak u Belgiju iskreno podržali. Svu zahvalnost dugujem na neizmernoj ljubavi i podršci, i bezrezervnom poverenju mojoj porodici, Luki, Mimici, Saši, Veri, Živku i Negi. Na kraju ali ponajviše, hvala na inspiraciji Nataši kojoj ovu tezu i posvećujem.

Abstract

In the research field of two-dimensional materials, computational modelling proves to be crucial in examining the electronic properties. This increases the experimental throughput and broadens our understanding of the fundamental phenomena. Furthermore, it presents a theoretical foundation for developing a concept of materials by design, where the goal is to achieve a desired functionality. Still, the accuracy that atomistic modelling offers proves to increase the already demanding computational complexity. In this thesis graphene heterostructures and moiré patterns are tackled starting from a tight-binding (TB) atomistic description in real-space, with the use of numerical approaches proposed as an alternative to the traditional exact diagonalisation techniques. Spectral methods that scale linearly with the system size and their implementations in two open-source codes, Pybinding and KITE, offer the possibility to simulate complex large-scale systems, such as the ones investigated in this thesis.

Firstly, delaminations in graphene together with a theoretical concept of a graphene diode are discussed. Boundaries between different stacking arrangements in bilayer graphene are proven to host electrostatically induced topological states that can act as transport channels in a nearly dissipationless regime, due to the weak backscattering. Furthermore, boundary states are discussed and directly compared to the experimental measurements in the case of twisted bilayer graphene (tBLG). The effects on the electronic properties and the signatures in the transport are shown.

Secondly, recent experimental results on the tuning of the electronic properties by periodically strained graphene superlattices formed as a consequence of a buckling transition are modelled with a periodic pseudomagnetic field (PMF). The spectrum reconstruction and the transition to the flat band regime is examined as a function of the superlattice period and the strength of the PMF. It is shown that the different flat bands possess different spatial localisation, where there exist flat bands that

percolate throughout the sample. These results match the experimental investigations of our collaborators.

Lastly, the appearance of multiple moiré patterns in encapsulated graphene closely aligned to two hexagonal boron-nitride (hBN) layers is examined. At low rotation angles energy reconstruction is observed, an effect that can be explained as a second-order scattering event at periodicities which correspond to the interference between the individual moirés. Furthermore, it is shown that the resulting super-moiré (SM) interference has a strong effect on the structural properties. We show that the SM is imprinted both in the interlayer spacing and in the bond-length as a consequence of lattice relaxation and further enhances the spectrum reconstruction. The SM description helps in explaining a recent experimental study and provides another path towards achieving tunable superlattice bands in 2D materials.

Nederlandstalige Abstract

Computermodellering van tweedimensionele materialen is cruciaal voor het onderzoek van de elektronische eigenschappen van deze materialen. Een goede modellering verhoogt het inzicht in experimentele kennis, maakt ontwerp van nieuwe experimenten eenvoudiger en verdiept het begrip van de fundamentele concepten die aan de basis liggen van geobserveerde fenomenen. Verder biedt het een theoretische basis om nieuwe materialen te ontwikkelen die speciaal ontworpen zijn om een gewenste functionaliteit te bekomen. De nauwkeurigheid die atomistische modellering biedt verhoogt echter de reeds veeleisende computationele complexiteit. In deze thesis worden grafeen heterostructuren en moiré-patronen bestudeerd vertrekkende van een tight-binding (TB) atomistische beschrijving in de reële ruimte. Door gebruik te maken van numerieke methoden worden deze voorgesteld als alternatief voor traditionele exacte diagonalisatietechnieken. Spectrale methoden die lineair schalen met de systeemgrootte en hun implementaties in twee open-source programma's, Pybinding en KITE, bieden de mogelijkheid bovendien om complexe grootschalige systemen te simuleren, zoals degene die in dit proefschrift zijn onderzocht.

Om te beginnen onderzoeken we delaminaties in grafeen. Deze worden samen met een theoretisch concept van een grafeen-diode besproken. De grenzen tussen verscheidene delen van bilaag grafeen die verschillend gestapeld zijn blijken elektrostatisch geïnduceerde topologische toestanden te bevatten die kunnen fungeren als transportkanalen in een vrijwel dissipatieloos regime als gevolg van zwakke terugverstrooiing. Verder worden grenstoestanden besproken en direct vergeleken met experimentele metingen in het geval van geroteerd bilaag grafeen (tBLG). Het effect op de elektronische eigenschappen van dit materiaal de manier waarop het de transportkarakteristieken wijzigt worden tevens besproken.

Ten tweede worden recente experimentele resultaten over de afstemming van de elektronische eigenschappen door periodiek vervormde grafe-

en-superroosters gemodelleerd. Deze superroosters worden gevormd als gevolg van een knik overgang, dewelke wordt beschreven door een periodiek pseudomagnetisch veld (PMV). De manier waarop het spectrum wordt gereconstrueerd en de overgang gemaakt wordt naar het vlakkeband regime wordt onderzocht als een functie van de superroosterperiode en de sterkte van het PMV. Er wordt aangetoond dat de verschillende vlakke banden verschillende ruimtelijke lokalisatie vertonen en er vlakke banden bestaan die zich over het hele materiale verspreiden. Deze resultaten komen overeen met de experimentele onderzoeken van onze collega onderzoekers.

Ten slotte onderzoeken we het verschijnen van meerdere moiré-patronen in ingekapseld grafeen dat nauw is uitgelijnd met twee hexagonale boor-nitride (hBN) lagen. Bij lage rotatiehoeken wordt energiereconstructie waargenomen, een effect dat kan worden verklaard als een tweede-orde verstrooiingseffect bij periodiciteiten die overeenkomen met de interferentie tussen de individuele moiré-patronen. Verder wordt aangetoond dat de resulterende super-moiré (SM) interferentie een sterk effect heeft op de structurele eigenschappen. We tonen aan dat de SM zowel de tussenlaagafstand als bindingslengte beïnvloed als gevolg van roosterontspanning en de reconstructie van het spectrum verder verbetert. De SM-beschrijving helpt bij het verklaren van een recente experimentele studie en biedt een andere manier om afstembare superroosterbanden in 2D-materialen te realiseren.

Contents

List of Abbreviations

acronym	meaning	acronym	meaning
1,2,3D	*1, 2 and 3 dimensional*	**MD**	*molecular dynamics*
ARPES	*angle-resolved photoemission spectroscopy*	**ML**	*monolayer*
BLG	*bilayer graphene*	**(N)NN**	*(next) nearest-neighbour*
BRSOC	*Bychkov-Rashba spin-orbit coupling*	**PMF**	*pseudo-magnetic field*
BTE	*Boltzmann transport equation*	**PLL**	*pseudo Landau levels*
CPGF	*Chebyshev polynomial Green's function*	**RAM**	*random access memory*
CPU	*central processing unit*	**RI**	*registry index*
CVD	*chemical vapour deposition*	**RTA**	*relaxation time approximation*
DC	*direct current*	**SDP**	*secondary Dirac point*
DFT	*density functional theory*	**SM**	*super moiré*
DOS	*density of states*	**SLDOS**	*spatial distribution of the LDOS*
FT	*Fourier transformation*	**SOC**	*spin-orbit coupling*
FW/BW	*forward/backward*	**STE**	*stochastic trace evaluation*
GPU	*graphics processing unit*	**STM**	*scanning tunnelling microscopy*
I/O	*input/output*	**STS**	*scanning tunnelling spectroscopy*
gr	*graphene*	**TB**	*tight-binding*
KPM	*kernel polynomial method*	**tBLG**	*twisted bilayer graphene*
LDOS	*local density of states*	**TMDC**	*transition metal dichalcogenide*
LL	*Landau levels*	**ZEM**	*zero-energy modes*

1 | Introduction

"I want Flatlands,
I want simplicity."
— Flatlands,
Chelsea Wolfe and Mark Lanegan

1.1 Introduction

The development of the electronic industry which is closely tied with consumer electronics has its roots in the beginning of the 20th century. Aside from the mechanical circuitry, in the early beginnings, electric circuits were controlled by vacuum tubes with two electrodes, invented by John Ambrose Fleming in 1904 (Fleming valve), and three electrodes, invented by Lee De Forest two years later (Audion), which acted as a diode and a triode. The latter is also considered to be the first amplifier. With the design similar to the one of a light bulb, once the filament in the tubes was heated, depending on the applied voltage between the two plates in the vacuum (Fig. 1.1(a)), electrons were either flowing between the electrodes, or their current was suppressed. This type of switches was electrically inefficient due to their design, the excess heat that was generated, and the power needed for their operation.

Four decades later, in December 1947 the first transistor was invented by Bardeen, Brattain and Shockley at Bell Labs for which they were awarded the Nobel prize in 1956 (Fig. 1.1(b)). From the invention of the first transistor until today there is more that 60 years of development of fundamental science, theoretical and experimental condensed matter physics which led to enormous advancements in the field of microelectronics and has pushed the semiconductor, and particularly silicon technology, to the point where we simply cannot imagine our everyday

lives without smartphones, laptops, tablets or smart-watches, all driven by transistor based logic.

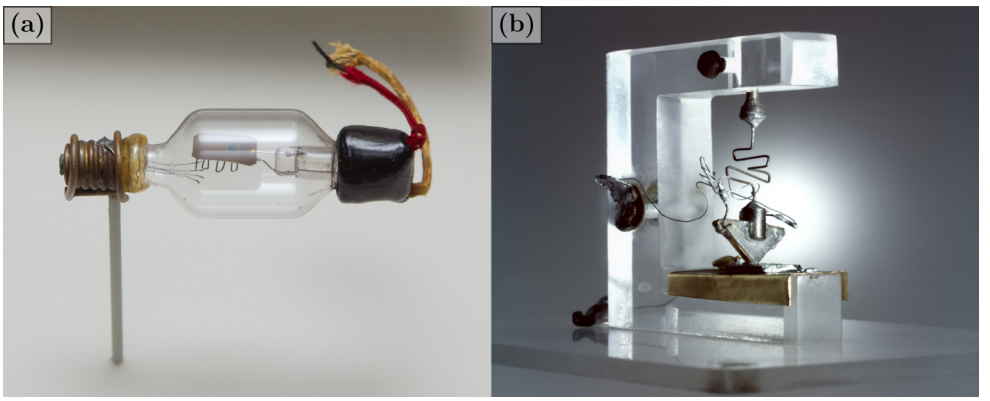

Figure 1.1: (a) Triode Audion from 1908 (adapted from https://commons.wikimedia.org/wiki/User:Gmaxwell) and the first transistor (adapted from www.extremetech.com).

In the meantime, the major idea how to develop and control electronic devices has not significantly changed; we are still in pursuit for more efficient ways of controlling the flow of electrons, their spins or condensates, which would consume less power and perform faster, all for the sake of applications in logical circuitry in electronic devices. Still, silicon technology is reaching its limitations in terms of working frequencies and component sizes which assure proper functionalities with well defined behaviour. Moore's empirical law of doubling the number of operations a microprocessor can perform every two years has slowed down and a question arises will there be more Moore, now driven with possibly a disruptive technology? Nowadays, the on-chip components are reduced to the scales of a couple of nanometers, Intel and Samsung have commercially available products using 10 nm lithography nodes, and one can already start discussing about the quantum interference and tunnelling effects that start to influence the device performance.

1.2 Era of two dimensional (2D) materials

Exactly a century after the discovery of the first vacuum tubes, graphene was rediscovered. Technological discoveries that have revolutionized our society happened as a combination of intuition and luck. Some of the examples are tungsten light-bulbs, penicillin, and Teflon [1]. In a similar manner, it was not without the great amount of creativity and the

pragmatic approach to the experimental physics of Andre Geim and Konstanin Novoselov that resulted in the rediscovery and the experimental observation of graphene [2], material which was theoretically described decades before but thought to be thermally unstable. Simplicity is a word that best describes this discovery, the discovery that has driven enormous number of experimentalists, theoreticians and entrepreneurs to study, design and invest in graphene in the past 15 years. Simplicity, because of the original experiment, and the approach which subsequently became known as a "scotch-tape" method.

Graphene boosted the initial interest in the research field of 2D materials, which soon became multidisciplinary, where chemistry, physics, mathematics, computer science, mechanical and electrical engineering and production technology are closely tied. Not without reason, as graphene constitutes properties absent in similar materials. The electrons move faster than in any other system, heat is transported more efficiently, it is thousand times stronger than steel of the same thickness, it is transparent and flexible. Still, it is only one atomic layer thick, it is a semi-metal which makes it unsuitable for conventional electronics and in many cases difficult to control. Furthermore, not only graphene, but instead a whole family of 2D materials provided a playground for expanding our understanding of the fundamental sciences. This abundance, and the properties they offer almost as a rule being different from the 3D analogues have raised questions and provided answers in various fields such as quasi-relativistic phenomena and Klein tunnelling [3], highly correlated physics [4], charge-density waves and superconductivity [4, 5], exciton physics [6, 7], structural deformations of thin-film-like membranes [8, 9], electron-spin dynamics [10] and many more. Beside graphene, particularly important for the presented work are graphene (hetero)structures which, for reasons of emphasising our motivation, are worth introducing in more detail even before properties of graphene are discussed.

1.2.1 Van der Waals heterostructures and moiré patterns

Consequence of the possibility to freely stack and modify layered materials [11, 12], as in the case of graphene hBN where the two layers are weakly coupled by the van der Waals force, introduces a concept of a *moiré pattern*. This long-range interference due to the mismatch or the rotation between different layers mimics the unit cell of a newly formed (hetero)structure. In Fig. 1.2 the effects of the graphene/hBN alignment

is presented. The importance of this case lies in the fact that hBN is a particularly good substrate for graphene which introduces low excess charge, Fig. 1.2(a), hence suitable for obtaining high quality devices. Under conditions that will be covered in later chapters, a moiré pattern (Fig. 1.2(b)) will appear in conjunction with band reconstruction. For example, surface reconstruction for large rotation angles between graphene and hBN results in a smooth modulation of the Young modulus on the scale of the moiré pattern, while at low rotation angles the same modulation shows that the strain is accumulated along the domain walls defined by the new period. In addition, the stacking energy is minimized

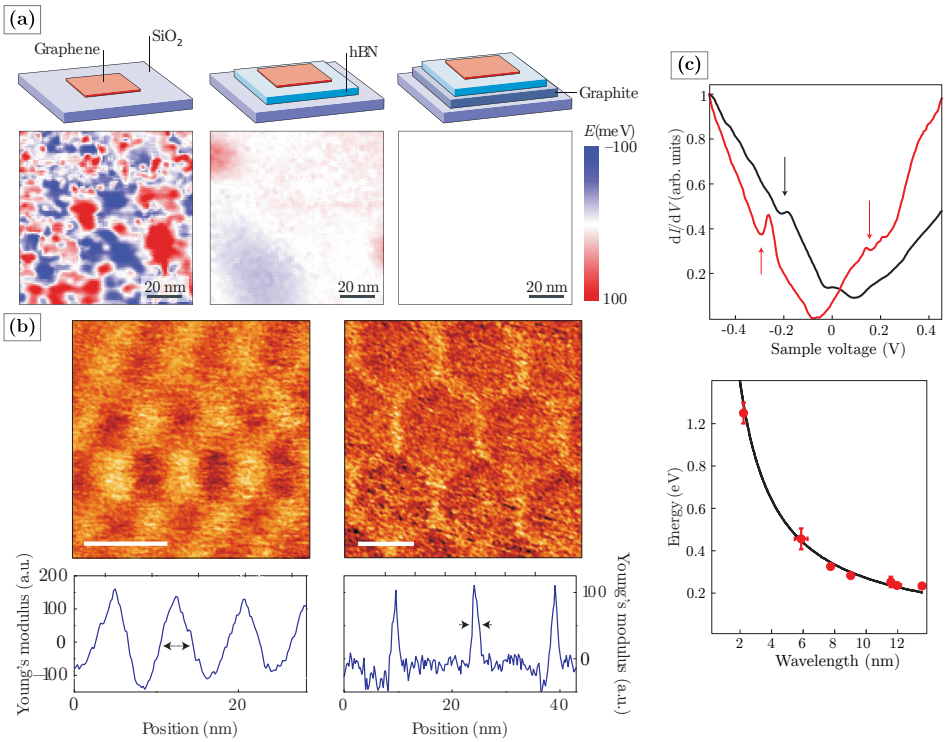

Figure 1.2: Van der Waals heterostructures and moiré patterns, graphene on hBN. (a) The low excess charge disorder can be obtained by using hBN as a substrate for graphene (adapted from Ref. [13]), which results in the formation of moiré patterns that as a consequence have (b) surface reconstruction, revealed in the measurement of the Young modulus for samples with different relative rotation angles (adapted from Ref. [9]) and (c) spectrum reconstruction, revealed in the measurement of the local density of states (adapted from Ref. [14]).

elsewhere to form a commensurate structure, which is a signature of an

angle dependent commensurate-incommensurate (in terms of stacking) transition [9]. Moreover, such moiré patterns induce band reconstruction on the level of the *mini-Brillouin zone*, induce secondary Dirac points, as can be seen in Fig. 1.2(c), and can open up a band gap in graphene due to spatial distribution of the sublattice mass-like terms [15–17], but also allow the observation of Hofstadter's butterfly [16, 18] due to their large spatial extent compared to the lattice of the constituent materials. Recent experimental reports have introduced an additional concept of multiple interfering moiré patterns, which is discussed in details in Sec. 7.

The moiré effect is even more important in the case of twisted bilayer graphene. In almost aligned samples long-range moiré periods are observed, showing locally varying stacking arrangement between the layers and offer gate dependent control over a network of helical states, which appear along the moiré boundaries, as shown in Fig. 1.3(a). This particular case will be further discussed in Ch. 6. Furthermore, depending on the stacking induced coupling between the layers, rotation will gradually tune the system from a semi-metal at large rotation angles [19], through a metallic phase due to the proximity of the van Hove singularities [20, 21] in neutral samples to a density dependent and interaction induced Mott insulating or superconductive phase [4, 22, 23]. Fig. 1.3(b) shows a low temperature measurement of carrier density dependent transport in low twist angle bilayer graphene, which reveals the tunable insulating-superconductive transition from an experiment that has, to say the least, brought back the focus to the twisted (hetero)structures.
A plethora of novel properties of 2D materials and their heterostructures has raised great expectations for their application, and soon after the first experiments they were named as possible successors of silicon, especially in the field of electronic devices. To emphasize the importance of graphene in recent years, in Fig. 1.4 the number of publications per year and the number of different types of published items is shown. The path of miniaturization taken by the semiconductor industry would eventually naturally lead to atomic layers or structures of even lower dimension, such as quantum dots or quantum point contacts. But it seems that the assumptions of graphene becoming a "game-changer" were made too soon. Significant obstacle in integrating graphene in the electronic devices is definitively the lack of a band gap. In addition, producing the high quality samples with a large reproducibility rates, as will be discussed further, is anything but easy. To introduce different 2D crystals and the occurring problems in more detail, the experimental setups for creating devices made of 2D materials and approaches for

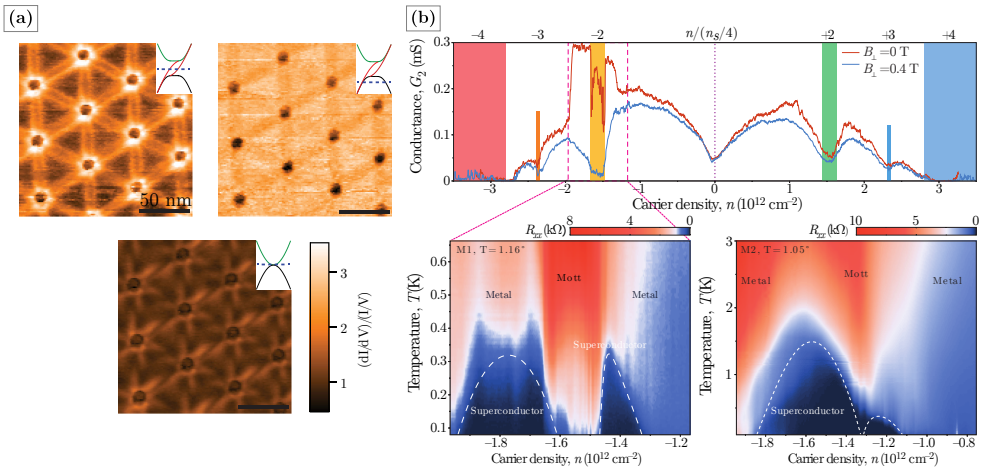

Figure 1.3: Van der Waals heterostructures and moiré patterns, low angle twisted bilayer graphene. (a) The gate induced appearance of a helical network of boundary states at energies within the AB region gap ($\theta \approx 0.245°$) (adapted from Ref. [24]) and (b) density dependent and interaction induced metal-insulator-superconductor transition close to the *magic angle* ($\theta \approx 1.1°$) twisted bilayer graphene. In the top panel, vanishing conductance at $n = \pm n_s$ correspond to the superlattice induced band gap while at intermediate filling the interaction induced bang gaps appear, measured at $T = 70$ mK. Temperature dependent four terminal resistivity is shown in the bottom panels for two different devices showing the vanishing resistance (superconductive phase) at densities close to the Mott insulating phase at half-fillings. Highest measured $T_C = 0.5$ K (adapted from Ref. [4]).

their synthesis will be discussed in the next section.

1.3 2D materials in the lab

The first experiments on graphene have investigated mechanically exfoliated graphene flakes on SiO_2 formed on the surface of Si substrates. The highly doped Si serves as a back gate with which the density in graphene can be finely tuned, and such samples could comply with silicon technologies [25]. Unfortunately, SiO_2 substrates were shown to induce large variations in the potential due to charge inhomogeneities from the trapped impurities at the surface of the sample [26] and to induce strain in the graphene layer forming ripples [25]. But even these samples allowed for the observation of half-integer quantum hall effect [27], which

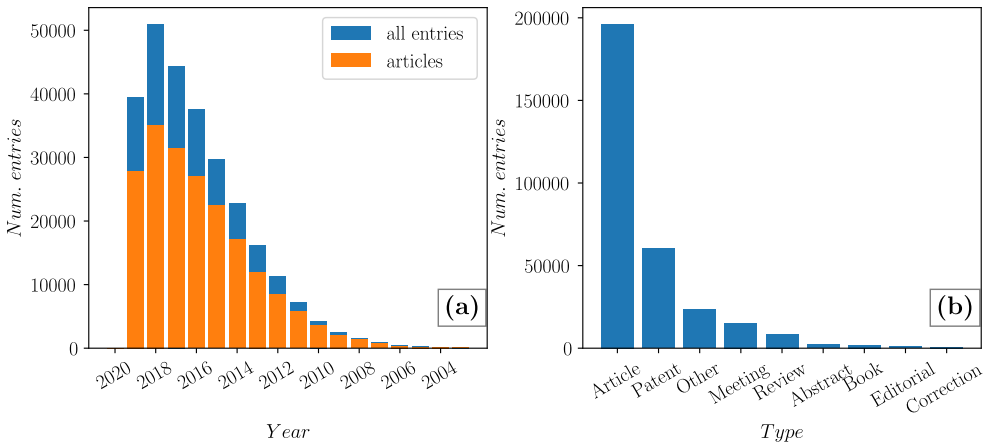

Figure 1.4: Significance of graphene. (a) Number of entries and the number of articles that mention graphene. (b) Different types of entries on graphene. Based on the topic "graphene" from *Web of Science*, up to 5 October 2019.

was later observed even at room temperature [28], vanishing electron mass and finite conductivity at vanishing density [29]. Initial problems were also related to locating the graphene samples. Raman spectroscopy is widely used today, and was introduced as a first non-invasive technique for identifying samples based on the widths and shifts of specific Raman peaks [30, 31].

A natural choice substrate for graphene would be graphite, the two lattice constants are the same, which leads to low strain and corrugation effects in graphene, and, due to advanced production methods, results in clean devices with exceptional properties. Still, in many experimental setups, the use of an insulating substrate is an imperative. This issue was later solved with the use of hBN as the underlying substrate. The two lattices differ only slightly ($\approx 0.018\%$), hBN is a large-band gap insulator and the interface between the two does not introduce additional defects and preserves the high mobility and linear spectrum of graphene [32, 33]. The cleanest samples in terms of charge inhomogeneities can be obtained when placing the hBN substrate on graphite, on top of which a graphene layer is transferred subsequently (Fig. 1.2(a)).

In addition, graphene flakes can be made free-standing, a result that initially intrigued the community because of the questions on the 2D thermal instability. These are overcome by the spontaneous corrugation of the layer. Experimentally, this setup offers much flexibility for measuring the strength of graphene [34], for manipulating the layers, but introduces many practical challenges when considering device applica-

tions.

Being the oldest member of the 2D family, the production of graphene is advanced compared to the manufacturing of other 2D materials. Initial interest in transition metal dichalcogenides (TMDC), where the transition metal belongs to the group IV, V, VI, VII IX or X of the periodic system, and chalcogen can be S, Se or Te, dates back to the 1980s with the first reports on suspensions of monolayer MoS_2 [35]. TMDCs gained increased research interest only after the advancement of the techniques for creating and manipulating layered 2D materials since the dawn of graphene. Hence, the synthesis techniques are very similar and include mechanical and liquid-phase exfoliation, chemical vapor deposition (CVD), and molecular beam epitaxy with the use of different base crystals or precursors. In contrast to graphene, TMDCs offer many different properties in terms of the constituent elements and the structural phases (2H or 1T) they form. As such, they give access to metallic, semi-metallic, semiconducting and insulating properties with strong spin-orbit coupling; some of them host charge-density waves and/or superconductivity [6], and provide more options for device application in fields of optoelectronics, spintronics and valleytronics, and more importantly provide necessary ingredients for designing transistor logic [36].

1.3.1 Realistic 2D materials

The samples of the highest quality, which are used in the experiments, up to now are obtained by mechanical exfoliation, as breaking of weak van der Waals bonds does not induce defects nor trapped charges. But to obtain the high quality devices, a price has to be paid. This technique has a low yield, and the resulted flakes are non-uniform. Experimentally, after exfoliation and when flakes of desired number of layers are identified, they are transferred to substrates of choice. This workflow is time demanding and all the manufacturing steps have to be applied to each and every produced device, which raises questions of efficiency and reproducibility of their production. The properties being offered are certainly interesting as noted previously, but for the application purposes the scaling of the production has to be brought to a different level. Different techniques of mass-producing 2D materials include CVD, liquid-phase exfoliation, reduction of oxidizes 2D materials and many more. Each of the methods comes with a tradeoff, the higher the yield is, the lower is the quality, while the cheaper the production becomes, the harder is the control over the number of layers.

Moreover, even high-quality samples necessarily contain disorder, if

not intrinsic from the manufacturing processes, then extrinsic from the environment. Realistic samples are imperfect, they contain corrugations, strains or excess charge, which appears on the surface and results in charge puddles. In the case of graphene, hBN substrates are harder to scale in size compared to graphene, which introduces yet another technological issue.

1.4 2D materials for the industry

Mass-production of devices that build upon 2D ingredients rely on solving different issues. In practice, although the graphene market has had a steady growth rate, the commercial availability of graphene reveals many problems. The biggest issue is certainly the problem of the uniformity, as the quality varies greatly depending on the production techniques and conditions [37]. In addition, the yield has to be high, and at this point, due to the intrinsic differences of graphene compared to silicon, instead of competing with it, a possible route for 2D materials would be to comply with silicon technology without disrupting it and facilitate the transition to 2D electronics through the integration in current production lines. Certainly, even now, layered materials have found their place in the industry of flexible and composite materials, where the quality of the samples and their uniformity is not crucial to the functionality of the device.

There is an enormous effort being made for this to happen, but as underlined previously, 2D materials still suffer from many unsolved fundamental questions. It was recently shown that even the story of graphene has more twists to offer [4], which has opened even more research directions. The goal also becomes the search for a "killer-application", but if such an application is discovered, producing devices is still a technological challenge. And in this way the issues in the industry of 2D materials lead us back to the fundamental questions.

1.5 Simulating 2D materials with code

Due to the ubiquitousness of the disorder in the 2D world, it is important to answer how different types of disorder affect the samples and moreover it is important to examine if those can be potentially used in defining a special functionality. The main reason is that layered materials are nothing but a surface, hence the bond disorder (including

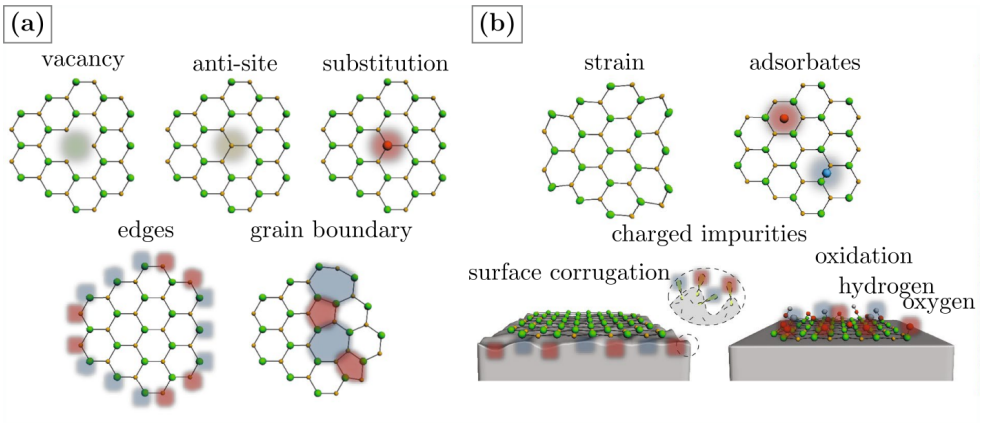

Figure 1.5: Different sources of disorder. (a) Intrinsic and (b) extrinsic. Adapted from Ref. [38]

dangling bonds), vacancies, substitute atoms or ad-atoms, grain boundaries, charge puddles or atomic corrugations (Fig. 1.5) will define the relevant properties of devices.

Experimental studies on 2D materials are limited by the complicated and time-demanding processes, which offer high-quality samples. Instead, computational modelling [39] can help not only in discovering new stable materials that are still not experimentally observed, but also in modelling the disorder, designing materials properties, and proposing novel devices. In such a way the experimental throughput can be increased and the understanding of the fundamental phenomena is improved. The newly defined "LEGO" heterostructures obtained when stacking different layers [11, 12] are still to be characterized, and in many cases their behaviour is still not fully understood [40]. Theoretical research is expected to advance the field as numerical experiments are to a certain extent easier to perform and to repeat than experimental techniques for handling and examining moiré patterns. But even in theoretical modelling there is still a lot of room for improvements. Tackling complex structures, while preserving the granular description of 2D crystals on samples of experimentally relevant sizes has proven very challenging. Some of these questions are tackled and further discussed along the course of this thesis.

Computational modelling is an approach very suitable for the atomistic description of 2D materials. It can serve in improving the agreement and close the gap between the theoretical description and the experimental observations, but can also serve as a validity test for the analytical descriptions. Still this as a rule becomes a daunting task. The complex-

ity in many cases increases exponentially with the level of details that we would like to describe, and the development of efficient algorithms and new approaches to solving a particular problem becomes a necessity.

This also presents the motivation behind the work in this thesis, the development of accurate computational modelling of (disordered) 2D materials and their heterostructures, that are either hard, not accurate enough or even impossible to tackle within the continuum descriptions. The ultimate aim is to provide theoretical support for novel ways, e.g. superlattices and moiré patterns, to control the electronic properties and in such a way make an effort in broadening our understanding of recent experimental work or possibly directing it towards intriguing novel phenomena. The atomistic description of such systems is obtained through the use of real-space tight-binding descriptions, which are solved with the use advanced spectral approaches that scale linearly with the system size, which not only tend to provide a feasible manner of modelling experimental phenomena, but also fill the gap between the more accurate ab-initio approaches, and as mentioned, the analytical (or continuum) descriptions, which treat the effects of the reduced dimensionality and the disorder as a perturbation.

1.6 Outline

Due to the effects presented in this brief introduction, it can be concluded that the research on 2D materials is still in its early stage, one could say its adolescence. Hence, detailed atomistic modelling of graphene and graphene-like structures, being discussed throughout this thesis, can help us in improving our understanding of 2D materials in general. The thesis is divided into 7 chapters, as outlined below.

Introduction presents a brief discussion on 2D materials, with the focus on recent experimental realisation of graphene heterostructures and moiré patterns, with the goal to introduce some of the unanswered question and problems that require further fundamental research and which are halting their wider use in the industrial sector.

Methodology introduces the tight-binding method and the continuum description of graphene. Transport regimes are reviewed and appropriate transport methodologies are introduced. Examining dilute concentration of disorder observed in the cleanest samples, graphene ripples or moiré patterns all require large-scale simulations. To be able to do

so and preserve the accuracy of atomistic models, advanced numerical approaches that include spectral methods are introduced followed by details on the Chebyshev expansions and the kernel polynomial method.

Numerical modelling is devoted to introducing different practical implementations of the discussed numerical methods in codes Pybinding and KITE. One of the main focuses in the present thesis will be on the latter software. KITE was especially developed for large-scale modelling of disordered systems. This was realised in a collaborative work through the course of different projects presented in this thesis. [1] My contributions include additional functionalities in Pybinding, such as density of states (DOS), Kubo-Bastin DC conductivity tensor and absorbing boundary conditions. In the KITE project my specific contribution was on interfacing Pybinding with KITE, developing the wave-packet propagation module together with J. M. V. P. Lopes and testing and benchmarking the code on various computational infrastructures. Furthermore, related to the example test cases presented in the KITE presentation paper, I have developed the examples on twisted bilayer graphene, spin dynamics and I performed the computational part of the section on phosphorene in the presence of the magnetic field.

Guiding electrons in graphene describes the modelling of simple graphene heterostructures, such as graphene diodes, and the use of structural defects, delaminations, to obtain unidirectional motion in bilayer graphene samples, within a theoretical study. My original contribution was to develop the tight-binding model and study the electronic properties of the delaminated structures, which were complemented by continuum approaches from the University of Manchester (V. Fal'ko group). The section on the graphene diode presents an ongoing work in collaboration with G. Berdiyorov from the Qatar Environment and Energy Research Institute.

Buckled graphene superlattice introduces the concept of substrate induced corrugations in monolayer graphene that, through superlattice effects, reconstruct the spectrum of graphene. In this study the experimental results obtained by our colleagues from Rutgers University (E. Andrei group) and the University of Manchester (A. Geim group) were

[1] S. M. João, J. M. V. P. Lopes (University of Porto), T. Rappoport (Federal University of Rio de Janeiro), and A. Ferreira (University of York).

supported by the theoretical modelling done by S. P. Milovanović and myself.

Twisted bilayer graphene examines the electronic effects induced by moiré patterns by modelling of electronic properties of bilayer graphene with relative rotation between the layers. The appearance of helical states in the presence of electric field, with the particular attention on asymmetrically gated samples are discussed and compared with the experimental results. The results in the clean limit are followed by a study on the vacancy disorder effects at different rotation angles. My main contribution was on the theoretical description, while the experimental results that are modelled and discussed in one of the sections of this chapter were courtesy of Y. Jiang, J. Mao, and E. Andrei affiliated to Rutgers University and the University of Chinese Academy of Sciences, and are part of an ongoing collaboration.

Super-moiré in encapsulated graphene discusses a novel phenomena of the super-moiré patterns in double-aligned hBN/graphene/hBN samples. A theoretical description of different moiré induced interference effects is explained. Further, the effects on the structural and electronic properties are discussed, and the results are directly compared with the recent experimental results. My original contribution was on the identification of the geometrical model of the super-moiré pattern as a function of twist angle and the tight-binding description of the electronic properties of the encapsulated graphene samples. This description was used as a theoretical support for results obtained by our experimental colleagues from the University of Manchester (K. Novoselov group).

2 | Theoretical considerations and the methodology

Computational modelling has proven very important for describing, developing functionalities of and even discovering novel materials. The goal of these computational experiments is to expand the understanding of phenomena that are otherwise either hard to tackle or hard to explain using solely laboratory experimental techniques. Conveying this study to the field of 2D materials, the understanding and accurate description of phenomena induced by the reduced dimensionality requires explanations that are deduced from quantum mechanical laws, as the number of properties that can be explained classically is limited. Long-wavelength continuum theories, such as the one introduced in the following section, suffer from inherent problems with modelling an arbitrary sample. In contrast, atomistic lattice simulations offer an approach for detailed modelling of samples of various shapes, in the presence of arbitrary disorder or with combination of different materials that define a heterostructure. As a rule of thumb, this accuracy in describing condensed matter systems, especially when a large-scale basis is required, proves to be increasingly demanding, which is obvious in the case of weakly disordered systems or complex heterostructures, such as moiré patterns. Although preferred methods would not require exponential increase in the required computational resources compared to the number of simulation elements [41], increase of the understanding of a phenomena requires the growth of the simulation complexity, which in most cases increases with a power-like dependence on the number of simulated entities (i.e. atoms, electrons, orbitals, spins). Fortunately, the atomistic description of materials offers a trade-off, non-interacting systems can be accurately described with approximative models that linearly scale with the size of the Hilbert space (multiplied by the average number of connections between the constituents of such space), such as *Tight-Binding*, which is introduced in the following section.

A common line among different chapters presented in this thesis whether the discussion is on graphene-heterostructures or defected layers is the presence of one or more graphene layers. Hence, because of its ubiquitousness, in this chapter devoted to methodology and models, there will be a section fully devoted to properties of graphene, with the aim to introduce concepts important for later chapters in a brief and simple manner starting from the continuum description.

In contrast, the methodology employed for obtaining electronic and optical properties from the TB models is fully applicable to a general solid state system. Similar as the underlying TB models, this methodology that heavily relies on polynomial expansions of TB Hamiltonians scales almost linearly with the size of the Hilbert space (this complexity is discussed in more detail after introducing the important concepts of the methodology) and provides in such a way access to probing resolutions otherwise inaccessible.

2.1 Tight-binding model

The TB description relies on the assumption of weakly perturbed electrons from their isolated atomic-like states that are tightly bound to the atoms (or more precisely their nuclei) residing in a crystal. Crystal electron bands can be described with wavefunctions that satisfy the Bloch condition $\Psi(\boldsymbol{r}+\boldsymbol{R}) = e^{i\boldsymbol{k}\boldsymbol{R}}\Psi(\boldsymbol{r})$ for lattice vectors $\boldsymbol{R}$, and that can be further expanded in terms of atomic stationary-state-like wavefunctions $\Phi(\boldsymbol{r})$, also known as *Wannier functions*

$$\Psi(\boldsymbol{r}) = \frac{1}{\sqrt{N}} \sum_{\boldsymbol{R}} e^{i\boldsymbol{k}\boldsymbol{r}} \Phi(\boldsymbol{r}-\boldsymbol{R}), \tag{2.1}$$

where N is the total number of orbitals from all atomic sites or the size of the Hilbert's space. Wannier functions can be further expressed as a sum of the atomic wavefunction (orbitals) or Slater-Koster-type states for isolated atoms $\psi_i(\boldsymbol{r})$

$$\Phi(\boldsymbol{r}) = \sum_i c_i \psi_i(\boldsymbol{r}), \tag{2.2}$$

hence the name, *linear combination of atomic orbitals* [42]. Combining Eqs. (2.1) and (2.2) with the Schrödinger equation $\hat{H}\Psi = E\Psi$, and integrating over the whole Hilbert space, a general form of a TB Hamiltonian

can be obtained

$$\begin{aligned} \hat{H} &= \sum_{i,j} H_{i,j}(\boldsymbol{k}) \hat{c}_i^\dagger \hat{c}_j, \\ \hat{S} &= \sum_{i,j} S_{i,j}(\boldsymbol{k}) \hat{c}_i^\dagger \hat{c}_j, \end{aligned} \tag{2.3}$$

where $\hat{c}_i^\dagger$ ($\hat{c}_j$) is the electron creation (annihilation) operator on site $i(j)$, and the Hamiltonian ($H_{i,j}$) and the overlap ($S_{i,j}$) matrix elements are defined as

$$\begin{aligned} H_{i,j} &= \frac{1}{N} \sum_{\boldsymbol{R},\boldsymbol{R'}} e^{i\boldsymbol{k}(\boldsymbol{R}-\boldsymbol{R'})} \int d\boldsymbol{r} \psi_i^\dagger(\boldsymbol{r}-\boldsymbol{R}) H \psi_j(\boldsymbol{r}-\boldsymbol{R'}), \quad \text{and} \\ S_{i,j} &= \frac{1}{N} \sum_{\boldsymbol{R},\boldsymbol{R'}} e^{i\boldsymbol{k}(\boldsymbol{R}-\boldsymbol{R'})} \int d\boldsymbol{r} \psi_i^\dagger(\boldsymbol{r}-\boldsymbol{R}) \psi_j(\boldsymbol{r}-\boldsymbol{R'}). \end{aligned} \tag{2.4}$$

In this case, the Schrödinger equation reads

$$\hat{H}\Psi = E\hat{S}\Psi, \tag{2.5}$$

and takes into account the non-orthogonality of the atomic basis functions. Still, the elements $S_{i,j}$ are negligible in most practical cases, which is especially the case in the course of this work and will be neglected further. TB matrix elements, $H_{i,j}$, can be described as a combination of on-site energies ($i = j$) and hopping integrals between different atomic orbitals ($i \neq j$), which can be estimated by means of other methods (e.g., Slater-Koster approach) or by fitting to experimental data or first-principles calculations for suitable reference systems [43–45]. For example, the parameters in the TB models can be derived using the recently developed Tight-Binding Studio [46], which provides Slater-Koster coefficients with orthogonal or non-orthogonal basis sets. In practice, a desirable parametrization will result in a small number of neighbour hoppings, which defines the coordination number of the lattice (Z) and satisfies $Z \ll N$. In that way, the complexity of the model will linearly depend on the total number of orbitals as $Z \times N$, which allows one to handle large-scale systems.

In addition, such a suitable scaling enables large-scale calculations of a plethora of equilibrium and non-equilibrium physical properties, including optical absorption spectra, simulations of amorphous solids, and wave-packet propagation. Disorder, interfaces, and defects can be conveniently added to a TB model by modifying on-site energies and hopping integrals and adding auxiliary sites. Such a multi-scale approach

has proven useful in describing impurity scattering [47, 48], moiré patterns [49, 50], complex interactions induced by adatoms [51], disorder-induced topological phases [52], optical conductivity of 2D materials with up to tens of millions of atoms [53], and geometrical properties, vibrational frequencies and interactions of large molecular systems [54]. Electronic properties will be particularly addressed when discussing the numerical methodologies.

2.1.1 Tight-binding description and electronic properties of graphene

Because of both the significance, and the ubiquitousness in the research of 2D materials, graphene will be given a more detailed introduction before discussing the methodology which enables handling disordered large-scale systems.

Graphene forms a crystal structure with a honeycomb lattice of sp^2 hybridized carbon (C) atoms. Geometrically, the honeycomb lattice can be described as a composition of two triangular Bravais lattices with lattice vectors

$$\boldsymbol{a_1} = a_0(+\sqrt{3}/2, +3/2), \quad \boldsymbol{a_2} = a_0(-\sqrt{3}/2, +3/2), \tag{2.6}$$

where $a_0 = 0.142nm$ is the carbon-carbon distance. Each of the two triangular lattices defines the one of the inequivalent sublattices, labelled **A** and **B**, and positioned at sites

$$\boldsymbol{r_A} = n\boldsymbol{a_1} + m\boldsymbol{a_1} + (0, -a_0/2), \quad \boldsymbol{r_B} = n\boldsymbol{a_1} + m\boldsymbol{a_1} + (0, +a_0/2) \tag{2.7}$$

as shown in Fig. 2.1(a). Nearest neighbours of each graphene site can be defined through vectors

$$\boldsymbol{\delta_1} = a_0(-\sqrt{3}/2, +1/2), \quad \boldsymbol{\delta_2} = a_0(-\sqrt{3}/2, +1/2), \quad \boldsymbol{\delta_3} = a_0(0, -1). \tag{2.8}$$

The reciprocal lattice has the same symmetry as the real-space one, with reciprocal lattice vectors

$$\boldsymbol{b_1} = \frac{4\pi}{3a_0}(+\sqrt{3}/2, 1/2), \quad \boldsymbol{b_1} = \frac{4\pi}{3a_0}(-\sqrt{3}/2, 1/2), \tag{2.9}$$

and the presence of two sublattices reflect in the origin of two equivalent (in neutral graphene) high-symmetry points

$$\boldsymbol{K} = \frac{2}{3}\boldsymbol{b_1} + \frac{1}{3}\boldsymbol{b_2} = \left(\frac{2\pi}{3\sqrt{3}a_0}, \frac{2\pi}{3a_0}\right), \quad \boldsymbol{K'} = \frac{1}{3}\boldsymbol{b_1} + \frac{2}{3}\boldsymbol{b_2} = \left(-\frac{2\pi}{3\sqrt{3}a_0}, \frac{2\pi}{3a_0}\right), \tag{2.10}$$

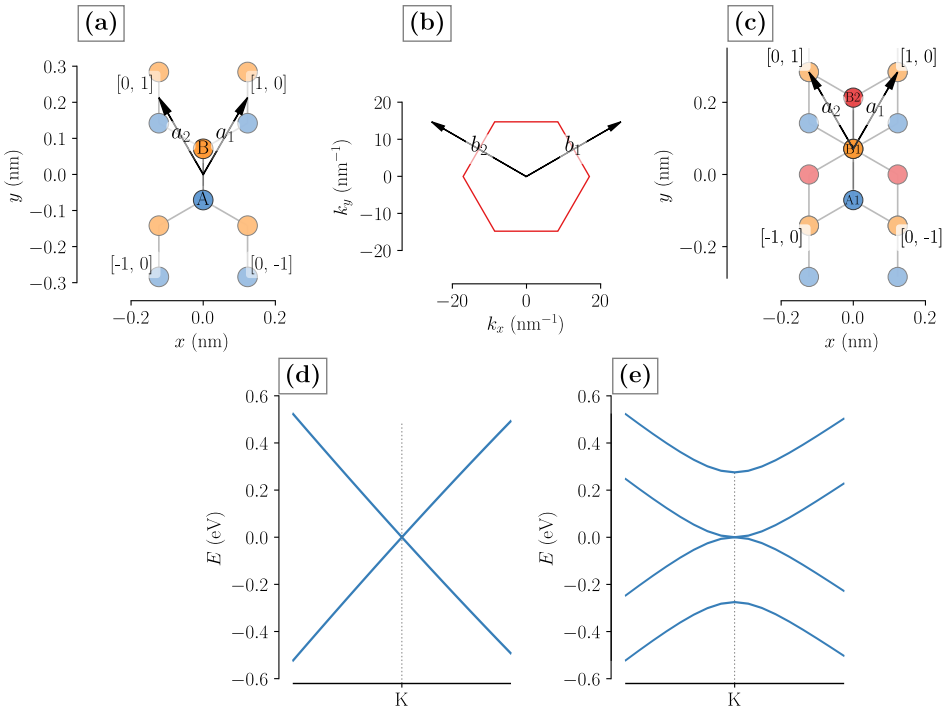

Figure 2.1: (a) Lattice of monolayer and (c) AB stacked bilayer graphene, and (b) the corresponding reciprocal lattice with the first Brillouin zone. In panels (d) and (e) bandstructure is shown in the vicinity of the high-symmetry $\boldsymbol{K}$ point for monolayer and bilayer graphene, respectively.

beside

$$\boldsymbol{\Gamma} = (0,0), \quad \boldsymbol{M} = \frac{1}{2}(\boldsymbol{b_1} + \boldsymbol{b_2}) = \left(0, \frac{2\pi}{3a_0}\right), \tag{2.11}$$

which are the center of the Brillouin zone, and the saddle point in the graphene spectrum (or the van Hove singularity), respectively.

There are two types of bonds of the outer-shell 4 electrons of carbon. The first ones are σ bonds, responsible for the structural properties, and they are well separated from the Fermi level of neutral graphene. These are in-plane bonds with bond angle of 120°. The remaining p_z electron forms the π states. Considering that there are two sublattices, one electron per sublattice (without taking into account spin degeneracy) results in zero energy Fermi level of the un-doped graphene, which makes graphene a semi-metal. Within the range of experimentally tunable Fermi energies, accurate description of the graphene low-energy spectrum can be obtained with taking into account only the p_z electrons.

Following the initial derivation by Wallace [55], and considering only the nearest neighbour coupling terms, in its simplest form, the graphene

Hamiltonian becomes

$$\hat{H} = t \sum_{\boldsymbol{R}_A, \boldsymbol{R}_B} |\Phi(\boldsymbol{R}_A)\rangle \, e^{i\boldsymbol{k}\boldsymbol{R}_A} \, \langle \Phi(\boldsymbol{R}_B)| \, e^{-i\boldsymbol{k}\boldsymbol{R}_B} + H.C. \tag{2.12}$$

Φ is the sublattice Wannier function positioned at A ($\boldsymbol{R}_A$) or B ($\boldsymbol{R}_B$), where the Bloch functions for each sublattice are

$$\Psi_A = \frac{1}{\sqrt{N}} \sum_{\boldsymbol{R}_A} \Phi(\boldsymbol{R}_A) e^{i\boldsymbol{k}\boldsymbol{R}_A}, \quad \text{and} \quad \Psi_B = \frac{1}{\sqrt{N}} \sum_{\boldsymbol{R}_B} \Phi(\boldsymbol{R}_B) e^{i\boldsymbol{k}\boldsymbol{R}_B}, \tag{2.13}$$

N being the number of unit cells. For a single unit cell and in terms of two-component spinor (wavefunction) $\Psi = (\Psi_A, \Psi_B)^T$, the Hamiltonian becomes

$$\hat{H}(\boldsymbol{k}) = \begin{bmatrix} 0 & \hat{h}(\boldsymbol{k}) \\ \hat{h}(\boldsymbol{k})^* & 0 \end{bmatrix}, \tag{2.14}$$

and

$$\hat{h}(\boldsymbol{k}) = t \sum_{i=1..3} e^{i\boldsymbol{k}\boldsymbol{\delta_i}} = 2e^{\frac{ik_y a_0}{2}} \cos \frac{k_x a_0 \sqrt{3}}{2} + e^{-ik_y a_0}. \tag{2.15}$$

The energy spectrum can be obtained by solving the eigenvalue problem

$$\hat{H}\Psi = E\Psi, \tag{2.16}$$

which leads to

$$E(\boldsymbol{k}) = \pm |h(\boldsymbol{k})| = \pm t \sqrt{3 + 2\cos\sqrt{3}k_x a_0 + 4\cos\frac{\sqrt{3}}{2}k_x a_0 \cos\frac{3}{2}k_y a_0}. \tag{2.17}$$

This is the solution of the graphene dispersion in the nearest neighbour approximation over the whole Brillouin zone, and the resulting band-structure can be seen in Fig. 2.1(d). The energy goes to zero at the $\boldsymbol{K}$ and $\boldsymbol{K'}$ points, and an expansion for $\boldsymbol{k} = \boldsymbol{K}, \boldsymbol{K'} + \boldsymbol{q}$ and small $\boldsymbol{q}$ ($\boldsymbol{q} \ll \boldsymbol{K}$) under a phase transformation that enter the spinor reads [3, 55]

$$\hat{H}_{\boldsymbol{K},\boldsymbol{K'}}(\boldsymbol{q}) = \hbar v_F \begin{bmatrix} 0 & q_x \mp i q_y \\ q_x \pm i q_y & 0 \end{bmatrix}. \tag{2.18}$$

$\boldsymbol{K}$ and $\boldsymbol{K'}$ are known as valleys in the graphene Brillouin zone. This Hamiltonian can be rewritten using the Pauli matrix representation as

$$\begin{aligned} \hat{H}_{\boldsymbol{K}}(\boldsymbol{q}) &= \hbar v_F \boldsymbol{\sigma}\boldsymbol{q}, \\ \hat{H}_{\boldsymbol{K'}}(\boldsymbol{q}) &= \hat{H}_{\boldsymbol{K}}(\boldsymbol{q})^T, \end{aligned} \tag{2.19}$$

where the Pauli matrices are (only σ_x and σ_y enter in Eq. (2.19))

$$\sigma_0 = \begin{bmatrix} 1 & 0 \\ 0 & 1, \end{bmatrix} \sigma_x = \begin{bmatrix} 0 & 1 \\ 1 & 0, \end{bmatrix} \sigma_y = \begin{bmatrix} 0 & -i \\ i & 0, \end{bmatrix} \sigma_z = \begin{bmatrix} 1 & 0 \\ 0 & -1, \end{bmatrix} \tag{2.20}$$

and $v_F = 3a_0t/(2\hbar)$ is the Fermi velocity of carriers in graphene. Around the $\boldsymbol{K}$ or $\boldsymbol{K'}$ point, the energy dispersion is linear in $\boldsymbol{q}$

$$E(\boldsymbol{q}) = \pm\hbar v_F|\boldsymbol{q}|, \tag{2.21}$$

with the wavefunction spinor

$$\begin{aligned} \Psi^{\boldsymbol{K}}(\boldsymbol{q}) &= \frac{1}{2}\begin{bmatrix} e^{-i\varphi_{\boldsymbol{q}}/2} \\ \pm e^{i\varphi_{\boldsymbol{q}}/2} \end{bmatrix}, \\ \Psi^{\boldsymbol{K'}}(\boldsymbol{q}) &= \Psi^{\boldsymbol{K}}(\boldsymbol{q})^*. \end{aligned} \tag{2.22}$$

Eq. (2.19) is a 2D analogue of Dirac-Weyl equation for massless spin 1/2 fermions (or Weyl fermions), which reveals photon-like spectrum of graphene electrons (Eq. (2.21) and Fig. 2.1(d)) with linear energy-momentum relation coming as a consequence of the massless nature of graphene low-energy electrons. The subtle difference between the two are that graphene electrons travel with a constant speed of $v_F \approx 10^6(m/s)$, which is $\approx$ 300 times smaller than the speed of light. In the case of graphene, the sublatice is taking the role of spin, hence the name of pseudo-spin. Still, the equivalence reveals experimentally observable properties that are further discussed.

In analogy with massless fermions, a *helicity* operator for graphene carriers, which is a projection of their momentum to the pseudo-spin direction, can be defined as

$$\hat{h} = \frac{1}{2}\boldsymbol{\sigma}\frac{\boldsymbol{k}}{|\boldsymbol{k}|}. \tag{2.23}$$

The helicity operator acts on the wavefunction spinor as

$$\begin{aligned} \hat{h}\Psi^{\boldsymbol{K}}(\boldsymbol{q}) &= \pm\frac{1}{2}\Psi^{\boldsymbol{K}}(\boldsymbol{q}), \\ \hat{h}\Psi^{\boldsymbol{K'}}(\boldsymbol{q}) &= \mp\frac{1}{2}\Psi^{\boldsymbol{K'}}(\boldsymbol{q}), \end{aligned} \tag{2.24}$$

and defines a well preserved helicity or equivalently *chirality* quantum number [56] as long as the carriers can be described with Eq. (2.19) and retain their massless nature.

Following from Eq. (2.19), low-energy excitations are valley decoupled. Perturbations like an electric field, entering as a term similar to $\Delta\sigma_z$, or a magnetic field which, within the Peierls approximation, is changing only the phase of the already existing coupling terms cannot couple the two in $k - space$ very distant valleys and is therefore not sufficient to induce intervalley scattering. The same applies to disorder that is smooth on the atomic scales. The Fourier transformation of such disorder introduces scattering between energy states with small $\boldsymbol{q}$ difference. In contrast, if atomic defects, such as ad-atoms or vacancies are introduced, the transfer of momentum is significant, and the valley coupling has to be included. As a result of the complexity or even impossibility of including an arbitrary type of disorder in continuum models, modelling graphene in real-space is much more versatile, and the price of the increase of the computation complexity is worth paying.

Still, properties of clean graphene can be obtained even from the simplest model. To further show this and to exemplify the consequences of chirality, one could imagine a scalar potential added to Eq. (2.19). Such a potential would act as a diagonal term in the Hamiltonian, which does not couple the two components of the pseudo-spinor, hence pseudo-spin is preserved. When graphene electrons come across a potential barrier under normal incidence, no matter the amplitude of the scattering potential, chirality is preserved and the electrons cannot backscatter. Instead, they tunnel through the classically forbidden potential, an effect that is known as *Klein tunnelling* [3, 56]. The tunnelling process can be explained as a consequence of pseudo-spin conservation and matching of the wavefunction between incident electrons and holes inside the barrier, which becomes converted again to an electron outside the barrier [57].

Beside electron scattering through potential barriers, chirality has a strong effect on the electron conductivity. If we consider graphene in a weakly disordered regime of ballistic transport, where $l_e \gg L$ where L defines the size of the system and l_e the elastic scattering length, conductivity is expected to strongly depend on the electron density. At high densities the conductivity reaches infinity (in "infinite" samples) as there is no disorder to suppress the electron motion. Analogously, at the Dirac point, vanishing density is supposed to reflect in vanishing conductivity, which is in contrast to experimental reports [29]. Conductivity at the Dirac point can be devised when considering transport through an n-p junction. The conductivity at the point where the electron becomes converted to a hole is equivalent to the former, and can be obtained through Landauer-Büttiker formalism from the transmission probabilities through a potential barrier [57] which leads to the *universal*

conductivity of $4e^2/(\pi h)$. The finite conductivity at the vanishing density additionally highlights the effect of zero gap and of quasi-relativistic electrons on the quantum transport through evanescent modes, known as *zitterbewegung* [3].

A natural extension of monolayer graphene is its bilayer analogue, which can exist in different stacking arrangements, for example AB or AA where the former is more stable. The low-energy band structure of Bernal stacked (AB or BA, Fig. 2.1(c)) bilayer graphene (BLG) is described by a 4-band $\vec{k}\cdot\vec{p}$ Hamiltonian [58, 59] and band dispersion,

$$E^{BLG}(\boldsymbol{q}) = \pm\sqrt{\hbar^2 v_F^2(q_x^2-q_y^2)+\frac{\Delta^2}{4}+\frac{t_\perp^2}{2}+r\sqrt{\frac{t_\perp^4}{4}+\hbar^2 v_F^2(q_x^2+q_y^2)(t_\perp^2+\Delta^2)}}, \tag{2.25}$$

as shown in Fig. 2.1(e). Here, $r=\pm$ indexes the low and high-energy BLG bands, Δ is the interlayer asymmetry gap, $q_{x,y}$ are the in-plane wavevectors of electrons in $K^\pm$ valleys, $t_\perp = 0.39$ eV is the interlayer coupling between dimmer sites (A and B) [60]. In contrast to the linear low-energy spectrum of monolayer graphene, spectrum of AB bilayer graphene reveals two parabolic bands at low energies, and additional two with minimum (maximum) at $\pm t_\perp$. This BLG spectrum suggests that at the energies $|E|<E_*$,

$$E_* = \frac{t_\perp|\Delta|}{2\sqrt{\Delta^2+t_\perp^2}}, \tag{2.26}$$

there are no states for electrons in a gapped bilayer, in further contrast with the monolayer where the constant applied potential serves for finely tuning the electron density and is unable to open a gap unless it spatially varies between the two sublattices (mass-term potential).

2.2 Introduction to transport methodologies and the case of graphene

Intuitively clear and well established approach of determining which of the different electronic transport regimes are at play is the comparison of different energy, time or length scales that present an averaged quantity between the two important scattering events of the same type. In that sense, elastic scattering time is the time before the electrons become scattered without changing the amplitude of their momentum, and instead

only its direction. The respective scattering length is $l_e = \tau_e v_F$, where v_F denotes the electron Fermi velocity. The elastic scattering processes are usually a result of collisions at lattice imperfections. Analogously, inelastic scattering events define the inelastic scattering time τ_{in}, which is the average timescale on which the electrons change their energy, for example due to the electron-phonon scattering, and $l_{in} = \tau_{in} v_F$ in the ballistic regime or $l_{in} = \sqrt{\mathcal{D}\tau_{in}}$ in the diffusive regime, where $\mathcal{D}$ is the diffusion coefficient. These two different scattering scales are defining the mean scattering time τ. Particularly important for coherent transport, the time before the electron loses its well defined phase defines the phase-coherence time τ_φ, $l_\varphi = \tau_\varphi v_F$ if $\tau_\varphi < \tau_e$ and $l_\varphi = \sqrt{\mathcal{D}\tau_\varphi}$ otherwise, and lastly, the size of the sample defines the scale of device length L. For example, the comparison between l_e, electron Fermi wavelength λ_F and L defines whether the transport is diffusive ($L \gg l_e, \lambda_F$) or ballistic ($L \ll l_e$). In the diffusive regime, the phase-coherence length defines whether the transport can be treated classically, $\lambda_\varphi < l_e$ or quantum mechanical treatment is necessary because of phase interference contributions for $\lambda_\varphi > l_e$. Furthermore, in the ballistic regime both l_e and l_φ are larger than the device length L, and the regime depends on the electron Fermi wavelength, where $\lambda_F \ll L$ requires classical and analogously $\lambda_F \approx L$ quantum treatment [61, 62]. In addition to the different transport regimes, there are various methodologies with which one can approach to solve the problem of electron transport. In what follows some of them are introduced while taking care about the range of their validity.

Drude model tackles the motion of electrons between two collisions in a purely classical manner, starting from the Newton's equation of motion

$$m^* \frac{d\boldsymbol{v}}{dt} = \boldsymbol{F} = -|e|(\boldsymbol{E} + \boldsymbol{v} \times \boldsymbol{B}), \tag{2.27}$$

where the effective electron mass takes into account the effect of the crystal potential, and electrons are subjected to electric ($\boldsymbol{E}$) or magnetic ($\boldsymbol{B}$) field. The effects of scattering enters through heuristic quantity of scattering time (τ) and reduces the drift velocity obtained from the equation of motion. Further, expression for the longitudinal (σ_{xx}) and Hall (σ_{xy}) conductivity can be obtained, which proves successfully in explaining the transport in metals. Magneto-transport measurements are particularly important, as from the expression for the conductivity tensor both the electron mobility (scattering time) and the carrier density can be extracted [63]. The validity of the model would be in the range of phase incoherent $L \gg l_\varphi$ and diffusive, $L \gg l_e$, transport.

Boltzmann transport equation (BTE) presents an extension of the Drude model, in which the quantum mechanical nature of electrons is accounted through the Fermi-Dirac statistics and their motion is treated semi-classically [63]

$$\frac{\partial f_i(\boldsymbol{k}_i,t)}{\partial t}+\frac{1}{\hbar}|e|(\boldsymbol{E}+\boldsymbol{v}_i\times\boldsymbol{B})\nabla_{\boldsymbol{k}_i}f_i(\boldsymbol{k}_i,t)=\left.\frac{\partial f_i(\boldsymbol{k}_i,t)}{\partial t}\right|_{collision}. \quad (2.28)$$

Still, the application of the BTE is limited and it becomes invalid when interference effects are important [3], as it solves a problem of electron distribution probability under the effect of different forces (i.e. Lorentz force) and not the amplitudes (wavefunctions), so the information about the phase is lost.

The collision term of the BTE can be obtained through the *relaxation time approximation* (RTA) which simplifies the expression to

$$\left.\frac{\partial f_i(\boldsymbol{k}_i,t)}{\partial t}\right|_{collision}=-\frac{f_i(\boldsymbol{k}_i,t)-f_i^{(0)}(\boldsymbol{k}_i,t)}{\tau_i}, \quad (2.29)$$

which accounts for the empirical scattering time of i-th subband (τ_i), similar as in the Drude's model, and introduces the timescale on which the non-equilibrium distribution $f_i(\boldsymbol{k}_i,t)$ reduces to the equilibrium one $f_i(\boldsymbol{k}_i,t)$. More rigorous description follows the *Born approximation*

$$\left.\frac{\partial f_i(\boldsymbol{k}_i,t)}{\partial t}\right|_{collision}=\sum_{\boldsymbol{k}'_j}w(\boldsymbol{k}_i,\boldsymbol{k}'_j)\left(f_{\boldsymbol{k}'_j}(1-f_{\boldsymbol{k}_i})-f_{\boldsymbol{k}_i}(1-f_{\boldsymbol{k}'_j})\right), \quad (2.30)$$

where the collision rates $w(\boldsymbol{k}_i,\boldsymbol{k}'_j)$ can be obtained from the scattering Hamiltonian $\hat{H}=\sum_{\boldsymbol{k}_i,\boldsymbol{k}'_j}V_{\boldsymbol{k}_i,\boldsymbol{k}'_j}\hat{c}^{\dagger}_{\boldsymbol{k}_i}\hat{c}_{\boldsymbol{k}'_j}$ in which $V_{\boldsymbol{k}_i,\boldsymbol{k}'_j}$ denotes the potential model of a given type of the disorder, and the *Fermi's golden rule*

$$w(\boldsymbol{k}_i,\boldsymbol{k}'_j)=\frac{2\pi}{\hbar}\left|\left\langle\boldsymbol{k}_i\left|V_{\boldsymbol{k}_i,\boldsymbol{k}_j}\right|\boldsymbol{k}'_j\right\rangle\right|. \quad (2.31)$$

The interference from multiple scattering effects are not taken into account in Eq. (2.31), which question the validity in regimes where $\tau_\varphi < \tau$ [61], and in strongly disordered systems, where it does not account for the Anderson metal-insulator transition [3]. Hence BTE is only valid when $L \gg l_\varphi$.

Instead, the *Kubo transport formalism* is a quantum-mechanical generalization of BTE that expands its validity. This formalism assumes

that the system experiences only a *weak perturbation* such that it results in a *linear* response. The Hamiltonian that describes such a system accounts for a perturbation at time t_0 while assuming that the system was in its thermodynamic equilibrium described with the Hamiltonian H_0 beforehand. In the following derivation of the conductivity tensor Ref. [64] is closely followed.

Prior to the perturbation, the system is attached to a thermal bath and the probability to be in a particular state ($\hat{H}_0 |\Psi_n\rangle = E_n |\Psi_n\rangle$) is determined by the Boltzman distribution

$$P(E_n) = \frac{1}{Z} e^{-\beta E_n}, \quad \beta = k_B T, \tag{2.32}$$

which for a system expressed through the Hamiltonian H_0 can be accounted through the *density matrix operator* ρ

$$\rho = e^{-\beta H_0} = \sum_{n=1}^{N} |\Psi_n\rangle \, e^{-\beta E_n} \, \langle \Psi_n| \,, \tag{2.33}$$

and the *partition function* Z

$$Z = \sum_{n=1}^{N} \langle \Psi_n \, |\hat{\rho} \, |\Psi_n\rangle = \mathrm{Tr}[\rho]. \tag{2.34}$$

From Eqs. (2.33) and (2.34) an expectation value for an arbitrary operator can be derived

$$\langle A \rangle = \frac{1}{Z} \sum_{n=1}^{N} \langle \Psi_n \, |\hat{A} \, |\Psi_n\rangle \, e^{-\beta E_n} = \frac{\mathrm{Tr}[\rho A]}{\mathrm{Tr}[\rho]}. \tag{2.35}$$

Note that in the term $\langle A \rangle_0$ the operator notation is left out because it represents an expectation value. After the system is perturbed the Hamiltonian can be described as

$$\hat{H}(t) = \hat{H}_0 + \hat{H}'(t)\theta(t - t_0), \tag{2.36}$$

where $\theta(t - t_0)$ denotes a step function. Even for $t > t_0$ the system is still described by the same Boltzman distribution, while the expectation value is described with time-evolved eigenstates of H_0

$$\langle A(t > t_0) \rangle = \frac{1}{Z_0} \sum_{n=1}^{N} \langle \Psi_n(t) \, |\hat{A} \, |\Psi_n(t)\rangle \, e^{-\beta E_n} = \frac{\mathrm{Tr}[\rho A]}{Z_0}, \tag{2.37}$$

where Z_0 denotes the partition function of the unperturbed Hamiltonian H_0. The time evolution of the state vectors and the operators can be defined in the interaction picture [64] that splits the contribution from the trivial Hamiltonian in the equilibrium (which is assumed to be the only time-independent quantity) and the perturbation

$$\begin{aligned} \left|\hat{\Psi}_n\right\rangle &= e^{i\hat{H}_0 t/\hbar} \left|\Psi_n\right\rangle, \\ \hat{A}(t) &= e^{i\hat{H}_0 t/\hbar} \hat{A} e^{-i\hat{H}_0 t/\hbar}. \end{aligned} \tag{2.38}$$

Time derivative of the state vector

$$i\hbar\partial_t \left|\hat{\Psi}_n\right\rangle = e^{i\hat{H}_0 t/\hbar} \hat{H}' \left|\Psi_n\right\rangle, \tag{2.39}$$

shows that the time-evolution will only depend on the perturbative part of the Hamiltonian, which leads to defining an operator $\hat{U}(t, t_0)$

$$\left|\hat{\Psi}_n\right\rangle = \hat{U}(t, t_0) \left|\hat{\Psi}_n(t_0)\right\rangle, \tag{2.40}$$

that evolves the state vectors. Combining Eq. (2.39) now for $\hat{U}(t, t_0)$ together with the boundary condition $\hat{U}(t_0, t_0) = 1$, operator $\hat{U}$ can be obtained by solving the following equation

$$\hat{U}(t, t_0) = 1 + \frac{1}{i\hbar} \int_{t_0}^{t} \hat{H}'(t') \hat{U}(t', t_0) dt', \tag{2.41}$$

which in the approximation of weak-perturbation reads

$$\hat{U}(t, t_0) \approx 1 - \frac{i}{\hbar} \int_{t_0}^{t} \hat{H}'(t') dt'. \tag{2.42}$$

Combining Eqs. (2.37), (2.38), and (2.40) leads to an expression which depends on the eigen-states of the unperturbed Hamiltonian

$$\begin{aligned} \langle A(t > t_0) \rangle = \frac{1}{Z_0} \sum_{n=1}^{N} e^{-\beta E_n} \\ \langle \Psi_n(t_0) | e^{-i\hat{H}_0 t_0/\hbar} \hat{U}^\dagger(t, t_0) e^{i\hat{H}_0 t/\hbar} \hat{A} e^{-i\hat{H}_0 t/\hbar} \hat{U}(t, t_0) e^{i\hat{H}_0 t_0/\hbar} \left|\Psi_n(t_0)\right\rangle, \end{aligned} \tag{2.43}$$

which due to Eq. (2.42) in the regime of linear response (higher-order

terms in $\hat{H}'$ are neglected) becomes

$$\begin{aligned}\langle A(t>t_0)\rangle &= \frac{1}{Z_0}\sum_{n=1}^{N}\langle\Psi_n(t_0)\,|\hat{A}(t)\,|\Psi_n(t_0)\rangle\, e^{-\beta E_n}\\ &-\frac{i}{\hbar}\int_{t_0}^{t}\frac{1}{Z_0}\sum_{n=1}^{N}\langle\Psi_n(t_0)\,|\hat{A}(t)\hat{H}'(t')-\hat{H}'(t')\hat{A}(t)\,|\Psi_n(t_0)\rangle\, e^{-\beta E_n}dt'\\ \langle A(t>t_0)\rangle &= \langle A\rangle_0 - \frac{i}{\hbar}\int_{t_0}^{t}\left\langle\left[\hat{A}(t),\hat{H}'(t')\right]\right\rangle_0 dt'.\end{aligned} \tag{2.44}$$

The importance of this expression lies in the fact that the non-equilibrium response can be calculated from strictly equilibrium expectation values, where the perturbative terms are accounted through the correlation function that modifies the operator. If we assume that the perturbation happened at $t_0 \to -\infty$, the previous equation can be rewritten

$$\begin{aligned}\delta\langle A(t)\rangle &= \langle A(t)\rangle - \langle A\rangle_0\\ &= \lim_{\eta\to 0^+} -\frac{i}{\hbar}\int_{-\infty}^{\infty}\left\langle\left[\hat{A}(t),\hat{H}'(t')\right]\right\rangle_0 e^{-\eta(t-t')}dt',\end{aligned} \tag{2.45}$$

where infinitesimally small η accounts for the divergent behaviour at $t \gg t'$. Expression (2.45) is also known as *Kubo linear response formula* and can account for any response to a weak perturbation given by $\hat{H}'$.

If one derives an explicit response current in a sample perturbed with an electro-magnetic field the *Kubo conductivity tensor* $\sigma_{\alpha,\beta}(\boldsymbol{r},\boldsymbol{r'},t,t')$ is given by [64]

$$J_\alpha(\boldsymbol{r},t) = \int dt'\int d\boldsymbol{r}'\sum_\beta \sigma_{\alpha,\beta}(\boldsymbol{r},\boldsymbol{r'},t,t')E_\beta(\boldsymbol{r}',t'), \tag{2.46}$$

which is assumed to be both time and space non-local, and expresses the current response $\boldsymbol{J} = J\boldsymbol{i_\alpha}$ subjected to $\boldsymbol{E} = E\boldsymbol{i_\beta}$, $\boldsymbol{i_{\alpha,\beta}}$ being the unit vectors along the two directions. To obtain the current, the expectation value of the current operator is needed ($\boldsymbol{J} = -e\langle\boldsymbol{J}\rangle$ for electrons). The current operator can be defined as a sum of two parts, diamagnetic, that is proportional to the magnetic vector potential and the paramagnetic part proportional to the gradient of the wave-function

$$\begin{aligned}\hat{\boldsymbol{J}}(\boldsymbol{r}) &= \hat{\boldsymbol{J}}^{param}(\boldsymbol{r}) + \hat{\boldsymbol{J}}^{diam}(\boldsymbol{r}),\\ \hat{\boldsymbol{J}}^{param}(\boldsymbol{r}) &= -\frac{i\hbar}{2m}\left[\Psi^\dagger(\boldsymbol{r})\left(\nabla\Psi(\boldsymbol{r})\right) - \left(\nabla\Psi^\dagger(\boldsymbol{r})\right)\Psi(\boldsymbol{r})\right],\\ \hat{\boldsymbol{J}}^{diam}(\boldsymbol{r}) &= -\frac{|e|}{m}\boldsymbol{A}(\boldsymbol{r})\Psi^\dagger(\boldsymbol{r})\Psi(\boldsymbol{r}).\end{aligned} \tag{2.47}$$

The perturbation Hamiltonian has two parts

$$\hat{H}'(t) = -|e| \int \hat{\rho}(\boldsymbol{r})\phi(\boldsymbol{r},t)d\boldsymbol{r} + |e| \int \hat{\boldsymbol{J}}(\boldsymbol{r})\boldsymbol{A}'(\boldsymbol{r},t)d\boldsymbol{r}, \tag{2.48}$$

where $\hat{\rho}(\boldsymbol{r})$ is the density operator and ϕ is the electrostatic potential than can be gauge neglected. The total magnetic vector potential has two components

$$\boldsymbol{A} = \boldsymbol{A}^0 + \boldsymbol{A}', \tag{2.49}$$

prior to the perturbation, $\boldsymbol{A}^0$, and after, $\boldsymbol{A}'$. Further, not all of the components from Eq. (2.47) needs deriving. For example, in Eq. (2.48) the total current can be replaced with the diamagnetic part and the contribution from the equilibrium state vector potential $\boldsymbol{A}^0$, as the component due to the perturbation would result in a non-linear dependence in $\boldsymbol{E}$. This current will be denoted as $\boldsymbol{J}^0$ Additionally, when computing the expectation value of the component induced by the perturbation, in the Kubo formula the current-current correlation function will result in higher-order terms in $\boldsymbol{E}$. Hence, terms next to $\boldsymbol{A}'$ can be taken in linear order. These simplifications when combined with the Kubo formula from Eq. (2.45) further lead to

$$\begin{aligned}
\left\langle \boldsymbol{J}^0 \right\rangle &= \left\langle \boldsymbol{J}^{param} - \frac{|e|}{m}\boldsymbol{A}^0(\boldsymbol{r})\rho(\boldsymbol{r}) \right\rangle \\
&= \left\langle J^0 \right\rangle_0 - \\
&\quad \frac{i}{\hbar}\int d\boldsymbol{r'} \int dt' \left\langle \left[\hat{\boldsymbol{J}}^0(\boldsymbol{r},t), \hat{\boldsymbol{J}}^0(\boldsymbol{r'},t')\right] \boldsymbol{A}'(\boldsymbol{r},t') \right\rangle_0, \\
\left\langle \frac{|e|}{m}\boldsymbol{A}'(\boldsymbol{r},t)\rho(\boldsymbol{r}) \right\rangle &= \frac{|e|}{m}\boldsymbol{A}'(\boldsymbol{r},t)\left\langle \rho(\boldsymbol{r}) \right\rangle_0, \\
\left\langle \boldsymbol{J} \right\rangle &= \left\langle \boldsymbol{J}^0(\boldsymbol{r}) \right\rangle - \left\langle \frac{|e|}{m}\boldsymbol{A}'(\boldsymbol{r},t)\rho(\boldsymbol{r}) \right\rangle,
\end{aligned} \tag{2.50}$$

where $\left\langle J^0 \right\rangle_0 = 0$ as the J^0 is the equilibrium current. Under the assumption of linearity in time of the conductivity, $\sigma(\mathrm{r},\mathrm{r}',t,t') = \sigma(\mathrm{r},\mathrm{r}',t-t')$, using $\boldsymbol{E}(\boldsymbol{r},\omega) = i\omega\boldsymbol{A}'(\boldsymbol{r},\omega)$ and $H'(\omega) = |e|/(i\omega)\int \boldsymbol{J}^0(\boldsymbol{r})\boldsymbol{E}(\boldsymbol{r},\omega)d\boldsymbol{r}$ the Fourier transformation ($X(t) = \int \exp(-i\omega t)X(\omega)d\omega$) of Eq. (2.50) becomes

$$\begin{aligned}
J_\alpha(\boldsymbol{r},\omega) = &-\frac{i|e|^2}{\hbar}\int dt \int dt' e^{-i\omega t} \sum_\beta \left\langle \left[\hat{\boldsymbol{J}}^0_\alpha(\boldsymbol{r},t), \hat{\boldsymbol{J}}^0_\beta(\boldsymbol{r'},t')\right] \boldsymbol{A}'_\alpha(\boldsymbol{r},t') \right\rangle_0 \\
&- i\frac{|e|^2}{\omega m}\boldsymbol{E}(\boldsymbol{r},\omega)\left\langle \rho(\boldsymbol{r}) \right\rangle_0 \delta_{\boldsymbol{r}-\boldsymbol{r'}}\delta_{\alpha,\beta},
\end{aligned} \tag{2.51}$$

where the second term is a paramagnetic response that is local in space. The conductivity tensor can also be expressed in the frequency domain

$$J_\alpha(\boldsymbol{r},\omega) = \int d\boldsymbol{r'} \sum_\beta \sigma_{\alpha,\beta}(\boldsymbol{r},\boldsymbol{r'},\omega) E_\beta(\boldsymbol{r'},\omega), \tag{2.52}$$

which, when combined with Eq. (2.51), leads to the final expression for the conductivity

$$\begin{aligned}
\sigma_{\alpha,\beta}(\omega) &= \sigma^g_{\alpha,\beta}(\omega) + \frac{e^2}{i\omega} S_{\alpha,\beta}(\omega), \\
\sigma^g_{\alpha,\beta}(\omega) &= -\frac{|e|^2}{\omega m} \left\langle \rho(\boldsymbol{r}) \right\rangle_0 \delta_{\boldsymbol{r}-\boldsymbol{r'}} \delta_{\alpha,\beta} \\
S_{\alpha,\beta}(\omega) &= \int d\boldsymbol{r'} \int dt \int dt' \sum_\beta -\frac{i}{\hbar} e^{-i\omega t} \left\langle \left[\hat{\boldsymbol{J}}^0_\alpha(\boldsymbol{r},t), \hat{\boldsymbol{J}}^0_\beta(\boldsymbol{r'},t') \right] \right\rangle_0 ,
\end{aligned} \tag{2.53}$$

which can be used for obtaining the frequency dependent conductivity in the linear response regime. This formula is particularly important as it presents the starting point of all transport related calculations in this work. Various ways to compute this formula, or its analogue in the zero frequency ($\omega \to 0$) that is also known as Kubo-Bastin conductivity [65], will be discussed in Sec. 2.3.6.

For the sake of completeness, the *Landauer-Büttiker* method will be briefly discussed as a method that is more appropriate in the case of finite size and in the ballistic transport regime where $l_e \gg L$. The Landauer method for obtaining transport properties relies on the very intuitive connection between the transmission probabilities of carriers (electrons) that travel through the nano-device, also known as the scattering region, which is attached to two-contacts (terminals, leads). From these assumptions the following sample-specific conductance can be derived [66] (previously conductivity was discussed)

$$G = \frac{2e^2}{h} \sum_{i=1}^{N_{modes}} \int T_i(E) \left(-\frac{\partial f_{FD}}{\partial E} \right) dE, \tag{2.54}$$

in which T_i denotes the transmission probability for the i^{th} mode (out of N_{modes}) supported by the nano-device that accounts for the scattering effects and f_{FD} is the Fermi-Dirac distribution. Büttiker has generalized this formula to account for multi-terminal devices. The interested reader can find detailed comparison between Kubo and Landauer-Büttiker in Sec. 3 in [61] and Sec. 2 in [67].

For the particular case of graphene, peculiar properties such as its universal conductivity cannot be explained within the semi-classical description of the BTE from Eq. (2.28) (without further corrections), which is also the case when discussing weak anti-localization or ballistic regime of weakly scattering electrons in graphene. Still, BTE agrees with fully quantum descriptions in the case of high electron density, or in the diffusive regime in the presence of strong disorder that does not induce localization (more precisely $k_F l_e \gg 1$) [3, 57, 61]. Hence, to fully describe the transport properties of graphene in the presence of various disorder effects and over a wide range of carrier concentration, a fully quantum mechanical approach such as the Kubo theory is more suitable, especially in the *real space description* where disorder is not treated perturbatively. Although the numerical effort increases because of the complexity of the approach, there exist techniques for computing the quantum transport that scale almost linearly with the size of the simulated Hilbert space, and those will be discussed in the following section.

2.3 Numerical methodology

2.3.1 Spectral Methods and Chebyshev Polynomial Expansion

To start with, a function of interest can be expanded and explicitly represented as an infinite sum

$$f(x) = \sum_{m=0}^{\infty} c_m p_m(x), \tag{2.55}$$

where c_m and $p_m(x)$ represent the expansion coefficients and a family of expansion polynomials, respectively.

For expanding a bounded function, in the general case, the best choice are the Chebyshev polynomials, due to their uniform convergence along the whole interval [68], where the first kind, T_n and second kind U_n are defined in their trigonometric form

$$\begin{aligned} T_m(x) &= \cos(m \arccos(x)), \\ U_m(x) &= \frac{\sin((m+1)\arccos(x))}{\sin(\arccos(x))}, \end{aligned} \tag{2.56}$$

with the orthogonality relations defined by the two scalar products $\langle..|..\rangle_{1,2}$

$$\begin{aligned}
\langle f|g\rangle_1 &= \int_{-1}^{+1} \frac{f(x)g(x)}{\pi\sqrt{1-x^2}}dx, & \langle T_m(x)|T_n(x)\rangle_1 &= \frac{1+\delta_{m,0}}{2}\delta_{m,n}, \\
\langle f|g\rangle_2 &= \int_{-1}^{+1} \pi\sqrt{1-x^2}f(x)g(x)dx, & \langle U_m(x)|U_n(x)\rangle_2 &= \frac{1+\delta_{m,0}}{2}\delta_{m,n}.
\end{aligned} \tag{2.57}$$

The first 5 polynomials of both the first and the second kind are shown in Fig. 2.2. Based on the their trigonometric representation, recursion relations reads

$$\begin{aligned}
T_{m+1}(x) &= 2xT_m(x) - T_{m-1}(x), \quad T_0(x) = 1, \quad T_1(x) = x, \\
U_{m+1}(x) &= 2xU_m(x) - U_{m-1}(x), \quad U_0(x) = 1, \quad U_1(x) = 2x.
\end{aligned} \tag{2.58}$$

Given Eqs. (2.55) and (2.57), the coefficients of the target function

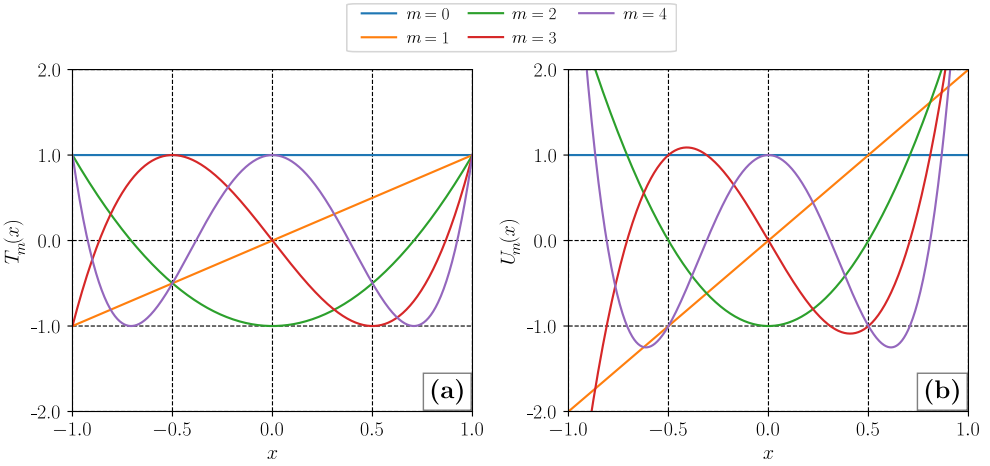

Figure 2.2: Chebyshev polynomials of the (a) first and (b) second kind.

evaluated in terms of Chebyshev polynomials of the first kind can be defined as

$$c_m = \frac{\langle f|T_m\rangle_1}{\langle T_m|T_m\rangle_1} = \frac{2}{1+\delta_{m,0}}\int_{-1}^{+1}\frac{T_m(x)f(x)}{\pi\sqrt{1-x^2}}dx. \tag{2.59}$$

When describing a system with its TB model, the variable x will be related to the Hamiltonian matrix whose spectral properties one would like to evaluate. Therefore, the integration in Eq. (2.59) with a weight function $\omega(x) = 1/\left(\pi\sqrt{1-x^2}\right)$ before obtaining the coefficients c_m would introduce a deviation from a simple iterative scheme like in Eq. (2.58) [69]. For this reason it is more useful to define a set of

modified coefficients which will be called moments in the following part. Starting with the expansion

$$f(x) = \sum_{m=0}^{\infty} c'_m(x)\Phi_m(x). \tag{2.60}$$

in terms of functions $\Phi_m(x) = T_m(x)/(\pi\sqrt{1-x^2})$ that satisfies

$$\begin{aligned} \langle T_m|T_m\rangle_1 &= \langle \Phi_m|\Phi_m\rangle_2 \,, \quad \text{and} \\ \langle f|\Phi_m\rangle_2 &= \int_{-1}^{+1} T_m(x)f(x)dx, \end{aligned} \tag{2.61}$$

similar as in Eq. (2.59) the coefficients read

$$c'_m(x) = \frac{\langle f|\Phi_m\rangle_2}{\langle \Phi_m|\Phi_m\rangle_2} = \pi\sqrt{1-x^2}\frac{2}{1+\delta_{m,0}}\int_{-1}^{+1} T_m(x)f(x)dx, \tag{2.62}$$

and the modified moments take the simple expression

$$\mu_m = \int_{-1}^{+1} T_m(x)f(x)dx, \tag{2.63}$$

which does not depend on the variable x, and the target function reads

$$f(x) = \frac{1}{\pi\sqrt{1-x^2}}\sum_{m=0}^{\infty}\frac{2}{1+\delta_{m,0}}\mu_m T_m(x). \tag{2.64}$$

When the function is evaluated, the infinite sum in Eq. (2.64) is truncated to a finite number of polynomials M. Similar to the approximation of Fourier series, the finite number of expansion terms results in Gibbs oscillations which can be suppressed by introducing a damping kernel factor, which modifies Eq. (2.64) into

$$f(x) \approx f_{KPM}(x) = \frac{1}{\pi\sqrt{1-x^2}}\sum_{m=0}^{M-1}\frac{2}{1+\delta_{m,0}}g_m\mu_m T_m(x), \tag{2.65}$$

where g_m is the chosen kernel, M is the number of polynomials in the truncated series. This expansion formulates the kernel polynomial method (KPM) [69]. For example, two of the most used kernels are Jackson:

$$\begin{aligned} g_m^J = \frac{1}{M+1}\Bigg((M-m+1)\cos\left(\frac{\pi m}{M+1}\right) + \\ \sin\left(\frac{\pi m}{M+1}\right)\cot\left(\frac{\pi}{M+1}\right)\Bigg), \end{aligned} \tag{2.66}$$

regarded as a best general purpose kernel [69] and Lorentz:

$$g_m^L = \frac{\sinh(\lambda(1 - m/M))}{\sinh(\lambda)}, \tag{2.67}$$

where λ is taken as an arbitrary real number, but empirical choice suggests $\lambda \in [3, 5]$ and is the best kernel choice for evaluating Green's function [69]. Broadening induced by the Lorentz kernel can be defined as $\eta \approx \lambda/M$. In Fig. 2.3 expansion in terms of Chebyshev polynomials are shown with and without the use of kernel, where the Gibbs oscillations can be seen around the discontinuity.

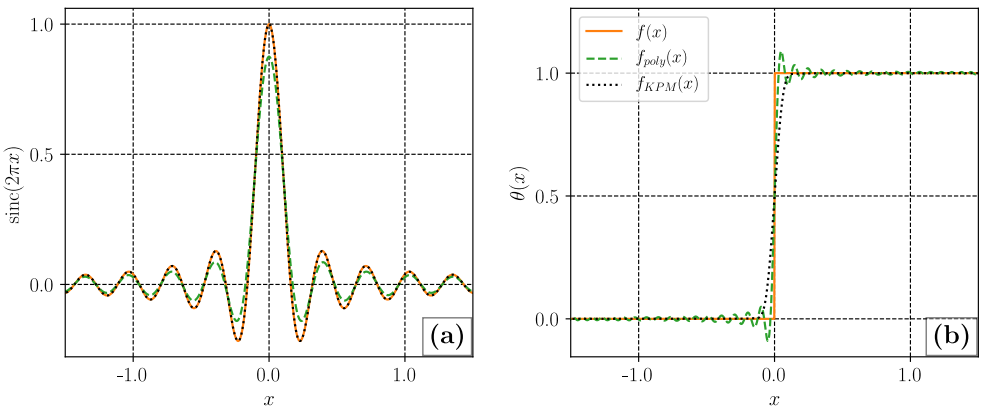

Figure 2.3: Chebyshev polynomial expansion f_{poly} and KPM expansion f_{KPM} using Jackson kernel with $M = 128$ of (a) $\mathrm{sinc}(2\pi x)$ and (b) Heaviside $\theta(x)$.

2.3.2 KPM and TB matrices

The polynomial expansion introduced in Sec. 2.3.1 can be easily extended to the application on matrices (operators). In such a way a desired function (operator) can be obtained without the necessity to perform direct diagonalisation, which enormously limits the performance and determines the size limits of the simulated system. Instead, polynomial expansions lead to obtaining expression which scale linearly or more precisely almost linearly with the size of the matrices.

In addition, TB problems are by their nature spectrum-bounded. The Hamiltonian obtained from matching the bandstructure calculation obtained from the density-functional theory (DFT), or phenomenologically describing the system otherwise unfeasible to DFT codes, is always describing the electronic properties within a certain energy range. To

be able to use the KPM for obtaining spectral properties of such Hamiltonians, the matrices have to be scaled such that its spectrum coincides with the domain of the Chebyshev polynomials $x \in [-1, +1]$. This can be simply satisfied by obtaining the maximal E_{max} and minimal E_{min} Hamiltonian eigenvalue, for example by means of the power method for finding a dominant eigenvalues [70] (Ch. 22). The scaled Hamiltonian and the corresponding energy then become

$$\tilde{H} = (\hat{H} - a_+ I)/a_-, \quad \tilde{E} = (E - a_+)/a_-, \tag{2.68}$$

where the scaling factors are related to the bounds of the Hamiltonian spectrum

$$a_+ = \frac{E_{max} + E_{min}}{2}, \quad a_- = \frac{E_{max} - E_{min}}{2 - \varepsilon}. \tag{2.69}$$

A small positive number ε is added to exclude the range limits, thus $\tilde{E} \in (-1, +1)$.

2.3.3 Spectral and the Green's function operator

The KPM can be further applied for obtaining two ubiquitous operators when speaking about spectral properties which are certainly the Dirac delta or simply the spectral operator, and the Green's function operator. Starting with the first one, KPM expansion reads

$$\begin{aligned} \tilde{\delta}(\tilde{E} - \tilde{H}) &\approx \frac{1}{\pi\sqrt{1 - \tilde{E}^2}} \sum_{m=0}^{M-1} \frac{2}{1 + \delta_{m,0}} g_m \mu_m T_m(\tilde{E}), \\ \mu_m &= \int_{-1}^{+1} \delta(\tilde{E} - \tilde{H}) T_m(\tilde{E}) d\tilde{E} \\ &= T_m(\tilde{H}). \end{aligned} \tag{2.70}$$

Single-particle Green's function of a non-interacting TB problem is an impulse response of the Hamiltonian operator. Starting from the time independent Schrödinger equation

$$[E - \hat{H}]\Psi = 0, \tag{2.71}$$

Green's function can be defined as

$$[E - \hat{H}]\hat{G}(E, \hat{H}) = 1, \quad \hat{G}(E, \hat{H}) = \frac{1}{E - \hat{H}}, \tag{2.72}$$

which is ill-posed at $E = E_k$, E_k being the solutions of the eigenvalue problem in Eq. (2.71). Following a limiting procedure, two sets of Green's functions are defined

$$\hat{G}(E, \hat{H}, \eta)^{\pm} = \frac{1}{E - \hat{H} \pm i\eta}, \quad \eta \to 0^{+}. \tag{2.73}$$

$\hat{G}^{+}$ and $\hat{G}^{-}$ are conventionally named *retarded* and *advanced* Green's function, as the corresponding Fourier transformation reveals their backwards and forwards in time-propagating nature, respectively [62]. Using Sokhotsli-Plemelj formula

$$\lim_{\eta \to 0^{+}} \frac{1}{x \pm i\eta} = \mp i\pi\delta(x) + \mathcal{P}\left(\frac{1}{x}\right), \tag{2.74}$$

the KPM expansion of $G^{\pm}(E, \hat{H}, \eta)$ can be split into two parts

$$\begin{aligned} &\mathrm{Im}\hat{G}^{\pm}(E, \hat{H}, \eta) = \mp\pi\hat{\delta}(E - \hat{H}), \\ &\mathrm{Re}\hat{G}^{\pm}(E, \hat{H}, \eta) = \mathcal{P}\left(\frac{1}{E - \hat{H}}\right) = \mp\frac{1}{\pi}\mathcal{P}\int_{-\infty}^{+\infty} \frac{\mathrm{Im}\hat{G}^{\pm}(E', \hat{H}, \eta)dE'}{E - E'}. \end{aligned} \tag{2.75}$$

Combining Eqs. (2.70) and (2.75), KPM expansion of the imaginary part of Green's operator reads

$$\mathrm{Im}\tilde{G}^{\pm}(\tilde{E}, \tilde{H}, \tilde{\eta}) \approx \mp\frac{1}{\sqrt{1 - \tilde{E}^2}} \sum_{m=0}^{M-1} \frac{2}{1 + \delta_{m,0}} g_m T_m(\tilde{E}) T_m(\tilde{H}). \tag{2.76}$$

The real part of Green's function derives from Eq. (2.75),

$$\mathrm{Re}\tilde{G}^{\pm}(\tilde{E}, \tilde{H}, \eta) \approx \sum_{m=0}^{M-1} \frac{2}{1 + \delta_{m,0}} g_m T_m(\tilde{H}) \mathcal{P}\int_{-\infty}^{+\infty} \frac{T_m(\tilde{E})}{(\tilde{E} - \tilde{E}')\sqrt{1 - \tilde{E}^2}} dE', \tag{2.77}$$

which, combined with $\mathcal{P}\int_{-1}^{+1} T_m(y)dy/((y - x)\sqrt{1 - y^2}) = \pi U_{m-1}(x)$ reads

$$\mathrm{Re}\tilde{G}^{\pm}(\tilde{E}, \tilde{H}, \tilde{\eta}) \approx \sum_{m=0}^{M-1} \frac{2}{1 + \delta_{m,0}} g_m T_m(\tilde{H}) U_{m-1}(x). \tag{2.78}$$

Finally, Green's function is obtained by combining Eqs. (2.76) and (2.78) and taking the two kinds of polynomials in their explicit form from Eq. (2.56)

$$\tilde{G}^{\pm}(\tilde{E}, \tilde{H}, \tilde{\eta}) \approx \sum_{m=0}^{M-1} \frac{\mp 2i}{1 + \delta_{m,0}} g_m T_m(\tilde{H}) e^{\pm im \arccos(\tilde{E})}. \tag{2.79}$$

2.3.4 Chebyshev polynomial Green's function and the exact expansion

As a powerful alternative to the KPM, an exact expansion of the Green's function can be derived following Ref. [71]. Returning to Eq. (2.73) and making use of the relation between the real-space Green's function and its Fourier transformation [72]

$$i\hat{G}^{\pm}(t,\hat{H}) = \frac{i}{2\pi}\int \hat{G}^{\pm}(E,\hat{H},\eta)e^{-iEt/\hbar}dE = \theta(t)e^{-i\hat{H}t/\hbar}e^{\mp\eta t/\hbar}, \quad (2.80)$$

and using the identity for the expansion of the propagator derived in [73] we obtain

$$e^{-ixz} = \sum_{m=0}^{\infty}\frac{2i^{-n}}{1+\delta_{m,0}}J_m(z)T_m(x), \quad |x|\leq 1, \quad (2.81)$$

and the Green's function becomes

$$\tilde{G}^{\pm}(\tilde{E},\tilde{H},\tilde{\eta}) = -i\int_0^{\infty} e^{i\tilde{E}t/\hbar}e^{i\mp\tilde{\eta}t/\hbar}\sum_{m=0}^{\infty}\frac{2i^{-m}}{1+\delta_{m,0}}J_m(t)T_m(\tilde{H})dt, \quad (2.82)$$

which combined with the Laplace transformation of the Bessel function

$$\int_0^{\infty} e^{-st}J_m(t)dt = \frac{1}{\sqrt{1+s^2}}\left(\sqrt{1+s^2}-s\right)^m \quad (2.83)$$

leads to the final expansion of the Green's function [71]

$$\begin{aligned}\tilde{G}^{\pm}(\tilde{E},\tilde{H},\tilde{\eta}) &= \sum_{m=0}^{\infty} g_m(\tilde{E}\pm i\tilde{\eta})T_m(\tilde{H}),\\ g_m(z) &= \frac{2i^{-1}}{1+\delta_{m,0}}\frac{\left(z-i\sqrt{1-z^2}\right)^n}{\sqrt{1-z^2}}.\end{aligned} \quad (2.84)$$

As a natural energy scale η acts as a broadening factor in the expression (2.84) defining the probing resolution of the expansion.

To compare CPGF and KPM the two approximations of the Lorentzian curve are shown in Fig. 2.4. In addition to the well defined resolution introduced in the expressions (Fig. 2.4(c)), CPGF also converges faster to the desired accuracy than KPM for the same probing resolution, as shown in Fig. 2.4(d) for a large graphene sample in the presence of a dilute concentration of vacancy disorder.

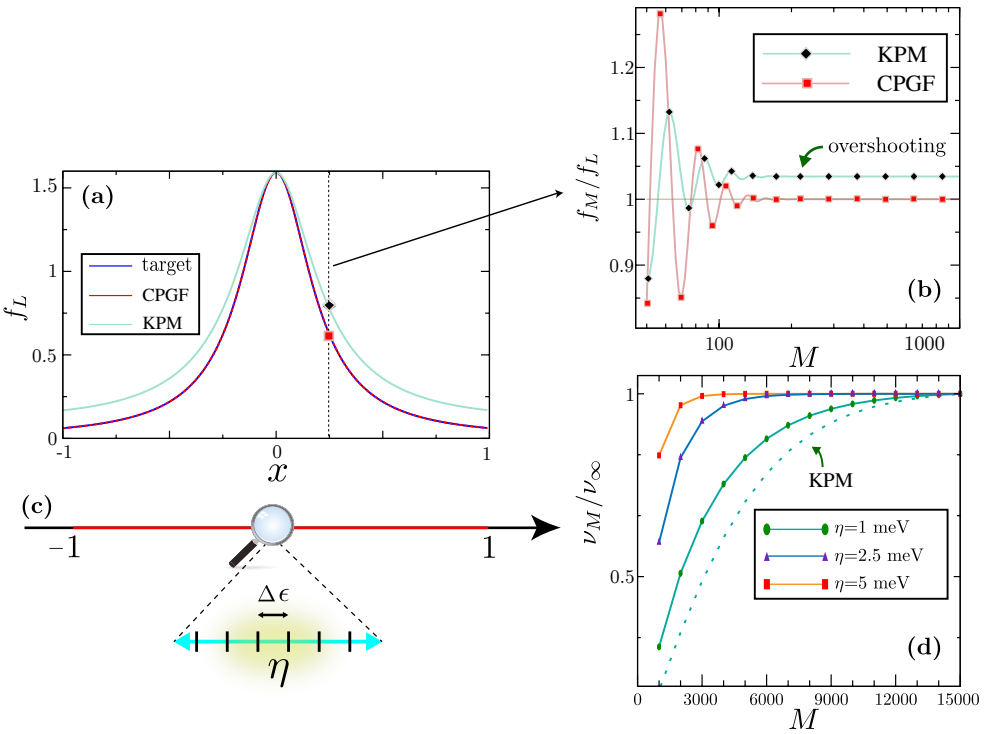

Figure 2.4: (a) Approximation to the Lorentzian curve $f_L(x)$ using the KPM with a Lorentz kernel [69] and the numerically exact CPGF method [74]. (b) Spectral convergence of the M^{th}-order approximation to the target function. For large M, KPM converges to $f_M/f_L > 1$ (overshooting), while the CPGF is asymptotically exact $f_M/f_L \to 1$. (c) Energy resolution ("broadening") η and energy level separation $\Delta\epsilon$ for simulations in a finite system. (d) Convergence of M^{th}-order approximation to the DOS at the band center of a giant honeycomb lattice with 60000×60000 sites and vacancy defect concentration of 0.4%. As a guide to the eye, the ratio of the DOS normalized to its converged value (to 0.1% accuracy) is plotted. The DOS obtained from a KPM expansion with a Lorentz kernel is shown for $\eta = 1$ meV. Panel (d) is adapted from Ref. [74]. Figure is taken from Ref. [75].

2.3.5 Evaluating the moments

The moments described in Eq. (2.70) are nothing other than a simple expectation value, where $\left\langle \alpha \left| T_m(\tilde{H}) \right| \alpha \right\rangle$ defines a dot product and should not be confused with scalar products defining the Chebyshev polynomials orthogonality relations in Eq. (2.57). This type of moments can be

represented in a more general form as

$$\mu_m = \left\langle \beta \left| \hat{A} T_m(\tilde{H}) \right| \alpha \right\rangle, \tag{2.85}$$

where α and β are arbitrary state vectors, and $\hat{A}$ is an additional operator which acts on the Hamiltonian expansion. Combining Eqs. (2.58) and (2.70) such moments can be obtained through efficient and robust recursion

$$\begin{aligned} |\alpha_0\rangle = |\alpha\rangle\,, \quad |\alpha_1\rangle = \tilde{H}\,|\alpha\rangle \\ |\alpha_{m+1}\rangle = 2\tilde{H}\,|\alpha_m\rangle - |\alpha_{m-1}\rangle\,, \end{aligned} \tag{2.86}$$

which results in

$$\mu_m = \left\langle \beta \left| \hat{A} \right| \alpha_m \right\rangle, \tag{2.87}$$

and explains the numerical procedure for obtaining the initial function, with repeating recursion M times (M being the total number of polynomials) on the initial state vector, calculating the dot product and reconstructing the function with obtained moments.

A special case of moments, present when discussing about global properties of the Hamiltonian operators, would require a trace over its expectation values, which can be efficiently estimated following the *stochastic trace evaluation technique* (STE) [76]

$$\mathrm{Tr}H \approx \frac{1}{R} \sum_{r=1}^{R} \langle r|\hat{H}|r\rangle, \tag{2.88}$$

with random vectors $|r\rangle = \sum_{i=1}^{N} \xi_i |i\rangle$. The choice of appropriate random variables ξ_i, either real- or complex-valued (depending on the type of Hamiltonian), should satisfy the following statistics: $\langle\langle \xi_i \rangle\rangle = 0$, $\langle\langle \xi_i \xi_{i'} \rangle\rangle = 0$ and $\langle\langle \xi_i^\star \xi_{i'} \rangle\rangle = \delta_{i,i'}$ [69, 76], where $\langle\langle .. \rangle\rangle$ denotes the statistical average. For example, appropriate choice of random vectors for complex-valued Hamiltonians would be a random phase vector $|r\rangle = \sum_{i=1}^{N} e^{\theta_i} |i\rangle$, where θ_i obtains its values from a uniform distribution on the interval $[0, 2\pi)$. Equivalently, for real-valued Hamiltonians, a choice of a random sign vector $|r\rangle = \sum_{i=1}^{N} \pm 1 |i\rangle$ where ξ_i is initiated randomly between ± 1, satisfies the statistical requirements [76]. The STE reduces the complexity of the trace calculation from N^2 to $R \times N$ where R is the number of random vectors with $R \ll N$, which is especially true for sparse matrices of large dimensions, further allowing substantial savings in computational time.

2.3.6 Application of the Chebyshev expansions

Throughout the following chapters, KPM or similar techniques have been used to obtain different spectral properties of TB Hamiltonians such as LDOS, DOS, DC conductivity or spin evolution. This section solely introduces the expansions for obtaining each one of them and in addition in the following chapter, different code implementations of the Chebyshev expansion are introduced and followed by a set of simple, yet instructive examples which reflect on the flexibility of the methods.

DOS

The density of states of a Hamiltonian matrix $\hat{H}$ with eigenvalues E_n is

$$\rho(E) = \frac{1}{N}\sum_{n=0}^{N-1}\delta(E - E_n), \tag{2.89}$$

which can be represented in terms of the spectral operator

$$\rho(E) = \frac{1}{N}\sum_{n=0}^{N-1}\langle n|\,\hat{\delta}(E-\hat{H})\,|n\rangle\,, \tag{2.90}$$

Combining Eq. (2.70) and Eq. (2.88) for the approximation of the trace, the final expression for DOS reads

$$\tilde{\rho}(\tilde{E}) = \frac{1}{N}\frac{1}{\pi\sqrt{1-\tilde{E}^2}}\sum_{m=0}^{M-1}\frac{2}{1+\delta_{m,0}}g_m\mu_m T_m(\tilde{E}), \tag{2.91}$$

with

$$\mu_m = \frac{1}{R}\sum_{r=1}^{R}\langle r|\,T_m(\tilde{H})\,|r\rangle\,. \tag{2.92}$$

For example, the evaluation of Chebyshev moments of the DOS function of a disordered system requires a total number of operations scaling as

$$P_{\mathrm{DOS}} = Z \times N \times M \times R \times S, \tag{2.93}$$

where Z is the coordination number, N is the size of the Hilbert space, R the number of random vectors, M the number of moments and S is the number of disorder realisations (for clean systems $S = 1$).

LDOS

Local density of states can be obtained in a similar manner

$$\rho_i(E) = \delta(E - E_i) \langle i| \hat{\delta}(E - \hat{H}) |i\rangle , \tag{2.94}$$

where the moments present simply individual diagonal terms from the expectation matrix, withouth the need to perform the trace (Tr) operation

$$\tilde{\rho}_i(\tilde{E}) = \frac{1}{D} \frac{1}{\pi\sqrt{1-\tilde{E}^2}} \sum_{m=0}^{M-1} \frac{2}{1+\delta_{m,0}} g_m \mu_m T_m(\tilde{E}), \tag{2.95}$$

where

$$\mu_m = \langle i| T_m(\tilde{H}) |i\rangle . \tag{2.96}$$

Kubo-Bastin DC conductivity tensor

The numerical approximation of the DC Kubo conductivity in the linear response regime from Eq. (2.53) starts from Bastin's simplification in the limit of zero frequency $\omega \to 0$ [65], which is also known as Kubo-Bastin conductivity, and reads

$$\begin{aligned} \sigma_{\alpha\beta}(\mu, T) = \frac{ie^2\hbar}{\Omega} \int_{-\infty}^{\infty} dE f(E, \mu, T) \\ \times \mathrm{Tr} \left\langle v_\alpha \hat{\delta}(E - \hat{H}) v_\beta \frac{d\hat{G}^+(E, \hat{H})}{dE} - v_\alpha \frac{d\hat{G}^-(E, \hat{H})}{dE} v_\beta \hat{\delta}(E - \hat{H}) \right\rangle . \end{aligned} \tag{2.97}$$

Functions $\hat{G}^\pm$ and δ are further expanded in terms of Chebyshev polynomials [77] and defined as a M^{th} order expansion

$$\begin{aligned} \tilde{G}^\pm(\tilde{E}, \tilde{H}) &\approx \mp \frac{2i}{\sqrt{1-\tilde{E}^2}} \sum_{m=0}^{M-1} g_m \frac{e^{\pm im \arccos(\tilde{E})}}{\delta_{m,0}+1} T_m(\tilde{H}), \\ \tilde{\delta}(\tilde{E} - \tilde{H}) &\approx \frac{2}{\pi\sqrt{1-\tilde{E}^2}} \sum_{m=0}^{M-1} g_m \frac{T_m(\tilde{E})}{\delta_{m,0}+1} T_m(\tilde{H}), \end{aligned} \tag{2.98}$$

as defined in Eqs. (2.70) and (2.79), where $\tilde{E}$ and $\tilde{H}$ are the scaled energy and the scaled Hamiltonian, respectively. The final expression reads

$$\begin{aligned} \sigma_{\alpha\beta}(\mu, T) \approx & \frac{4e^2\hbar}{\pi\Omega} \frac{4\eta^2}{\Delta E^2} \times \\ & \int_{-\eta}^{\eta} d\tilde{E} \frac{f(\tilde{E}, \tilde{\mu}, T)}{(1-\tilde{E}^2)^2} \sum_{m_1=0, m_2=0}^{M-1, M-1} \Gamma_{m_1 m_2}(\tilde{E}) \mu_{m_1 m_2}^{\alpha\beta}, \end{aligned} \tag{2.99}$$

with

$$\mu^{\alpha\beta}_{m_1m_2} = \frac{g_{m_1}g_{m_2}}{(1+\delta_{m_1,0})(1+\delta_{m_2,0})} Tr\left[\tilde{v}_\alpha T_{m_1}(\tilde{H})\tilde{v}_\beta T_{m_2}(\tilde{H})\right], \tag{2.100}$$

$$\begin{aligned}\Gamma_{m_1m_2}(\tilde{E}) = (\tilde{E} - im_1\sqrt{1-\tilde{E}^2})e^{im_1 \arccos(\tilde{E})}T_{m_1}(\tilde{E}) \\ + (\tilde{E} + im_2\sqrt{1-\tilde{E}^2})e^{-im_2 \arccos(\tilde{E})}T_{m_2}(\tilde{E}),\end{aligned} \tag{2.101}$$

where μ is the chemical potential, T the temperature, Ω is the area of the structure, $T_{m_1,m_2}(\tilde{H})$ Chebyshev polynomial expansions of the scaled Hamiltonian, $f(\tilde{E},\tilde{\mu},T) = 1/(1+e^{(\tilde{E}-\tilde{\mu})/k_{\tilde{B}}T})$ is the Fermi-Dirac distribution, and $\tilde{v}_\alpha$ is the velocity component in the α direction given by the Heisenberg expression $\boldsymbol{v} = -i\left[\boldsymbol{l}, H\right]/\hbar$, where $\boldsymbol{l}$ is the distance vector.

Efficient evaluation Following the STE, the trace of the matrix $\tilde{v}_\alpha T_{m_1}(\tilde{H})\tilde{v}_\beta T_{m_2}(\tilde{H})$ can be effectively approximated as an average over random phase vectors [76]

$$\begin{aligned}Tr\left[\tilde{v}_\alpha T_{m_1}(\tilde{H})\tilde{v}_\beta T_{m_2}(\tilde{H})\right] \approx \\ \frac{1}{R}\sum_{r=1}^{R}\langle r\left|\tilde{v}_\alpha T_{m_1}(\tilde{H})\tilde{v}_\beta T_{m_2}(\tilde{H})\right| r\rangle,\end{aligned} \tag{2.102}$$

where the random vectors are defined as discussed in Sec. 2.3.5, N is defined by the size of the Hamiltonian H, and R is the number of random vectors. If we examine the most demanding part, the calculation of the Chebyshev moments – $\mu_{m_1m_2}$, which requires a double polynomial expansion, there are two ways to solve it. One is by expanding all the vectors $|\tilde{r}_{m_2}\rangle = \tilde{v}_\beta T_{m_2}|r\rangle$ for each of the vectors $|\tilde{r}_{m_1}\rangle = T_{m_1}|\tilde{r}_{m_1}\rangle$. In this way we only have to store two vectors in each part that are used in the recursion. An alternative is to split the double iteration into two independent parts, $|\tilde{r}_{m_2}\rangle = \tilde{v}_\beta T_{m_2}|r\rangle$ and $|\tilde{r}_{m_1}\rangle = T_{m_1}\tilde{v}_\alpha|r\rangle$. This requires the use of a large amount of memory because all the vectors in the iterations must be stored. The first approach can be efficiently used on GPUs, where one can perform fast sparse matrix - vector multiplication. When a large amount of fast storing memory needs to be used, this can only be done on the RAM, therefore the second approach is more suitable for CPUs. A mixed approach can use benefits of both methods, where we can save as many vectors as we have available memory on the GPU.

At zero temperature the set of equations simplifies, and the calculation of the longitudinal conductivity for a single Fermi energy can be done with the same $\mathcal{O}(P)$ complexity [71, 78] (Eq. 2.93) as needed for the DOS expansion [69], which is used in the following sections to calculate the longitudinal DC conductivity in large samples. Still, this approach includes only the contributions from the Fermi surface of a given system, and does not take into account all the states from the Fermi sea, therefore it is not applicable to a general calculation of the Hall conductivity, where the latter might be crucial.

Time evolution

The time propagation for any time-independent Hamiltonian is determined by the time-evolution operator $\hat{U}(\hat{H}, t)$ according to

$$|\psi(t)\rangle = e^{-i\hat{H}t/\hbar}|\psi(0)\rangle = \hat{U}(\hat{H}, t)|\psi(0)\rangle, \tag{2.103}$$

where $|\psi(0)\rangle$ is the initial state, and provides the description of a real-space propagation of a wave-packet $|\psi(t)\rangle$ [79, 80].

The spectral expansion of the time-evolution operator in terms of Chebyshev polynomials of the first kind is given by [81]

$$\tilde{U}(\tilde{H}, \Delta t) = \tilde{U}(\tilde{H}, t - t_0) = e^{-ia_+\Delta t/\hbar} \sum_{m=0}^{M-1} \frac{2}{1+\delta_{m,0}} c_m(a_-\Delta t/\hbar) T_m(\tilde{H}), \tag{2.104}$$

where $\tilde{H}$ is the rescaled Hamiltonian with eigenvalues in the interval $E \in (-1, +1)$, $a_\pm$ are the scaling factors defined in Eq. (2.69). The Chebyshev expansion coefficients are defined as

$$c_m(a_-\Delta t/\hbar) = \int_{-1}^{1} \frac{T_m(\tilde{E}) e^{-i\tilde{E}a_-\Delta t/\hbar}}{\pi\sqrt{1-\tilde{E}^2}} d\tilde{E} = (-1)^m J_m(a_-\Delta t/\hbar), \tag{2.105}$$

where J_m are the Bessel functions of the first kind and

$$J_m(a_-\Delta t/\hbar) \approx \frac{1}{\sqrt{2\pi m}} \left(\frac{e a_- \Delta t}{2\hbar m}\right)^m, \tag{2.106}$$

for $m \to \infty$. Note that this formula allows us to estimate the number of coefficients required to converge to a given accuracy. Importantly, the convergence is exponential so the cost for performing unitary evolution is well below the cost of Kubo calculations.

Expectation values The time-evolution is valuable for obtaining time-dependent expectation values of a given operator $\hat{A}$

$$\left\langle \Psi(0)|\hat{U}(\hat{H},t)^{\dagger}\hat{A}\hat{U}(\hat{H},t)|\Psi(0)\right\rangle . \tag{2.107}$$

For example, spin operator along an arbitrary direction can be defined as

$$\hat{S}^{\alpha}=\frac{\hbar}{2}(\boldsymbol{u}_x\hat{\sigma}_x+\boldsymbol{u}_y\hat{\sigma}_y+\boldsymbol{u}_z\hat{\sigma}_z), \tag{2.108}$$

where $\boldsymbol{u}_x$, $\boldsymbol{u}_y$, $\boldsymbol{u}_z$ are the unit vectors and σ_i are the Pauli matrices as defined in Eq. (2.20).

This expansion proves usefull when considering spin-relaxation by computing the time evolution of a pre-defined wave packet in a system where spin-orbit coupling is present, as shown in the following section. The expression for the spin-relaxation reads

$$S_{relax}=\left\langle \Psi_0|\hat{U}(t)^{\dagger}\hat{S}^{\alpha}\hat{U}(t)|\Psi_0\right\rangle , \tag{2.109}$$

where $\Psi(0)$ denotes a pre-defined wave packet, being non-zero only in a small region inside the simulated system, with a well defined spin-expectation value. Further, inserting Eq.(2.104) into Eq. (2.109) an expression for the spin-relaxation (decay) expanded in terms of Chebyshev polynomials T_m is obtained

$$S_{relax}=\sum_{m_1=0,m_2=0}^{M-1,M-1}\mu_{m_1}(\Delta t)\mu_{m_2}(\Delta t)\left\langle \Psi_0\right|T_{m_1}(\tilde{H})\hat{S}^{\alpha}T_{m_2}(\tilde{H})\left|\Psi_0\right\rangle , \tag{2.110}$$

where

$$\mu_m(\Delta t)=e^{-ia_+\Delta t\hbar}\frac{2}{1+\delta_{m,0}}c_m(a_-\Delta t/\hbar)T_m(\tilde{H}), \tag{2.111}$$

which is very similar to the full-spectrum of the Kubo DC conductivity in linear response. In terms of the numerical implementation, Eq. (2.110) can be naively evaluated with complexity $M^2\times N_t$, where N_t is the total number of propagation timesteps, and the needed number of polynomials M for each timestep, as shown in Eq. (2.106), is much smaller as compared to the computation of the Kubo formula. Still, if one examines more closely, the left part of the expansion $\langle L_p\,|=\sum_{m_1}\langle\Psi(0)|\,T_{m_1}(\tilde{H})$, which is a conjugate of the right part $|R_p\rangle=\sum_{m_2}T_{m_2}(\tilde{H})\,|\Psi(0)\rangle$, the computation can be simplified as only one half of the recursion needs computing. Finally, the complexity becomes $M\times N_t$, which is of the

same order as the computation of the single-shot conductivity, as outlined in Sec. 2.3.6.

Additional quantities that will prove important for the later discussions are the mean-square displacement, which defines the diffusion coefficient, and the mean displacement that will define the position of wave-packet at a given moment in time. Starting again from Eqs. (2.107) and (2.104), the desired displacement ($disp$) and mean-square displacement (msq) read

$$\begin{aligned} D_{i,mean} = & \sum_{m_1=0,m_2=0}^{M-1,M-1} \mu_{m_1}(\Delta t)\mu_{m_2}(\Delta t) \\ & \langle\Psi(0)|\, T_{m_1}(\tilde{H})(\hat{x}_i - x_{0,i})T_{m_2}(\tilde{H})\,|\Psi(0)\rangle\,, \\ D_{i,msq} = & \sum_{m_1=0,m_2=0}^{M-1,M-1} \mu_{m_1}(\Delta t)\mu_{m_2}(\Delta t) \\ & \langle\Psi(0)|\, T_{m_1}(\tilde{H})(\hat{x}_i - x_{0,i})^2T_{m_2}(\tilde{H})\,|\Psi(0)\rangle\,, \end{aligned} \tag{2.112}$$

$i = \{x, y\}$ (considering 2D propagation), $\hat{x}$ is the coordinate operator and $x_{0,i}$ is the initial position of the wave packet.

In addition, the calculation of the mean-square displacement of a wave-packet can be employed for obtaining the conductivity through the Einstein relation [82, 83]

$$\sigma(E) = e^2\rho(E)\mathcal{D} = e^2\rho(E)\lim_{t\to\infty}\frac{1}{2}\frac{d}{dt}\Delta X^2(E,t), \tag{2.113}$$

where $\rho(E)$ represents the density of states, and $\mathcal{D}$ is the diffusion coefficient. Such an approach allows distinguishing which regime of transport the system exibits, ballistic, diffusive, or localized, based on the properties of the diffusion coefficient [61], and requires the same complexity as the single-shot approach.

2.3.7 Absorbing boundary conditions

When we want to study only bulk properties of materials, a very large system or appropriate boundary conditions are needed. As the maximal size of the system depends on the computational resources available, it is usually suitable to impose boundary conditions rather than to increase the system size. The periodicity of the structure is relatively easy to implement for basic structures in the TB model, as we need only a well defined unit cell. The problem appears for more complex structures,

as is the case of bilayer moiré patterns with an arbitrary twist angle between the layers, in particular for the case of incommensurate stacking between the two layers for which the unit cell is not well defined. When a magnetic field is added, it breaks the lattice translational symmetry. In this case the periodicity of the magnetic vector potential and the unit cell of the moiré must match, which imposes on top of discrete values of the field a specific periodic gauge for the vector potential. However, if we apply the so-called absorbing boundary conditions the above limitations are lifted, and the calculation can be done for arbitrary magnetic field. A drawback is in the slight increase of the calculation time because of two additional matrix-vector multiplications, as shown below.

One may say that none of these choices is perfect, because periodic boundary conditions give discrete states around the Dirac point and increase the number of the sampling $\boldsymbol{k}$ points in the inverse space needed, while absorbing boundary conditions can give false reflections, which results in a finite increase of low-energy states. Depending on the particular purpose, one should choose the most appropriate approximation, which in the case of twisted bilayer graphene is the latter one.

The procedure for the application of absorbing boundary conditions is the following [84]. The recursion relation for the regular Chebyshev expansion reads

$$|r_m\rangle = 2\tilde{H}\,|r_{m-1}\rangle - |r_{m-2}\rangle\,, \tag{2.114}$$

which in the presence of the absorbing boundary is changed to[85]

$$|r_m\rangle = e^{-\gamma}\left[2\tilde{H}\,|r_{m-1}\rangle - e^{-\gamma}\,|r_{m-2}\rangle\right], \tag{2.115}$$

in order to account for the damping of the wave functions at the edges of the system.

The initial conditions for the modified recursion relation in Eq. (2.115) are now: $|r_0\rangle = \left|e^{i\phi_i}\right\rangle$ and $|r_1\rangle = e^{-\gamma}H\,|r_0\rangle$. We also set the initial random vectors in Eq. (2.102) to have non-zero elements only in the region where there is no absorption, and therefore the reconstruction of the expanded functions [84, 85] is analogous to the reconstruction obtained in the absence of the absorbing potential.

The function $\gamma(x)$ is a position dependent damping factor adopted from Refs. [86] and [87] as $\gamma(x) = \sinh^{-1}[V(x)]$. $\Gamma(x) = -iV(x)$ is defined as the complex absorbing potential (CAP)

$$\Gamma(x) = -i\left(\frac{2\pi}{\Delta x}\right)^2 f(x'), \tag{2.116}$$

where $\Delta x = x_2 - x_1$ is the width of the absorbing region. Finally, $f(x')$ is non-zero only between x_1 and x_2

$$f(x') = \frac{4}{(c - x')^2} + \frac{4}{(c + x')^2} - \frac{8}{c^2}, \tag{2.117}$$

where $x' = c(x - x_1)/\Delta x$, while $c = 2.62$ is a numerical constant. Similar absorbing potential can be defined in a cylindrical geometry, where γ depends only on the radial direction and is non-zero in the absorbing region.

Two different vectors in Eq. (2.115) need to be multiplied by the absorbing function, but we can simplify and remove one product with the following modification of the Hamiltonian $\tilde{H}_{\text{abs}} = 2e^{-\gamma}\tilde{H}$

$$|r_m\rangle = \tilde{H}_{abs}\,|r_{m-1}\rangle - e^{-2\gamma}\,|r_{m-2}\rangle\,. \tag{2.118}$$

3 | Numerical modelling: Code implementations of KPM in Pybinding and KITE

Computational modelling has become an essential tool in both fundamental and applied research that has propelled the discovery of new materials and their translation into practical applications [88]. The study of condensed phases of matter has benefited from significant advances in electronic structure theory and simulation methodologies. Among these advances are: explicitly correlated wave-function-based techniques achieving sub-chemical accuracy [89], first-principles methods to tackling electronic excitations [90], charge-self-consistent atomistic models for accurate electronic structure calculations [91], and the use of machine learning as means to finding density functionals without solving the Khon-Sham equations [92, 93].

Semi-empirical atomistic methods are amongst the most simple and effective methods to calculate ground- and excited-state properties of materials [94–97]. The increasingly popular tight-binding approach [43] has been employed for accurate and fast calculations of total energies and electronic structure in complex materials, including semiconductors [98, 99], quantum dots [100] and superlattices [101, 102], and is particularly well-suited for implementation of $\mathcal{O}(N)$ (linear scaling) algorithms for efficient calculations of total energies and forces [103].

Accurate tight-binding models have been devised for a plethora of model systems, ranging from metals to ionic materials [104], and shown to correctly predict the optical spectra of multi-shell structures with atomic-scale variations in composition [97], layer-thickness dependence of energy gaps in strained-layer semiconductor superlattices [101], and fine spectral features in the Hofstader butterfly of moiré graphene superlattices [78]. Tables of energy (hopping) integrals for many elements and crystal structures can be found in the literature (see e.g. [105]),

while new tight-binding parameterisations can be easily constructed by fitting to experimental data or ab initio calculations. Foulkes and Haydock showed that the tight-binding approximation emerges as a stationary solution to density functional theory [106], which has provided a solid foundation to improve the accuracy of the tight-binding scheme. Environment-dependent tight-binding models, capturing the essential features of charge transfer and local environmental dependence of overlap integrals (e.g., to reproduce lattice deformations under strain [107]), have further improved the transferability and robustness of the tight-binding approach [104, 108–111].

A key feature of the real-space empirical TB approach is its versatility. It can accommodate disorder, strain, magnetic interactions and external perturbations (see Appendix A), and, as such, provides a particularly attractive framework to tackle realistic non-equilibrium device conditions in nanosystems and mesoscopic structures [83]. Recent methodological developments exploiting accurate spectral expansions of TB Green's functions are rendering an efficient description of ever-larger and complex systems. The underlying principle in the spectral approach—firmly rooted in the Chebyshev spectral method [68]—consists in expanding the lattice Green's function in orthogonal polynomials by means of an efficient and stable recursive procedure [68, 69, 78]. Recent applications include studies of dynamical correlations in the Anderson model [69], charge transport in graphene [48, 112], Monte Carlo simulations [113–115] and matrix product states [116]. Because spectral expansions are fully nonperturbative (in some cases numerically exact [74, 117]), they also provide a solid benchmark for analytical methods that can be subsequently used to shed light onto the underlying microscopic mechanisms.

Some open-source codes already exist and cover different aspects of computational modelling of electronic structure and quantum transport properties of TB models [83]. For example, KWANT is based on the Landauer-Büttiker formalism and the wave-function-matching technique for obtaining transport properties from the transmission probabilities of nanodevices which act as scattering regions [118]. PythTB [119] is a Python package with which tight-binding Hamiltonians can be easily setup and basic quantities, such as the energy dispersion relation or densities of states, can be calculated for small computational domains. GPUQT is a transport code fully implemented for the use on graphical processor units (GPUs), where the size of simulated domains are limited by the device memory to 2×10^7 [120]. ESSEX-GHOST [121] and TBTK [122], are C++ codes based on the kernel polynomial method

that provide Chebyshev expansions of the Green's functions for tight-binding models.

In the following, two implementations of TB codes, Pybinding and KITE, are introduced. Although Pybinding is predominantly used for modelling of systems presented in this thesis, hence the examples will be covered in different chapters, the focus of this section will be on the newly developed KITE code, introducing the possibilities the code offers, covering the development ideas that provide efficient implementations of some of the concepts already discussed, and on benchmarking the code. Both codes heavily rely on the basic theoretical concepts of the TB models and on the methodology of the spectral approaches that are introduced in Ch. 2. Regarding the KITE project, as a part of the presented work, my contributions are related to the connection between Pybinding and KITE, which include building a user friendly interface, and further, work related to the wave-packet propagation, which includes implementations of this particular module together with J. M. V. P. Lopes, and a part that is often neglected when discussing about the scientific software that includes testing and benchmarking the code on various computational infrastructures.[1]

3.1 Pybinding

The Pybinding TB code developed by D. Moldovan at the University of Antwerp [123] provides a straightforward definition of orbitals and spin degrees of freedom, on-site energies and hopping parameters, together with the user friendly possibility to introduce a modification to the Hamiltonian by specifying the desired function. It provides a Python interface to the core written in C++, which are combined to setup and model finite size systems with disorder, strains, magnetic fields, adatoms, or similar phenomena. A simple example script for the graphene honeycomb lattice with nearest neighbour hopping is shown below.

Listing 3.1: Setting up the tight-binding Hamiltonian.

```
a = 0.24595  # [nm] unit cell length
a_cc = 0.142 # [nm] carbon-carbon distance
t = -2.8     # [eV] nearest neighbour pz-pz hopping
# create a lattice with 2 primitive vectors
lat = pb.Lattice(
    a1=[a, 0],
    a2=[a/2, a/2*sqrt(3)])
# add orbitals 'A' and 'B' (sublattices)
```

[1] The results of this chapter are available as: S. M. João, M. Anđelković, L. Covaci, T. Rappoport, J. M. V. P. Lopes and A. Ferreira, arXiv:1910.05194 (2019).

```
lat.add_sublattices(
    ('A', [0, -a_cc/2]),
    ('B', [0,  a_cc/2]))
# add hoppings
lat.add_hoppings(
    # inside the main cell
    ([0,  0], 'A', 'B', t),
    # between neighbouring cells
    ([1, -1], 'A', 'B', t),
    ([0, -1], 'A', 'B', t))
```

The simplicity of defining different models, together with their intuitive construction being offered by a scripting language such as Python makes Pybinding suitable for use even without any programming expertise. The basic idea is to construct a model which has different components, such as an underlying *lattice*, that defines the lattice of a desired crystal and includes parametrised TB matrix elements, *modifiers*, that introduce changes to the resulting TB Hamiltonian, or *shapes* that define a sample of a finite size. The methodology relies on exact diagonalisation techniques that make use of SciPy eigensolvers (Arpack or Lapack), or differently, on the spectral methods, where Pybinding implements the kernel polynomial method [69] introduced in Ch. 2.

Different contributions in the Pybinding code arising as a consequence of the necessity to compute particular properties that were not previously available are essential for the work presented. For example, the implementation of the conductivity tensor [77] and the efficient single-shot conductivity [71], which are introduced in Sec. 2.3.6, resulted from the need to simulate electronic transport properties in moiré patterns in twisted bilayer graphene. At arbitrary rotations these systems can have in the general case very large unit cells or even be incommensurate, which introduces a major problem in defining a lattice that is the foundation of the periodic TB system. In this particular case, absorbing boundary conditions, introduced in Sec. 2.3.7 where implemented in Pybinding, which gave us access to non-periodic systems and arbitrary rotation angles, while at the same time suppressing any edge and finite size effects. Different implementations discussed here can be accessed on the author's Github page [124]. In addition, in the spirit of the open science initiative, different scripts used for simulating systems that are discussed in this thesis together with this thesis and related works are available on the same Github page.

To reflect more on the use of Pybinding without providing further detailed examples, different electronic properties, such as band-structure calculations, spatial electron density distributions, global density of states, and transport properties in the linear response using Kubo formula (Sec. 2.2) were computed and provide examples of the use of Pybinding

for modelling much more complex systems when compared to the simple case of graphene. These were applied to delaminated bilayers (Ch. 4.1), the modelling of flat bands in the periodic-pseudo-magnetic field (Ch. 5), the majority of the calculations on twisted bilayer graphene (Ch. 6) and super-moiré patterns (Ch. 7) in encapsulated graphene.

3.2 KITE

KITE is a general purpose open-source tight-binding software for accurate real-space simulations of electronic structure and quantum transport properties of large-scale molecular and condensed systems with tens of billions of atomic orbitals ($N \sim 10^{10}$). KITE's core is written in C++, with a versatile Python-based interface, and is fully optimised for shared memory multi-node CPU architectures, thus scalable, efficient and fast. At the core of KITE is a seamless spectral expansion of lattice Green's functions, which enables large-scale calculations of generic target functions with uniform convergence and fine control over energy resolution. Several functionalities are demonstrated, ranging from simulations of local density of states and photo-emission spectroscopy of disordered materials to large-scale computations of optical conductivity tensors and real-space wave-packet propagation in the presence of magneto-static fields and spin-orbit coupling. On-the-fly calculations of real-space Green's functions are carried out with an efficient domain decomposition technique, allowing KITE to achieve *nearly ideal linear scaling* in its multi-threading performance. Crystalline defects and disorder, including vacancies, adsorbates and charged impurity centers, can be easily set up with KITE's intuitive interface, paving the way to user-friendly large-scale quantum simulations of equilibrium and non-equilibrium properties of molecules, disordered crystals and heterostructures subject to a variety of perturbations and external conditions.

Previous numerical implementations real-space quantum transport, either based on linear response theory or the non-equilibrium Green's function method [125], have so far been limited to mesoscopic structures with up to ten millions of orbitals [48, 50, 53, 77, 83, 112, 126], hampering the extraction of maximum mileage from the tight-binding scheme (except for a recent report, where Kubo calculations with billions of atoms $N = 3.6 \times 10^9$ were demonstrated [74]). The accessible energy resolution η in tight-binding calculations is fundamentally bounded by the typical mean level spacing of the spectrum $\eta \gtrsim \delta E$. On the other hand, large-scale calculations (with energy resolution on the order of mili-electron-

Volt (meV) and below) are vital, for example, to capture fine details of multifractal spectra approaching a quantum critical point [127] or in studies of spin-orbit coupled transport effects, where a correct treatment of 4-point vertex functions (e.g., spin Hall conductivity) requires fully converged calculations with fine η [128].

In this environment, KITE strives to bring the spectral expansions methods applied to tight-binding simulations to the next level in accessible system sizes and energy resolution. It combines the easy setup of the Python-based packages with a highly optimised and robust C++ core that handles memory-intensive large-scale simulations efficiently. The strengths of KITE rely on a combination of significant improvements in *versatility, accuracy, speed, and scalability.*

Accuracy and speed: Target functions are computed employing efficient spectral algorithms based on a *numerically exact* Chebyshev polynomial expansion of Green's functions discovered independently by A. Ferreira and E. Mucciolo [74, 129] and A. Braun and P. Schmitteckert [117]. KITE exploits the locality of interactions to employ a multiscale memory management scheme that improves data affinity and dramatically reduces the computation time.

Versatility: KITE's code uses as input arbitrary TB models that can be imported from standard formats or defined directly via its versatile and user-friendly Pybinding interface. The same Python interface can be used to setup the desired type of disorder, either as vacancies, charge, or spin disorder, utilising an intuitive "disorder cell" approach. The model and calculation parameters can be set up, without the need to recompile the core C++ code.

Methodology and Implementation: A large-RAM "single-shot" recursive algorithm developed by one of us enables the evaluation of Fermi surface properties for systems with multi billions of orbitals $N \sim 10^{10}$ [129]. In TB models with small coordination number $[Z = \mathcal{O}(1)]$, the numerical evaluation of $T = 0$ DC conductivity (with tens thousands of spectral coefficients for each Green's function) takes only a few hours on large-memory nodes with 16 cores [74]. This gives access to accuracy and energy resolutions up to 3 orders of magnitude beyond previous approaches [78]. To assess response tensors $\hat{\sigma}(\omega, T)$ at finite temperature/frequency, KITE implements its accurate spectral approach to carry out a direct evaluation of the Kubo-Bastin formula as proposed by J.H. Garcia, L. Covaci and T. G. Rappoport in Ref. [77]. The same method is employed to evaluate non-linear optical conductivities of non-interacting systems, following Ref. [130].

Functionalities: The first version of KITE contains the following

functionalities:

- average density of states (DOS) and local DOS (LDOS);
- spectral function;
- generic multi-orbital local (on-site) and bond disorder;
- linear response DC conductivity tensors;
- linear and non-linear optical (AC) conductivity tensors;
- wave-packet propagation,

for generic TB models, in the presence of magnetic fields and disorder.

Scalability: Quantum transport calculations in disordered conductors and complex structures with large unit cells (e.g., twisted bilayers of two-dimensional materials) require large-scale simulations. To optimise multi-threading and speed up spectral expansions, KITE provides the option to thread pre-defined partitions in real space (i.e., lattice domains) through a domain decomposition technique in close resemblance to the ones used in specialised pseudospectral and spectral techniques for solving partial differential equations [68, 131].

3.2.1 Organization and general description of the KITE code

KITE is designed and optimised to maximize system sizes, to improve self-averaging and to achieve fine energy resolution. TB Hamiltonian matrices have typically $\mathcal{O}(Z \times N)$ non-zero entries. The elementary matrix-vector multiplication that lies at the heart of the Chebyshev iteration could be done with any standard sparse matrix scheme if all the non-zero entries of the Hamiltonian are stored [121]. Depending on the lattice, the storage of the Hamiltonian can be a relevant computational cost. Using graphene as an example, if one considers the first and second neighbour hoppings, the number of non-zero elements of the Hamiltonian is $18N$, which is much larger than the $2N$ elements needed to store the two random vectors for the CPGF recursion. KITE was designed to benefit from the periodic nature of the underlying lattice and avoid the storage of the periodic part of the Hamiltonian by using a set of pattern rules to encode it.

Within this section we review the design options that rule KITE's development in order to maximise its efficiency and flexibility.

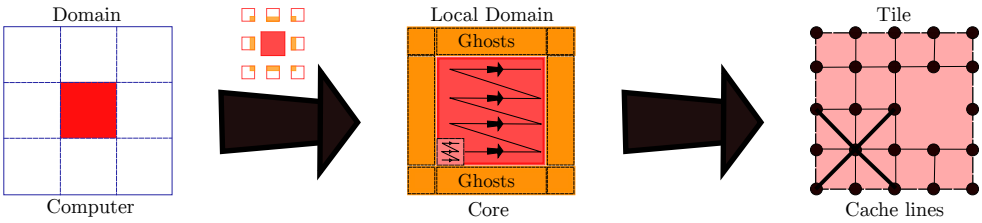

Figure 3.1: Multi-scale organization of KITE. The lattice (left) is divided into domains, which are assigned to different computing processor units. Each core also gets information about the neighbouring domains (orange slices in the middle image). Each domain is divided into TILES and the computation in each core is done inside each of these tiles first, before moving on to a neighbouring tile. Finally, each tile is composed of several unit cells (right).

Template design of the operators

In general, a tight-binding system is constructed with the translation of unit cells by the lattice vectors. The hoppings relate neighbouring orbitals and can be encoded by a floating-point number with the value of the hopping integral and an integer associated with the distance between orbitals. For a periodic lattice, these numbers are kept constant along the lattice, which permits encoding N elements into just two numbers. This property leads to massive memory saving and efficient vector/matrix multiplication.

For structural defects and vacancies, a strategy based on patterns is also implemented. A defect is a set of local energies and hoppings connecting orbitals in the vicinity of a given point. The memory needed to store those relations does not scale with N, and only a set of integers with the positions of the (random) reference lattice point are stored in memory. The memory usage is proportional to the concentration c of impurities or defects and does not depend on the number of orbitals per unit cell. This choice leads to a memory usage that is always smaller (often much smaller) than the memory needed for the random vectors. Similar to Anderson local disorder, defects entail a memory cost on the order of κN with $\kappa \ll 2$, which is typically much smaller then the memory necessary to store the random vectors for the Chebyshev iteration.

Efficiency and parallelisation

Spectral methods are memory-bound due to their low arithmetic intensity. Minimizing the redundant information of the Hamiltonian reduces

memory transfers during computations, leading to a positive impact on performance. KITE exploits the locality of the Hamiltonian in real space to improve memory management through a multi-scale approach, depicted in Fig. 3.1.

On the large scale, KITE uses a domain decomposition strategy to distribute spatial regions through the available processors to improve the data affinity. Neighbouring domains are not fully independent, and each Chebyshev iteration requires communication between processors. By adding a "ghost" to each subdomain, which is an extra layer at the borders with copies of elements of the neighbour subdomains, it can independently perform the full iteration. After the iteration, it synchronises the ghosts between all subdomains. The ghosts synchronisation is the non-parallel component of the algorithm, leading to an efficiency bottleneck. Fortunately, this bottleneck scales with the border/volume ratio, which is negligible for large system sizes.

At the subdomain level, KITE has a smaller length scale, a TILE, to reorganise the matrix-vector multiplication. The subdomain is tiled by identical D-dimensional hypercubic sections of linear length TILE. The multiplication is then performed inside each hypercube before moving on to the next one. This reorganisation of the multiplication permits two significant optimisations:

- independently of number of dimensions, TILE is always defined in the compilation, and it controls the size of memory chunks. This allows the vectorization of the inner loop in the matrix/vector multiplication;

- contributions for each vector element are determined by the neighbours in all directions. Multiplications along the memory alignment could result in any memory element being called each time the multiplication is performed on one of its neighbours, as the lattice typically does not fit in the cache memory. Iterating sequentially inside the small hypercube, allows KITE to fully fit it inside the memory cache and minimise the transfers and cache misses.

During the regular multiplication (the one pertaining to the periodic part of the Hamiltonian) inside each of the hypercubes, KITE is also performing the multiplication related to the disorder and defects, leading to a major performance boost. The ideal value of this TILE compilation parameter is highly dependent of the hardware architecture and should be optimised for each computer to allow maximal performance.

KITE workflow

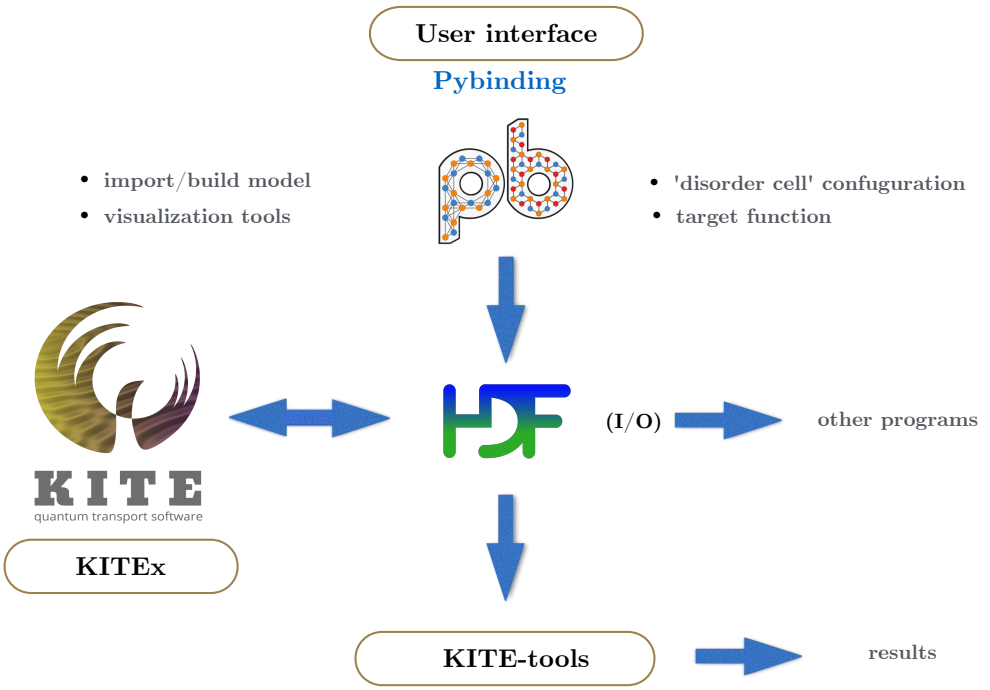

Figure 3.2: Code workflow. The user specifies the TB model, disorder and other simulation parameters in a Python configuration script with Pybinding syntax. The script writes the information into a HDF5 file. The executable KITEx uses the HDF5 file as an input to perform the calculations. KITEx writes the resulting tables of Chebyshev moments to the original HDF5 file, which then serves as an input file for KITE-tools, a post-processing tool that provides the final data files for the calculated quantities. The HDF5 logo is adapted from Ref. [132].

The KITE workflow is divided into three phases (see Fig. 3.2). First, the user specifies the TB model in a Python configuration script by using the Pybinding syntax. This configuration file also includes information about the target functions to be evaluated, number of energy points required, etc. The model, together with the calculation settings, is exported to a HDF5 file which becomes the I/O of the main program (KITEx).

In the second phase, the pre-compiled KITEx executable reads the HDF5 file and computes the matrices of Chebyshev polynomials that correspond to each of the requested quantities (DOS, optical conductivity, etc). This part of the computation only requires information about

the Hamiltonian and number of polynomials and is usually the most computationally-demanding part of the process. Calculated quantities are written back into the HDF5 file.

In the third phase, the KITE-tools executable, a post-processing tool, reads the Chebyshev moments from the I/O file and uses them to compute the final quantities. The post-processing is the only part of the calculation that needs information about the free parameters in the formulas, such as the resolution η in the Green's functions and number of energy points. Consequently, it is possible to pass them as command-line arguments to the executable, ignoring those specific parameters in the configuration file, which can be useful, for example, for re-calculating the same response function for different temperatures or different chemical potentials. It is also possible to use a smaller number of polynomials than those originally requested to KITEx, for example to study convergence. Each of the quantities that KITE-tools calculates has its own set of parameters that can be modified through command-line arguments. This scheme allows the user to calculate several quantities with a single KITEx usage. The post-processing usually takes less than one minute.

Python interface

For setting up the tight-binding model, KITE relies on the Pybinding code introduced in section 3.1.

Next, the Python interface is used to setup the disorder configuration

Listing 3.2: Disorder configuration.

```
# define an object based on the lattice
disorder = kite.Disorder(lattice)
# add Gaussian distributed disorder at
# all sites of a given selected sublattice
disorder.add_disorder('A', 'Gaussian', 0.1, 0.1)
```

the system size and the decomposition domains,

Listing 3.3: System configuration.

```
# Number of domains, each of which is calculated in parallel
nx = ny = 16
# number of unit cells in each direction.
lx = ly = 512
# make config object which caries info about
# precision can be 0 - float, 1 - double, and 2 - long double.
configuration = kite.Configuration(divisions=[nx, ny], length=[lx, ly],
    boundaries=[True, True],is_complex=False, precision=1)
```

and finally the type of calculation that will be performed by the C++ core. For example, for evaluating the xx component of the optical conductivity tensor invoke the command

Listing 3.4: Simulation details.

```
calculation = kite.Calculation(configuration)
calculation.conductivity_optical(num_points=1000, num_disorder=1,
    num_random=20, num_moments=512, direction='xx')
```

Multiple calculations can be set up on the same script. Examples are covered in the next section. For more details about the usage of the post-processing tool and a complete list of functionalities and options, please refer to the KITE website [133].

3.2.2 Examples

The following examples are also provided as script files in the examples folder from the Github repository of KITE [134].

Complex structures: low-angle twisted bilayer graphene

Twisted bilayer graphene systems display flat bands near the Fermi level and provides a platform to explore strongly correlated phases and unconventional superconductivity [4, 135–137]. Computational modelling of such systems is extremely demanding, especially at low twist angles [50]. As shown below, thanks to its ability to deal with very large systems, KITE enables studies of tBLG at “magic angles" in real space with high probing resolution.

We focus on the largest "magic angle", 1.05° [138]. We start from a TB Hamiltonian for a non-interacting system

$$\hat{H} = -\sum_{i,j} t(\boldsymbol{d}_{ij})\hat{c}_i^\dagger \hat{c}_j, \tag{3.1}$$

where $\hat{c}_i^\dagger$ ($\hat{c}_j$) is the electron creation (annihilation) operator on site $i(j)$. The transfer integral between the sites is taken as in Refs. [139] and [138]

$$-t(\boldsymbol{d}_{ij}) = V_{pp\pi}\left[1 - \left(\frac{\boldsymbol{d_{ij}}\cdot\boldsymbol{e}_z}{d}\right)^2\right] + V_{pp\sigma}\left(\frac{\boldsymbol{d_{ij}}\cdot\boldsymbol{e}_z}{d}\right)^2, \tag{3.2}$$

$$\begin{aligned} V_{pp\pi} &= V^0_{pp\pi} e^{-\frac{d-a_0}{\delta}}, \\ V_{pp\sigma} &= V^0_{pp\sigma} e^{-\frac{d-d_0}{\delta}}, \end{aligned} \tag{3.3}$$

with $V^0_{pp\pi} = -2.7$ eV and $V^0_{pp\sigma} = 0.48$ eV are intralayer and interlayer hopping integrals, $a_0 \approx 0.142$ nm and $d_0 \approx 0.335$ nm are carbon-carbon distance in graphene and interlayer distance in bilayer graphene, respectively. $\boldsymbol{d}_{ij}$ is the vector connecting two sites, $d = |\boldsymbol{d_{ij}}|$ is the distance

between them, and $\delta = 0.3187a_0$ is chosen in order to fit the next-nearest intra-layer hopping to $0.1V^0_{pp\pi}$. All neighbours within the distance of $4a_0$ are being considered.

The numerical analysis of special features in the electronic structure of tBLG systems, such as gap-opening and flat bands, require a small probing energy window to be resolved, usually on the order of 1 meV. To avoid finite-size effects this resolution has to be finer than the mean-level spacing which originates from the discreteness of the simulated finite lattice. This brings, besides the intrinsic large unit cell of the twisted structures, the requirement for a large system. Due to the implementation of "memory saving" algorithms explained in Sec. 3.2.1, KITE can handle such requirements. In this example, the simulated system contains 640×512 unit cells, with 11908 atomic sites within one unit cell, which leads to a total number of orbitals $N \simeq 4 \times 10^9$, the largest TB simulation reported to our knowledge. In addition to its giant dimension, the TB Hamiltonian also has a very high coordination number of Z (around 60 neighbours).

Given the large size of the system, the STE can be safely done using a single random vector for resolutions down to 1 meV. The DOS calculation can be requested with the following command

Listing 3.5: Code used for the DOS calculation.

```
calculation.dos(num_points=10000, num_moments=12000, num_random=1,
    num_disorder=1)
```

where a large number of moments ($M = 12000$) are requested to allow post-processing of DOS data with fine energy resolution (c.f. Fig. 2.4 (d)). KITEx code returns the set of calculated CPGF moments and KITE-tools reconstructs the DOS with the requested resolution. Figure 3.3 shows the calculated DOS in two cases: a rigid, non-relaxed structure (a) and a lattice on which a molecular dynamics relaxation was performed (b). For the latter, we implemented Brenner potentials for in-plane interactions while for the out-of-plane van der Waals interaction, we considered the registry-dependent Kolmogorov-Crespi potential [140] with parameters given in Ref. [141]. As suggested previously, refined features are resolved only at high energy resolution (≈ 1 meV). Notably, the DOS peak at $E = 0$ eV indicates the presence of a flat band due to the specific twisting angle. Away from the flat band, the situation in the two cases is quite different. Mini-gaps around the flat bands start appearing only after relaxing the sample [142, 143], and agree with recent experiments [23, 144]. The P-complexity factor for this calculation (Eq. (2.93)) is $P = \mathcal{O}(10^{15})$. Despite its high complexity, this calculation

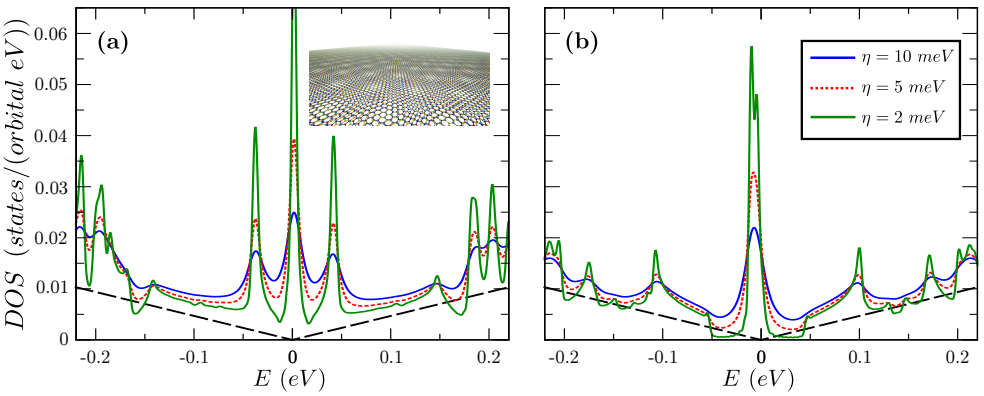

Figure 3.3: Comparison between the DOS of tBLG for (a) rigid non-relaxed lattice and (b) lattice relaxed by molecular dynamics, for different values of η. The inset of panel (a) depicts the tBLG lattice structure. Simulation details: 640×512 units cells, with 11908 atomic sites per unit cell, M=12000 and $R = 1$. Total RAM required $\approx$ 83 GB (single real precision).

requires a modest 83 GB RAM using single real precision vectors for the STE evaluation, which means that even larger systems can be simulated if the calculations are run on special large memory nodes.

Topological materials

The scalability, accuracy and speed of KITE make it an ideal tool to simulate spectral properties and response functions of materials with non-trivial band topology [52, 77]. To illustrate this capability, we consider the quantum anomalous Hall insulating regime of a magnetised graphene monolayer with interfacial broken inversion symmetry. The minimal model, incorporating spin-orbit coupling, proximity-induced magnetic exchange and scalar disorder [145, 146], is given by

$$\hat{H} = -t \sum_{\langle ij \rangle, s} \hat{c}^{\dagger}_{is} \hat{c}_{js} + \frac{2i}{3} \sum_{\langle i,j \rangle, s, s'} \hat{c}^{\dagger}_{is} \hat{c}_{js'} \left[\lambda_R \left(\hat{\boldsymbol{s}} \times \boldsymbol{\delta}_{ij} \right)_z \right]_{ss'} + \Delta_{\text{ex}} \sum_{i,s} \hat{c}^{\dagger}_{is} \hat{\boldsymbol{s}}_z \hat{c}_{is} + V_{\text{dis}}. \tag{3.4}$$

The first term describes nearest neighbour hopping processes ($\hat{c}^{\dagger}_{is}$ adds electrons with spin state $s = \uparrow, \downarrow$ to site i). The second term is the Bychkov–Rashba interaction with coupling strength λ_R. $\boldsymbol{\delta}_{ij}$ is the unit vector pointing from site j to i and $\hat{\boldsymbol{s}}$ is the vector of Pauli matrices. The third term describes an uniform exchange field with strength Δ_{ex}.

The last term is the disorder potential (see below). The presence of Bychkov–Rashba spin-orbit coupling (BRSOC) and exchange field endows the electronic states of the clean system with non-coplanar spin texture in momentum space [146] and opens a topologically nontrivial insulating bulk gap [145]. The exchange field breaks time-reversal symmetry and the insulating phase is topologically non-trivial, characterised by a Chern number $\mathcal{C} = 2$ in the bulk and spin-polarised states protected against elastic backscattering at the edges (see Fig. 3.4 (b)). Consequently, the quantum anomalous Hall insulator of the clean system has quantised Hall conductivity of $\sigma_{xy} = 2e^2/h$ inside the gap. Several types

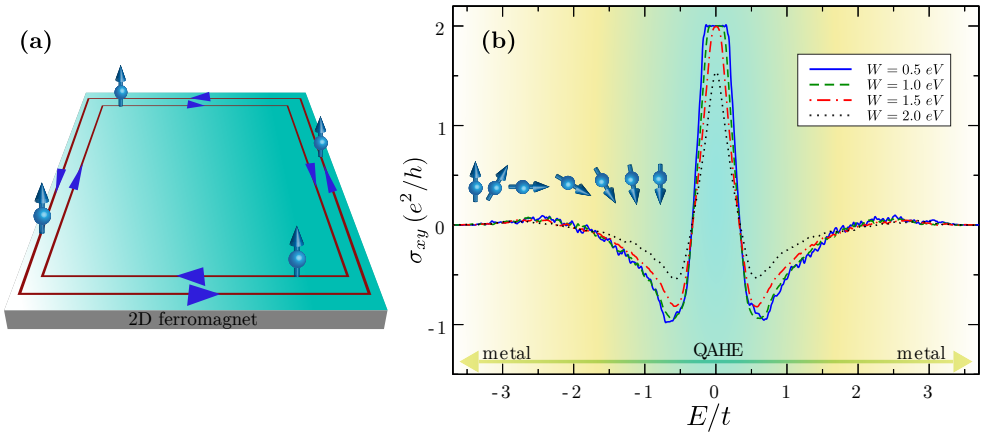

Figure 3.4: (a) Spin-polarised edge states of a 2D quantum anomalous Hall insulator (b) calculated Fermi energy dependence of the transverse charge conductivity for selected values of the disorder potential. The topological gap closes for $W \approx 2.0$ eV indicating a quantum phase transition driven by disorder fluctuations. Parameters: $\lambda_R = 0.3t$ and $\Delta_{\text{ex}} = 0.4t$. Simulation details: 8192×8192 unit cells and a total number of Chebyshev moments $M \times M$ with $M = 2048$. Results obtained for single random vector and disorder realisation $(R, S = 1)$. Minimum RAM required ≈ 8 GB (double complex precision).

of disorder can be defined in the configuration file. Given its high efficiency and fine energy resolution, KITE allows to assess the robustness of the topological phase directly from the behavior of the Hall conductivity at a modest computational cost. For illustration purposes, we model $V_{\text{dis}} = \sum_{i,s} V_{i,s} \hat{c}^\dagger_{is} \hat{c}_{is}$ as a white-noise random potential distributed on the box $V_{i,s} \in [-W/2, W/2]$. To make the disorder spin-independent and thus time-reversal symmetric, $V_{i,\uparrow} = V_{i,\downarrow}$, one separates A and B sublattices on kite.configuration, using

Listing 3.6: Specifing the spin-independent random disorder potential.

```
disorder = kite.Disorder(lattice)
disorder.add_disorder(['Aup', 'Adown'], 'Uniform', 0.0, W)
disorder.add_disorder(['Bup', 'Bdown'], 'Uniform', 0.0, W)
```

Finally, one needs to set kite.calculation. The post-processing tool requires spectrum endpoints to be specified $E \in [E_{\min}, E_{\max}]$, so that Fermi sea integrations can be carried out correctly. Tight bounds to $E_{\min}$ and $E_{\max}$ are generally hard to extract, so it is recommended to couple the DOS and Hall conductivity calculations using

Listing 3.7: Code used for the DOS and DC conductivity calculations.

```
calculation.dos(num_points=6000, num_moments=2048, num_random=1,
    num_disorder=1)
calculation.conductivity_dc(num_points=6000, num_moments=2048,
    num_random=1, num_disorder=1, direction='xy', temperature=1)
```

By default, KITE carries estimates spectrum endpoints $E_{\max(\min)}$ by using a small system build from the defined Hamiltonian, unless predefined values are specified (see Eqs. (2.68)-(2.69)). The automated estimation for a small system *does not* necessarily guarantee that the transformed spectrum of the large-scale system will fall inside the canonical interval $\epsilon \in [-1 : 1]$. We recommend that users inspect DOS curves obtained with the automatic rescaling in order to better approximate endpoints.

The Hall conductivity functionality implements a full-spectral expansion of the Kubo-Bastin formula, where KITEx computes $M \times M$ Chebyshev moments, and KITE-tools uses the Γ matrix to reconstruct σ_{xy} over any desired energy integral. The energy resolution is limited by the system size and number of moments retained (Sec. 2). Both temperature and num_ points are parameters used by KITE-tools, and it is possible to modify them without re-running KITEx. This type of calculation typically requires more memory than DOS or single-shot DC conductivity. Nevertheless, an efficient memory management enables to reach large system sizes only limited by the available RAM. Figure 3.4 (b) shows the $T = 0$ transverse conductivity σ_{xy} for a lattice of 8192×8192 unit cells and a total number of Chebyshev moments 2048×2048. The corresponding P-complexity factor is $P = \mathcal{O}(10^{15})$. KITE captures the anomalous quantum Hall plateau extremely well, with a relative error of less than 1%. The behavior in the metallic regime agrees well with theoretical predictions for magnetised 2D materials with dilute disorder [146]. Moreover, the CPGF approach is not limited to the diffusive transport regime, so it describes accurately the closing of the topological gap with increasing disorder strength. The results in Fig. 3.4(b) indi-

cate a critical disorder strength of about $W \approx 2.0$ eV for the simulated system.

Electronic structure and the spectral functions

KITE can compute spectral functions of direct relevance for angle-resolved photoemission spectroscopy (ARPES). As shown in what follows, the calculations momentum-space spectral quantities rely on a single Chebyshev expansion and, as such, are extremely fast and accurate.

For the calculation of spectral function, instead of using a random vector to compute the density of states, KITE uses a specific vector $\boldsymbol{k}$, defined in the Brillouin zone

$$\rho_{\boldsymbol{k}}(\epsilon) = \frac{1}{N} \langle \boldsymbol{k} | \, \delta\left(\epsilon - \hat{H}\right) | \boldsymbol{k} \rangle \,, \tag{3.5}$$

where $|\boldsymbol{k}\rangle$ is a sum of Bloch vectors

$$|\boldsymbol{k}, \alpha\rangle = \sum_i \exp\left(i\boldsymbol{k} \cdot \boldsymbol{R}_i^{\alpha}\right) |i, \alpha\rangle \,, \tag{3.6}$$

weighted by a structure factor $w_\alpha(\boldsymbol{k})$

$$|\boldsymbol{k}\rangle = \sum_\alpha w_\alpha(\boldsymbol{k}) \, |\boldsymbol{k}, \alpha\rangle \,, \tag{3.7}$$

where i runs through all lattice sites and α labels the orbitals. The structure factor is formally given by the Fourier transform of the localised Wannier wavefunctions $\omega_\alpha(\mathbf{r})$ [148]. The intensity of the response for each band at each $\boldsymbol{k}$ point depends on the specific form of $w_\alpha(\boldsymbol{k})$ and cannot be accurately described without it. However, if the system possesses translation symmetry, its band structure may be computed by averaging over a distribution of $w_\alpha(\boldsymbol{k})$. For this, one needs to express the $|\boldsymbol{k}, \alpha\rangle$ states in terms of the band states

$$|\boldsymbol{k}, \alpha\rangle = \sum_n |\boldsymbol{k}, n\rangle \, \langle \boldsymbol{k}, n | \, \boldsymbol{k}, \alpha\rangle \,. \tag{3.8}$$

Then, $\rho_{\boldsymbol{k}}(\epsilon)$ takes the form

$$\rho_{\boldsymbol{k}}(\epsilon) = \sum_{\alpha\beta n} w_\alpha^*(\boldsymbol{k}) \, w_\beta(\boldsymbol{k}) \, \langle \boldsymbol{k}, n | \, \boldsymbol{k}, \beta\rangle \, \langle \boldsymbol{k}, \alpha | \, \boldsymbol{k}, n\rangle \, \delta\left(\epsilon - \epsilon_n(\boldsymbol{k})\right) . \tag{3.9}$$

Averaging over the orbital weights with $\langle w_\alpha^*(\boldsymbol{k}) \, w_\beta(\boldsymbol{k})\rangle = \delta_{\alpha,\beta}$, we obtain

$$\langle \rho_{\boldsymbol{k}}(\epsilon)\rangle_w = \frac{1}{N} \sum_n \delta\left(\epsilon - \epsilon_n(\boldsymbol{k})\right) . \tag{3.10}$$

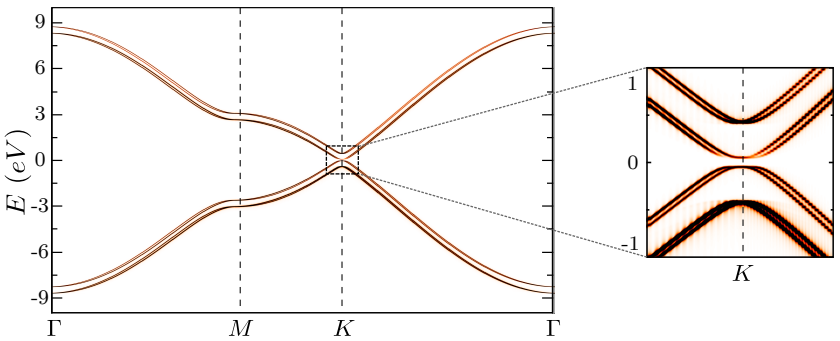

Figure 3.5: Spectral function of an electrically-biased AB graphene bilayer with Bychkov–Rashba interaction in the presence of Anderson disorder ($W = 0.07t$) based on a modified version of the ARPES module with a single value of orbital weights, which reflects in the non-equal contribution of different bands. The spin splitting of bands caused by interfacial broken inversion symmetry and broadening of spectral lines due to disorder are clearly visible. Model parameters [147]: $t = -2.8$ eV, $t_\perp = -0.4$ eV, $U = 0.05$ eV and $t_R = \lambda_R$ with $\lambda_R = 0.075$ eV. Simulation details: 1024×1024 unit cells with $M = 4096$ (corresponding to an energy resolution of ≈ 10 meV). Total RAM required ≈ 200 MB (double complex precision).

All the bands have the same intensity which is independent of the $\boldsymbol{k}$ point. If the system does not possess translation symmetry, then $\langle \rho_{\boldsymbol{k}}(\epsilon) \rangle_w$ will no longer be related to the band structure.

To demonstrate this functionality, we consider a Bernal (AB)-stacked graphene bilayer subject to a perpendicular (bias) electric field [48, 147, 149]. We use KITE's in-built ARPES functionality to reverse engineer the band structure and resolve the broadening of quasiparticle states due to the presence of disorder. Bychkov–Rashba interaction due to broken mirror reflection symmetry is also included. Without BRSOC and bias, the system is a semimetal, and the band structure presents four spin-degenerate bands. As shown in Fig. 3.5, a small bias opens a gap in the spectrum at the corners of the Brillouin zone (K) points, while a weak BRSOC lifts the spin degeneracy, leading to spin-split bands with a rich spin texture in momentum space [146].

Listing 3.8: Code used for the spectral function calculation.

```
b1, b2 = lattice.reciprocal_vectors()
Gamma = [0, 0]
K = 1 / 3 * (b1[0:2] + b2[0:2])
M = b1[0:2]/2
points = [Gamma, M, K, Gamma]
```

```
k_path = pb.results.make_path(*points[path_num], step=0.005)
weights = [10.0, 5.0, 78.0, 16.0, 1.0, 0.01, 31.0, 9.0]
configuration = kite.Configuration(divisions=[4, 4], length=[1024,
    1024], boundaries=[True, True], is_complex=True, precision=1,
    spectrum_range=[-10,10])
calculation_arpes = kite.Calculation(configuration)
calculation_arpes.arpes(k_vector=k_path, num_moments=4096, weight=
    weights,num_disorder=1)
```

Spintronics: time-evolution of spin polarised wave-packets

KITE also provides the functionality of performing real-space wave-packet propagation [79, 80]. The time evolution of wave-packets $|\psi(t)\rangle$ for any time-independent Hamiltonian is determined by the time-evolution operator $\hat{U}(t)$ according to

$$|\psi(t)\rangle = e^{-i\hat{H}t/\hbar}|\psi(0)\rangle = \hat{U}(t)|\psi(0)\rangle, \tag{3.11}$$

where $|\psi(0)\rangle$ is the initial state. The spectral expansion of the time-evolution operator is introduced in Sec. 2.3.6. To exemplify this functionality, we use KITE to resolve the spin dynamics in heterostructures of graphene and semiconducting (group VI) TMDC monolayers. The point group is C_{3v}, which allows for two types of interfacial spin-orbit effects [150, 151]: (i) intrinsic-like SOC invariant under the symmetries of the isolated monolayers; and (ii) emergent Bychkov–Rashba interaction due to broken mirror reflection ($z \to -z$) symmetry. The characteristic spin-valley coupling of the TMDC monolayer [10] is "imprinted" on graphene states, becoming the dominant interfacial intrinsic-type SOC [152]. This spin-valley coupling acts as an effective pseudo-magnetic field oriented along $\hat{z}$ for electrons at $K(K')$, leading to highly anisotropic spin dynamics characterised by long out-of-plane spin relaxation times [153–155]. A proximity-induced spin relaxation anisotropy in graphene/TMDC bilayers was observed in recent Hanle-type spin precession measurements [156, 157]. To simulate spin-relaxation dynamics in the presence of disorder, we consider a nearest-neighbour TB model for monolayer graphene subject to Bychkov–Rashba effect

$$\hat{H} = -\sum_{\langle i,j\rangle,s} t\,\hat{c}^{\dagger}_{is}\hat{c}_{js} + \frac{2i}{3}\sum_{\langle i,j\rangle,s,s'} \hat{c}^{\dagger}_{is}\hat{c}_{js'}\left[\lambda_R\left(\hat{\boldsymbol{s}}\times\boldsymbol{\delta}_{ij}\right)_z\right]_{ss'} + \sum_{i,s}\Delta_{is}\,\hat{c}^{\dagger}_{is}\hat{c}_{is}, \tag{3.12}$$

where the first two terms are defined below Eq. (3.4) and the last term accounts for an on-site potential that can represent either an Anderson disorder or a magnetic impurity. In this example, we illustrate how the spin dynamics of in-plane and out-of-plane spins is affected by both

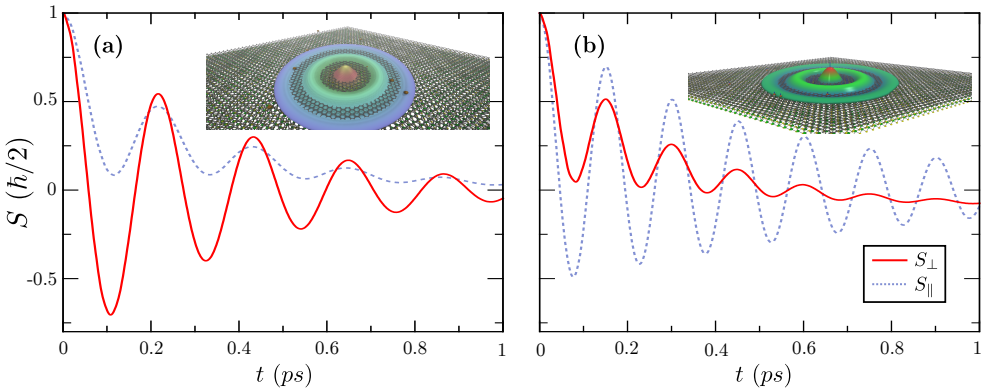

Figure 3.6: Time evolution of in-plane ($S_\parallel$) and out-of-plane ($S_\perp$) spin components of a spin-polarised wave-packet in a medium-size graphene/TMDC heterostructure flake with ≈ 103 million (p_z-) orbitals in the presence of (a) Anderson disorder with $W = 1.5$ eV and (b) Anderson disorder ($W = 1.5$ eV) superimposed with magnetic short-range disorder ($W_{\text{res}} = 0.25$ eV) with concentration $c = 0.04$. The average self energy mediated by the impurities $\Delta_{\text{ex}} = cW_{\text{res}}$ matches the SOC energy scale, thus strongly affecting the spin dynamics. Other parameters: $t = -2.507$ eV, $\lambda_R = 10$ meV, Fermi energy $E = 0.1$ eV, initial wave-packet width $\sigma \approx 110$ nm. The insets illustrate snapshots of the wave-packet profile. Simulation details: 7168×7168 unit cells, time steps of 2 fs and $M = 70$ Chebyshev moments per time step. Total RAM required ≈ 17 GB (double complex precision).

types of disorder. Section 3.2.2 presented the on-site disorder entry in KITE, with $\Delta_{is} \in [-W/2, +W/2]$. Magnetic impurities are modelled as resonant Ising scatterers with opposite sign for each spin, $\Delta_{is} = W_{\text{res}} s_z$ (if i is occupied by an impurity), distributed with a given concentration c. The latter can be incorporated with the following command

Listing 3.9: Code used for implementing resonant magnetic impurities.

```
# Aup(down) and Bup(down) are spin-orbitals
conc = 0.04 #concentration of impurities
struc_disorder_one = kite.StructuralDisorder(lattice, concentration
=conc)
struc_disorder_two = kite.StructuralDisorder(lattice, concentration
=conc)
struc_disorder_one.add_structural_disorder(
# in this way we can add on-site disorder in the form
#"[unit cell], 'sublattice', value"
    ([0, 0], 'Aup'   , +w_res),
    ([0, 0], 'Adown', -w_res),
)
# One can add multiple disorder types, which should be forwarded to
 the export_lattice function as a list.
```

```
struc_disorder_two.add_structural_disorder(
    # in this way we can add on-site disorder in the form [unit
cell], 'sublattice', value
    ([0, 0], 'Bup'  , +w_res),
    ([0, 0], 'Bdown', -w_res),
)
```

An initial spin-polarized wave-packet can be constructed in the following manner:

$$|\Psi(0,\boldsymbol{r})\rangle = e^{-\frac{1}{2\boldsymbol{r}^2\sigma^2}} \sum_{\boldsymbol{k}_j} e^{i\boldsymbol{k}_j\boldsymbol{r}} |\psi(\boldsymbol{k}_j)\rangle_S, \tag{3.13}$$

where $|\psi(\boldsymbol{k}_j)\rangle_S$ is a spinor defined over the full Hilbert space, and which has a well defined spin expectation value. Since in graphene the pseudospin, manifest in the sublattice polarization, is aligned with the momentum, this spinor will depend on $\boldsymbol{k}_j$.

For the use of the time-evolution module, it is necessary to define the lattice and type of disorder, as usual, and invoke the time-evolution calculation:

Listing 3.10: Code used for the wave-packet time evolution calculation.

```
calculation.Gaussian_wave_packet(num_moments=num_moments, num_disorder
    =1, k_vector=k_vector, spinor=spinor, width=sigma, num_points=
    num_points, mean_value=[int(lx / 2), int(ly / 2)], timestep=scale_a
    * deltaT / hbar)
```

where the parameters k_vector and spinor are lists of sampling vectors, $\boldsymbol{k}_j$, in reciprocal space and the corresponding spinors. Width is the parameter which defines the standard deviation in real space of the "Gaussian" wave-packet, and mean_value specifies around which point (in unit cell coordinates) the wave-packet is centered. Additional parameters for this type of calculation are num_points and timestep, which represent the number of timepoints at which the observables are computed, and the time step Δt, respectively.

Within KITE, the following observables are calculated:

- the spin expectation along x, y and z direction, $S_{x,y,z} = \langle\Psi(t)|\hat{\sigma}_{x,y,z}|\Psi(t)\rangle$, where $\sigma_{x,y,z}$ are the Pauli matrices, returned in the units of $\hbar/2$.

- the mean displacement, or the mean position of the wave-packet in all three directions, $\langle\Psi(t)|\hat{x},\hat{y},\hat{z}|\Psi(t)\rangle$, returned in the units of specified lattice vectors, usually nm,

- the mean square displacement, $\langle\Psi(t)|\hat{x}^2, \hat{y}^2, \hat{z}^2|\Psi(t)\rangle$, returned in the square of the units of specified lattice vectors, usually nm^2.

The output of the wave-packet simulation (i.e., mean displacement, mean square displacement andspin expectation values) is directly written to the HDF5 file.

For a typical spin dynamics simulation, the energy uncertainty of the wave-packet σ_E needs to be chosen much smaller than significant energy scales in the model. This guarantees that the computed spin dynamics is limited by elastic scattering processes at the Fermi surface leading to spin relaxation (and not by energy dephasing). The constraint $\sigma_E \ll \lambda_R$ further leads to the requirement of a significant standard deviation σ, and in turn a large computational domain (system size).

To illustrate this capability, we simulate the spin dynamics of graphene on a TMDC monolayer in the strong SOC regime ($\lambda_R\tau \gg \hbar$), where τ is the scattering time [155]. The BRSOC acts as an in-plane pseudo-magnetic field, and both $S_\parallel \equiv S_{x,y}$ and $S_\perp \equiv S_z$ are subjected to precession. In our computational experiment, the originally defined wave-packet (defined as a sum of plane waves with a Gaussian envelope) diffuses isotropically in the presence of Anderson scalar disorder only (Fig. 3.6(a)) or Anderson disorder combined with a resonant concentration of magnetic impurities (Fig. 3.6(b)). In both cases, spin-precession is anisotropic and the spin executes full precession cycles around the spin-orbit field before relaxing (see Fig. 3.6). In this strong SOC regime, the spin dynamics is characterised by fast damped oscillations, with spins relaxing on the timescale of a single scattering event. The two spin components are precessing accordingly with predictions, and KITE captures the $\cos(\lambda_R\tau/\hbar)$ evolution of the $S_\perp$ spin, as well as the fine effect of the higher-order precession terms which result in the $\cos^2(\lambda_R\tau/\hbar)$ evolution of $S_\parallel$ [155]. Once the magnetic impurities are added, the spin precesses about two different axes, one coming from the in-plane BRSOC, and the other originated from the out-of-plane component of the impurity term, which explains the dramatic change in the time evolution of the spin expectation value.

Magnetic Field

KITE allows to compute response functions in the presence of an external magnetic field with the use of Peierls substitution method [158] (Appendix A), which depends on the lattice structure and hopping matrices. In the current version of KITE, this functionality is only available for lattices with periodic boundary conditions. Hence, the achievable

magnetic flux per unit cell is limited by the system size [158]. However, the simplicity and flexibility of KITE in implementing TB models is extended to the Peierls substitution that is *automatically defined* for any lattice structure in two dimensions. To invoke the automated magnetic field functionality, one needs to include a modification function in the configuration file, as shown below

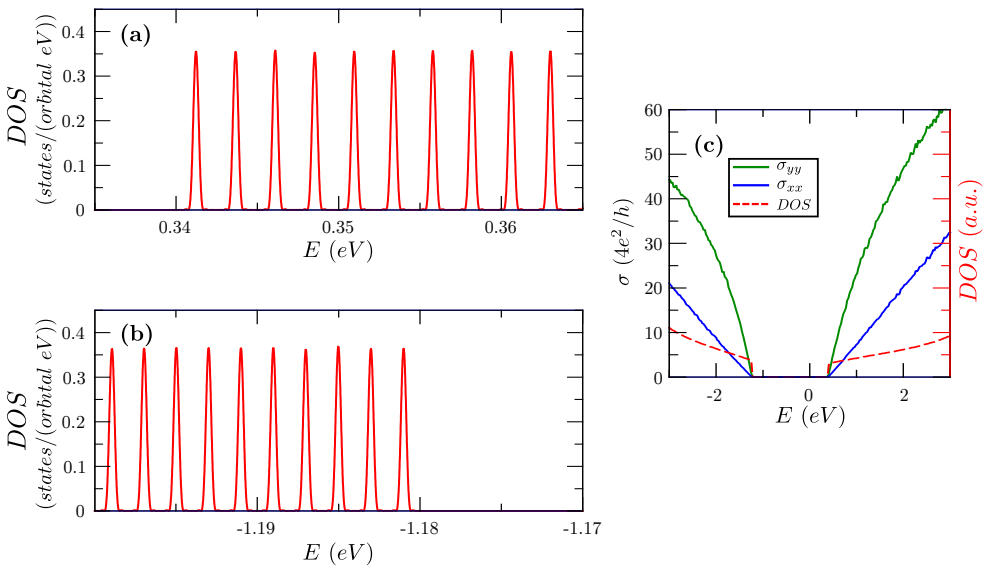

Figure 3.7: (a)-(b) Average DOS of phosphorene under a perpendicular magnetic field of 7.94 T. Panels (a) and (b) show the different Landau levels spacing for (a) holes and (b) electrons. Panel (c) shows $\sigma_{xx}(E_F)$ and $\sigma_{yy}(E_F)$ at zero fields, revealing the anisotropy in the DC conductivity of phosphorene. Simulation details: 14336×14336 unit cells, $M = 143360$ Chebyshev moments and one random vector $R = 1$. Total RAM required for DOS calculation ≈ 39 GB (double complex precision).

Listing 3.11: Specifing the magnetic field.

```
mod = kite.Modification(magnetic_field = 10)
kite.config_system(lattice, configuration, calculation, modification=
    mod, filename='magnetic.h5')
```

where it is possible to define either the magnetic field (in Tesla) or the magnetic flux per unit cell (in unit of flux quantum, h/e). When KITE generates the HDF5 file, it automatically calculates the magnetic field that best matches the one defined by the user. In previous studies, real-space (tight-binding) approaches were limited to small system sizes,

and the Peierls substitution in periodic systems gives rise to unrealistic large magnetic fields. As discussed previously, the efficient algorithms in KITE enable high-resolution spectral calculations in extremely large lattices. Consequently, it is easy to perform calculations with realistic magnetic fields using modest computational resources. We exemplify this functionality by considering a single layer of black phosphorous [159]. Although the TB model implemented is relatively simple, it contains 4 orbitals and 5 hopping terms in a unit cell and illustrates well the generality of our Peierls substitution. In the presence of a perpendicular magnetic field, the energy spectrum consists of equally spaced Landau levels in both electron and hole sectors. However, the level separation is different for electrons and holes as a consequence of their different anisotropic effective masses [159, 160]. Figures 3.7(a) and (b) present our results for the DOS of phosphorene under a perpendicular magnetic field of 7.94 T. Our simulations are performed for a system with 14336×14336 unit cells (corresponding to a total of $N = 0.822 \cdot 10^9$ orbitals). Note that owing to the small energy separation between Landau levels (less than 3 meV), it was necessary to compute a very large number of Chebyshev moments ($M = 143360$).

The puckered orthorhombic structure of black phosphorus with reduced symmetry (D_{2h}) is responsible for its highly anisotropic in-plane electronic properties [161]. To illustrate the anisotropic behavior of black phosphorus, we use KITE to calculate the different components of the conductivity tensor (see Fig. 3.7(c)). The results show that the mobility of single-layer black phosphorus is very sensitive to the direction of in-plane current.

As demonstrated in this example, KITE is extremely advantageous for studies of Landau levels, since it allows the user to probe the effect of realistic magnetic fields on the order of 1 Tesla and even smaller with a modest computational. As a comparison, previous computational studies of black phosphorus were carried out in small lattices (500×500 unit cells [162]), limiting the accessible magnetic fields to the range 32.5 - 130 T.

Molecular Ensembles

KITE is well suited for the calculation of optical and electronic properties of molecular systems. These are described by a finite set of atomic orbitals, and it is possible to simulate an ensemble of disordered molecules with a single numerical calculation. One approach is to define a molecule as a single unit cell disconnected from any neighbouring unit cells. If the

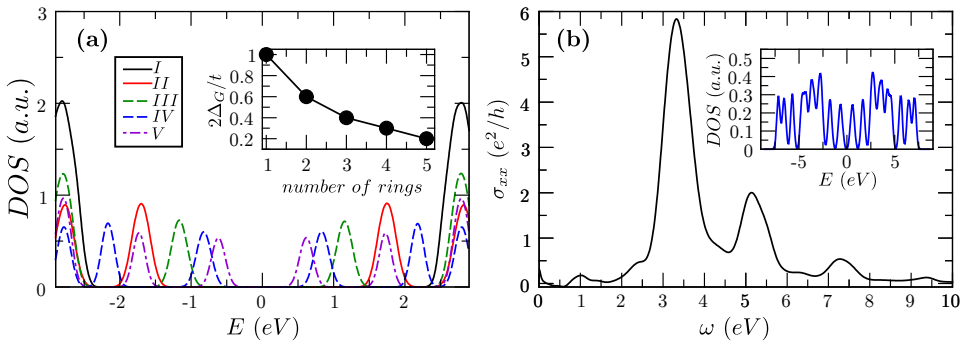

Figure 3.8: (a) Density of states of oligoacenes with increasing number of benzene rings. The inset shows the size of the gap as a function of the number of rings. (b) Optical conductivity of an ensemble of strongly disordered pentacene molecules. The inset shows the density of states for the sample ensemble. Simulation details: 128×128 unit cells containing one molecule each and $M = 512$ Chebyshev moments

user provides an arbitrary set of lattice vectors, a lattice constant larger than the unit cell and lateral sizes, the system is a set of $lx \times ly$ copies of the original molecule. When including any disorder in the unit cell, the system mimics an ensemble of $lx \times ly$ molecules. To illustrate this functionality, we consider a family of oligomers. Oligoacenes are planar molecules consisting of repeated, basic units of a benzene ring [163]. For simplicity, we model the benzene ring as a hexagonal structure with a single π orbital per vertex and hopping t between the orbitals. The hoppings within a benzene ring can be specified with the following command

Listing 3.12: Specifing the hopping terms in a benzene ring.

```
lat.add_hoppings(
        ([0, 0], 'C1', 'C2', t),
        ([0, 0], 'C1', 'C3', t),
        ([0, 0], 'C3', 'C5', t),
        ([0, 0], 'C5', 'C6', t),
        ([0, 0], 'C4', 'C6', t),
        ([0, 0], 'C2', 'C4', t)
)
```

It is clear, from the Python script, that there is no connection between a given unit cell and its neighbours. As such, the script implements isolated benzene molecules. The script can be easily generalised for calculations of any number of benzene rings, always expanding the size of the unit cell to ensure that we are dealing with isolated molecules. This approach can be extended to more complex scenarios, involving multiple

orbitals. When including Anderson disorder (see Sec. 3.2.23.2.2), the system produces different disorder configurations for each unit cell, which gives rise to a disordered ensemble. Figure 3.8(a) shows the density of states of ensembles of disordered oligoacenes with increasing number of rings: benzene, naphthalene, anthracene, tetracene, and pentacene. As expected, the size of the central gap ($E = 0$ eV) decreases as a function of the number of rings.

Small oligoacenes, like the ones presented here, can be synthesised on a substrate, in the form of a film. However, due to the fabrication process, the samples can be strongly disordered [164]. To illustrate the convenience of using KITE for molecular analysis, we consider a strongly disordered ensemble of pentacene molecules and calculate their optical conductivity for $E_F = 0$ eV. The results are summarised in Fig. 3.8(b).

3.2.3 Benchmarks

To display the efficiency and verify the scalability of the code, we perform a set of simulations to benchmark how the most critical computational resources scale for different system parameters. As a first test, we benchmark the density of the states for a monolayer of graphene with $Z = 3$. The results are displayed in Fig. 3.9 and the numerical values are shown in Tables 3.1, 3.2 and 3.3. Large-scale simulations are often memory bound, and the calculations involve intensive transfer between the working memory and the processor. Consequently, the efficient use of fast cache memory and an optimised memory transfer can translate in significant speed-ups. This problem is architecture-dependent, and different super-computing machines/clusters offer different speeds of bus lines and different amounts of cache. KITE allows users to tune the code at compilation time and change the rate of transferred data from the main memory. The parameter *TILE* defines the size of the simulation subdomain within a singe decomposition block that is sent to the processor for calculation. It is important to notice that the optimal value is not only dependent on the size of the system and the amount of cache memory, but also the coordination number of the lattice, precision of the calculation, and chosen decomposition.

To explore further this effect we give particular attention to the scaling with the number of cores for different *TILE* values in Table 3.1. A large graphene system with nearest neighbour coupling is simulated for three different values of *TILE*: 64, 128 and 256. For each value, we perform a set of simulations for different number of cores (*Num. Cores.*) and different number of decomposition domains along the directions of

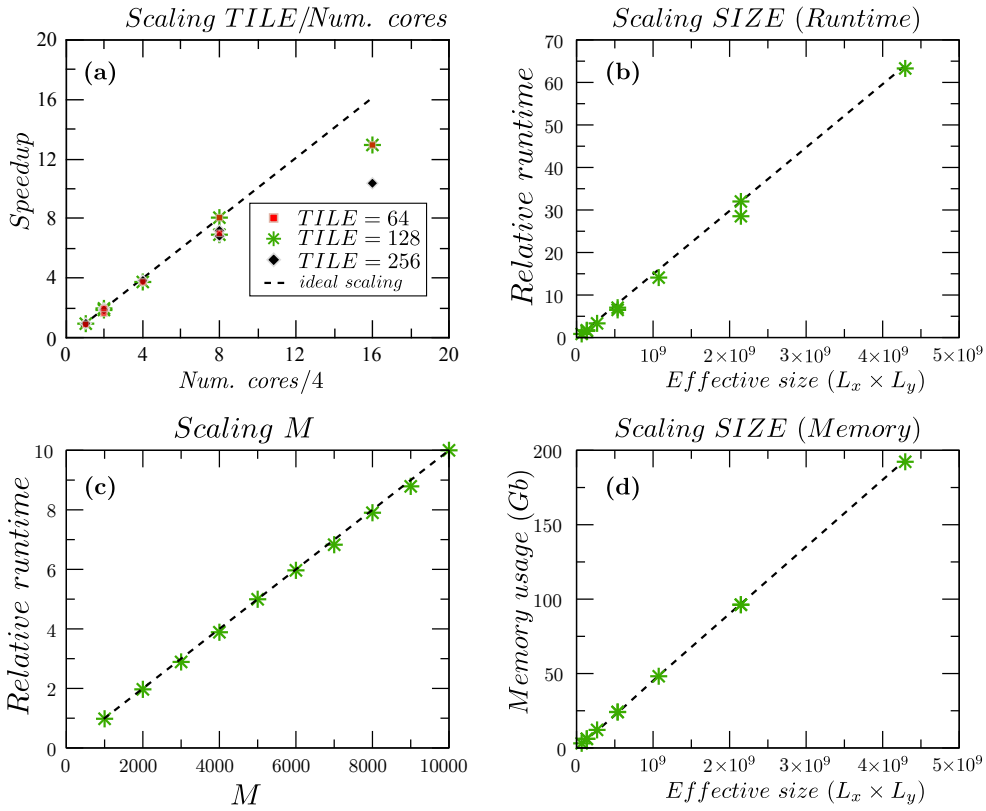

Figure 3.9: Benchmarking the DOS simulations in KITE. (a) Speedup versus number of cores for a given system size, (b) relative runtime versus effective size of the Hilbert space, (c) relative running time versus number of Chebyshev moments, (d) memory usage versus effective size of the Hilbert space. In panels (b)-(d) 64 cores were used, with a corresponding domain decomposition of 8×8 and $TILE = 64$.

lattice vectors (*Thr. Distr.*). We define the relative efficiency (*Rel. Eff.*) in the following way: we first take the ratio between the simulation runtime and the runtime of the 4 cores simulation. This is further scaled by the expected speedup, given by *Num. Cores*/4. We observe that in some cases, the relative efficiency can become larger than 1. This effect can be explained when considering the different distribution of threads, done both by the user and by the operating system on the computational machine. Namely, datasets in KITE are aligned along the directions of the first lattice vectors. For example, in memory, the neighbouring unit cells are $[0, 0]$, $[1, 0]$, $[2, 0]$ etc. and it is more efficient to have more decomposition domains along this direction. The second effect is the distribution of threads when a small number of cores is chosen. All the threads are

bound to cores where they were initially spawned using the *OpenMP* `OMP_PROC_BIND` flag, but their initial distribution depends on the operating system. Due to these uncontrollable effects small variations in the relative efficiency arise. We therefore further rescale the relative efficiency with the maximum one. This ensures that the maximal relative efficiency is fixed to 1, which although decreases the efficiency of some simulations, ensures that the reference is solely defined by the "most efficient" simulation.

We further define the speedup (*Speedup*) as the product between the relative efficiency and the expected speedup. As shown in Fig. 3.9(a), the speedup is almost linear with a noticeable saturation effect for large *TILE* of 256. We use this parameter to define the optimal value of 64 (or almost equally efficient 128), which is the value we use further in this section.

We also benchmark the relative running time (*Rlt. rnt.*), taking into account the previous discussion on the efficiency, and the used RAM memory (*Mem. (GB)*) with respect to the system size, or the simulation complexity (*Sim. Cplx.*), which is a measure of number of the operations that have to be performed, and it is equal to the product between the system size (L_1 and L_2), number of orbitals within the unit cell (n_O), coordination number Z, number of expansion moments M and number of random vectors (R). The results are presented in Table 3.2 and plotted in Fig. 3.9 panels (b) and (d). One can see that the scaling is excellent, i.e. close to the theoretical $\mathcal{O}$(*Sim. Cplx.*) scaling, for all system sizes. Regarding the memory requirements, the scaling is perfectly linear, which further proves that memory usage is highly optimised.

We finally present the benchmark of the DOS with respect to the number of moments in the expansion KPM/CPGF (M). The results, presented in Table 3.3 and plotted in Fig. 3.9(c), demonstrate that the relative running time follows the trend of perfect scaling when increasing the number of moments. From this, we can conclude that KITE is well optimised; most of the simulation time is spent on the calculation of the Chebyshev moments. This is also important for estimating the runtime of other simulations in KITE. The conductivity, for example, needs a double-expansion, therefore M^2 moments are needed. In this case, the simulation scales quadratically with M.

In addition to the optimization that KITE offers, users are encouraged to test the hardware and fine tune TILE and other parameters to their needs. Different topologies determined by the lattice connectivity results in different performances, and we firmly suggest that for the best performance, one should first perform a similar benchmarking test.

The results in this section were obtained using KITE v1.0, compiled with gcc 7.3. All the simulations were run on high memory nodes of the VIKING cluster, the York Super Advanced Research Computing Cluster.

3.2.4 Conclusions

KITE is an open-source software suite for accurate electronic structure and quantum transport calculations in real-space based on Chebyshev spectral expansions of lattice Green's functions. It features a Python-based interface that allows for an intuitive simulation setup and workflow automation of tight-binding calculations, with a wide range of predefined observables to assess electronic structure and non-equilibrium properties of complex molecular and condensed systems in the presence of disorder, defects and external stimuli. However, the main advantage of KITE is the way the software is written, being ideal for *user-friendly quantum transport calculations*, at the same time allowing unprecedented simulations of *realistic structures containing multi-billions of orbitals*. The user can optimise the calculations, workflow and post-processing at various levels on standard and high-performance computing machines to best maximise resources. The computational cost is divided physically among the processor units by means of a lattice domain decomposition technique for efficient evaluation of Chebyshev recursions on large Hilbert spaces. Combined with an efficient memory management scheme, this strategy enables KITE to achieve nearly linear computational speedups with increasing numbers of processors, to our knowledge not previously demonstrated in a tight-binding code. We have also demonstrated linear scaling in the multi-threading performance with respect to the number of Chebyshev polynomials and size of computational domain (Hilbert space), showing that KITE is capable to take full advantage of available computational resources in a variety of scenarios. Through the provided examples we showed that KITE can easily outperform previous state of the art tight-binding simulations. For example, the DOS calculation for low-angle twisted bilayer graphene, using a tight-binding model with high coordination number $Z = 60$ (Sec. 3.2.23.2.2), employed 3.9 billion orbitals, which is 2–3 orders of magnitude larger than typical sizes used in studies of simple (sparse) graphene lattices ($Z = 3$), using either the kernel polynomial method [48] or hybrid spectral approaches [112]. It also overturns previous world-record tight-binding calculations with 3.6 billion orbitals [74], where the Chebyshev polynomial Green's function methodology was pro-

posed. The major difference with respect to the custom FORTRAN code with standard OPENMP parallelisation in Ref. [74] lies in the superior memory management of KITE, which allows to simulate ever larger and more complex tight-binding models with the same computational cost. Another significant advance is demonstrated in the calculation of the conductivity tensor of disordered topological materials at finite temperature where 268 million orbitals were used, far above the previous reports in the literature for systems with equivalent complexity (for example, 16 million orbitals in an similar calculation in [165]). KITE can handle even larger systems provided enough RAM memory is available. Since the memory usage is proportional to the system size, calculations of systems with $N = \mathcal{O}(10^{10})$ and beyond can be run on high-memory nodes ($\geq$ 256 GB) already available in most computing clusters.

KITE has a sophisticated, yet flexible way of introducing crystalline defects and disorder, which preserves the efficiency of the underlying Chebyshev recursion schemes. When combined with its efficient domain decomposition algorithm allowing accurate and fast calculations with billions of orbitals, this capability makes KITE particularly suited for investigations of the effect of disorder and external perturbations on two-dimensional materials and their heterostructures, thin films and multilayer structures.

With its first release, KITE already boasts a wide range of electronic observables, including average density of states, local density of states, spectral functions, wave-packet propagation, longitudinal and transverse dc and optical conductivity, and non-linear optical conductivity. Because of its modular design and open-source nature, it is possible to implement new features in KITE efficiently, and the authors hope that new functionalities can be constructed by users and groups interested in interfacing their codes with KITE. Further developments and extensions of KITE will be driven by the needs of the communities actively using it. To lower the entry-level for researchers to use and help developing KITE, the KITE website is used as a platform for providing extensive tutorials with hands-on sessions.

Table 3.1: Benchmark of the density of states simulation for monolayer graphene with next-nearest hopping, with the system size of $L_1 = L_2 = 16384$, coordination number $Z = 3$ and simulation complexity 4.8×10^{12}, number of moments $M = 1000$ and number of random vectors $R = 1$. The simulations are performed for different values of *TILE*, and for each *TILE*, for different number of decomposition domains.

TILE	Num. Cores	Thr. Distr.	Rnt. (s)	Rel. Eff.	Speedup
64	64	8×8	110	0.81	12.95
64	32	8×4	178	1	8
64	32	4×8	203	0.88	7.01
64	16	4×4	378	0.94	3.77
64	8	4×2	732	0.97	1.95
64	8	2×4	860	0.83	1.65
64	4	2×2	1623	0.88	0.88
128	64	8×8	119	0.81	12.91
128	32	8×4	192	1	8
128	32	4×8	221	0.87	6.95
128	16	4×4	406	0.94	3.78
128	8	4×2	790	0.97	1.94
128	8	2×4	815	0.94	1.88
128	4	2×2	1566	0.98	0.98
256	64	8×8	153	0.65	10.38
256	32	8×4	222	0.89	7.15
256	32	4×8	234	0.85	6.79
256	16	4×4	411	0.97	3.86
256	8	4×2	794	1	2
256	8	2×4	869	0.91	1.84
256	4	2×2	1620	0.98	0.98

Table 3.2: Benchmark of the density of states simulation for monolayer graphene with next-nearest hopping. $TILE$ is 64, and number of cores is 64 with a domain decomposition of 8×8. Coordination number $Z = 3$, number of moments $M = 1000$ and number of random vectors is $R = 1$. Different simulations were performed for different system sizes.

L_1	L_2	Sim. Cplx.	Rnt. (s)	Rel. Eff.	Rel. rnt.	Mem. (GB)
8192	8192	1.2×10^{12}	31	0.85	0.85	3.10
8192	16384	2.4×10^{12}	63	0.86	1.72	6.12
16384	8192	2.4×10^{12}	57	0.78	1.56	6.12
16384	16384	4.8×10^{12}	122	0.83	3.33	12.13
16384	32768	9.7×10^{12}	238	0.81	6.50	24.16
32768	16384	9.7×10^{12}	257	0.88	7.02	24.16
32768	32768	1.9×10^{13}	516	0.88	14.10	48.18
32768	65536	3.9×10^{13}	1044	0.89	28.53	96.25
65536	32768	3.9×10^{13}	1171	1	32	96.25
65536	65536	7.7×10^{13}	2316	0.99	63.29	192.29

Table 3.3: Benchmark of the density of states simulation for monolayer graphene with next-nearest hopping. System size is $L_1 = L_2 = 16384$, coordination number $Z = 3$ and number of random vectors is $R = 1$. Simulations were performed for different number of moments.

Num. moments	Sim. Cplx.	Rnt.	Rel. Eff.	Rel. rnt.
1000	4.8×10^{12}	115	0.98	0.98
2000	9.6×10^{12}	231	0.98	1.97
3000	1.4×10^{13}	339	0.96	2.89
4000	1.9×10^{13}	456	0.97	3.89
5000	2.4×10^{13}	586	1.00	4.99
6000	2.9×10^{13}	700	0.99	5.97
7000	3.4×10^{13}	801	0.98	6.83
8000	3.9×10^{13}	927	0.99	7.90
9000	4.3×10^{13}	1031	0.98	8.79
10000	4.8×10^{13}	1173	1	10

Part I

Graphene heterostructures

4 | Guiding electrons in graphene, ballistic electron channels and graphene diodes

4.1 Electron transport in delaminated bilayer graphene

In this section delaminations in BLG with electrostatically induced interlayer asymmetry are investigated, and it is shown how it gives rise to ballistic channels for electrons with energies inside the electrostatically induced BLG gap. These channels are formed by a combination of valley-polarised evanescent states propagating along the delamination edges (which persist in the presence of a strong magnetic field) and standing waves bouncing between them inside the delaminated region (in a strong magnetic field, these transform into Landau levels in the monolayers). For inverted stacking between BLGs on the left and right of the delamination (AB-2ML-BA or BA-2ML-AB), the lowest energy ballistic channels are gapless, have linear dispersion and appear to be weakly topologically protected. When BLG stacking order on both sides of the delamination is the same (AB-2ML-AB or BA-2ML-BA), the lowest energy ballistic channels are gapped, with gap E_g scaling as $E_g \propto W^{-1}$ with delamination width and as $E_g \propto \delta^{-1}$ with the on-layer energy difference within the delamination. Depending on their width, delaminations may also support several "higher energy" waveguide modes.[1]

[1]The results of this chapter were published as:
T. L. M. Lane, M. Anđelković , J. R. Wallbank, L. Covaci, F. M. Peeters, V. I. Fal'ko, Phys. Rev. B **97**, 045301 (2018).

4.1.1 Motivation

Demand for increasingly dense computational architectures is driving the miniaturisation of conventional electronic circuits to their limit, requiring novel technologies to be developed. Single layer graphene, with its gapless band structure, high mobility carriers, and high thermal conductivity [29] has been considered as a candidate for the creation of conducting nano-channels. However, lithographic processes used for the patterning of such wires spoil graphene edges, introducing defects which make fabrication of ballistic channels in graphene a technological challenge. At the same time, the use of a split-gated structure on monolayer graphene does not help to confine electrons due to high transparency of p-n interfaces [166].

An alternative approach to creating ballistic "one-dimensional" channels in graphene is to use a gate-controlled gap in its Bernal (AB) stacked bilayer allotrope, which has an electrostatically tunable band gap [58, 59, 167–169]. Earlier studies [170–174] have shown that sharply switching the direction of the vertical displacement field across these split-gated structures leads to ballistic "topological" modes localised near the boundaries, persisting across junctions of interfaces [175, 176]. It has also been found that delaminations of BLG can provide well-defined one-dimensional channels [177, 178] with counter-propagating modes in the opposite valleys (K^+ and K^-). Here we study electronic properties of delaminations in a BLG sheet and their dependence on the electrostatically controlled displacement field applied to the structure. Such a system, modelled by the numerical TB approach, is illustrated in Fig. 4.1. The delamination is considered as two de-coupled monolayers of graphene (2ML) between two BLG regions in either the same (AB-2ML-AB or BA-2ML-BA) stacking configuration, or with opposite (AB-2ML-BA or BA-2ML-AB) stacking. The vertical displacement field E_z (in real devices, controlled by top and bottom gates) induces a band gap in the BLG, $\Delta = eE_z d$, and also mutually shifts on-site energies on the two delaminated monolayers by $\delta = eE_z d'$.

The low-energy band structure of Bernal stacked (AB or BA) BLG is described by a 4-band $\boldsymbol{k}\cdot\boldsymbol{p}$ Hamiltonian, with a band dispersion given in Eq. 2.25. This BLG spectrum suggests that at the energies $|E| < E_*$ (Eq. 2.26),

$$E_* = \frac{t_\perp |\Delta|}{2\sqrt{\Delta^2 + t_\perp^2}}, \tag{4.1}$$

there are no states for electrons in a gapped bilayer ($t_\perp = 0.39$ eV). In contrast, the electron spectrum in the delaminated region is gapless (see

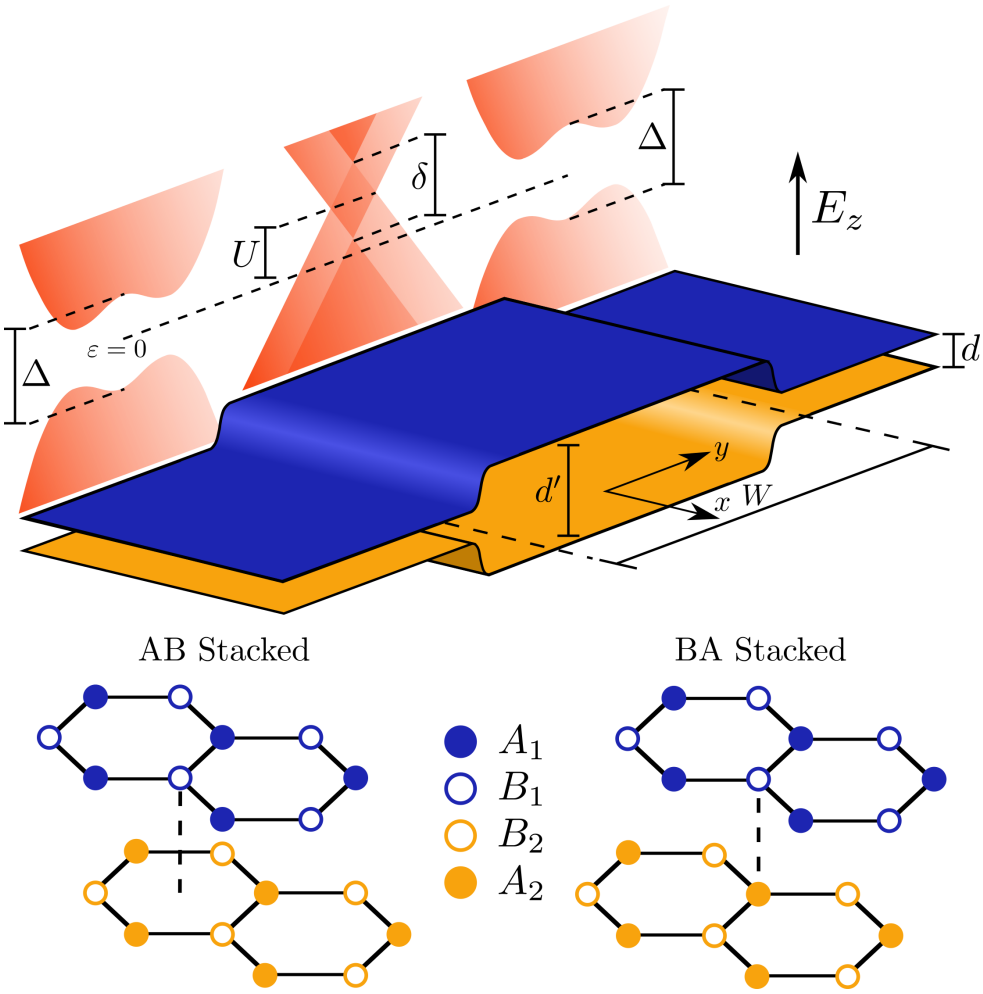

Figure 4.1: Sketch of the considered delamination. The decoupled monolayers lie in region $0 < y < W$, connected to two bilayer graphene regions ($y \leq 0$ and $y \geq W$). Corresponding energy dispersions within each distinct zone are shown with the electrostatic variables of the model indicated. These would be tuned by varying the vertical displacement field, E_z, across the system via top and bottom gates in each region. Below are images depicting the two different Bernal stacking arrangements discussed in the text.

Fig. 4.1),

$$E^{2ML} = U + l\frac{\delta}{2} \pm \hbar v_F \sqrt{q_x^2 - q_y^2}. \tag{4.2}$$

Here $v_F \approx 10^6 (m/s)$ is the Fermi velocity of Dirac electrons in graphene, $\hbar$ is reduced Planck's constant, $q_{x,y}$ are in-plane wavevectors of electrons

around $\boldsymbol{K}$,$\boldsymbol{K}'$ valleys, U is an energy shift between the BLG and 2ML regions, $l = \pm$ is upper(+)/lower(-) monolayer index, and δ is the energy offset between them produced by the displacement field (in principle, $\delta = eE_z d'$ can be larger than the BLG gap, Δ, due to the larger interlayer distance within the delamination, $d' > d$). Due to its continuous spectrum, the delamination can support states within the BLG gap, and, in the following, we will analyse the dispersion of electrons channelled by the delamination.

In Section 4.1.3, we study evanescent edge states and standing waves inside a delamination using TB calculations. The form of these states depends on the choice of interlayer stacking on either side of the decoupled monolayers. Inequivalent BLG stacking on either side of the delamination (AB on one side and BA on the other) results in the valley-polarised channels propagating in the same direction along both interfaces, leading to a gapless dispersion with two weakly topologically protected modes with dispersion spanning across the BLG gap. Having the same stacking in the outer BLG parts of the structure reverses the direction of one of these channels, so that the resulting counter-propagating evanescent modes hybridise, producing a gapped spectrum. We also analyse the higher-energy "gapped" modes resulting from standing waves bouncing between the gapped BLG regions, and we study the dependence of the spectrum on the displacement-field-shifted energies of Dirac points in the delaminated layers. In Section 4.1.4, we study how a strong magnetic field transforms the modes in the AB-2ML-BA structure into Landau levels in the delaminated monolayers.

Before going into technical details of Sections 4.1.3-4.1.4, we note that edges in graphene flakes can take two different forms; zig-zag and armchair [179, 180]. For the armchair edge, electron scattering from it mixes electron states in the two valleys. In contrast, for a zig-zag edge or arbitrarily cut edge, the large momentum difference between K^+ and K^- projections onto the delamination axis suppresses intervalley mixing [179]. For this study, we assume general boundary conditions that coincide with those of a zig-zag edge, but will underline features of the armchair edge in Section 4.1.5.

4.1.2 Model

We employ a numerical TB approach, by modelling the considered structure as a semi-infinite zig-zag BLG nanoribbon of lattice sites with a delaminated region separating two BLG regions with opposite stacking. We incorporate a mismatch of one carbon-carbon bond-length into the

widths of the layers in the 2ML region [181]. Modifying the standard TB Hamiltonian for BLG to include the desired structure produces,

$$\begin{aligned}\hat{H} = &-\sum_{l}\sum_{\langle i,j\rangle}(t\hat{c}^{\dagger}_{l,i}\hat{c}_{l,j}) \\ &-\sum_{\langle i\rangle}\Big\{\left(\Theta(-y_i)+\Theta(y_i-W)\right)t_{\perp}\hat{c}^{\dagger}_{1,i}\hat{c}_{2,i}+\text{h.c}\Big\} \\ &+\sum_{i}V_{\pm}(y_i)\hat{c}^{\dagger}_{i}\hat{c}_{i}.\end{aligned} \tag{4.3}$$

In this Hamiltonian, hopping parameter $t_{\perp}$ describes coupling of the "dimer" sites, A_1 and B_2, of the bilayer, W is the delamination width as shown in Fig. 4.1 whilst terms that describe skew hopping t_3 (between non-dimer sites) are neglected. On-site energies, $V_{\pm}(y)$, are defined as

$$V_{\pm}(y) = \begin{cases} \pm\frac{\Delta}{2} & \text{if } y \leq 0 \text{ or } y \geq W \\ U \pm \frac{\delta}{2} & \text{if } 0 < y < W \end{cases}. \tag{4.4}$$

with $t = 3.1$ eV the intralayer nearest neighbour coupling, $t_{\perp} = 0.39$ eV the interlayer nearest neighbour coupling, and $c^{\dagger}_{l,i}$ ($c_{l,i}$) being the creation (annihilation) operator for electrons at site $\boldsymbol{R}_i = (x_i, y_i)$ in layer l. On-site potentials, $V_{+}(y_i)(V_{-}(y_i))$, on the upper (lower) layer are given by Eq. (4.4). The sum in the first line runs over all nearest neighbours, $\langle i, j\rangle$, the second line runs over all the coupled dimer sites $\langle i\rangle$, and the final term sums over all lattice sites, i. The difference between the AB and BA regions is taken into account as a change of the 'dimer' sites, meaning that the coupling is present between sites A_1-B_2 ($\Theta(-y_i)$), and B_1-A_2 ($\Theta(y_i - W)$) respectively.

For numerical diagonalisation, we used 200 nm for the total width of the AB-2ML-BA nanoribbon along the y axis, and zig-zag edges. To prevent states localised along these terminating edges [179, 182, 183] from obscuring the states in the delaminated region, we apply a large positive (negative) on-site potential on the edge atoms which pushes these states to higher (lower) energies.

Using TB Hamiltonian (4.3) we find the spectrum of states guided by the delamination by solving the equation, $(H(q_x) - E(q_x)I)\,\Psi = 0$, for different values of wavevector, q_x. Additionally, using the KPM [69] implemented in the Pybinding package [123] and introduced in Ch. 2 we investigate the DOS and the LDOS.

4.1.3 Electronic Spectrum of a Delamination in BLG

Here, we analyse the electronic spectrum of a delamination (2LG) between two bilayer regions to the left ($y \leq 0$) and right ($y \geq W$) hand sides (see Fig. 4.1) for the opposite (AB-2ML-BA) and same (AB-2ML-AB) stacking on the two sides.

AB-2ML-BA Stacking

Depending on the fabrication process generating the delamination, the layers in a BLG may be shifted from one Bernal stacking configuration to another, producing the inverted (BA vs AB) stacking on the opposite side of the delamination. The resulting deformation, of the order of one carbon-carbon bond length of graphene ($a_{cc} = 0.142$ nm), is then absorbed by a weak strain/shear of the delaminated monolayers.

In the following, we neglect the weak effects of strain and focus on the qualitative change in the delamination spectrum brought about by the stacking order: its gapless character.

The spectra found using the TB approach are shown in Fig. 4.2(i-k), for $\Delta = 0.2$ eV, $U = 0$ eV, $W = 20$ nm and different values for δ [184] and represent the main features of the delamination. Note that the change in stacking order breaks the $E(q_x) = E(-q_x)$ symmetry for the states in one valley and that $E_{K^+}(q_x) = E_{K^-}(-q_x)$.

Figure 4.2 illustrate the bands (a-d) and wavefunctions (e-h) for a range of monolayer band offsets, calculated from the TB model. These plots show the spectra of electrons in valley K^+. Dispersions in the valley K^- can be obtained using the time reversal, $E(K^-, q_x) = E(K^+, -q_x)$. Wavefunctions for the interface states are displayed in Figs. 4.2(g,h), which demonstrate localisation of these valley-polarised modes at both interfaces. Note, that although an increasing number of bands become available as we open up the 2ML gap, δ, there are only these two interface states which span the entire range $|E| < E_*$ (identified in red in (a-d)). Therefore, tuning the Fermi level of the system such that it lies close to zero will select states corresponding to one-dimensional topological channels propagating simultaneously along each interface. Having noticed an almost linear dispersion of such states, we also find that the dispersion of evanescent modes is almost linear for arbitrary values of all electrostatically controlled parameters in our theory, assuming that $\hbar v q_x, \Delta, \delta, U \ll t_\perp$. The gap, E_g, between the lowest "conduction" and "valence" bands is shown to decrease as $E_g \propto W^{-1}$ with delamination width (see Sec. 4.1.5). Although the band structure in this stacking arrangement is gapless, the terms "conduction" and "valence" band are

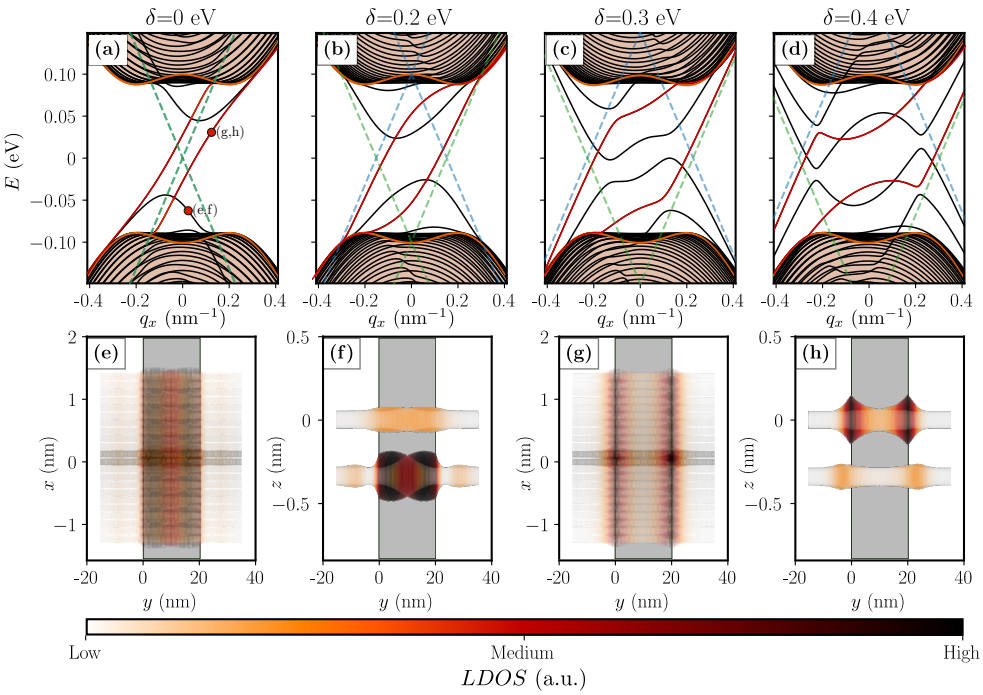

Figure 4.2: (a-d) Permitted energy bands calculated from the TB model within the bilayer gap. Interface modes (red curves) are identified crossing between the low-energy bilayer band edges (orange shaded regions). Plotted in blue (green) dashed lines are the conical dispersions of the upper (lower) monolayer with energy difference, δ, between their Dirac points. (e-h) Top and side profiles of the LDOS for the parameters indicated in the plot (a). Calculations performed for $W = 20$ nm, $\Delta = 0.2$ eV and $U = 0$ around the K^+ valley.

used to denote the monolayer graphene bands, in which the wavefunctions appear along the delamination.

Furthermore, because the direction of electron's propagation is given by group velocity, $\bar{v} = \hbar^{-1}\partial E/\partial q$, electrons in the monolayer "conduction" band with wavevector $\boldsymbol{q}$ move in the opposite direction to those in the monolayer "valence" band with the same wavevector and evanescent modes in the opposite valleys, $\eta = \pm 1$, propagate in opposite directions.

Additionally, we studied how an off-set, U, between the BLG and 2ML regions affects the energy dispersions of the AB-2ML-BA structures. Figure 4.3 depicts this for two different offsets, in (a) and (b) are bands found using the TB model in the form of the density of state maps. It shows that an increase in either U or δ (or both) brings more sub-bands into the delamination spectrum inside the BLG gap.

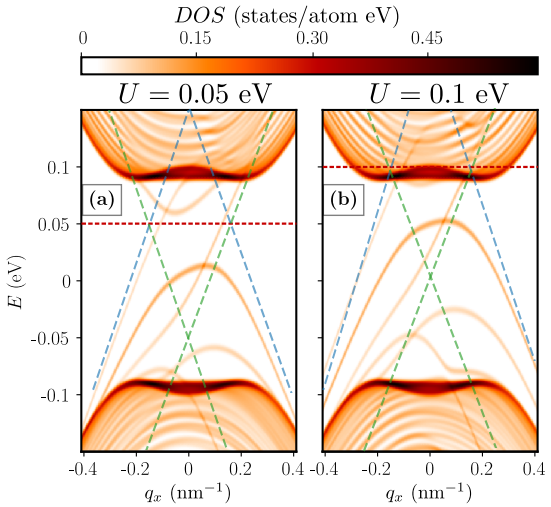

Figure 4.3: Inter-band states for different symmetry-breaking energy offsets, U, for AB-2ML-BA stacking with $W = 20$ nm and $\Delta = \delta = 0.2$ eV. In figures the red dashed line indicates the 2ML region energy mid-point and green/blue dashed lines indicate the positions of the bulk 2ML Dirac cones. Density of states of each band is shown.

AB-2ML-AB Stacking

Having established a description of inverted stacking at the two sides of a delaminated bilayer graphene (AB-2ML-BA), we study a delamination with the same stacking in the outer BLG regions, as shown in Fig. 4.4. As with the AB-2ML-AB system, the delamination exhibits both localised channels along the interface and standing wave modes

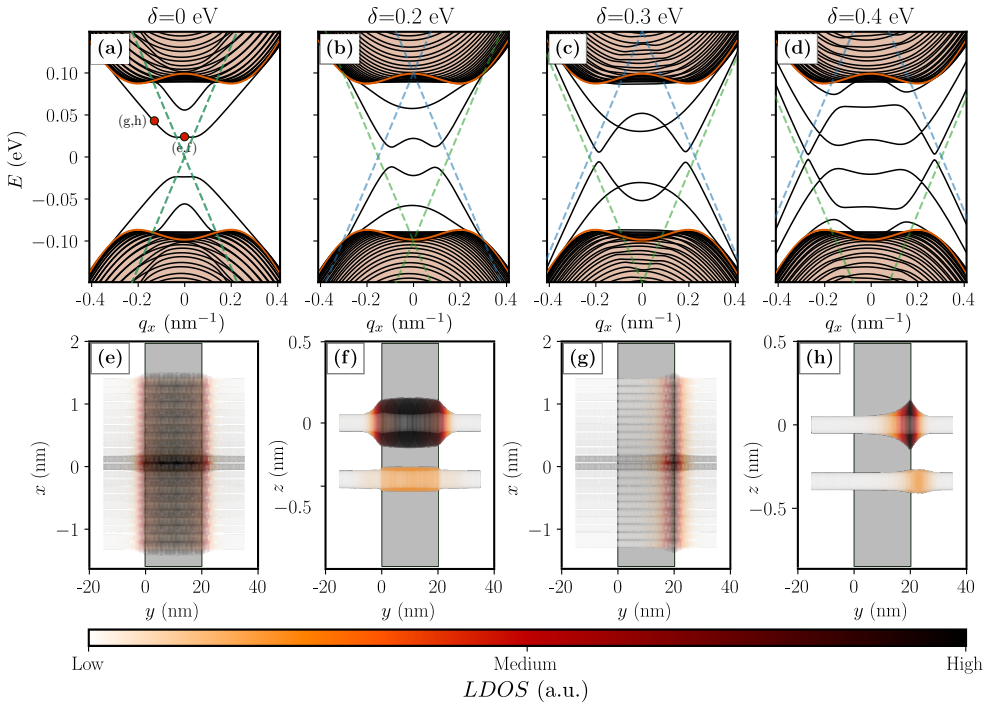

Figure 4.4: (a-d) Energy structure of the delamination for increasing interlayer energy gap (δ) within the monolayer region. Blue (green) dashed lines denote the upper (lower) monolayer Dirac cones in the 2ML region, whilst the orange region denotes the low-energy bulk bilayer band edge. (e-d) Top and side profiles of the LDOS for the parameters indicated in the plot (a). Calculations performed for $W = 20$ nm, $\Delta = 0.2$ eV and $U = 0$ around the K^+ valley.

across the delaminated monolayers, but in contrast, these spectra are formed by the hybridisation of evanescent modes coming from the opposite edges of the delamination and standing waves bouncing between the edges. For wider delaminations or larger δ, we find more "sub-bands" that can fit the BLG asymmetry gap. Higher sub-bands correspond to bouncing modes within the monolayers. Note that the spectra shown in Fig. 4.4 are gapped. As with the AB-2ML-BA system, the values of energy gaps between bands exhibits $E_g \propto (W + W_0)^{-1}$ dependence with delamination width (see Sec. 4.1.5). The gaps in the delamination spectrum also depend on the interlayer asymmetry, δ, which is controlled by the displacement field E_z.

4.1.4 Delamination spectrum in a perpendicular magnetic field

To investigate the effects of a perpendicular magnetic field on the interface states, we use the TB model and applying a Peierls substitution to the in-plane coupling terms in Eq. (4.3),

$$\begin{aligned}\hat{H} = &- \sum_{l} \sum_{\langle i,j \rangle} (t e^{i2\pi\Phi_{ij}/\Phi_0} \hat{c}^{\dagger}_{l,i} \hat{c}_{l,j}) \\ &- \sum_{\langle i \rangle} \Big\{ (\Theta(y_i) + \Xi(y_i))\, t_{\perp} \hat{c}^{\dagger}_{1,i} \hat{c}_{2,j} + \text{h.c} \Big\} \\ &+ \sum_{i} V_{\pm}(y_i) \hat{c}^{\dagger}_{i} \hat{c}_{i}.\end{aligned} \tag{4.5}$$

Here $\Phi_0 = h/e$ is the magnetic flux quantum and $\Phi_{ij} = \int \boldsymbol{Adl}$ is the flux accumulated between atomic sites i and j due to the external magnetic field, as derived in Appendix A. Figs. 4.5(a-d) show that a perpendicular magnetic field increases [185] the visibility of the interface states. The wavefunction of the standing wave states are delocalised over the relatively wide delaminated region and therefore readily form Landau levels when the radius of the cyclotron orbit of monolayer graphene drops below half the delamination width ($r_0 \sim l_B = \sqrt{\hbar/eB} < W/2$). For a $W = 20$ nm structure (Figs. 4.5(a-d)), this corresponds to a magnetic field of $B \approx 7$ Tesla, and results in the energies of these states being pushed out of the energy range of the band gap in bilayer graphene. In contrast, the interface states are less susceptible to Landau level formation as their unidirectional propagation and confinement near the edges inhibits the formation of cyclotron orbits. Nevertheless, as the magnetic field strength increases from 0 to 30 T, a clear precursor to a zeroth Landau level is seen in the flattening of the dispersions near $q_x = \epsilon = 0$ and a concomitant localisation of the wavefunction in the centre of the delaminated region (compare 4.5 (a-c,e-g)). Similar flattening of the interface bands is found for a finite interlayer shift near $q_x = 0$, $\epsilon = \pm 0.045$ eV (e.g yellow dot, 4.5 (d)). The energies of these features are well approximated by the first Landau level energy counted from the Dirac cone in the appropriate layer, $\epsilon = \pm(v\sqrt{2}/l_B - \delta/2) = 0.041$ eV, and the corresponding wavefunction (4.5 (h)) displays characteristics of the first graphene Landau level.

For energies away from these band flattenings (e.g. red dots in 4.5 (b-d)) the wavefunction is found to be pushed towards the left interface (4.5 (j-l)), rather than in the centre of the delamination as is found for the

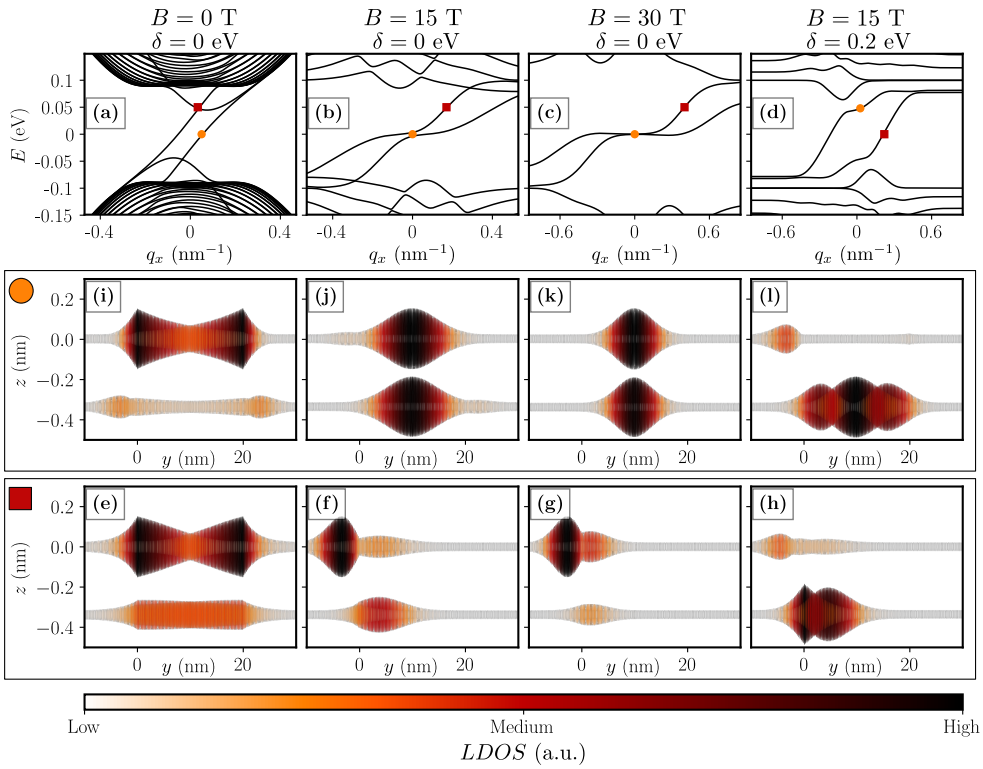

Figure 4.5: (a-d) Band structure and (e-l) LDOS maps at specific values of energy and wavevector for the nanoribbon in the presence of a perpendicular magnetic field. Insets (e-h) and (i-l) depict the distribution of the states at the value of E and q_x marked on the band structure plots with yellow circles and red squares respectively. Calculations are for $W = 20$ nm, $\Delta = 0.2$ eV and $U = 0$ in the vicinity of the K^+ valley.

Landau level like features 4.5 (f-h). This behaviour can be interpreted as the result of a Lorentz force, $e\mathbf{v} \times \mathbf{B}$, for an electron with velocity in the x-direction. As the velocity of the interface states is reversed for the other (K^-) valley the corresponding states there are pushed towards the opposite edge. This produces a spatial separation of the wavefunctions in the two valleys and consequently an enhanced robustness of these states against intervalley scattering disorder [174].

4.1.5 Energy gaps in delaminated systems

The number of available states within the BLG gap and their corresponding energies are highly sensitive, not only to the electrostatic parameters (as demonstrated in Figs. (4.2 and 4.4)) but also to the width of the

stacked monolayer channel. Decreasing the width, W, of the delamination opens up larger energy gaps between subsequent bands and pushes them out of our energy range of interest. Figure 4.6 illustrates how the energy gaps of the band minima vary with increasing delamination width for both AB-2ML-AB and AB-2ML-BA interlayer stacking, calculated assuming $\delta = 0$ for simplicity (though this is not experimentally viable). Fittings are of the form,

$$E_g = a(W + b)^{-1}, \tag{4.6}$$

with fitting parameters given in Table. 4.1. Dashed curves are fit to data from systems with the same interlayer stacking in each bilayer (empty squares) whilst solid lines are fit to data from systems with different interlayer stacking to either side of the delamination (filled squares). Black circles show data from the AB-2ML-BA TB model to be in good agreement with the corresponding wavematching model.

Curve	a	b
- - - -	12.2	53.6
- - - -	30.1	72.3
- - - -	54.2	61.2
- - - -	74.5	102.5
———	22.7	55.9
———	59.2	123.1
———	68.2	52.7

Table 4.1: Fitting parameters for curves in Fig. 4.6.

The lowest energy (dashed blue) curve corresponds to minima arising from avoided crossings of counter-propagating evanescent states localised at each interface in the AB-2ML-AB system. There is no complementary curve for the AB-2ML-BA system since the localised channels for this configuration are co-propagating and the resulting low-energy bands span the entire gap. The energy gap between higher energy bands follows the same general form, with an especially close agreement between green and red curves in each system.

The above results have been obtained for the delamination with an almost arbitrary crystallographic direction, except for the orientation where the delamination edge exactly coincides with the armchair direction in graphene. In the latter case, the armchair edge mixes states in graphene's two valleys and the spectrum of an AB-2ML-BA delamination, obtained by TB model calculation and shown in Fig. 4.7, has

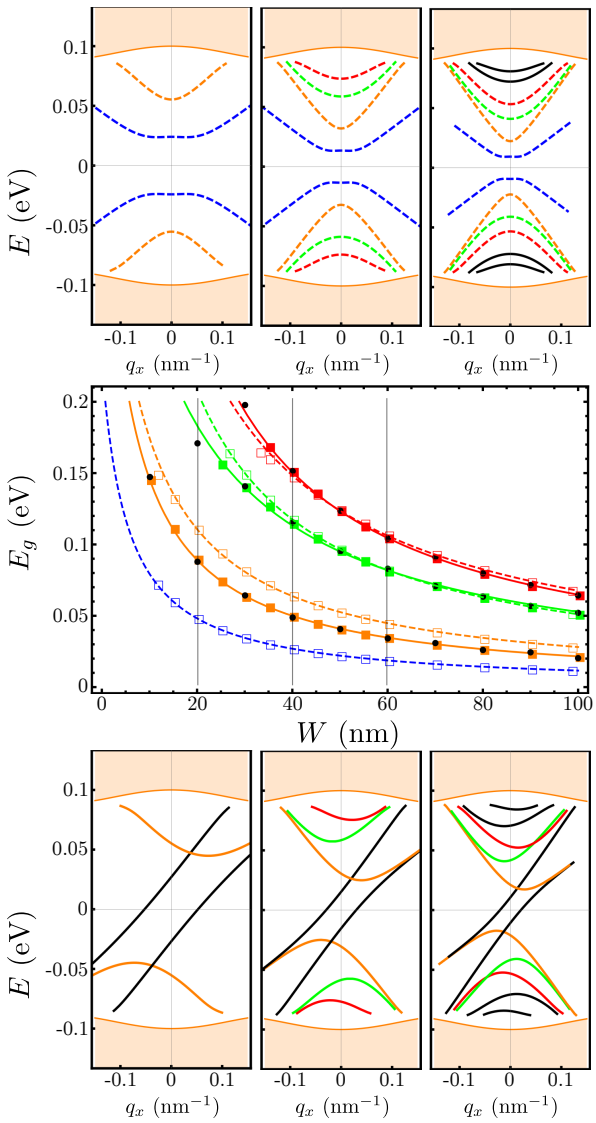

Figure 4.6: Dependence of energy gaps on delamination width extracted from a continuum description [186]. Empty squares and dashed curves show data and fitting for the AB-2ML-AB system respectively, whilst filled squares and solid curves show data for the AB-2ML-BA system. Black points represent data extracted from the TB model for the AB-2ML-BA system. (a-c) Band structures at $W = 20$ nm, $W = 40$ nm and $W = 60$ nm respectively for the AB-2ML-AB system. (d-f) Band structures at $W = 20$ nm, $W = 40$ nm and $W = 60$ nm respectively for the AB-2ML-BA system. Plots are calculated for $\Delta = 0.2$ eV and $\delta = U = 0$ around the K^+ valley.

modes inside the BLG gap which are not protected against anticrossing by the valley structure of electron states. Such states seem to retain linear dispersion similar to the case of a generic orientation of delamination edges. Another point to mention is related to the role of t_3 hopping

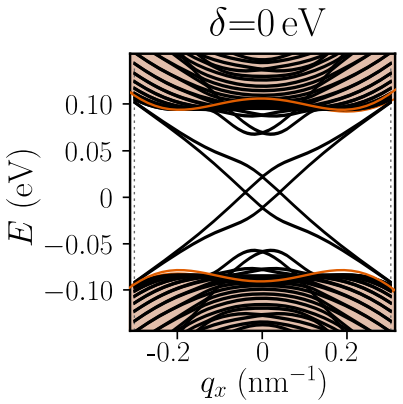

Figure 4.7: Energy dispersion for an AB-2ML-BA delamination with armchair edges, calculated using the TB model for $\Delta = 0.2$ eV, $\delta = U = 0$ and $W = 20$ nm.

terms in the TB model, which were neglected in modelling the electronic spectra. Those terms produce [167] only weak trigonal warping effects in BLG and can be neglected, but also (together with the variation of $t_\perp$ coupling along the delamination edge) may generate a source of scattering at the exact delamination edge with arbitrary (different from exact zig-zag) orientation.

4.1.6 Comparison with experiment

Experimental observations of states along delaminations naturally occurring in mechanically exfoliated graphene have already been reported [185, 187]. These results are shown in Fig. 4.8 where both transport measurements Figs. 4.8(c, d) of a device along a domain wall (delamination) with AB/BA stacking change (Figs. 4.8(a, b)) and the STS (dI/dV) maps Figs. 4.8(e, h) reveal the existence of the boundary channels. Transport measurements along the delamination show decreased resistance (Fig. 4.8(d)) when compared to the resistance of the plain bilayer graphene (Fig. 4.8(c)). Additional conductivity measurements reveal ballistic-like channels observed in devices along the shortest domain walls [187]. Furthermore, the STS spectra (Figs. 4.8(e-h)) reveal that the boundary channels can be observed at energies within the bilayer

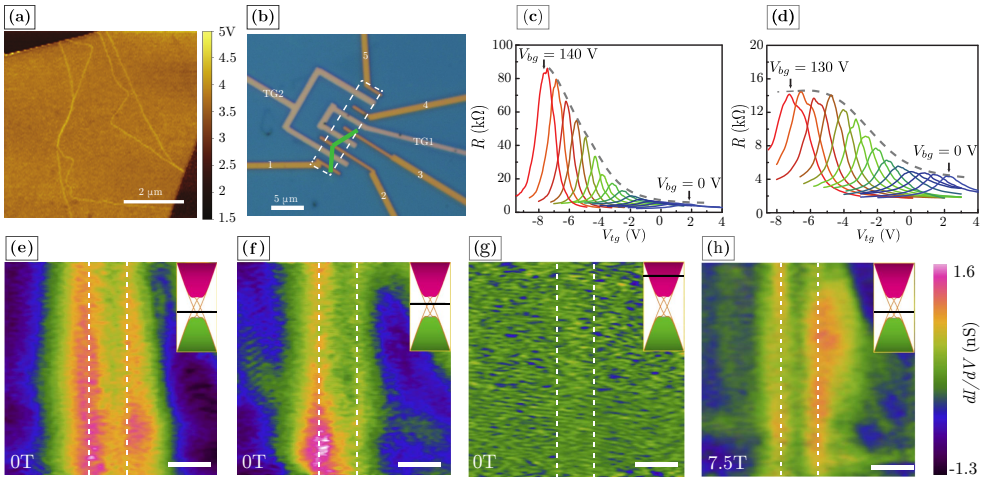

Figure 4.8: Experimental realisations of electron channels along AB/BA domain walls. (a) Near-field infrared nanoscopy image which reveals the existence of a domain wall. (b) Dual-gate field effect transistor constructed to measure transport properties along the delamination marked with the green line. Gates labelled with numbers, 1, 2 and 3 are connected to the domain wall, while other gates are patterned along a region with perfect stacking. (c, d) Transport properties along the region of perfect stacking and along the domain wall, respectively. Adapted from [187]. (e-h) STS (dI/dV) maps along the delamination induced domain wall (e-g) without the magnetic field ($B = 0$ T) at fixed sample bias voltage 30 mV, 40 mV, 300 mV, and (h) with the magnetic field $B = 7.5$ T and bias voltage 30 mV, which reveal the boundary channels along the delamination edge, that are preserved even in the presence of the magnetic field. Adapted from [185].

gap (panels 4.8(e, f)) and are not visible in the continuum of the spectra (panel 4.8(g)). More importantly, the boundary states are preserved even in the presence of the magnetic field, which confirms their robustness discussed in Sec. 4.5.

4.2 Graphene diode

Beside defining electron nanochannels in graphene, a direct application in logic devices would require fine control over the switching processes of the electron flow, which proves to be very difficult due to Klein tunnelling (Sec. 2.1.1). To exemplify the concept of rectification in a monolayer graphene device in the presence of gate induced barriers, the time

evolution of electron wavepackets is studied.

4.2.1 Model

We start from a TB Hamiltonian

$$\hat{H} = -\sum_{i,j} t\hat{c}_i^\dagger \hat{c}_j + h.c. + \sum_i V_\pm(\boldsymbol{R}_i)\hat{c}_i^\dagger \hat{c}_i, \tag{4.7}$$

where $\hat{c}_i^\dagger$ ($\hat{c}_i$) are the creation (annihilation) operators at site $\boldsymbol{R}_i = (x_i, y_i)$. The effect of the gate induced barriers is accounted through a mass potential term, or a potential of opposite sign on the two graphene sublattices within the region defined by the gate, taken with a large value of $\max(V_\pm(\boldsymbol{R}_i)) = 2.5$ eV. In different simulations the length of the triangular gates, W (Fig. 4.9(a, b)) is kept constant, together with the system size (L_x and L_y), while the size of the gate constriction is varied. To diminish finite size effects periodic boundary conditions are applied along both boundaries of the sample.

The initial wavepacket is defined as a plane wave with a Gaussian envelope centred at x_0

$$|\Psi(0, \boldsymbol{r})\rangle = e^{-\frac{1}{2x - x_0{}^2\sigma^2}} e^{ik_x(x-x_0)} |\psi(\boldsymbol{k})\rangle_S. \tag{4.8}$$

The motion is defined by the initial wavevector k_x and is taken along the x axis (symmetry axis between the two gates) which also aligns with the armchair edge of graphene. The amplitude of the wavevector is defined from an eigenstate of graphene's Hamiltonian for a chosen Fermi energy, and defines the Fermi wavelength, $\lambda_F = 2\pi/k_x$. $|\psi(\boldsymbol{k})\rangle_S$ is a spinor defined over the full Hilbert space, and which locks the pseudo-spin (or the sublattice) to the direction of motion. Starting from Eq. 3.11, evolution of the wavepacket is computed in KITE (Sec. 3.2).

In the studied example two configurations of the gates are discussed and labelled *backward* (BW) and *forward* (FW), as shown in Fig. 4.9(a, b). For both cases the time dependence of the wavepacket modulus summed over the y axis ($\sum_y |\Psi(t, \boldsymbol{r})|^2$) is shown in Figs. 4.9(e-h) for two different sizes of the constriction, $\delta = \lambda_F$ and $\delta = 10\lambda_F$. Note that the difference between the BW and FW cases originates from the arrangement of the gates, where the incident wavepacket encounters the barriers under the normal incidence or under the angle defined by the constriction ($\theta = \arctan((L - y - \delta)/(2W))$), respectively. In the later case, gradual reflection increases the transmitted portion of the wavepacket. To further investigate the transmission of the wavepackets in Fig. 4.9(g-j)

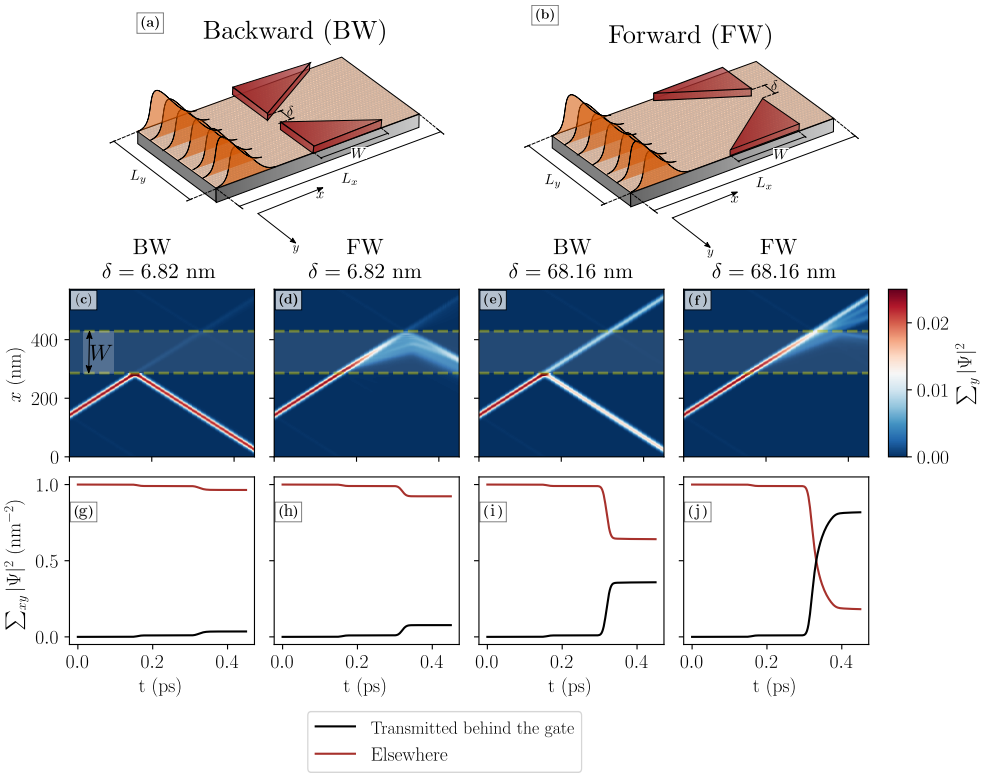

Figure 4.9: Graphene diode. (a, b) Schematics of the simulated systems for BW and FW gate configuration, respectively. (e-h) Time evolution of the wavepacket probability for different configurations and different widths of the constriction δ, all labelled in the corresponding panels. (g-j) Time evolution of the total probability showing which portion of the wavepacket is transmitted behind the gate regions. In all cases forward configuration results in higher transmission. Simulation details: standard deviation of the wavepacket $\sigma = 10$ nm, system size $L_x = 572.54$ nm and $L_y = 188.89$ nm, length of the gates $W = L_x/4 = 143.135$ nm, Fermi energy of the wavepacket $E_F = 548.9$ meV and its Fermi wavelength $\lambda_F = 6.82$ nm.

the evolution of the total probability behind the gates ($x > 3/4L_x$) and in all other regions ($x < 3/4L_x$) is shown. Note that a finite probability in the region behind the gate before the wavepacket passes is a consequence of the Gaussian envelope. Namely, although $e^{ik_x x}$ is chosen to be the solution of graphene Hamiltonian, all the modifications to the initial wavepacket will introduce different frequencies at the initial step of the time-evolution, which introduces a small portion of the wavepacket that propagates in the opposite direction and due to the periodic boundaries

reaches the region behind the gate.

Our focus now is on comparing the two gating configurations. Different cases shown in Fig. 4.9 display that the forward gate configuration results in the considerably larger transmission probability when compared with the backward configuration. To examine how the size of the constriction changes the transmission probabilities in the two cases, in Fig. 4.10 ratios between the transmitted probabilities is plotted for different values of δ. At small constriction sizes the effect of the rectification is largest, and as expected the increase of δ decrease the ratios as the gates have less effect on the transmission. Importantly, this further proves the conceptual use of gated structures as graphene diodes that could partially suppress the motion of Dirac electrons.

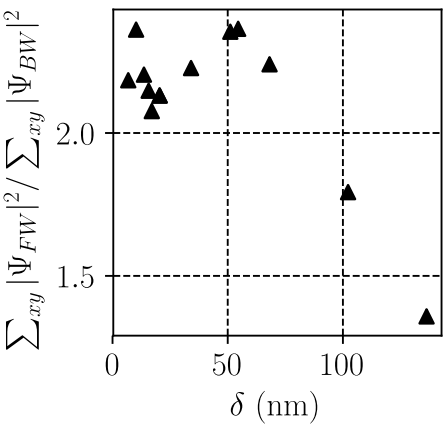

Figure 4.10: Ratio between the transmission probabilities of the wavepackets for forward and backward gate configuration. Ratio is computed for various constriction sizes.

Still, this particular example is a toy model used for a brief description of a concept of modulating and controlling the flow of electron that suppresses the Klein tunnelling, that does not include the effect of disorder nor the effect of distorted wavepackets. Furthermore, an experimental realisation of gate controlled electron barriers with a mass-term like potential would remain a practical challenge. Even if the applied potential varies on a sublattice scale, the experimentally feasible band gaps would be orders of magnitude lower than the modelled Fermi energy. An alternative approach could include substrate induced sublattice imbalance, for example in the case of hexagonal boron-nitride, with patterning the gate electrodes [188], which would nevertheless result in small energy gap on the order of 50 meV [16]. Finally, patterning a graphene anti-dot in the place of gates would suppress the electrons but also include localisation problems, at vacant sites and dangling bonds, induced by the nanopatterning process [189], which can be improved by etching fully encapsulated graphene [190].

4.3 Conclusions

To conclude, we have studied the electronic properties of delaminations in bilayer graphene with a gate induced band gap. Starting with a delamination stripe with opposite stacking of the outer BLG, we have shown that there exist evanescent states localized at the interface which span the bilayer energy gap and have opposite carrier velocity in each of graphene's two valleys. These evanescent states give rise to the gapless channels counter propagating in opposite valleys. The delamination, with both AB-2ML-BA and AB-2ML-AB stacking, also support channels produced by bouncing modes in the two delaminated monolayers. The number of such modes increases with delamination width, W, as well as with the transverse electric field, E_z, which controls the difference, $\delta = eE_z d'$, between on-layer electron energies in the delamination.

In this chapter the concept of boundary helical states is introduced, that will be examined in Ch. 6, in the light of twisted-bilayer graphene where the stacking change naturally occurs in the low rotation angle regime, where well-defined AB and BA regions appear and are separated by a boundary region where stacking gradually switches.

Furthermore, the possibility to suppress the motion of Dirac electron in graphene samples with different arrangements of the gating configuration was studied based on the time-evolution of wavepackets. Such structures conceptually introduce a realisation of graphene diode. In contrast, practical realisation of a similar concept would remain a technological challenge.

Furthermore, the possibility to suppress the motion of Dirac electron in graphene samples with different arrangements of the gating configuration was studied based on the time-evolution of wavepackets. Such structures conceptually introduce a realisation of graphene diode. In contrast, practical realisation of a similar concept would remain a technological challenge.

Part II

Graphene superlattices

5 | Buckled graphene superlattices: Flat bands engineering

Interactions between stacked two-dimensional (2D) atomic crystals can radically change their properties, leading to essentially new materials in terms of the electronic structure. In this chapter it is shown that monolayers placed on an atomically flat substrate can be forced to undergo a buckling transition, which results in periodically strained superlattices. In a collaboration with experimental colleagues from Rutgers University, we show that such lateral superlattices in graphene lead to a periodically modulated pseudo-magnetic field, which in turn creates a post-graphene material with flat electronic bands. The described approach of controllable buckling of 2D crystals offers a venue for creating other superlattice systems and, in particular, for exploring interaction phenomena characteristic of flat bands.[1]

5.1 Motivation

Buckling transitions in thin stiff membranes including graphene are ubiquitous. They generally occur when in-plane compressive strain causes a periodic out-of-plane deformation of the membrane [8, 191, 192]. The compression can be generated by thermal cycling, processing in the presence of solvents or substrate-induced stress. Upon exceeding a critical strain, the membrane can reduce its elastic energy through out of plane distortions resulting in intriguing periodic 1D or 2D patterns (Fig. 5.1) whose specific structure is dictated by boundary conditions, geometry

[1]The results of this chapter are available as: Y. Jiang, M. Anđelković, S. P. Milovanović, L. Covaci, X. Lai, Y. Cao, K. Watanabe, T. Taniguchi, F. M. Peeters, A. K. Geim, E. Y. Andrei, arXiv:1904.10147 (2019).

and strain distribution [192]. In graphene membranes, the buckling can produce a periodic PMF [193–196] which reconstructs the low energy band structure into a series of flat bands [197–199]. The quenched kinetic energy in flat bands promotes electron-electron interactions and facilitates the emergence of strongly correlated electronic phases that could survive up to high temperatures when the flat bands take up a large fraction of the Brillouin zone [200–202]. A celebrated example is the sequence of the magnetically generated flat energy bands, Landau levels. Bringing the Fermi energy within a Landau level leads to correlated phases including fractional quantum-Hall states [203–206] and the Wigner crystal [207]. Magnetically-induced flat bands have however limited applicability because the broken time reversal symmetry precludes the emergence of certain other correlated states such as superconductivity. More recently, twisted bilayer graphene that is finely-tuned to a *magic angle* at which the bands flatten, has introduced a new platform for the creation of correlated phases including superconductivity [4, 23].

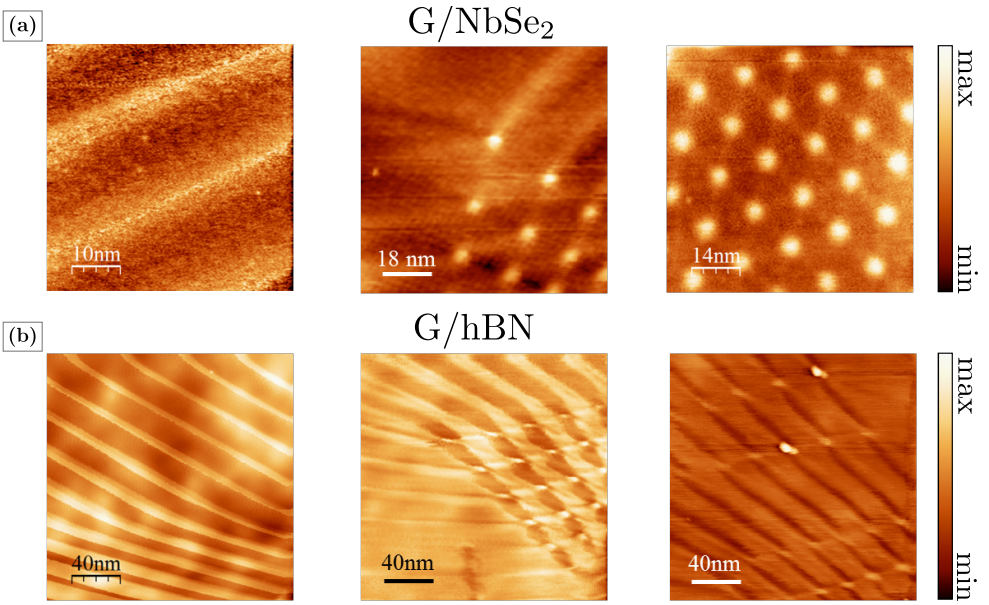

Figure 5.1: Buckled structures in graphene membranes. (a) 2D buckling modes observed by STM topography in $G/NbSe_2$ and (b) 1D and 2D buckling modes observed by STM topography in G/hBN.

5.2 Designing flat bands

An alternative route to flat bands that does not require fine-tuning or breaking time reversal symmetry is to create a periodic PMF by imposing a periodic strain on the 2D membrane [199, 201, 202]. Unlike earlier realisations of PMF which were mostly local in nature, we show here that buckling of graphene membranes produces a global change in the electronic structure resulting in a sequence of almost flat bands that percolate throughout the material.

To demonstrate the feasibility of achieving tunable flat bands, we use strain superlattices with period of ≈ 14 nm, which is induced in graphene deposited onto a $NbSe_2$ substrate and exhibits the characteristic behaviour. Fig. 5.2(a) shows the scanning tunnelling microscope (STM) topography image of a graphene crystal where the buckling results in a triangular lattice of alternating bright (crests) and dark (troughs) regions. The large lattice mismatch between graphene and $NbSe_2$, 0.246 nm and 0.36 nm respectively, rules out an interpretation of this structure in terms of a moiré pattern [208–210]. We first focus on the electronic structure obtained from the dI/dV spectra (I is the current, V is the bias) in the crest regions (Fig. 5.2(b)). The spectra consist of a sequence of peaks that are attributed to PMF-induced pseudo Landau levels (PLL) [197–199]. The energy of the most pronounced peak (labelled by $N = 0$) is aligned with the Dirac point (E_D). It is shifted by doping from the $NbSe_2$ substrate [211] to ≈ 0.5 eV above the Fermi energy (E_F) which serves as the energy origin. Labelling the remaining peaks in order of increasing (decreasing) energy as $N = \pm 1, \pm 2$, ... we find that they follow the sequence expected of Landau levels in monolayer graphene [212, 213], $E_N = E_D + sgn(N)v_F\sqrt{2e\hbar|N|B_{PMF}}$. This PLL sequence provides clear evidence of a strain induced PMF in the buckled graphene. Using the standard value of the Fermi velocity, $v_F \approx 10^6$ m/s , we estimate the PMF in the center of the crest region as $B_{PMF} = 108 \pm 8$ T (Inset, Fig. 5.2(b)). Outside the buckled region where the STM topography is flat, the spectrum exhibits a featureless "V" shape as expected of flat graphene on $NbSe_2$ (Fig. 5.3). This again supports the interpretation of the observed periodic pattern in terms of buckling-induced strain rather than a moiré pattern. One of the hallmarks of PLLs is the sublattice polarization in the $N = 0$ level such that, for a given orientation of the PMF, the electronic wavefunction is confined to only one of the sublattices, say A, while in areas where the PMF orientation is reversed, the wavefunction is localized on the B sublattice. The sublattice polarization in the presence of a PMF is the

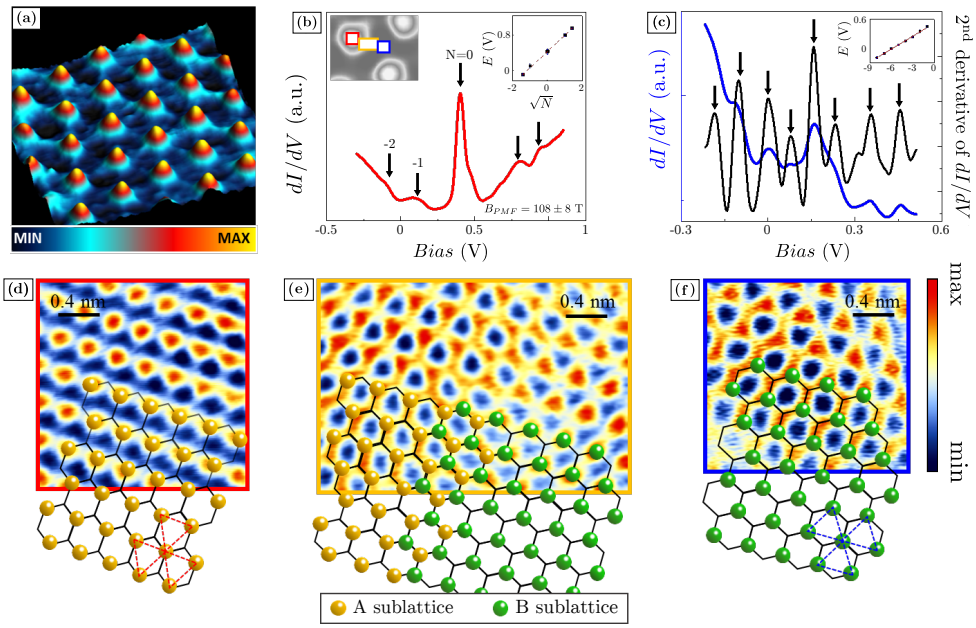

Figure 5.2: Pseudo Landau level quantization and sublattice polarization in buckled graphene. (a) STM topography of buckled graphene membrane supported on $NbSe_2$ reveals a 2D triangular lattice of crests with period 14 nm ($V_b = 600$ mV, $I = 20$ pA). (b) dI/dV curve on the crest area labelled by the red square in the left inset. Right inset: PLL energy plotted against the square root of the LL index, $N = 0, \pm 1, \pm 2, \ldots$. (c) Same as (b) but on a trough site (blue square in the left inset of (b)). The negative second derivative of the dI/dV signal is superposed (black curve) to better reveal the peaks sequence. Inset shows the approximately linear dependence of the peak energy on the level index, N. (d-f) Atomic resolution STM topography in crest (red square in left inset of (b)), transition (orange rectangle) and trough (blue square) regimes (color scale shown in panel (f)). A schematic honeycomb lattice with the orange and green balls representing the two sublattices is superposed to highlight the sublattice polarization in the different regimes. The dashed-line triangles indicate opposite orientations of the lattice polarization in each region.

counterpart of the valley polarization of the $N = 0$ level in an external magnetic field and follows directly from the opposite signs of the PMF in the $\boldsymbol{K}$ and $\boldsymbol{K}'$ valleys. Since the STM topography is also an reflection the LDOS, the sublattice polarization in atomic structure in STM experiment provides an experimental signature that reveals the presence of a PMF [214–218].

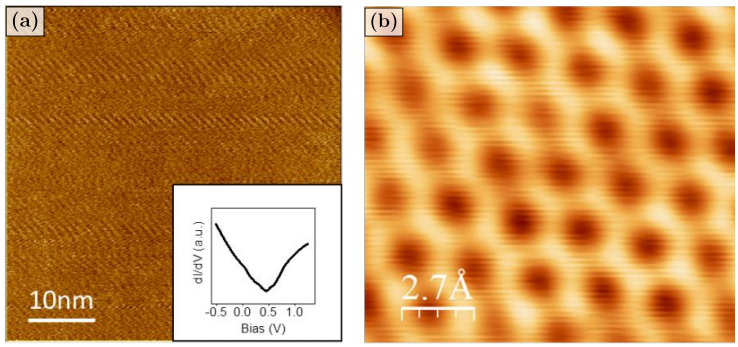

Figure 5.3: (a) STM topography of a flat G/$NbSe_2$ surface far from the ridges. (b) Atomic resolution of G/$NbSe_2$ in (a) showing only the underlying graphene lattice with no superlattice modulation.

In Figs. 5.2(d-f) we show atomic resolution STM topography in the crest, intermediate and trough regions of the superlattice, respectively. In both crest and trough regions, the sublattice polarization is clearly revealed by the triangular structure (dashed triangles). The opposite orientations of the triangles in the two regions indicate the presence of PMFs with opposite signs. Here, the triangular structure reflects the fact that only A (B) sublattice in the honeycomb is visible in crest (trough) area, corresponding to the wavefunction being localized within one sublattice in the crest, and within the other in the trough, as illustrated by the ball and stick cartoons. However, in the transition regime between the crest and the trough (Fig. 5.2(e)), there is a narrow boundary where both sublattices in the honeycomb are visible, indicating a zero crossing of the PMF between the two regions. By contrast, in all regions of the sample where the topography is flat, we observe the full honeycomb structure which is accompanied by a "V" shaped spectrum, in agreement with the absence of the PMF outside the buckled region. This sublattice symmetry breaking given by the pseudomagentic field is also confirmed by our simulation results in Fig. 5.5 that would be discussed later.

The spectra in the trough regions, shown in Fig. 5.2(c), also exhibit a sequence of peaks. The second derivative spectrum shows the LL peaks much more clear which were therefore used to identify the peak positions. Plotting the peak energy versus the level index we find that the sequence is linear in N, instead of the square root scaling seen in the crest region, with a roughly equidistant energy spacing of $\approx 89 \pm 2$ meV.

5.3 Modelling flat bands

To better understand the electronic structure of buckled graphene, we performed tight-binding calculations in the presence of a periodically modulated PMF configuration with a triangular structure (Fig. 5.5(d), Bottom) similar to that in experiment (Fig. 5.5(d), Top),

$$\boldsymbol{B_{PMF}}(x,y) = B\left(\cos(\boldsymbol{b_1 r}) + \cos(\boldsymbol{b_2 r}) + \cos(\boldsymbol{b_3 r})\right)\boldsymbol{i}_z, \tag{5.1}$$

where B is the PMF amplitude, $\boldsymbol{b_1} = 2\pi/a_b(1, -\frac{1}{\sqrt{3}})$, $\boldsymbol{b_2} = 2\pi/a_b(0, 2\frac{1}{\sqrt{3}})$, $\boldsymbol{b_3} = \boldsymbol{b_1} + \boldsymbol{b_2}$ and a_b is the buckled superlattice period (for here, $a_b = 14$ nm). More details on the PMF and how it is introduced in the TB Hamiltonian are given in Appendix A. This field configuration corresponds to a periodic array of PMF crests peaked at a maximum PMF of $3B$, that are surrounded by a percolating network of troughs where the minimum PMF is $-1.5B$ (Fig. 5.5(d)). The zeros of this PMF configuration form circles that surround each crest. Because of the spatial variation of the PMF, the experimentally measured spectra correspond to an effective PMF, B_{eff}, which approximately averages the field over the cyclotron orbit. This averaging effect becomes more pronounced as the ratio between the magnetic length and the lattice period decreases, so that the B_{eff} on the crest could be significantly smaller than $3B$. Fig. 5.4 shows the spectra in the crest region as a function of PMF amplitude for several values of the super-period, a_b , as marked. The dashed lines represent the field dependence of Landau levels (LLs). Note that as the lattice spacing increases the spectra approach the uniform LL sequence at lower fields. This is consistent with the fact that LLs, which correspond to cyclotron motion, can only form if the magnetic field is fairly constant over length scales that are several times the magnetic length, $l_B = \sqrt{\hbar/(eB)} \approx 25.7nm/\sqrt{B}$. Theoretically, we found that the PLL sequence obtained for $B_{eff} = 112$ T ($B = 120$ T) matches the experimentally measured sequence shown in Fig. 5.2(b). Figures 5.5(a-c) plot the evolution of the LDOS with PMF, for each sublattice (A - top; B - bottom) in the crest, intermediate and trough regions respectively, marked by the symbols in Fig. 5.5(d) bottom. Importantly, there is a strong imbalance in the LDOS intensity between the upper (sublattice A) and lower panel (sublattice B) in Figs. 5.5(a) and 5.5(c), but with opposite trend. These figures clearly show the polarization on the A sublattice, transiting through an un-polarized state where the honeycomb structure is recovered, to the B sublattice polarization, consistent with the experimental results shown in Figs 5.2(d-f). In Fig. 5.5(e) we show the simulated LDOS spectrum in the crest region for $B_{eff} = 112$ T (top)

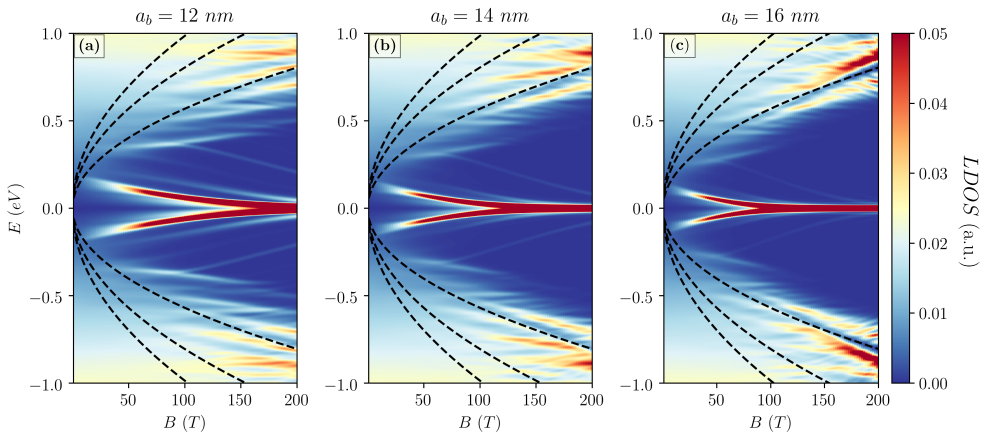

Figure 5.4: Calculated LDOS for a A sublattice site in the crest region, evolution with the PMF amplitude for different superlattice periods, (a) $a_b = 12$ nm, (b) $a_b = 14$ nm and (c) $a_b = 16$ nm. Dashed lines represent the pseudo-Landau level energy dependence on field for a uniform field.

together with a fit to the dependence on $\sqrt{N}$ (bottom) which agrees with the experimentally measured spectra shown in Fig. 5.2(b). The simulated LDOS spectrum in the trough region (Fig. 5.5(f)) is approximately linear in N with a level spacing of ≈ 90 meV, which is also consistent with the experimental results of Fig. 5.2(c). To elucidate this unusual linear peak sequence, we calculated the LDOS evolution (Fig. 5.5(g)) along a path connecting two crests shown by the red line in Fig. 5.5(d) bottom. The peak positions extracted from the experiment in the crest and trough regions are shown by orange dashed arrows. In the center of the trough the almost equidistant level sequence is seen. We note that these levels are not solely determined by the local value of the magnetic field and that they do exhibit weak dispersion in the strain superlattice mini-Brillouin zone, which will be confirmed in Fig. 5.6. Furthermore, these states are not completely localized in the trough region, but spread into the crest region. However, they do not merge with the Landau levels seen in the crest, but rather disappear as they approach it. The discrete nature of these equidistant levels indicates that they originate from strain induced confinement within the quantum well defined by the PMF, which is analogous to magnetic confinement in quantum dots in 2D semiconductor materials [219, 220]. As in the case of quantum dots, here the electrons are trapped in a PMF-induced potential well, which result in a set of levels spaced by a characteristic (geometry dependent) energy scale $\Delta E \approx \hbar v_F \pi / W$, where W is the dot size. Using the energy scale of the levels in the trough region, ≈ 94 meV, we estimate

$W \approx 21$ nm, which is approximately the size of the well indicated by the grey dashed lines in Fig. 5.5(g). In this region, the energy of each level decreases with increasing PMF until the magnetic length becomes considerably smaller than the dot size, at which point these levels merge into one degenerate level that approaches the Dirac point, as seen in Fig. 5.5(c). We now discuss the emergence of flat bands in this system. The periodic potential imposed by the PMF superlattice breaks up the low energy conical band of graphene into a series of mini-bands whose width is controlled by the strength of the PMF amplitude, B. At low values of B, the minibands restructure the LDOS into a series of semi-discrete levels as shown in Figs. 5.5(a-c). As B increases, these levels evolve into increasingly narrow bands that become flat in the limit of large B. In Fig. 5.6 we plot the first few minibands (5.6(a)), dI/dV maps (5.6(b)) and corresponding LDOS maps (5.6(c)) in the buckled graphene for $B = 120$ T. All the minibands show flat-band segments along the $K - M$ line in the BZ. We note that the higher the miniband order, the flatter it becomes, with the 3^{rd} miniband taking up almost the entire BZ. In Figs. 5.6(b, c) we show the LDOS maps for the flat-band energy slices in three minibands, $E_0 = -0.03$ eV, $E_2 = -0.17$ eV, $E_3 = -0.28$ eV marked in Fig. 5.6(a). The wave-function in the E_0 state is mostly localized within the crest region and, in spite of the very large LDOS, it is unlikely to create conditions for a macroscopic correlated state. In contrast, in the higher order minibands, the LDOS is concentrated in the trough regions which percolate throughout the entire sample, indicating the emergence of global flat bands. The periodic structures studied here are typically nested between wrinkles in the graphene membrane which often form during sample fabrication. Topographical analysis of the wrinkles suggests that the buckling was triggered by the compressive strain produced by the collapse of these wrinkles during thermal cycling. With this understanding in mind, the experiment was repeated by depositing graphene not only on $NbSe_2$ but also on hexagonal boron nitride substrates to prove this universality of buckling transition induced periodic PMF and related flat bands. Many of the wrinkles introduced during fabrication collapsed upon annealing and led to the appearance of a variety of buckling patterns ranging from $1D$ to $2D$ with nanometre-scale periods (Fig. 5.1). The strong similarity of the formed patterns in G/$NbSe_2$ and G/hBN samples suggests the features originating from the same mechanism which is substrate lattice constant unrelated, i.e., a common configuration is triggered by the compressive strain.

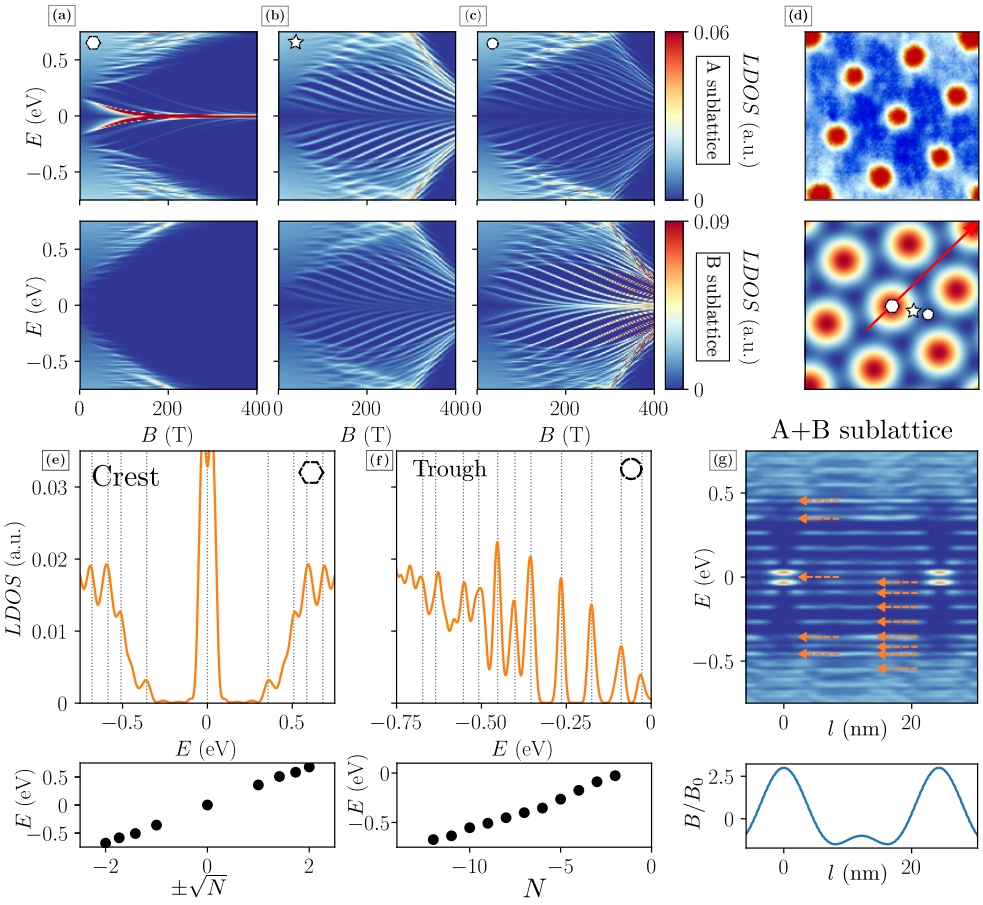

Figure 5.5: Simulated LDOS in buckled graphene. (a-c) Simulated LDOS evolution with the PMF amplitude for the crest, intermediate and trough regions respectively. Top (bottom) panels represent the A (B) sublattice. (d) Top panel: STM topography ($V = 500$ mV, $I = 20$ pA) showing the alternating crest and trough regions. Bottom panel: PMF configuration used in the simulation. The symbols indicated the positions of the calculated LDOS in (a-c). (e, f) Calculated LDOS as a function of energy in the crest and trough regions for $B = 120$ T, respectively. Bottom panels show the level-index dependence of the energy levels. (g), Top panel, contour plot of the LDOS spectra (sublattice averaged) connecting two crest areas (along the red line in panel (d)) and bottom panel, distribution of the PMF profile (along the same red line in panel (d)). Orange dashed arrows indicate the positions of the peaks in the measured spectra shown in Figs. 5.2(b, c).

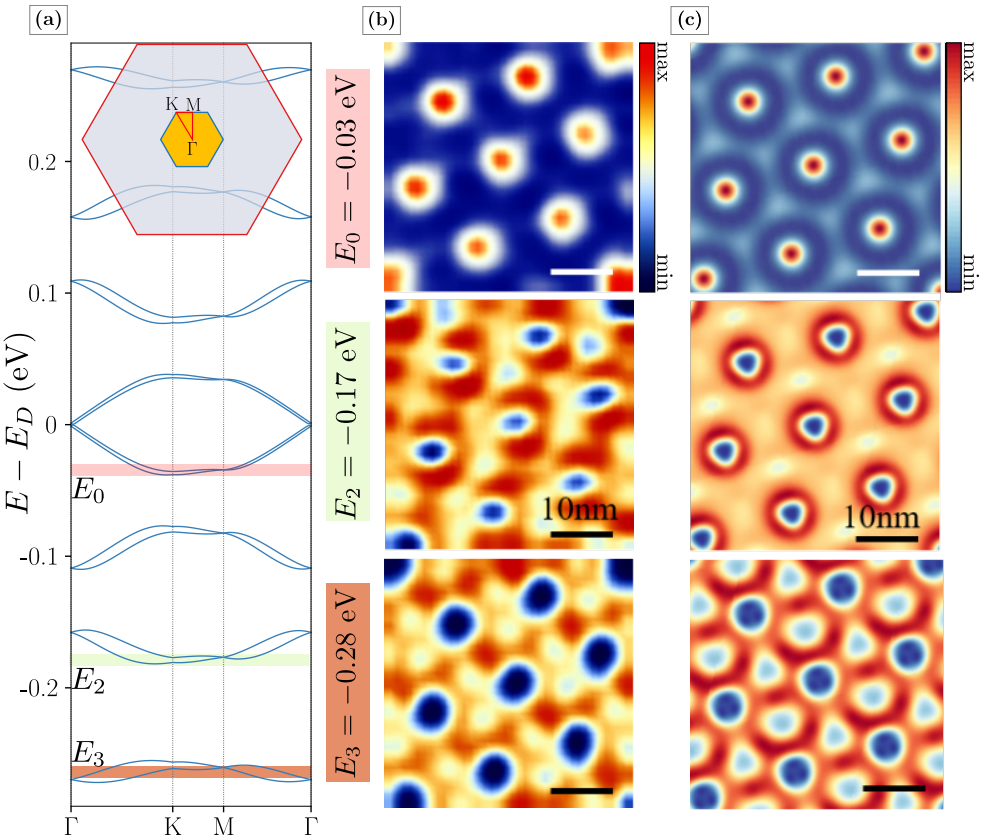

Figure 5.6: Flat bands and LDOS maps. (a) Calculated band structured for buckled graphene superlattice with period ≈ 14 nm and PMF amplitude $B = 120$ T. Inset: superlattice mini-Brillouin zone (which is exaggerated for clarity), nested within the original Brillouin zone of flat graphene is shown together with the trajectory of along which the band structure is calculated. (b, c), Measured dI/dV maps and calculated LDOS maps at $B = 120$ T for the three energies that correspond to the flat band regions in panel (a) as indicated by the color coding.

5.4 Conclusions

Similarly to folding paper in the art of origami, the shape, period and symmetry of the buckled structures can be controlled by experimentally adjustable parameters, such as boundary geometry and strain distribution. In addition, the buckling transition happens on different substrates which is a phenomena unrelated to the moiré patterns discussed in other chapters. As such, it provides further possibilities to study the superlattice effects in graphene heterostructures, with a flexible way for the

realisation of flat bands, which are proven to induce various interaction phenomena [4, 23], by the PMF in a prescribed geometry, as a venue for exploring the effects of strong interactions and the emergence of correlated phases.

6 | Angle-dependent electronic properties of twisted bilayer graphene

In this chapter tBLG is modelled for different rotation angles, and the in-plane DC conductivity is calculated using an expansion of the real-space Kubo-Bastin conductivity in terms of Chebyshev polynomials. Within a TB approach the transport properties are investigated as a function of rotation angle, applied perpendicular electric field and vacancy disorder. We find that for high-angle twists, the two layers are effectively decoupled, and the minimum conductivity at the Dirac point corresponds to double the value observed in monolayer graphene. This remains valid even in the presence of vacancies, hinting that chiral symmetry is still preserved. On the contrary, for low twist angles, the conductivity at the Dirac point depends on the twist angle and is not protected in the presence of disorder. The obtained results show that in the clean limit the conductivity increases as compared to the high-angle (decoupled) tBLG, or AB stacked bilayer graphene. Furthermore, for low angles and in the presence of an applied electric field, the chiral boundary states emerging between AB and BA regions contribute to the DC conductivity, despite the appearance of localised states in the AA regions and a finite value of the conductivity almost constant over a wide energy range of ~ 200 meV around the Dirac point is obtained. The results agree qualitatively with transport experiments in low-angle twisted bilayer graphene.[1] Furthermore, as a part of an ongoing collaboration, gated and relaxed low-angle twisted bilayer graphene samples show a well resolved network of helical states together with a possibility to switch the layer-polarisation by changing the gate polarity, which is motivated by a recent experimental study by our colleagues Y. Jiang, J. Mao (Rutgers University and

[1] The results of this chapter are available as:
M. Anđelković, L. Covaci, and F. M. Peeters, Phys. Rev. Materials **2**, 034004 (2018).

the University of Chinese Academy of Sciences) and E. Andrei (Rutgers University).

6.1 Motivation

The fabrication of multilayer structures is a promising route for developing novel devices engineered for specific purposes, where one has the freedom to choose between metallic, semiconducting or insulating individual layers. Bilayer graphene with its two stacking types, AA and the energetically more stable AB, is one of the most studied examples [221, 222]. A misalignment between the layers, produces a moiré structure, whose electronic properties are greatly affected by the rotation angle. Rotated bilayers can be produced by growing on the C face of a SiC substrate [223–225], by CVD [19–21], or by folding single graphene sheets [226, 227]. Intentional rotation leads to diverse electronic and optical properties, such as a Dirac like spectrum [19], the renormalisation of the Fermi velocity [19, 227, 228], the appearance of low energy van Hove singularities [20, 21], and the localisation of low energy states [228], which are all angle dependent. Very recently, experimental evidence suggests that strong correlations play an important role in low twist angle bilayers [22]. Due to this plethora of interesting properties, the twisting of bilayer graphene can be used as a modulation technique for solid-state devices [229, 230].

A detailed theoretical investigation of the transport properties in twisted bilayer, covering consistently all twist angles and disorder effects, is still lacking. The reason is that real-space modelling of the electrical and optical properties of such structures is very demanding. The moiré pattern period is related to the twist angle as $L \approx a_0\sqrt{3}/\left(2\sin(\theta/2)\right)$ ($a_0 = 0.142$ nm is the carbon-carbon distance) for $\theta < 30^\circ$ and the angle changes to $\theta^{'} = \pi/3 - \theta < 30^\circ$ for $30^\circ < \theta \leq 60^\circ$. For small rotation angles the period becomes $L \sim 1/\theta$. This results in a large increase of the computational unit cell. For example, if one builds a dense Hamiltonian matrix, the requirements of an exact diagonalisation for the system of size L scales in memory like L^2, and L^3 in time. The situation is more favourable for sparse matrices, which is actually the case for TB Hamiltonians, and when only a selected part of the spectrum is of interest [69]. For mesoscopic disordered systems the eigenvalue problem can be solved only for a small number of energies, which relates then to other quantities of interest. There are several different methods available based on approximate spectral functions such as the Lanczos

recursion technique, and the KPM [69]. There are also the recently developed real-space implementations of KPM for the calculation of the conductivity as given in Refs. [77], [71], and [78]. The great benefit of latter methods is the possibility to include atomistic disorder effects such as charged impurities, modelled by a random on-site potential, or vacancies, and inspect the localisation effects at the TB level with an unparalleled accuracy.

Regarding different regimes based on the rotation angle, small angles are of interest because of the large moiré superlattice, the suppression of the Fermi velocity, the localisation of low energy states, and the appearance of conductive topological boundary modes [231] when an electric field is applied perpendicular to the bilayer. Large angles are also peculiar because of the small super-cell, and the Dirac like spectrum owing to the layers being effectively decoupled. Vacancy disorder effects are studied as there is still a low number of reports on the disorder effects on tBLG, while most of them are limited to high-rotation angles or continuum models. To the authors knowledge, the only study of vacancy induced effects in twisted bilayer graphene was presented in Ref. [232] within a DFT formalism and was limited to the high-angle limit. The band-structure and spatial density of states were investigated and it was found that the effect of a vacancy is very similar to the case of single layer graphene.

6.2 Model

Following Refs. [233] and [234] we briefly discuss the geometrical properties of twisted bilayer graphene. The structure consists of two graphene layers, and we start with AA stacked bilayer graphene, which is rotated over an arbitrary angle θ with respect to an atomic site. A rotation of $\pi/3$ results in AB stacked bilayer graphene. After the rotation, the lattice vectors of the different layers become

$$\begin{aligned} \boldsymbol{a}_{1,2} &= a_0 R(\theta/2)[3/2, \pm\sqrt{3}/2, 0], \\ \boldsymbol{a}'_{1,2} &= a_0 R(-\theta/2)[3/2, \pm\sqrt{3}/2, 0], \end{aligned} \tag{6.1}$$

where $a_0 = 0.142$ nm is the carbon-carbon distance, $R(\theta)$ the rotation matrix and $\boldsymbol{a}_{1,2}$ and $\boldsymbol{a}'_{1,2}$ are lattice vectors of bottom and top layer, respectively. The position of the carbon atoms (A/B in the bottom and

A'/B' in the top layer) are defined as

$$\begin{aligned} \boldsymbol{r}_{\boldsymbol{n}}^{A} &= n\boldsymbol{a_1} + m\boldsymbol{a_2}, \\ \boldsymbol{r}_{\boldsymbol{n}}^{B} &= n\boldsymbol{a_1} + m\boldsymbol{a_2} + \boldsymbol{\delta}, \\ \boldsymbol{r}_{\boldsymbol{n}}^{A'} &= n\boldsymbol{a_1'} + m\boldsymbol{a_2'} + \boldsymbol{\delta_z}, \\ \boldsymbol{r}_{\boldsymbol{n}}^{B'} &= n\boldsymbol{a_1'} + m\boldsymbol{a_2'} + \boldsymbol{\delta'} + \boldsymbol{\delta_z}, \end{aligned} \tag{6.2}$$

and $\boldsymbol{\delta} = a_0 R(\theta/2)[1,0,0]$, $\boldsymbol{\delta'} = a_0 R(-\theta/2)[1,0,0]$, $\boldsymbol{\delta_z} = d_0[0,0,1]$ where $d_0 = 0.335$ nm is the interlayer distance.

Commensurate structure, with the well defined unit cell, can be obtained only for a discrete set of angles. For extracting the angle, commensurability condition from Ref. [235] reads

$$\cos(\theta_i) = \frac{3w^2 + 3w + 1/2}{3w^2 + 3w + 1}, \tag{6.3}$$

w being an integer. After finding a suitable angle and selecting the parameter w, unit cell vectors can be expressed in terms of monolayer graphene unit vectors $\boldsymbol{a}_{1,2}$

$$\begin{aligned} \boldsymbol{L}_1 &= wa_1 + (w+1)a_2, \\ \boldsymbol{L}_2 &= -(w+1)a_1 + (2w+1)a_2, \end{aligned} \tag{6.4}$$

which are defining the size of the unit cell $L = |\boldsymbol{L}|$ (size of the unit cell can also be expressed as $L = 1/2a_0\sqrt{3}/\sin(\theta/2)$ and the number of atoms it contains

$$N_{atoms} = 4(3w^2 + 3w + 1). \tag{6.5}$$

Due to the discreteness of available "commensurate" rotation angles, it is more suitable to chose a different approach. Here, a circular sample with a radius of 80 nm with absorbing boundary condition defined in Sec. 2.3.7 is simulated. The width of the absorbing boundary region is taken to be 5% of the radius, with a small additional region of complete absorption, i.e. $e^{-\gamma} = 0$, around the edges of the sample.

Hamiltonian defined in Sec. 3.2.2 can be used once again. By comparing the low energy spectrum it can be concluded that the interlayer hoppings between sites further away than the next-nearest neighbour distance, and further from the distance of $1.5d_0$ in the interlayer case, contribute only to small energy shifts of the spectra, without modifying it significantly. Due to this fact, a Heaviside θ_c cutoff function can be applied

$$F_c(d) = \begin{cases} \theta_c(d - 1.5d_0), & dz \geq 0.5d_0 \\ \theta_c(d - 1.1\sqrt{3}a_0), & dz < 0.5d_0. \end{cases} \tag{6.6}$$

Neglecting the above mentioned hoppings resulted in a considerable gain in calculation time due to a reduced number of non-zero elements in the Hamiltonian.

Long-range interlayer coupling breaks the electron/hole symmetry in the TB Hamiltonians and results in a shift of the Dirac point energy (E_D). In calculations where the interlayer neighbours beyond the nearest ones are included, the energy axis is shifted with $E_{D0} = 3t_{nn} = 0.3V^0_{pp\pi} =$ 0.81 eV, i.e. the energy of the Dirac point in monolayer graphene when next-nearest neighbours are included.

To visualize the stacking order in the tBLG structure a modification of the registry index (RI) is used [236, 237], which is a geometrical parameter for quantifying the matching between different layers. The RI is normalised to a range between the RI of AB stacked bilayer, $RI = 0$, and AA stacked graphene, $RI = 1$.

One important aspect to consider is the possibility of lowering the energy of the bilayer due to the van der Waals interaction between the layers. We, therefore, in order to find the relaxed bilayer structure, performed an energy minimisation through the use of molecular dynamics simulations. For in-plane interactions we use the Brenner potentials, while for the out-of-plane van der Waals interaction we use the registry dependent Kolmogorov-Crespi potential [140] with parameters given in Ref. [238]. The relaxation results in a configuration that lowers the van der Waals energy through the maximisation of the AB regions, which have the lowest energy, at the expense of in-plane strain [239].

After calculating the registry index for each atom, the minimal value between the A and B sublattices is plotted in Fig. 6.1. In Figs. 6.1(a) and 6.1(b) one can see wide regions of nearly AA stacked graphene, which become suppressed after the structure is relaxed, in favour of the AB and BA regions, see Figs. 6.1(c) and 6.1(d).

For computing the LDOS, global DOS and the conductivity KPM methodology introduced in Sec. 2.3.6 is used. In order to mitigate spurious effects due to Gibbs oscillations, the Lorentz kernel, $g_n = \sinh[\lambda(1 - n/N)]/\sinh(\lambda)$[69], is chosen for the calculation, with $\lambda = 4$. Spin degeneracy is taken into account. In the calculation of single-shot conductivity based on Eq. (2.99) (Sec. 2.3.6) $R = 56$ random vectors are used and around $M = 10000$ moments are computed, which for the width of the spectrum of the Hamiltonian, and the kernel used, based on the Ref. [69] gives us an estimate for a lower bound of the obtainable resolution to be 4 meV. It's important to notice that the actual resolution depends on the studied model Hamiltonian [71, 78].

Different regimes depending on the twisting angle exist. Rotations by

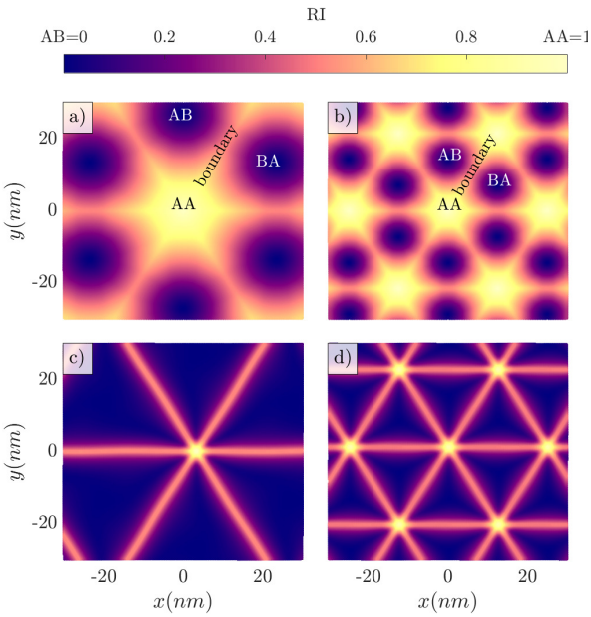

Figure 6.1: Spatially dependent registry index for tBLG with twist angle: (a) $\theta = 0.3°$, (b) $\theta = 0.565°$, and after relaxation for $\theta = 0.3°$ and $\theta = 0.565°$, in (c) and (d) respectively.

angle in the range $15° - 30°$ (high angles) result in tBLG behaving as two decoupled layers, both with linear dispersion near the Dirac point [19]. Lower angles in the range $2° - 15°$ (intermediate angles) still show a linear dispersion but the velocity is renormalised, i.e. it is suppressed. For very small rotation angles in the range of $0° < \theta < 2°$ (low angles) the low energy spectrum is no longer linear and the velocity has an oscillating behaviour with a considerable suppression at specific angles of rotation, $1.13/n$ with n an integer, obtained from a TB Hamiltonian in Ref. [240], resulting in the localisation of the electronic states in the AA regions [233, 240, 241]. The resulting angles are slightly different from those introduced in Ref. [241], where an effective continuum model was used. tBLG with $30° < \theta < 60°$ results in the same unit-cell as the one in the range of $0° < \theta < 30°$. First, the density and transport properties of tBLG for the purpose of making an unified description of different regimes with an arbitrary twist angle are investigated.

In structures with rotation angles below 1°, AB, BA and AA-like bilayer regions are easily distinguishable because of the large size of the moiré super-cell. When a perpendicular voltage is applied, a gap opens in the AB and BA regions [221, 222, 242], while the localisation of the states in the AA region is enhanced [228], where the voltage effectively

changes the intralayer hopping [222]. The topological change between the AB and BA regions induces the appearance of topological boundary states, which were theoretically predicted [231, 243–245], and only recently experimentally confirmed [246, 247] in the AB bilayer graphene domain walls. For these states to appear in tBLG, large regions of nearly AB stacked bilayer graphene and/or high voltage are required [231].

In the following the DC conductivity near the Dirac point and the effect of vacancies, as strong short-range scatterers is examined, as well as the appearance of boundary states and their influence on the conductivity of tBLG structures with small rotation angles.

6.3 Results and discussion

6.3.1 Angle dependent conductivity of plain tBLG

As a reference point, the conductivity of monolayer graphene and high-angle tBLG with $\theta = 21.78°$ is calculated, which resulted, respectively, in the known value of $\sigma_0 = 4e^2/\pi h$ and $8e^2/\pi h$, at the neutrality point. This result proves that the high-angle tBLG at low energies behaves as two decoupled monolayers. Next, the conductivity of TLBG is explored as a function of twist angle, from low to high. Fig. 6.2 shows the DC conductivity of tBLG at the Dirac point for different rotation angles, from AA bilayer graphene ($\theta = 0°$) to AB ($\theta = 60°$). For the angles in the range $\theta \in [2°, 58°]$ the constant value of $2\sigma_0$ means that layers are decoupled for a broad range of angles. In this regime, the minimal value of the conductivity is given by the pseudo-diffusive transport that is a consequence of the chirality of the carriers and is protected by the chiral symmetry.

A very different regime emerges at low-angles where we find that the conductivity at low energies is strongly enhanced as compared to the decoupled case. In order to clarify this further, in Fig. 6.3(a) ($V = 0$ V) the DOS near the Dirac point as a function of rotation angle is plotted. For high-angle of rotation, the DOS of decoupled layers is found to be linear as a function of energy, together with a shift of the van Hove peaks towards the Dirac point with decreasing twist angle. For angles below $\sim 1.5°$, states with a small Fermi velocity which are restricted to the AA stacked regions appear at the Dirac point due to the merging of van Hove singularities [233, 248]. These states can be even called quasi-localised, as their velocity is not completely vanishing.

The increase in conductivity at low-angles can be explained through

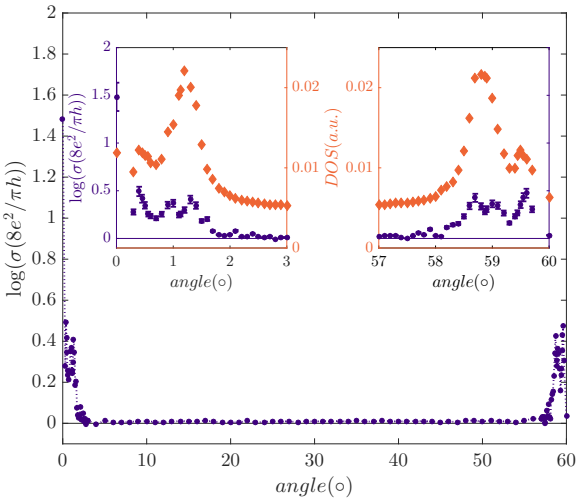

Figure 6.2: Conductivity at the Dirac point as a function of the rotation angle. The conductivity of decoupled layers is $2\sigma_0 = 8e^2/\pi h$. The inset shows the conductivity and DOS of structures with $\theta \in [0°, 3°]$ (left inset) and $\theta \in [57°, 60°]$ (right inset). The shape of the conductivity as a function of the rotation angle follows qualitatively the change in DOS (orange diamond markers) at the neutrality point. Error bars shown together with the conductivity values in the insets account for the estimate of the maximal error in the calculation (<10%).

the finite density of states in regions other than the AA (opposed to the vanishing density in the decoupled case), and a finite non-zero, albeit much smaller compared to the monolayer, value of the Fermi velocity, together with the large density of the AA states that contribute to the conductivity. This fact will be proven in the latter section, where the effect of the applied interlayer potential which will further localize the AA states is considered. There is an oscillating behaviour (shown in the insets of Fig. 6.2), with a slight suppression of the conductivity at the angles that are close to the so-called magic angles (as detailed in Ref. [240]). Our calculation suggests that the enhancement in the density of states prevails over the suppression of the velocity. As we can see, the value of conductivity follows the shape of DOS at the neutrality point.

The conductivity of the two limiting cases, i.e. the AB and AA alignments, is worth mentioning. Values of $\sim 2\sigma_0$ (AB stacked) and high value of $\sim 60\sigma_0$ (AA stacked) are obtained. Our findings agree with an increase in the DC limit of the optical conductivity of AA stacked bilayer as found in Refs. [249] and [222] where a strong Drude peak appearing

at low frequencies was reported. The reasons behind the value of the Dirac conductivity of AB stacked graphene are twofold. The first one is the Lifshitz transition due to skew interlayer hopping that induces the trigonal warping and increases the value of the conductivity to $6\sigma_0$ [221, 250, 251], which is implicitly taken into account in Eq. (3.3). The second reason that changes the minimal conductivity is the disorder [221, 251], which broadens the low energy states caused by the Lifshitz transition, and hence decreases the conductivity. In addition, absorbing boundary conditions effectively act as disorder contributing to the broadening of the states, finally resulting in the decrease of the conductivity.

In the following the methodology is further applied to specific structures, i.e. the low-angle tBLG in applied electric field, and low and high-angle tBLG with vacancy disorder.

6.3.2 Low-angle tBLG in perpendicular electric field

An electric potential difference applied to the tBLG layers depletes the low energy states in the AB regions due to the appearance of an induced electronic gap whose size is experimentally tunable. In addition, topological changes between AB and BA regions are expected to give rise to gapless boundary states protected from valley mixing, which can act as transport channels [245], and should preserve the non-zero conductivity.

First, the density of states for small-angle tBLG without and with an applied interlayer potential difference $V = 0.85$ V is presented in Fig. 6.3(a) and Fig. 6.3(b), respectively. The applied voltage ($V = 0.85$ V) is chosen to result in the maximal size of the gap of bulk AB stacked graphene [222]. By comparing different structures, we observe on one hand that by decreasing the angle, a merging of the low energy van Hove singularities occurs and results in an increased density around the Dirac point (AA states). On the other hand, by applying a voltage difference (the DOS for AB stacked graphene shows a large gap on the order of 0.3 eV), the states are depleted in the AB like regions.

The finite DOS at the energies where AB regions are gaped, and away from the localised AA peak, is predominantly the result of the boundary states going from an AA region to the neighbouring one. Both the localisation in the AA regions and the boundary states can be clearly seen in the spatial LDOS map of generic and relaxed $\theta = 0.3°$ structures for $V = 0.85$ V at different energies, see Fig. 6.4. Because of the finite area of the AB regions the local density of states in those regions is finite but strongly suppressed when compared to the density of the boundary

states.[2]

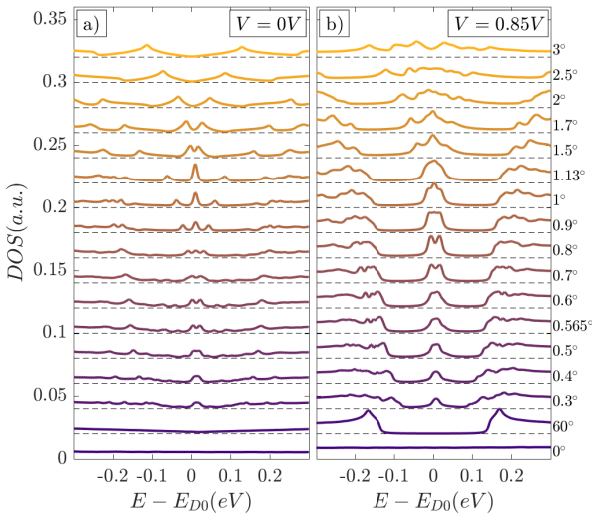

Figure 6.3: Low energy DOS for different rotation angles (a) without, and (b) with applied interlayer potential. The Dirac point exhibits a shift on the order of $\sim$ meV when comparing two different angles, originating from a slight change in interlayer hoppings. The merging of the van Hove singularities can be seen at lower energies with decreasing angle. Below 1.5° the increased density (and decreased velocity) of states at the Dirac point is a result of quasi-localised states in the AA region.

In Fig. 6.5 we compare the DOS and DC conductivities of generic and relaxed structures for tBLG with $\theta = 0.3°$ in the presence and absence of a perpendicular electric field. The non-zero conductivity when an electric field is applied, showed in Figs. 6.5(c, d), is a consequence of the boundary region states (between AB and BA regions) whose both density and velocity are dominant in the low energy range. To further prove this claim, let us consider in more detail how are different spatial regions affected by the electric field (Fig. 6.4(e-h)). As stated before, the depletion of the states in the AB like regions is a sign of the gap opening, which only in the case of perfect AB bilayer would be total. In tBLG, we have the finite (but negligible compared to other regions) density influenced by the neighbouring regions. An additional effect is that the AA states are more isolated, concluded from the fact that although their density is increased (Fig. 6.3), we see a drop of the conductivity at the Dirac point, meaning that effectively a stronger localisation is induced.

[2]See Supplemental Material [50] for movies of LDOS maps at different energies.

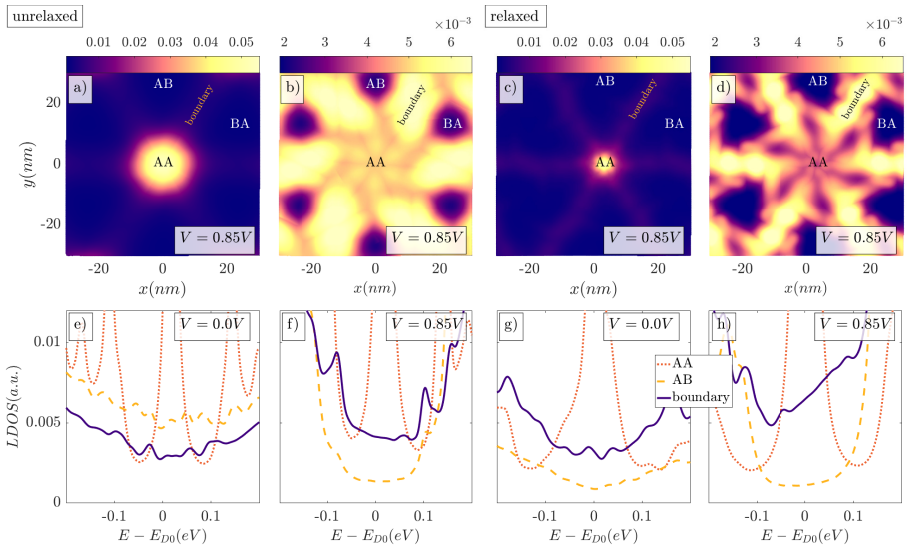

Figure 6.4: Local density of states for $\theta = 0.3°$ angle tBLG before (a, b, e, f) and after relaxation (c, d, g, h). Spatially dependent LDOS maps with the applied interlayer potential $V = 0.85$ V, are shown at energies (a) $E = 0.01$ eV, (b) $E = -0.06$ eV, c) $E = 0.01$ eV, and (d) $E = -0.06$ eV. LDOS at different central sites in AB, AA, and AB/BA boundary region are presented in order to differentiate the dominant states in the low energy spectrum. The LDOS is plotted at sites belonging the dimer pair. Insets (e, g) show LDOS without ($V = 0$ V) and (f, h) with ($V = 0.85$ V) the applied potential.

AB/BA boundary regions host now the topological states which are the cause of LDOS increase at the boundary sites, see Fig. 6.4(f, h) compared to Fig. 6.4(e, g). We observe a nearly flat value of the conductivity in the energy range corresponding to the gap appearing in the AB regions. The correlation between the LDOS and the conductivity is not apparent before making the distinction between localised modes (resonances in the LDOS) and a continuum background [231] responsible for transport. On average (DOS shown in Fig. 6.5(a, b)), this background, whose monotonousness is influenced by the sublattice and layer polarisation of the LDOS as well, result in the almost constant value of conductivity.

In order to further promote the appearance of boundary states, and enhance the low energy conductivity, we should enlarge the energetically favourable AB (gaped) regions, while on the other hand decrease the localised AA regions. This can be achieved by relaxing the low-angle structures, thus by minimising the van der Waals interaction. The results

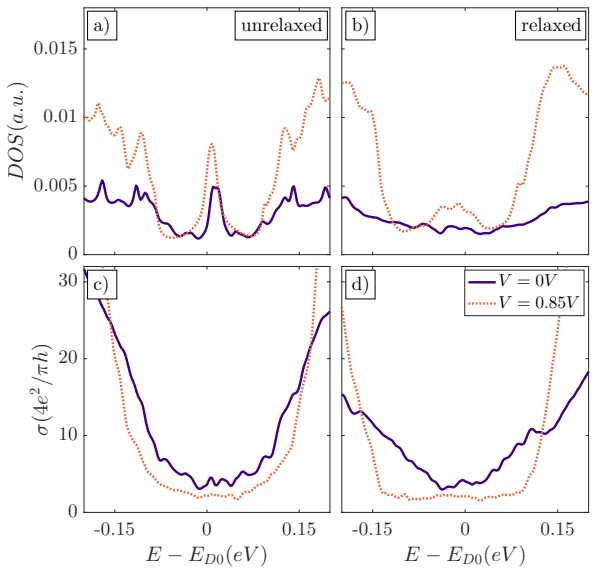

Figure 6.5: Spectral properties of $\theta = 0.3°$ tBLG without (a) and (c), and with relaxation (b) and (d). Panels (a) and (b) are showing DOS, while panels (c) and (d) show the low energy DC conductivity in the presence and absence of the applied interlayer potential.

shown in Fig. 6.4 confirm our goal, we see well defined boundary states and narrowing of the AA regions. The flatness of the conductivity is now on a broader energy range, which is a result of the gap increase in the enlarged AB regions (Fig. 6.5(d)). The decrease of the DOS at the Dirac point did not result in a significant decrease of the conductivity, further confirming the statement on the increased localisation, and hence small contribution of the AA states in the presence of the applied electric field.

Recent experiments on low-angle tBLG show that electron-electron interactions have a strong effect on the transport properties in flakes with accurately controlled angles [22]. The interactions are reported to affect the transport properties only when the width of the flat bands localised in the AA region is comparable to the energy scale of the interactions. Although in our work interactions are not considered, the validity of our results stand when interactions are not significant. Our results agree qualitatively with the experimental findings at finite temperature and for specific angles, where the interactions induced gaps are closed. At rotation angle close to the second magic angle ($\theta \sim 0.5°$) the correlations are not altering the transport properties (Fig. 3(b) for ($\theta \sim 0.43°$) in Ref. [22]), which is also the case for the higher temperature conductance measurements (Fig. 1(f) $T = 80$ K in Ref. [22]). These measurements

agree with the description of nearly flat conductivity at low energies obtained from our calculation. Our claim is that the main contribution to the conductivity comes from the boundary region states, which results in an almost constant DC conductivity.

Effects of the asymmetric gating

As a part of a separate but closely related study we will show what happens when the electric potential is applied asymmetrically to the two layers, and when the polarity of the potential is changed.

Changes in the electronic properties along different spatial directions are important for understanding the nature and the origin of states that appear in the low energy tBLG spectrum. For example, LDOS across the AA region over the domain boundary and from AB to BA regions would reveal how the corresponding states change both spatially and at different energies (these regions are marked in the top-right insets of Figs. 6.6 and 6.7). Furthermore, in the case of a gated sample, the same plot will reveal how different potential affects the helical and the states in the AA and AB/BA regions. Experimentally, the potential is controlled by the bottom SiO_2 buried gate that induces layer asymmetry in the sample, which is now taken to be significantly smaller compared to the Fig. 6.4, making this case particularly relevant. Cuts along these regions are shown for both layers and, due to the pronounced sublattice asymmetry, at different sublattices labelled as A and B (top layer), and C and D (bottom layer). In the case of a non-gated sample Figs. 6.6 and 6.7(f-i), the state in the AA region appears at the Fermi level (0 meV), which is surrounded with features resembling the zero-pseudo Landau level (0PLL) [252]. The state in the AA region is present in both sublattices and both layers, while the 0PLL switches the sublattice when going across the center of the AA region. States that originate from AB/BA regions have finite density which can be seen in Fig. 6.7(f-i), they are sublattice polarised and span over the boundary region. Still, note here that these states are not unidirectional channels that go along the AB/BA interface, but rather extended states which disappear when the potential is applied. When the sample is gated, Figs. 6.6 and 6.7(a-d) for positive and (k-n) negative gate potential on the bottom layer (in both cases potential is $|V_b| = 200$ meV) a gap is opened in the AB and BA like regions, which, due to the changes of the structural stacking order, closes at the boundary and, as discussed in the previous section, boundary channels appear. Those states (labelled as helical) can be seen as a background density at energies inside the gap which is marked with

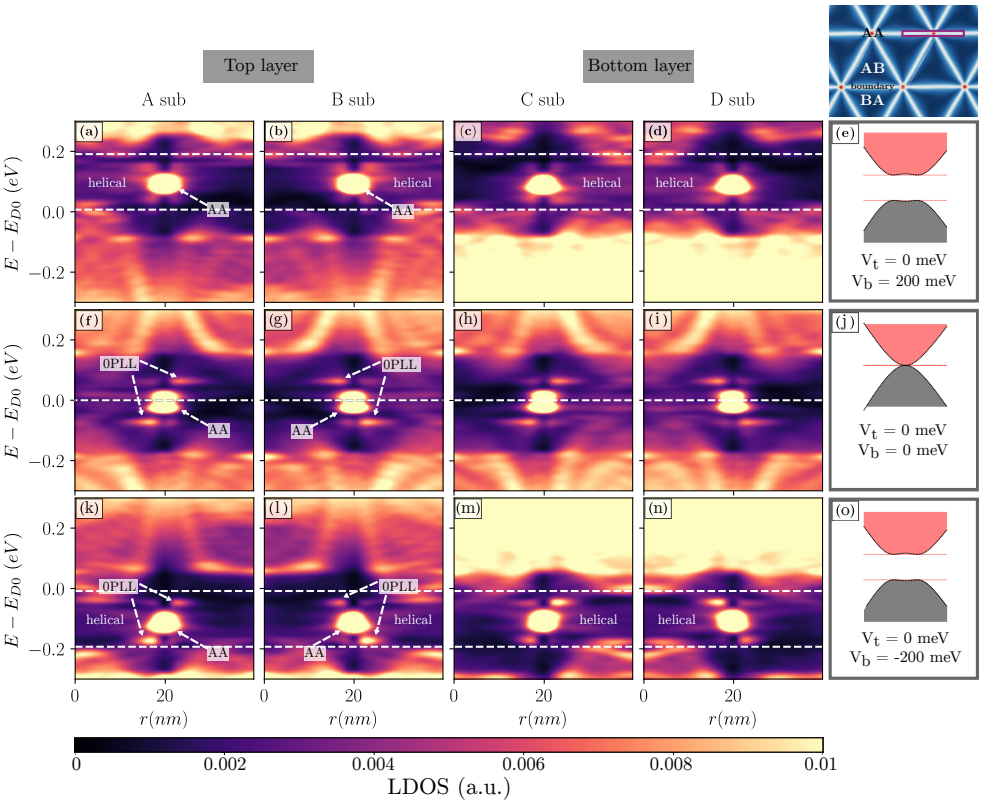

Figure 6.6: LDOS of a gated (a-d) $V_b = 200$ meV $V_t = 0$ meV, (k-n) $V_b = -200$ meV $V_t = 0$ meV, and non-gated sample of relaxed $\theta = 0.3°$ tBLG along the directions across the AA region, specified in the top-right inset. Size of the band gap estimated from the gated AB bilayer, nature (origin) of the states in the low energy spectrum, sublattice, and layer are noted in the figure. Panels (e, j) and (o) present a schematic of the gating configuration.

dashed white lines, both along the boundaries away from the state in the AA region (Fig. 6.6) and across the boundary in Fig. 6.7. To a certain extent these states show both sublattice and layer polarisation. Along the domain wall (boundary region) they are distributed over both sublattices. On the contrary, when the boundary is crossed and they are closer to the center of AB/BA regions, the sublattice polarisation becomes more pronounced. The layer polarisation is apparent at different energies. Closer to the band gap edges helical states become localised in one of the layers. Closer inspection reveals that the 0PLL becomes less pronounced in the case of positively gated bottom layer (Fig. 6.6(a-d)) compared to the other two cases.

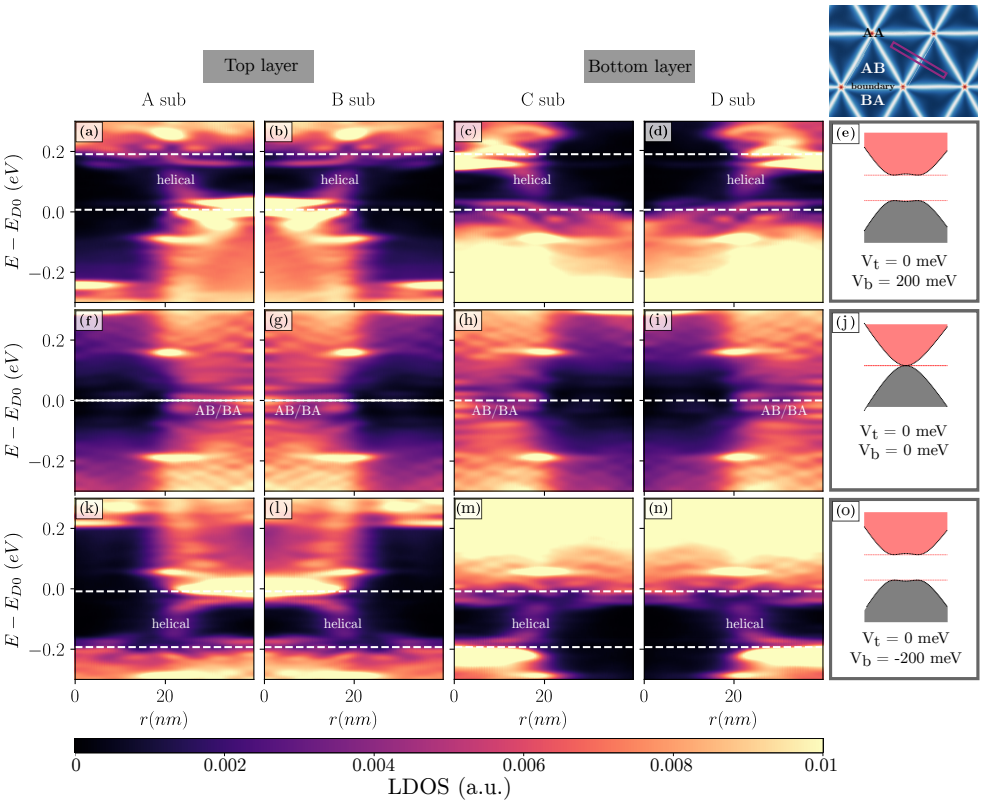

Figure 6.7: LDOS of a gated (a-d) $V_b = 200$ meV $V_t = 0$ meV, (k-n) $V_b = -200$ meV $V_t = 0$ meV, and non-gated sample of relaxed $\theta = 0.3°$ tBLG along the directions across the boundary region, specified in the top-right inset. Size of the band gap estimated from the gated AB bilayer, nature (origin) of the states in the low energy spectrum, sublattice, and layer are noted in the figure. Panels (e, j) and (o) present a schematic of the gating configuration.

More importantly, when the layer potential is changed, it can be observed, from for example Fig. 6.7 panels (a, b) and (m, n), that the switch of the field polarity exchanges both the layer and the sublattice of the helical states, suggesting in such a way a possibility to electrically control the layer polarisation of the helical channels.

6.3.3 Comparison with experiment

The motivation to explore the LDOS distribution in tiny angle twisted layer graphene comes from a recent experimental study by our colleagues Y. Jiang, J. Mao, and E. Andrei (as mentioned in the beginning of this

chapter). To further explore the relevance of the simulated results, in Fig. 6.8 the numerical simulations are compared with the experimental results for $\theta \approx 0.3^\circ$ gated tBLG. In panels 6.8(a-d) STS (dI/dV) maps for different gating polarity ($V_g = 55$ V and $V_g = -60$ V) are compared with the theoretical LDOS maps in different layers of a relaxed tBLG, all at energies that are within the bilayer gap, corresponding to the appearance of the helical states network, as discussed in Sec. 6.3.2. This comparison directly confirms the assumption of gate-induced layer polarity switch, as the experimental results at different gate voltages agree nicely with the simulated results at different layers for the same gating configuration ($V_b = 200$ meV). In addition, by controlling the gate voltage, the nature of the boundary channels is modified (single or double channel depending on the energy) which is also supported by our theoretical results. Furthermore, to emphasise the agreement between the two results, in panels (e) and (f) we compare the spatial LDOS across a the AB/BA boundary, along the same path as in Fig. 6.7. Both results clearly show a number of similar features: (i) the signature of the field induced bilayer gap in the AB/BA regions, corresponding to the gap induced in plain AB bilayer graphene (marked with dashed black lines in panel (f)), (ii) continuum of boundary states in the boundary region (experiment, in the range of $r = (15, 30)$ nm, and theory in the range of $r = (8, 22)$ nm), and finally, (iii) band-gap edge away from the boundary agrees in the two cases, which confirms the validity of the model used for simulating tBLG at low rotation angles.

6.3.4 Disorder effects

Long-range impurities in graphene can result in a localisation only when the induced disorder potential is strong enough to affect the intervalley scattering rates [253]. More interesting are the topological defects that are the limiting factor for the transport even for single realisation [254]. Vacancies, as short-range resonant scatterers, form quasi-localised states in the vicinity of missing atoms, appearing in the energy spectrum near the Dirac point, with their amplitude decaying as $\sim 1/r$ [255]. They can result in the scattering of carriers over large momentum and induce intervalley scattering, which, if strong enough, would turn graphene into an Anderson insulator [256]. A remarkable feature of vacancy induced zero energy mode (ZEM) in monolayer graphene is the protection provided by the chiral symmetry at the Dirac point manifested as the preserved universal value of conductivity over a wide range of disorder concentrations [71, 257], which is the known value for the conductivity of clean

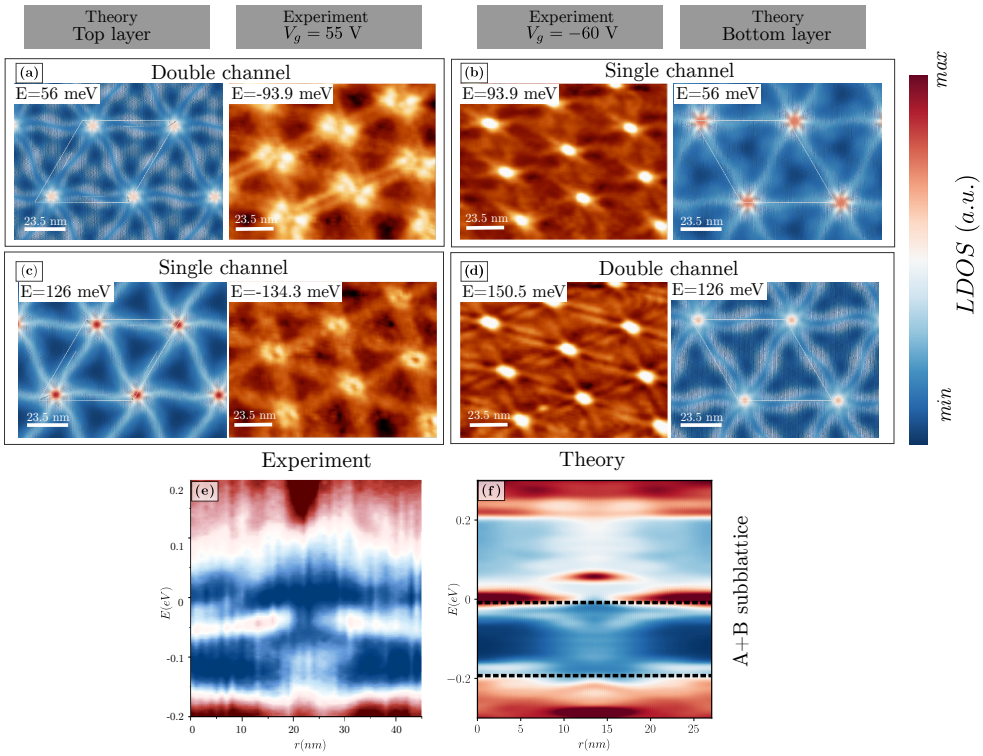

Figure 6.8: Comparison with the experiment of $\theta \approx 0.3°$ gated tBLG. (a-d) LDOS (theory) and STS (dI/dV) (experiment) maps at different energies inside the bilayer gap, shown in panels, which show the appearance of helical boundary states. Changing the layer theoretically (top and bottom) for the same gating configuration, $V_b = 200$ meV, is equivalent to changing the gate polarisation in the experiment ($V_g = 55$ V and $V_g = -60$ V). (e-f) Comparison between the measured (experiment) and simulated (theory) sublattice averaged LDOS across the boundary (same path as in Fig. 6.7).

graphene in the thermodynamic limit [258], and shows that vacancy induced ZEM is delocalised. On the other hand, the vacancy states are in particular sensitive to electron-hole symmetry. In the case of monolayer graphene, the asymmetry induces a shift of the vacancy peak away from the Dirac point to the continuum of the extended states [255, 259].

In the following we investigate the effects of vacancies on the low-angle $\theta = 1.13°$ and high-angle $\theta = 21.78°$ tBLG conductivity. All the values obtained are an average of 6 randomly distributed vacancy realisations. For the case of high-angle tBLG, we refer to the clean limit conductivity calculation $\sigma(E_{D0})$ at the Dirac point, presented in Fig. 6.2.

Our main reasoning is that the equivalent picture of high-angle tBLG, for a large range of twist angles, is the combination of two decoupled monolayers. Therefore, we conclude that if the picture of independent monolayers holds, we can expect the value of conductivity to be a simple superposition, leading to value $\sigma(E_{D0}) = 2 \times 4e^2/\pi h = 8e^2/\pi h$.

Our first conclusion is that the vacancy peak seen in the density of states, shown in Fig. 6.9, becomes broadened and is shifted away from the Dirac point when considering particle asymmetric model Hamiltonian with longer intralayer range hopping. This agrees with previous reports on monolayer graphene with electron-hole asymmetry induced by the inclusion of the next-nearest in-plane neighbour in the TB Hamiltonian [259]. We also report a concentration dependent shift on the order of ~ 10 meV of the vacancy peak, see Fig. 6.9 for the DOS of $\theta = 21.78°$ tBLG, without and with the next-nearest neighbours included in the TB model for different vacancy concentrations, shown respectively in Fig. 6.9(a) and Fig. 6.9(b). The transport properties of tBLG for two

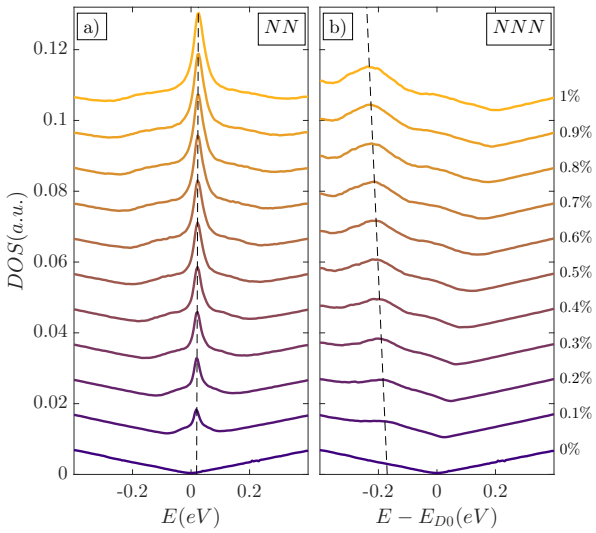

Figure 6.9: Low energy DOS for different vacancy concentrations without (NN) (a) and with (NNN) (b) next-nearest neighbour hopping for $\theta = 21.787°$ tBLG. In the latter case states are quasi-localised, in the energy region of the extended states. The vacancy peak when next-nearest neighbours are included has a shift (~ 10 meV) which is concentration dependent, while without taking them into account a shift is observed only with respect to the initial Dirac point (0 eV). Each line is offset with $\Delta y = 0.02$ with respect to the previous one for better distinction.

different concentrations of vacancy disorder are investigated, 0.5% and

1%, shown in Fig. 6.10. Similar to the behaviour observed for monolayer graphene with only NN intralayer hopping, reported in Ref. [71], the vacancies induce localisation, concluded from the conductivity calculation. This can be seen in Fig. 6.10(d), where one observes a clear suppression of the conductivity at energies near the Dirac point. The value of conductivity at the neutrality point for $\theta = 21.78°$ tBLG is around the value of the sample without vacancies, with a small shift of the Dirac point energy also observed in the DOS, which points to the fact that there are no additional effects due to induced intervalley scattering, and no effects due to the decrease or increase of interlayer tunnelling [260]. This means that the chiral symmetry is preserved, and that zero energy modes are delocalised.

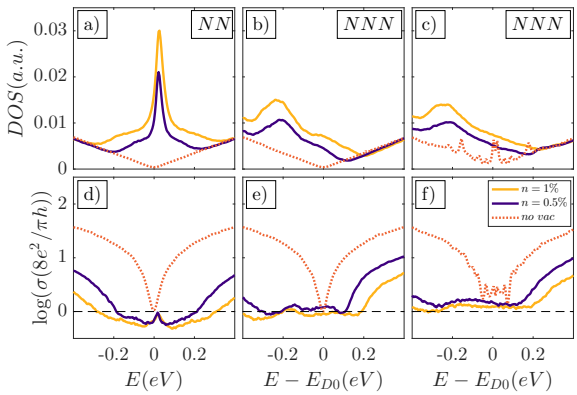

Figure 6.10: Comparison of the conductivity and DOS at low energies without vacancies and with vacancy concentration of 0.5% and 1%. Results for $\theta = 21.787°$ tBLG are shown in panels (a, b) as DOS and (d, e) as DC conductivity. Results for $\theta = 1.13°$ tBLG are shown in panels c) as DOS and f) as DC conductivity. In panels (a) and (d) only NN are considered, while in other panels the NNN are included in the Hamiltonian.

The result with (NNN) and without (NN) the effect of next-nearest neighbour hopping are now compared for the same angle. The model Hamiltonian and the nature of the vacancy induced states are very different. Although the DOS shows the resonant states at finite energy, and a different broadening of the vacancy peak, as shown in Fig. 6.10(b), the conductivity has a similar behaviour at the Dirac point. We can distinguish a plateau, shown in Fig. 6.10(e), theoretically described previously in monolayer graphene [261], which still has the value around the conductivity of the vacancy free sample ($8e^2/\pi h$). The suppression of the

conductivity in NNN is weaker around the vacancy peak point, when compared to the short-range NN interactions, meaning that these states are not fully localised. Furthermore, based on the values of conductivity, at high-angles the physical picture of two decoupled monolayers remains valid even in the presence of strong disorder.

At low-angles, here $\theta = 1.13°$, the universal value of the clean limit of $2\sigma_0$ is not preserved as chiral symmetry is already broken (Fig. 6.2) due to the presence of low energy van Hove singularities or quasi-localised states which can be seen in Fig. 6.10(c), similar to the experimentally confirmed [262] broken chirality close to the van Hove singularities of monolayer graphene. Vacancies will therefore have a strong effect and suppress the conductivity at all energies, even at the Dirac point, as can be seen Fig. 6.10(f). The low energy van Hove singularities are completely smeared by the presence of the vacancy induced states, and the resulting plateau has similar behaviour and value as in the case of high-twist angles. Upon this, it can be concluded that distinguishing the transport properties of differently rotated structures of bilayer graphene depends fully on the level of the resonant disorder, which experimentally correspond to the quality of the sample.

6.4 Conclusions

In conclusion, a real-space method for the calculation of the DC conductivity is applied to twisted bilayer graphene with a wide range of rotation angles. Both high and low twist angles and effects of an applied perpendicular electric field and vacancies are examined. For low rotation angles and in the presence of an electric field, a strong effect of the boundary modes on the DC conductivity is shown, proving that the real-space method clearly captures the change in topology. In addition, switch of the gate polarity in an asymmetrically gated system shows similar effects as the exchange between the layers, both observed experimentally and supported by our theoretical results. An agreement with previous investigations of the conductivity of vacancy induced ZEM in monolayer graphene and reported results for large angle tBLG is observed. Furthermore, these results infer the preservation of chiral symmetry for high-angles, and its breaking in the low twist angle limit. This has important consequences for disordered systems, because the minimal conductivity at the neutrality point is universal only when chiral symmetry is conserved. In addition, a nearly flat conductivity due to AB/BA boundary states when a perpendicular electric field is applied is

in qualitative agreement with recent experimental findings in low-angle tBLG [22]. As the boundary states are expected to survive in the presence of magnetic fields, they will also contribute to the conductivity.

7 | Double moiré with a twist: super-moiré in encapsulated graphene

A periodic spatial modulation, as created by a moiré pattern, has been extensively studied with the view to engineer and tune the properties of graphene. In this chapter we study graphene encapsulated by hBN when slightly misaligned with the top and bottom hBN layers, which experiences two interfering moiré patterns, resulting in a so-called super-moiré (SM). This leads to a lattice and electronic spectrum reconstruction. A geometrical construction of the non-relaxed SM patterns allows us to indicate qualitatively the induced changes in the electronic properties and to locate the SM features in the density of states and in the conductivity. To emphasize the effect of lattice relaxation, band gaps at all Dirac-like points in the hole doped part of the reconstructed spectrum are reported, which are expected to be enhanced when including interaction effects. Our result is able to distinguish effects due to lattice relaxation and due to the interfering SM and provides a clear picture on the origin of recently experimentally observed effects in such trilayer heterostuctures.[1] This work presents a detailed study on the electronic properties of encapsulated graphene motivated by our recent collaboration with colleagues from Manchester University, in which the experimental observation of the super-moiré effects are discussed [263].

7.1 Motivation

Encapsulation of graphene by hBN is a widely used technique for obtaining devices with exceptional electronic properties [33, 264]. This is

[1] The results of this chapter are available as:
M. Anđelković, S. P. Milovanović, L. Covaci, F. M. Peeters, arXiv:1910.00345 (2019).

due to the fact that hBN serves as a protective layer for graphene, isolating it from the contaminants from the environment, and to flatten the graphene layer. Although graphene and hBN have similar crystal structure (difference between lattice constants is $\approx 1.8\%$), hBN is an inert band insulator that does not alter the electronic properties of graphene when the two layers are misoriented. In contrast, when different lattices are closely aligned, spectrum [14] and surface [9] reconstruction becomes significant as a consequence of the moiré periodicity between the two or more crystals. Moiré reconstruction further induces effects that are of great importance in the light of gap engineering and insulating phases [16, 17], tuning between metallic and superconductive phases [265] and even exploring interaction effects [266] in hBN/gr multilayers. In addition, recent experimental advancement showed that it is possible to align two monolayer sheets to a high rotation precision of $0.1^\circ - 0.2^\circ$ [4, 267]. Even dynamical tuning of the rotation angle with precision below 0.2° has been demonstrated [268]. Further, high rotation controllability led to encapsulated graphene devices almost aligned to both hBN layers, gaining attention when additional spectrum reconstruction was reported [40, 263, 269].

If a moiré pattern, formed by e.g. two monolayers, is brought in contact with another monolayer, the interference will lead to a supermoiré (SM) structure, leading to additional Dirac-like points. In this chapter a detailed study on the origin of the SM features is presented, the resulting effects on the electronic properties and on the lattice reconstruction. Even in the rigid form, small misorientation in the trilayer creates reconstructed bands that are different from those found in bilayer graphene/hBN systems. The effects are modelled as a function of the relative twist between the layers and compare the results against a simple, geometrical description of the moiré systems. Further, the renormalisation of the Fermi velocity and the appearance of bands with almost vanishing dispersion are discussed. Lastly, experimentally detectable band gaps at all Dirac-like points induced by the moiré patterns as a result of lattice relaxation are reported. Moreover, the used methodology can be applied to different almost aligned multilayer-heterostructures with small difference in lattice constants of individual layers where similar effects can be expected.

7.2 Geometrical considerations in rigid trilayers

Before further exploring the effects of the alignment between graphene and multiple hBN layers, a qualitative description of the moiré pattern is worth reviewing. In its rigid form, graphene and hBN can be defined as bipartite honeycomb lattices, as illustrated in Fig. 7.1, with unit cell vectors of graphene $\boldsymbol{a}_1^{gr} = a[1, 0]$, $\boldsymbol{a}_2^{gr} = a[1/2, \sqrt{3}/2]$, and bottom ($i = 1$) and top ($i = 2$) hBN $\boldsymbol{a}_{1,2}^{hBN_i} = \boldsymbol{R}(\theta_i)\boldsymbol{a}_{1,2}^{gr}/(1 + \delta_i)$, where $a \approx 0.246$ nm is the length of graphene unit cell, $\boldsymbol{R}(\theta_i)$ represents a rotation matrix in counter-clock wise direction by an angle θ_i, and $\delta_{1,2}$ are the relative ratios between graphene and bottom/top hBN lattice constants, with the unrelaxed value of $56/55 - 1 \approx 0.018$. Reciprocal vectors are defined as $\boldsymbol{b}_1^{gr} = 2\pi/a[1, -\sqrt{3}/3]$, $\boldsymbol{b}_2^{gr} = 2\pi/a[0, 2\sqrt{3}/3]$, $\boldsymbol{b}_{1,2}^{hBN_i} = \boldsymbol{R}(\theta_i)\boldsymbol{b}_{1,2}^{gr}/(1 + \delta_i)$ satisfying $\boldsymbol{b}_j^{gr}\boldsymbol{a}_k^{gr} = \boldsymbol{b}_j^{hBN_i}\boldsymbol{a}_k^{hBN_i} = 2\pi\delta_{j,k}$.

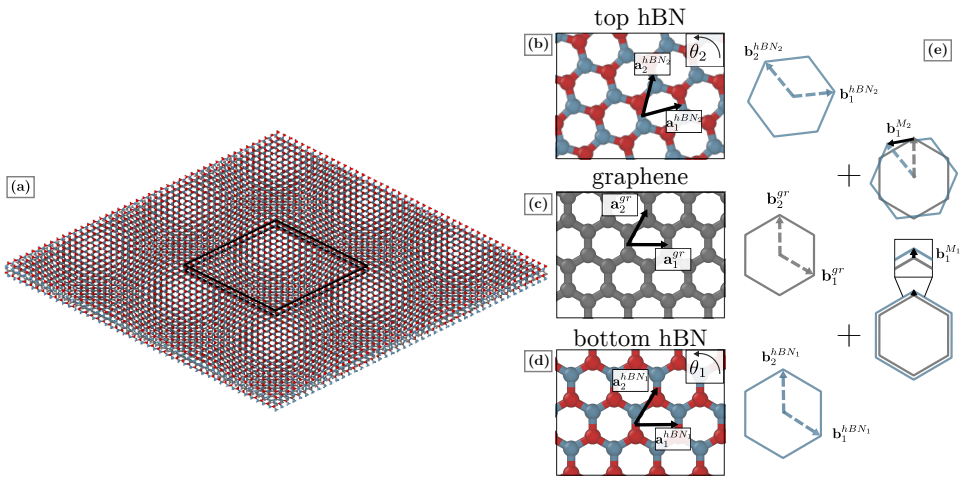

Figure 7.1: (a) Schematic of trilayer hBN/gr/hBN structure. Bottom and top hBN layers are twisted over $\theta_1 = 0°$ and $\theta_2 = 60°$, respectively. In panels (b - d) top hBN (θ_2), graphene, and bottom hBN ($\theta_1 = 0°$) lattices and corresponding unit cell vectors are shown. (e) Brillouin zone of each lattice, and the moiré reciprocal vector between graphene and top/bottom hBN are depicted. The ratio between the two lattices is exaggerated $\delta = 16/15 - 1$ for visualization purposes.

From there, the top and the bottom moiré reciprocal vectors can be defined as a difference between the reciprocal vectors of graphene and hBN, $\boldsymbol{b}_{1,2}^{M_i} = \boldsymbol{b}_{1,2}^{gr} - \boldsymbol{b}_{1,2}^{hBN_i}$.

The massless Dirac-Weyl equation describes the behaviour of a single graphene layer, while hBN layers can be modelled as an effective potential and a gauge field in the continuum approximation [270]. Still, in the continuum description strain and relaxation effects are fitted parametrically, which results in loosing the generality of the model. This is why in the following a real-space representation of a tight-binding Hamiltonian will be used. In a similar manner as in the continuum description, hBN substrate can be effectively modelled as a modification of both hopping terms and the on-site energy. Following the work in [271], but considering only an additional potential that respects the periodicity of the underlying moiré patterns, the change of the on-site energy is given by

$$\begin{aligned} \varepsilon_{i,+}^{m,n} &= c_1(\theta_i, \delta_i) \left[\cos(\boldsymbol{g}_1^i \boldsymbol{r}_{m,n}) + \cos(\boldsymbol{g}_3^i \boldsymbol{r}_{m,n}) + \cos(\boldsymbol{g}_5^i \boldsymbol{r}_{m,n})\right], \\ \varepsilon_{i,-}^{m,n} &= c_2(\theta_i, \delta_i) \left[\sin(\boldsymbol{g}_1^i \boldsymbol{r}_{m,n}) + \sin(\boldsymbol{g}_3^i \boldsymbol{r}_{m,n}) + \sin(\boldsymbol{g}_5^i \boldsymbol{r}_{m,n})\right], \end{aligned} \tag{7.1}$$

where the parameters c_1 and c_2 contain the lattice information of the two crystals and the rotation angle between them, m and n are indexes of the unit cell, and $\boldsymbol{r}_{m,n} = m\boldsymbol{a}_1^{gr} + n\boldsymbol{a}_2^{gr}$. The two terms in Eq. (7.1), $\varepsilon_{i,+}$ and $\varepsilon_{i,-}$ denote sublattice symmetric and antisymmetric potential, respectively (due to hBN layer i). Rotated moiré reciprocal lattice vectors $\boldsymbol{g}_j^i$ are $\boldsymbol{g}_j^i = \boldsymbol{R}\left((j-1)\pi/3\right)\boldsymbol{b}_1^{M_i}$.

In the case of almost aligned graphene with multiple hBN layers, the effective on-site terms will become superposition of the changes due to each of the hBN layers, taking into account the exponential decrease of the interlayer interaction. Without loss of generality, it is further assumed (except when considering the effect of the misalignment) that graphene is perfectly aligned with the bottom hBN layer, while the top hBN is twisted. Taking this into account, in Fig. 7.2 the superimposed on-site potential in graphene layer, and the Fourier transformation of this potential, originating from the encapsulation, are shown.

From both the real and the reciprocal space it is clear that in addition to the moiré pattern due to aligned bottom hBN (marked in Fig. 7.2 with black unit cell in real space, and black mini-Brillouin zone in reciprocal space with $\lambda \approx 13.9$ nm), and the rotated moiré between graphene and top hBN (red colour), there exist additional periodicities of longer range. The Fourier transformation (FT) in reciprocal space further reveals which components are important. From this qualitative analysis, a comprehensive description of possible moiré patterns are obtained. Straightforward geometrical consideration shows that beside the aligned and the rotated graphene-moiré spots in the FT, different combinations of the two result in additional SM patterns, similar to the case of two-layered systems with hexagonal symmetry [272]. The corresponding FT

harmonics can be derived as translation (difference) vectors that match the two of the original moiré patterns. Hence, the SM reciprocal vectors can be obtained as a difference between the aligned and rotated reciprocal vectors, or their multiples.

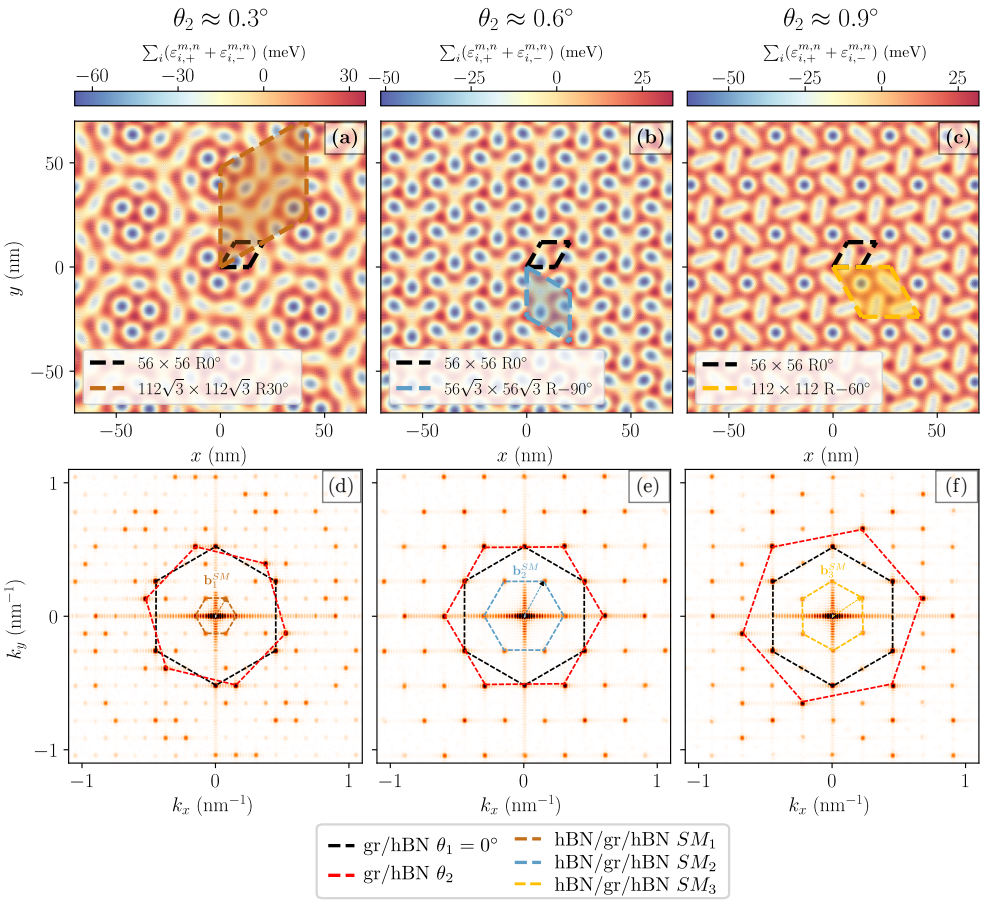

Figure 7.2: (a - c) Real space distribution of the potential in graphene defined in Eq. (7.1) due to two hBN layers for $\theta_1 = 0°$ with top hBN layer twisted over $\theta_2 \approx 0.3°$, $\theta_2 \approx 0.6°$ and $\theta_2 \approx 0.9°$. The parallelograms are the aligned moiré (black) and the different SM unit cells, defined in Wood's notation. (d - f) FT of the potential shown in panels (a - c), from which super-moiré period can be obtained. Hexagons show the mini-Brillouin zones of aligned (black), twisted (red) and different super-moirés.

The real space description of the SM starts with previously introduced graphene and hBN lattices and the corresponding moiré patterns.

From there, an arbitrary super-moiré vector is

$$\boldsymbol{b}^{SM} = i\boldsymbol{b}_1^{M_1} + j\boldsymbol{b}_2^{M_1} - k\boldsymbol{b}_1^{M_2} - l\boldsymbol{b}_2^{M_2}, \tag{7.2}$$

with $i, j, k, l \in \mathbb{Z}$, which can be represented using a more compact notation

$$\boldsymbol{b}^{SM} = \sum \begin{pmatrix} i & j \\ -k & -l \end{pmatrix} \odot \begin{pmatrix} \boldsymbol{b}_1^{M_1} & \boldsymbol{b}_2^{M_1} \\ \boldsymbol{b}_1^{M_2} & \boldsymbol{b}_2^{M_2} \end{pmatrix}, \tag{7.3}$$

where $\odot$ denotes the element-wise product. This frequency analysis leads to analytical expressions for possible SM patterns obtained for an arbitrary rotation between the two moiré patterns. The shortest reciprocal (or the longest real space) SM vectors are the ones affecting the low energy spectrum. Different SM harmonics at low rotation angles which emerge as the difference between the moiré harmonics of different order agree well with the experimentally observed features from [263] (Sec. 7.4.3). These are shown in the inset of Fig. 7.3, where the coloured hexagons represent their mini-Brillouin zones. Under the assumptions of $\theta_1 = 0°$, and $\delta_1 = \delta_2 = \delta$, four different low-energy, low-angle harmonics, which will be later used for comparison against the numerical results, and the corresponding real space periodicities λ_i^{SM} (using relation $\lambda = 4\pi/\sqrt{3}/|\boldsymbol{b}_i|$) are

$$\begin{aligned}
\boldsymbol{b}_1^{SM} &= \sum \begin{pmatrix} 0 & 1 \\ 0 & -1 \end{pmatrix} \odot \begin{pmatrix} \boldsymbol{b}_1^{M_1} & \boldsymbol{b}_2^{M_1} \\ \boldsymbol{b}_1^{M_2} & \boldsymbol{b}_2^{M_2} \end{pmatrix}, \\
\lambda_1^{SM} &= \frac{a(1+\delta)}{\sqrt{2 - 2\cos(\theta_2)}}, \\
\boldsymbol{b}_2^{SM} &= \sum \begin{pmatrix} 0 & 1 \\ -1 & -1 \end{pmatrix} \odot \begin{pmatrix} \boldsymbol{b}_1^{M_1} & \boldsymbol{b}_2^{M_1} \\ \boldsymbol{b}_1^{M_2} & \boldsymbol{b}_2^{M_2} \end{pmatrix}, \\
\lambda_2^{SM} &= \frac{a(1+\delta)}{\sqrt{(2-\delta)(1-\cos(\theta_2)) + \delta^2 - \sqrt{3}\delta\sin(\theta_2)}}, \\
\boldsymbol{b}_3^{SM} &= \sum \begin{pmatrix} 0 & 1 \\ -2 & 0 \end{pmatrix} \odot \begin{pmatrix} \boldsymbol{b}_1^{M_1} & \boldsymbol{b}_2^{M_1} \\ \boldsymbol{b}_1^{M_2} & \boldsymbol{b}_2^{M_2} \end{pmatrix}, \\
\lambda_3^{SM} &= \frac{a(1+\delta)}{\sqrt{2 + 3\delta^2 - 2\cos(\theta_2) - 2\sqrt{3}\delta\sin(\theta_2)}}, \\
\boldsymbol{b}_4^{SM} &= \sum \begin{pmatrix} 1 & 0 \\ 0 & -1 \end{pmatrix} \odot \begin{pmatrix} \boldsymbol{b}_1^{M_1} & \boldsymbol{b}_2^{M_1} \\ \boldsymbol{b}_1^{M_2} & \boldsymbol{b}_2^{M_2} \end{pmatrix}, \\
\lambda_4^{SM} &= \frac{a(1+\delta)}{\sqrt{(2+\delta)(1-\cos(\theta_2)) + \delta^2 + \sqrt{3}\delta\sin(\theta_2)}},
\end{aligned} \tag{7.4}$$

as being shown in Fig. 7.3(a). Further, energy of the reconstruction is related to the period as $E_D = \pm 2\pi\hbar v_F/(\sqrt{3}\lambda)$ and is shown in Fig. 7.3(b).

Previous consideration also applies for any combination of 2D materials with honeycomb lattice. Notice that it is the close matching of the lattice constants of the two materials that results in the reconstruction of both the energy dispersion through the formation of moiré induced mini-bands and secondary Dirac points (SDPs) and the reconstruction of the surface due to the van der Waals interaction as further discussed in section 7.4.2.

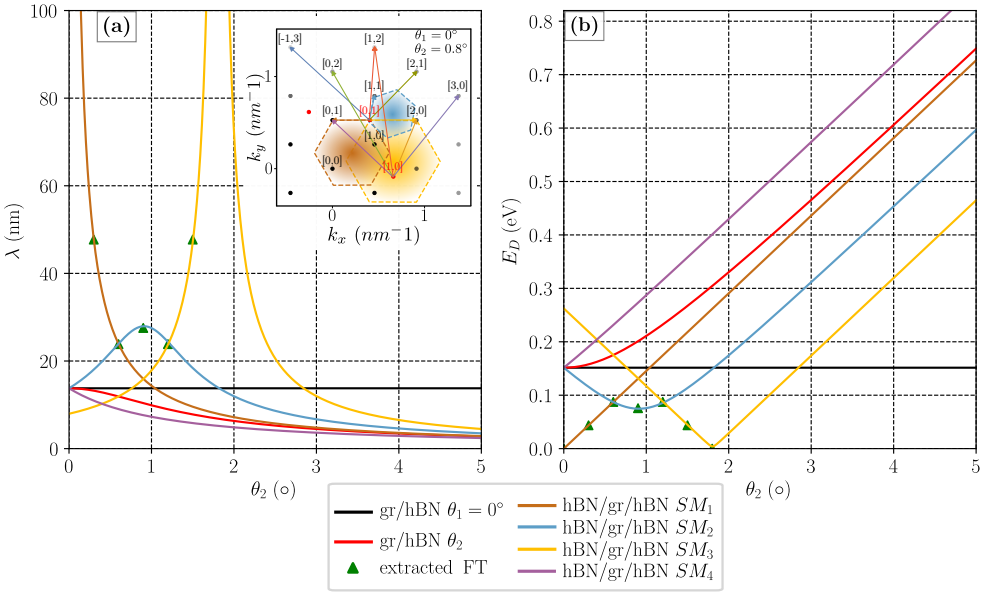

Figure 7.3: Change of the (a) moiré and super-moiré period and (b) the energy of the additional Dirac-like points as a function of rotation angle θ_2. Different lines represent the super-moiré harmonics defined in the inset of panel (a), the aligned graphene-hBN ($\theta_1 = 0°$) and the rotated graphene-hBN moiré (θ_2). Super-moiré unit cell lengths extracted from FT in Fig. 7.2 and two additional angles ($\theta_2 \approx 1.2°$ and $1.5°$) are shown with green triangles.

The qualitative analysis of multiple superimposed moiré patterns does not include a quantitative description of the coupling between the layers. Experimental reports have shown that the van der Waals coupling leads to straining of the lattice, resulting in a commensurate state of the hBN/gr bilayers for almost aligned structures with angle smaller than 1° [9]. For larger rotation angles, the hBN potential only weakly

affects the graphene layer due to the fast moiré oscillations [9]. It is only in the regime of highly coupled layers that the fine effect of mini-band formation will occur. This is why in the following section, hBN/gr/hBN trilayers are simulated following the real space methodology, where the hBN layers are considered fully and not as an effective potential, which captures the subtle SM and, after relaxing the sample, the strain effects.

7.3 Model

Model Hamiltonian for graphene/hBN heterostructures resembles the one introduced in Sec. 3.2.2 for twisted bilayer graphene. In addition to the distance dependent Slater-Koster-like hoppings, hBN is modelled through on-site terms of boron and nitrogen species that are set to $V_B = 3.34\ eV$ and $V_N = -1.40\ eV$. The next-next-nearest neighbour coupling in graphene and the coupling within the radius of $1.5c_0$ in between graphene and hBN layers are taken into account.

For obtaining electronic properties from the Hamiltonian defined in Eq. (3.1) the KPM [69] implemented in Pybinding [123] is used. Band structure is calculated as the DOS of a $\boldsymbol{k}$-dependent Hamiltonian, where $\boldsymbol{k}$ takes its values along significant points in the super-moiré mini-Brillouin zone. The total DOS in the periodic system can be defined as $\mathrm{DOS} = 1/N_k \sum_{k_i} \mathrm{DOS}(H(\boldsymbol{k}_i))$, where $\boldsymbol{k}_i$ takes values from the full super-moiré mini-Brillouin zone, and N_k is the total number of points.

Similar to the case of twisted bilayer graphene (Sec. 6.2), in general, the simulated structure for arbitrary rotation angles θ_1 and θ_2 is incommensurate, which means that the unit-cell is not properly defined. Commensurate lattice appears when an additional condition given by the Diophantine equation is fulfilled

$$\begin{aligned} &\boldsymbol{L_{SM}} = i\boldsymbol{a}_1^{gr} + j\boldsymbol{a}_2^{gr} = k\boldsymbol{a}_1^{hBN_1} + l\boldsymbol{a}_2^{hBN_1} = m\boldsymbol{a}_1^{hBN_2} + n\boldsymbol{a}_2^{hBN_2}, \\ &i,j,k,l,m,n \in \mathbb{Z}, \end{aligned} \tag{7.5}$$

together with $|\boldsymbol{L_{SM}}| = \lambda^{SM}$ as given in Eq. (7.4). These conditions are only met for a discrete set of rotation angles, which are sparsely distributed at low twists. To be able to obtain bulk properties of systems with an arbitrary rotation, angle dependent LDOS, spatial distribution of the LDOS and the Kubo-Bastin DC conductivity in the linear response regime, as presented in Sec. 2.3.6, are calculated using circular hBN/gr/hBN flakes with radius $R = 150$ nm, where the effect of the boundaries is minimized by using absorbing boundary conditions (Sec. 2.3.7). High resolution conductivity results are obtained using the

single-shot algorithm [74]. For calculating the DC conductivity, Anderson disorder (zero average on-site energy) with width of $W = 0.1V^0_{pp\pi}$ is considered. Typically 15000 KPM moments are computed, and Lorentz kernel is used for reconstructing desired quantities.

In addition to the rigid alignment, molecular dynamics simulations (MD) for the double-aligned structure are performed for relaxing the structure. This was done through total energy minimization of the unit cell, with certain constraints. Brenner potentials are used for the graphene layer, Tersoff potentials for the B-N interaction in the top hBN and the Morse potential developed in [273] for the inter-layer interactions. Simulations were performed within the "Large-scale atomic/-molecular massively parallel simulator" (LAMMPS) software [274, 275]. In order to mimic a thicker hBN substrate (in most of the experimental setups hBN substrate is usually a thick slab [32]) bottom hBN configuration is fixed, while the relaxation of the other two layers is freely allowed. The total energy was minimized until the error in forces calculated between two iteration steps was below 10^{-6} eV/Å.

7.4 Results and discussions

7.4.1 Evidence of the super-moiré in the electronic properties

To further investigate the behaviour of the hBN/gr/hBN system all three layers are considered, as well as coupling between them. All three layers are kept rigid, and the lattice relaxation is discussed later in detail. The change of the LDOS with tuning the rotation angle is shown in Fig. 7.4. In panels (a) the LDOS of a lattice site of graphene that sits on top of boron and in (b) for a graphene lattice site on top of a nitrogen atom from the bottom layer are shown for low rotation angles. In agreement with previous theoretical descriptions of bilayer gr/hBN samples [270, 276], strong asymmetry between electron and hole states exists, with much stronger features on the hole doped side. This asymmetry can be traced back to the correlation between spatial variations of the on-site energy and the variations in the effective hopping with neighbouring atoms in the graphene layer [277].

Focusing on panels (a) and (b) of Fig. 7.4, one notices that different SM reconstruction points can be observed. The band gap that occurs in LDOS between energies $\approx (-125, -135)$ meV (marked with black dashed line) remains constant in energy with rotation angle. Converting

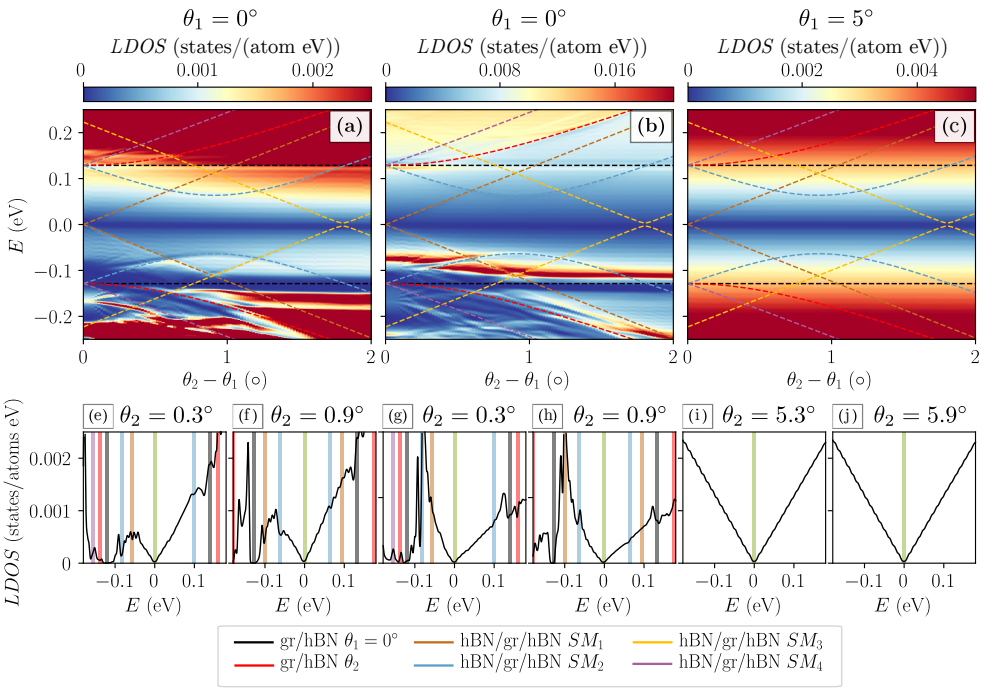

Figure 7.4: LDOS versus the angle of rotation and the energy. (a) LDOS at a graphene site that sits on top of boron and (b) on top of a nitrogen atom from the bottom layer for rotation θ_2 of the top hBN layer, keeping the bottom layer aligned. (c) Shows the low energy LDOS at the same site as in (a), for the same relative rotation between the hBN layers $(\theta_2 - \theta_1)$, while the graphene layer is misaligned for $\theta_1 = 5°$. Other than moiré SDPs, additional harmonics from Eq. (7.4) are shown with dashed lines, using $v_F \approx 0.75 \times 10^6$ m/s. Panels (e-j) show LDOS cuts at angles $\theta_2 \approx 0.3°$ and $\theta_2 \approx 0.9°$ from panels (a-c), respectively. The fit of the dominant harmonic effects on the LDOS is shown with coloured stripes.

the energy to the corresponding period gives $\lambda \approx 13.9$ nm, which can be addressed to the SDP from the aligned graphene/hBN moiré pattern. The dip in the LDOS observed at energy lower than this one corresponds to the secondary Dirac point due to graphene and rotated graphene hBN, and is marked with red dashed curve. Additionally, in the low energy regime, LDOS exhibits a series of peaks marked with brown, blue and yellow dashed curves, again stronger on the hole doped side. Having in mind that these dips appear at lower energies than the SDPs due to aligned and rotated hBNs, they can be attributed to the SM periods. In fact, these are none other than angle-energy features of three

harmonics as defined by Eq. (7.4) and shown in Fig. 7.3(b), which are now reproduced in all panels. In contrast with the plot in Fig. 7.2(b), suppressed Fermi velocity of $v_F \approx 0.75 \times 10^6$ m/s was used in order to obtain good agreement between the SM features in the LDOS and the derived harmonics, suggesting that the SM effect alters the electron velocity.

The pronounced sublattice asymmetry when comparing the LDOS of the two graphene sublattices in panels (a) and (b) of Fig. 7.4 is resulting from the local stacking arrangement between graphene and the encapsulating hBN layers. As mentioned previously, important aspect not considered in section 7.2 is the strength of the interlayer coupling. Weaker features on the electron doped side and the disappearance of the SM features cannot be explained with former description. It is the effect of the interlayer coupling that is reflected in the appearance of SM dips. Once the effective interlayer coupling is weakened through the effect of the misalignment, similar as in the case of the commensurate-incommensurate transition [9], the effect of the SM is lost. To further explore the importance of close-alignment, Fig. 7.4(c) shows the LDOS of misaligned graphene layer of $\theta_1 = 5^\circ$ with the same relative angle between the two hBN layers as in Figs. 7.4(a) and (b), where no signature of SM is observed. This explains why the SM effect is only recently reported [40, 263, 269] when one was able to achieve accurate control over the rotation angle between the layers, although hBN encapsulation has been a technique of choice for graphene transport devices for a much longer period [33].

In Fig. 7.5 band structure, DOS, and the conductivity of the hBN/gr/hBN system with $\theta_2 \approx 0.6^\circ$ are shown and compared against the expected energy of different moirés from section 7.2. Significant energies are marked with coloured stripes, each one corresponding either to the moiré or SM effect labeled in Fig. 7.2(c) and Fig. 7.5(d), or to the primary Dirac point of graphene. Band structure and the corresponding DOS are important to unravel the different SM effects on the two types of carriers. At positive Fermi energies (electron doped side), around $E \approx 70$ meV, a Dirac-like point appearing at the $\boldsymbol{K}$ point of the super-lattice mini-Brillouin zone is observed within the probing resolution. In contrast, the hole doped SM effect results in the appearance of band anti-crossing around $E \approx -70$ meV, implying a different effect of the two features on the electronic properties. Further, due to the band folding, the moiré $\theta_{1,2}$ SDPs are appearing at the Γ and the K point of the SM mini-Brillouin zone at energies $E_{SDP1} \approx \pm 130$ meV and $E_{SDP2} \approx \pm 150$ meV, respectively. In between the two SDPs on the hole

doped side, a band with reduced Fermi velocity appears, reflecting in a peak in the DOS. Due to its small dispersion low conductivity can be observed. Compared against the SM effect in the DOS, transport properties reveal less pronounced electron-hole asymmetry, with drops in the conductivity around the SM energy at both sides. In Fig. 7.5(d), different features are compared against the expected energy at which the moiré harmonics affect the spectrum. Vertical line intersect different harmonics at angle $\theta_2 \approx 0.6°$, while the circular markers are obtained from Fig. 7.5(b) and (c), once again confirming their origin.

In addition, further comparison between local properties - LDOS, and global - DOS and conductivity is given in the Appendix B, showing that the SM effect in transport vanishes already at rather small angles of $\theta_2 \approx 0.9°$, different from the effect on the LDOS shown in Fig. 7.4, where it was observed even for rotations larger than 1.5°.

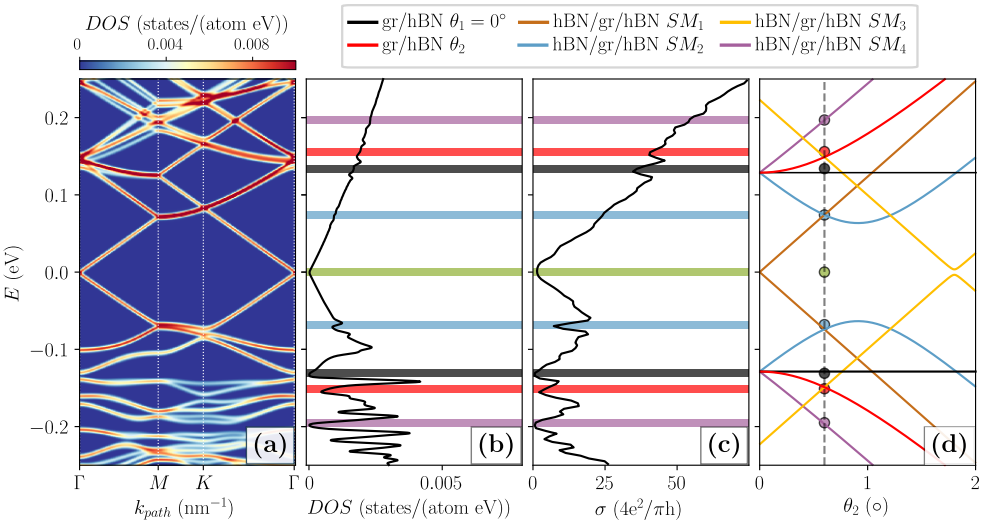

Figure 7.5: Electronic properties of hBN/gr/hBN system with $\theta_1 = 0°$ and $\theta_2 \approx 0.6°$. (a) Band structure along the $\Gamma - M - K - \Gamma$ path of the super-moiré mini-Brillouin zone. (b) DOS, and (c) conductivity. Dominant super-moiré feature is marked with blue colour, black marks the aligned θ_1 hBN/gr, and red rotated 0.6° hBN/gr features. Purple marks the higher order super-moiré feature. Green line marks the primary graphene Dirac point. (d) Expected positions of the super-moiré features using $v_F \approx 0.75 \times 10^6$ m/s. Different lines correspond to harmonics defined in Eq. 7.4.

Although STM measurements in this type of samples would remain

a practical challenge due to the encapsulation with the top hBN layer, it is interesting to discuss the SM effects on the spatial distribution of the LDOS (SLDOS). As expected, SLDOS is modulated by the hexagonally symmetric potential which originates from moiré patterns with different spatial lengths. In Fig. 7.6(a) clear modulation respecting the symmetry of the super-moiré can be observed. The energy is just above the SM induced Dirac-like point, where the modulation is the strongest. Notice that the highest LDOS appears in the corners of the SM unit-cell, where graphene atoms are maximally covered with boron and nitrogen atoms from both the top and the bottom hBN. Differently, in Figs. 7.6(b-d) close to the θ_1 and θ_2 moiré SDPs, different symmetry of the SLDOS patterns reveals the dominant effect of the two underlying moirés. In this case, the LDOS distribution at the corners of the SM is minimized.

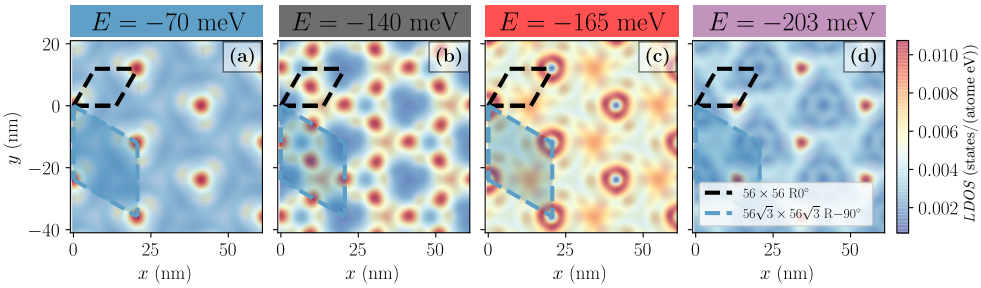

Figure 7.6: SLDOS maps of trilayer hBN/gr/hBN with $\theta_1 = 0°$ and $\theta_2 \approx 0.6°$ at different energies near the features shown with the same colours in Fig. 7.5.

7.4.2 Enhancement of super-moiré by lattice relaxation

When graphene and hBN are put on top of each other and aligned, two effects occur. Firstly there is band energy reconstruction through the appearance of mini-bands and of secondary Dirac points. The second effect is related to the van der Waals energy which is minimized through the formation of stacking areas with minimal energy [9]. This induces strain which further changes the tunnelling probability (or the hopping energy) throughout the sample. In the case of incommensurate alignment of layers, when no or little relaxation occurs, the effects of the opposite boron and nitrogen species on the graphene layer are averaged out on the area of the moiré unit cell, and no gaps appear [9].

Relaxation changes the interatomic registry, which further results in the appearance of significant gaps at the primary and secondary Dirac points [278, 279], which was confirmed experimentally [9, 16, 17, 269, 280, 281].

If the goal is to preserve the gapless linear spectrum, an addition of misaligned top layer to the hBN substrate, would again average out the mass-like boron/nitrogen terms and preserve the gapless graphene spectrum. More interesting effects come into play when the second hBN layer is close to align [269].

The sample relaxation was done using MD simulations. Bottom hBN layer is kept rigid to mimic the effect of a thick substrate, while graphene and top hBN are freely relaxed. The resulting effect on the interlayer distance (Δz) and the bond lengths ($\boldsymbol{r}_{i,j}$) is shown in Fig. 7.7. Interlayer distance between graphene and bottom hBN in Fig. 7.7(a) shows a clear evidence of the symmetry which follows the moiré pattern between these two layers, as marked with the black unit cell. Notice also that the bond lengths in top hBN reveal the symmetry of the moiré between graphene and this layer shown in (d). In contrast, the distance between top hBN and graphene in panel (b) and the distribution of the bond lengths in graphene in panel (c) follow the symmetry of the SM, marked with the blue unit cell. This shows that the SM is imprinted in the in-plane distribution of the strain in graphene, and the interlayer distance between graphene and the relaxed hBN layer, modifying in such a way all the hopping terms in Eq. (3.3) and further enhancing the super-moiré effect.

In the electronic spectrum, both the rigid, Fig. 7.5(a), and the relaxed sample, Fig. 7.8(a), show similar behaviour around the two SDPs at the hole side. The main difference is that in the relaxed sample gaps appear at the primary (see figure S5 in [263]), and in both of the secondary Dirac points on the hole doped side [279], consistent with broken inversion symmetry where the gap does not average out over the area of the SM pattern. It is important to note that relaxation effects are believed to be only partially responsible for the appearance of the experimentally observed gaps, while they are expected to increase when many-body interactions are included [16, 278, 282]. More importantly, the band structure in Fig. 7.8(a) reveals a gap at the hole doped SM Dirac-like point as well. The appearance of the SM reconstruction is highly tunable within the low energy spectrum through the change of the twist angle. In the small misalignment regime, the minimization of the van der Waals energy induces surface reconstruction that further results in SM gaps. Hence, the hBN/gr/hBN trilayers might provide a feasible route for gap

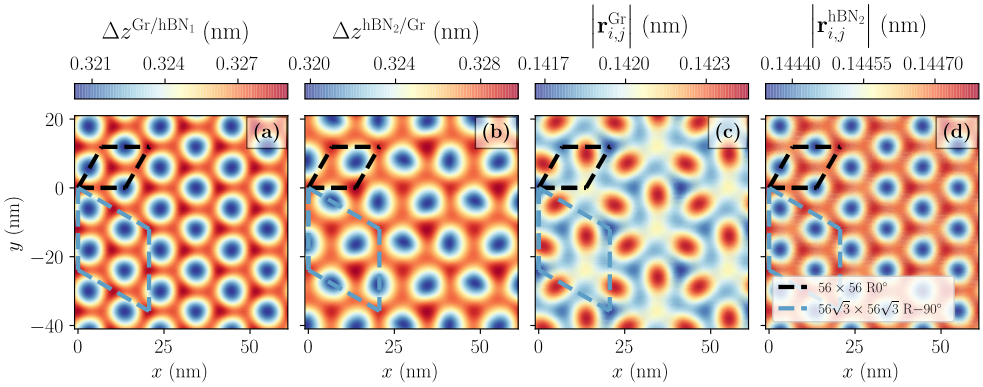

Figure 7.7: Relaxation of trilayer hBN/gr/hBN with $\theta_1 = 0°$ $\theta_2 \approx 0.6°$. Interlayer distance between graphene and (a) bottom and (b) top hBN layer. In panels (c) and (d) bond lengths in relaxed graphene and top hBN layer are shown, respectively.

engineering at arbitrary energies, which was not possible previously in moiré like structures. Simply, the lowest energy SDP ($E_{SDP} \approx \pm 140$ meV) is limited by the largest bilayer hBN/gr period which is $\lambda \approx 13.9$ nm.

The slight misalignment brings the two SDPs to a close proximity, which then results in the appearance of a narrow band in between the two energy features, E_{SDP1} and E_{SDP2} [269]. Due to relaxation of the sample, this band becomes even narrower. In addition, the SM gap edge shows similar dispersionless property, which was absent in the rigid sample. This means that by relaxing the sample, two almost flat bands appear, which suggests even richer physics in this regime.

Relaxation partially recovers the electron-hole symmetry in the spectrum. Although gaps appear only in the hole doped side, the moiré and SM become more visible on the electron side, as shown in the DOS, Fig. 7.8(b), and the conductivity, Fig. 7.8(c).

7.4.3 Comparison with experiment

To further confirm the SM effects on the electronic properties of hBN/gr/hBN devices, theoretical results discussed in previous sections are directly compared with experimental results in a study with colleagues from Manchester University.[2] In Fig. 7.9 transport properties (a-c) of

[2]The results of this section are published as: Z. Wang, Y. B. Wang, J. Yin, E. Tóvári, Y. Yang, L. Lin, M. Holwill, J. Birkbeck, D. J. Perello, S. Xu, J. Zultak,

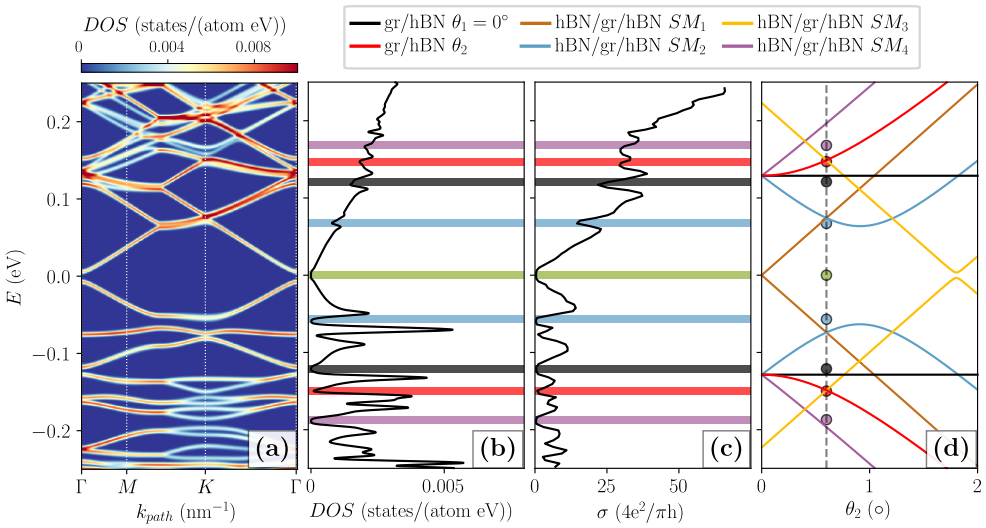

Figure 7.8: Electronic properties of relaxed hBN/gr/hBN system with $\theta_1 = 0°$ and $\theta_2 \approx 0.6°$, corresponding to the unrelaxed system of Fig. 7.5. (a) Band structure along the $\Gamma - M - K - \Gamma$ path of the super-moiré mini-Brillouin zone. (b) DOS, and (c) conductivity. Dominant super-moiré feature is marked with blue colour, black marks the aligned θ_1 hBN/gr, and red rotated 0.6° hBN/gr features. Purple marks the higher order super-moiré feature. Green line marks the primary graphene Dirac point. (d) Expected positions of the super-moiré features using $v_F \approx 0.75 \times 10^6$ m/s.

double-aligned hBN/gr/hBN samples are shown. The longitudinal and the transversal or Hall (R_{xy}) measured resistance show clear signs of features additional to the main Dirac point of graphene and two secondary Dirac points due to the moiré between aligned (θ_1) and rotated (θ_2) gr/hBN, which can be explained by additional harmonics due to the interference from the two moiré patterns. Most of the peaks correspond to the change of sign of R_{xy} which is a signature of additional Dirac-like points, that can also be confirmed by both positive and negative slopes in the Landau fan diagrams in Fig. 7.9(c).

Additional confirmation of the SM effects on the lattice relaxation follows from the comparison between the experimental Raman spectra

R. V. Gorbachev, A. V. Kretinin, T. Taniguchi, K. Watanabe, S. V. Morozov, M. Anđelković, S. P. Milovanović, L. Covaci, F. M. Peeters, A. Mishchenko, A. K. Geim, K. S. Novoselov, V. I. Fal'ko, A. Knothe, C. R. Woods, To appear in Science Advances (2019).

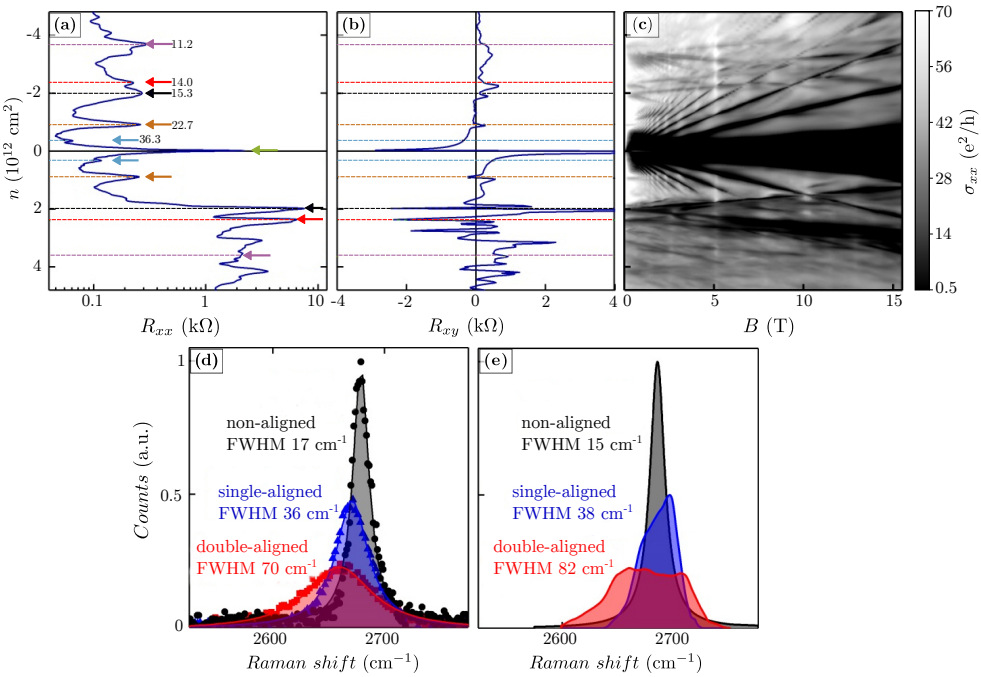

Figure 7.9: Experimental observation of the SM effects in double-aligned hBN/graphene/hBN devices. (a-c) Longitudinal resistance (R_{xx}), Hall resistance (R_{xy}), and Landau fan diagram of the longitudinal conductance (σ_{xx}), respectively, for a device with $\theta_1 \approx 0°$ ($\lambda_1 = 15.3$ nm) and $\theta_2 \approx 0.4°$ ($\lambda_2 = 14.0$ nm, with lattice mismatch taken as $\delta_{1,2} = 1.64$ %). Arrows and dashed lines correspond to different moiré and super-moiré features with the same colour scheme as in previous figures, while numbers shown next to different arrows correspond to the length of the appropriate moiré pattern. Hall resistance (R_{xy}) is measured at $B = 0.2$ T, with symmetrised values to avoid contributions from (R_{xx}). All transport properties are measurements at $T = 1.7$ K. (d, e) Raman spectra (2D-peak region) for the unaligned sample (grey), single-aligned sample (blue), and double-aligned sample (red), experimental results and MD simulation, respectively. Figure are adapted from Ref. [263].

of the non-aligned, single-aligned and double-aligned sample. The full-width at half-maximum changes significantly between the three cases, where with each new alignment the peak width, as the sign of the strain induced lattice relaxation, increases. As shown in Fig. 7.7 the super-moiré is imprinted in the strain which further broadens the 2D-peak and changes the Raman response of the aligned structures. Furthermore,

the results of the MD simulation agree with the experimentally obtained Raman measurements (Fig. 7.9(d, e)).

7.5 Conclusions

To conclude, in this chapter the effects of slightly misaligned hBN encapsulation layers on the electronic properties of monolayer graphene are examined. A simple model in terms of Bragg scattering vectors is able to explain the origin of the super-moiré spectrum. Using a real space tight-binding method a quantitative description of the angle dependent SM effects that result in additional spectrum reconstruction, velocity suppression and spatial electron redistribution is obtained.

In addition to rigid alignment between the layers, the effects of lattice relaxation are studied. Bottom hBN layer was kept rigid, which simulates the effect of a thick substrate, while the top hBN and graphene were freely relaxed. By relaxing the trilayer sample, the SM features are enhanced, and multiple asymmetrical low-energy gaps and flat bands whose energy can be controlled by misalignment appear. The opening of band gaps, and the expected enhancement due to many-body interactions appearing alongside flat bands are of high interest to the community working on twisted 2D (hetero)structures. The fact that flat bands are apparent in the case of graphene almost aligned to two encapsulated hBN layers, means only that further theoretical studies starting from the picture of interacting electrons are needed to understand all the different aspects of close aligned hBN/gr/hBN layers.

Finally, these results agree well with recent experimental studies [40, 269], and particularly [263], adding to the understanding of more subtle effects of complex moiré patterns that can appear when combining hetero-multi-layers.

8 | Summary

In this thesis electronic properties of graphene (hetero)structures are investigated within a tight-binding description with the use of numerical methodology introduced in Chapter 2 that scales almost linearly with the size of the Hilbert space and allows one to tackle complex and large systems. The open-source Pybinding and KITE codes are presented, with the particular focus given to KITE, a TB software for high-performance computation that gives access to disordered systems with multi-billions of orbitals. The release of KITE resulted from a collaboration with groups from Brasil, Portugal and UK during the previous three years, and is complemented with a recent publication presented in Chapter 3.

In Chapter 4 we discussed on the delaminations in bilayer graphene with a gate induced band gap and on the concept of graphene diodes. The former introduces the appearance of evanescent states localized at the delamination interface that span through the whole gap, in the case of different stacking on the two sides of the delamination, or hybridise and open a gap when the stacking is identical. In addition to the evanescent modes that survive even in the presence of the magnetic field, both configurations support the bouncing modes that form Landau levels when delamination width becomes comparable with the cyclotron radius of a given Landau level. Furthermore, the concept of a graphene diode with gate defined constriction proves possible because of a significant suppression of the transmission ratios between the backward and the forward propagating waves.

Strain induced graphene superlattices, discussed in Chapter 5 provide a flexible way to construct systems that host flat bands, which are of particular interest for interaction induced effects. Strain is induced experimentally by controlling the boundary geometries of the graphene flakes. Here, we studied theoretically how a periodic pseudo-magnetic field with the same period as the one in the sample topography captures the experimentally observed pseudo-Landau levels with $\propto \sqrt{N}$ dependence in the regions of the highest PMF, and equidistant states which

indicate confinement within the quantum well defined by the strain induced PMF.

Chapter 6 is devoted to the properties of twisted bilayer graphene at different rotation angles, in the presence of electric field and disorder. At low rotation angles a change in the DC conductivity at the Dirac point is observed, when compared to the tBLG at high rotation angles, where twice the minimal conductivity of monolayer graphene is a signature of layer decoupling. In the presence of electric field almost flat conductivity over a wide range of Fermi energies is revealed, as a consequence of the boundary helical states induced by the electric field. Studies on the vacancy disordered samples with high-rotation angles hint that the minimal conductivity at the neutrality point is conserved as a consequence of the protected chiral symmetry. In addition, asymmetric gating proves possible in changing the layer polarisation where the switch of the gate polarity shows similar effects as the exchange between the layers, which is observed in a recent experiment and supported by our theoretical studies.

In Chapter 7 we introduced a simple geometrical model to explain the origin of the super-moiré spectrum in terms of Bragg scattering vectors. We studied electronic properties of rigid and relaxed samples, such as the spatial distribution of the LDOS, DOS and the DC conductivity which all reveal signatures of the super-moiré with pronounced electron-hole asymmetry. Furthermore, sample relaxation results in the enhancement of the super-moiré features and in the appearance of experimentally detectable band gaps on the hole part of the spectrum.

8.1 Outlook

The study of the electronic properties of super-moiré patterns in hBN/-Gr/hBN heterostructures can be improved by examining electronic, and especially, transport properties in the presence of magnetic field, which require improvements in the way we currently describe the system. Simply the systems are currently too large to be able to obtain full-spectrum results. These improvements can be either at the level of computational efficiency or by devising simpler effective models.

If we return to the underlying TB models, there are questions which are not discussed in details, that would define how accurate the chosen TB approximation is. These questions include

- How to obtain an effective parametrisation of the model?

- Is the validity defined by this parametrisation sufficient for the particular purpose?
- Is the approximation valid without the a priori neglected effects, such as many-body interactions?

This presents a validity test for any TB description. The reason why they are not covered is that the employed model Hamiltonians are (well) established models for the particular system, and no new parametrisation is presented.

Still, among other, moiré heterostructures and the superlattices offer a possibility to study systems that host flat bands. As the presented models in this thesis rely on studying the non-interacting Hamiltonians, and can be used only as a starting description of a more complex reality, an obvious improvement would include the interaction terms. This can initially be at the mean-field level, which will certainly degrade the almost linear scaling with the number of simulated orbitals and it will increase the complexity significantly, but would help in explaining recent experimental results on twisted bilayer graphene.

Furthermore, regarding improvements of the presented TB software, our short term plans include the development of functionalities for obtaining TB parameters, for example through interfacing with TB-Studio [46] (developed in the CMT group by M. Nakhaee) or the Wannier90 software [283]. This would give us the access to more accurate parametrisation techniques starting from DFT codes, which would further provide the possibility to generalize our software and simulate new materials that were not previously modelled at the TB level. At this point the validity of a new approximation discussed above has to be checked. We will further improve the numerical techniques for electronic transport, with the goal to develop Chebyshev expansions of the nonequilibrium Green's function, and through these reformulation to obtain the transmission probabilities through a device, modelled as a scattering region, at all energies at the same time, allowing us to consider even larger systems with less computational time.

And to re-phrase the famous Feynman's quote: "there is still plenty of room at the bottom". Moreover, this is particularly the case in the field of 2D materials. Even if we only consider the research that was done or presented in the previous year, the "bottom" seems further than before. It is the beauty of the small things, isn't it?

9 | Samenvatting

In deze thesis worden elektronische eigenschappen van grafeen (hetero)structuren onderzocht binnen een tight-binding beschrijving met behulp van de numerieke methodologie geïntroduceerd in Hoofdstuk 2 die bijna lineair schaalt met de grootte van de Hilbert-ruimte en toelaat om complexe en grote systemen aan te pakken. De open-source Pybinding- en KITE-programma's worden gepresenteerd, met speciale aandacht voor KITE, een TB-software voor krachtige berekeningen die toegang geeft tot wanordelijke systemen met miljarden orbitalen. De lancering van KITE is het resultaat van een samenwerking met groepen uit Brazilië, Portugal en het VK in de afgelopen drie jaar en wordt aangevuld met een recente publicatie getoond in Hoofdstuk 3.

In Hoofdstuk 4 hebben we gesproken over de delaminaties in bilaag grafeen met een gate geïnduceerde bandkloof en over het concept van grafeendioden. De eerste leidt tot het verschijnen van uitdovende toestanden gelokaliseerd op de delaminatie-interface die zich doorheen de hele bandkloof bevindt in het geval van verschillende stapeling aan de twee zijden van de delaminatie, of tot het hybridiseren en openen van een bandkloof wanneer de stapeling identiek is. Naast de uitdovende toestanden die zelfs in de aanwezigheid van het magnetische veld overleven, ondersteunen beide configuraties de stuiter toestanden die Landau-niveaus vormen wanneer de delaminatiebreedte vergelijkbaar wordt met de cyclotronstraal van een bepaald Landau-niveau. Verder blijkt het concept van een grafeendiode met door de gate gedefinieerde vernauwing mogelijk vanwege een significante onderdrukking van de transmissieverhoudingen tussen de achterwaartse en voorwaartse voortplantingsgolven.

Door vervorming geïnduceerde grafeen-superroosters besproken in Hoofdstuk 5 bieden een flexibele manier om systemen te construeren die vlakke banden bevatten, welke van bijzonder belang zijn voor ef-

fecten veroorzaakt door interactie. Vervorming wordt experimenteel geïnduceerd door de grensgeometrieën van de grafeenvlokken te controleren. Hier hebben we theoretisch bestudeerd hoe een periodiek pseudomagnetisch veld met dezelfde periode als die in de topografie van het experimenteel waargenomen pseudo-Landau-niveau met $\propto \sqrt{N}$ afhankelijkheid produceert in de regio's van de hoogste PMV en equidistante toestanden die duiden op opsluiting binnen de kwantum put gedefinieerd door de vervorming-geïnduceerde PMV.

Hoofdstuk 6 is gewijd aan de eigenschappen van geroteerd bilaag grafeen onder verschillende rotatiehoeken, in aanwezigheid van een elektrisch veld en wanorde. Bij lage rotatiehoeken wordt een verandering in de DC-conductiviteit op het Dirac-punt waargenomen, als vergeleken met de tBLG bij hoge rotatiehoeken, waarbij tweemaal de minimale conductiviteit van monolaag grafeen een kenmerk is van ontkoppeling van de lagen. In de aanwezigheid van een elektrisch veld wordt bijna vlakke conductiviteit over een breed interval van Fermi-energieën gevonden als een gevolg van de helische grenstoestanden die worden geïnduceerd door het elektrisch veld. Studies over de holte-wanordelijke monsters met hoge rotatiehoeken wijzen erop dat de minimale conductiviteit op het neutraliteitspunt behouden blijft als gevolg van de beschermde chirale symmetrie. Bovendien blijkt asymmetrische gating het veranderen van de laagpolarisatie mogelijk te maken waarbij de schakelaar van de gatepolariteit vergelijkbare effecten vertoont als de uitwisseling tussen de lagen, wat is waargenomen in een recent experiment en wordt bevestigd door onze theoretische studies.

In Hoofdstuk 7 hebben we een eenvoudig geometrisch model geïntroduceerd om de oorsprong van het super-moiré-spectrum te verklaren in termen van Bragg-verstrooiingsvectoren. We hebben de elektronische eigenschappen van rigide en ontspannen monsters bestudeerd, zoals de ruimtelijke verdeling van de LDOS, DOS en de DC-conductiviteit die alles aanwijzingen vertonen van de super-moiré met uitgesproken elektron-gat asymmetrie. Bovendien resulteert monsterrelaxatie in de verbetering van de super-moiré-kenmerken en in het verschijnen van experimenteel detecteerbare bandkloven in het gatengedeelte van het spectrum.

9.1 Vooruitzichten

De studie van de elektronische eigenschappen van super-moiré-patronen in hBN/gr/hBN heterostructuren kan worden verbeterd door elektronische, en vooral transporteigenschappen in aanwezigheid van een magnetisch veld te onderzoeken die verbeteringen vereisen in de manier waarop we momenteel het systeem beschrijven. De systemen zijn momenteel gewoonweg te groot om volledige spectrumresultaten te kunnen bekomen. Deze verbeteringen kunnen ofwel op het niveau van de rekenefficiëntie zijn of door eenvoudigere effectieve modellen te ontwikkelen.

Vertrekkend van de onderliggende TB-modellen zijn er vragen die hier niet in detail worden besproken en die zouden bepalen hoe nauwkeurig een benadering is, waaronder

- Hoe een effectieve parametrisering van het model te verkrijgen?
- Is de geldigheid gedefinieerd door deze parameterisatie voldoende voor het specifieke doel?
- Is de benadering geldig zonder a priori verwaarloosde effecten, zoals interacties tussen veel deeltjes?

Dit is een geldigheidstest voor elke TB-beschrijving. De reden waarom ze niet worden besproken, is dat de gebruikte model Hamiltonianen betrouwbare modellen zijn voor het specifieke doel en dat er geen nieuwe parametrisering wordt gepresenteerd.

Moiré heterostructuren en de superroosters bieden de mogelijkheid om systemen te bestuderen die vlakke banden bevatten. Aangezien de gepresenteerde modellen in deze thesis steunen op het bestuderen van niet-interagerende Hamiltonianen, zou het in beschouwing nemen van interactietermen, aanvankelijk op het gemiddelde-veldniveau, een duidelijke verbetering zijn. Dit zal zeker de bijna lineaire schaling met het aantal gesimuleerde orbitalen verminderen en het zal de complexiteit aanzienlijk verhogen, maar zou helpen bij het verklaren van recente experimentele resultaten over geroteerd bilaag grafeen.

Verder, wat betreft de verbeteringen aan de gepresenteerde TB-programma's, omvatten onze kortetermijnplannen de ontwikkeling van functionaliteiten voor het verkrijgen van TB-parameters, bijvoorbeeld door middel van een interface met TB-Studio [46] (ontwikkeld in de CMT groep door M. Nakhaee) of de Wannier90-software [283]. Dit zou ons

toegang geven tot meer nauwkeurige parametreringstechnieken vertrekkende van DFT-codes, die verder de mogelijkheid bieden om onze software te generaliseren en nieuwe materialen die niet eerder op TB-niveau werden gemodelleerd. Op dit punt is de geldigheid van de hierboven besproken nieuwe benadering geverifieerd. We zullen de numerieke technieken voor elektronisch transport verder verbeteren, met het doel om Chebyshev-expansies van het non-equilibrium Greense functies te ontwikkelen, en, door hun herformulering, om de transmissiekansen doorheen een apparaat te verkrijgen, gemodelleerd als een verstrooiings regio, bij alle energieën tegelijkertijd, waardoor we nog grotere systemen kunnen beschouwen met minder rekentijd.

Tot slot kunnen we nu het beroemde citaat van Feynman herformuleren: "er is nog steeds genoeg ruimte onderaan". Dit is met name het geval in het veld van 2D-materialen. Zelfs als we alleen rekening houden met het onderzoek dat in het vorige jaar is gedaan of gepresenteerd, lijkt de "onderaan" verder dan voorheen. Schoonheid zit in de kleine dingen, nietwaar?

A | Versatility of the real-space TB model

In addition to the simple TB Hamiltonian for monolayer graphene in the nearest neighbour approximation that is introduced in Ch. 2 various modifications are added to introduce different physical phenomena, such as the effects of fields (electric or magnetic), disorder, spin-orbit coupling, strain or the rotation dependent hoppings. In this appendix these modifications are summarised and explained in more detail.

To start with, a general Hamiltonian, which combines all the modifications introduced in different chapters of this thesis, can be written as

$$\begin{aligned}\hat{H} = &- \sum_{\langle i,j\rangle,s} t(\boldsymbol{d}_{ij}) e^{i2\pi\frac{\Phi_{ij}}{\Phi_0}} \hat{c}^\dagger_{is}\hat{c}_{js} + \frac{2i}{3}\sum_{\langle i,j\rangle,s,s'} \hat{c}^\dagger_{is}\hat{c}_{js'}\left[\lambda_R\left(\hat{\boldsymbol{s}}\times\boldsymbol{\delta}_{ij}\right)_z\right]_{ss'} \\ &+ \Delta_{\text{ex}}\sum_{i,s}\hat{c}^\dagger_{is}\hat{\boldsymbol{s}}_z\hat{c}_{is} + V_{\text{dis}} + \sum_{i,s}\Delta_{is}\,\hat{c}^\dagger_{is}\hat{c}_{is} + \sum_{i,s}V_i\hat{c}^\dagger_{is}\hat{c}_{is},\end{aligned} \tag{A.1}$$

where $\hat{c}^\dagger_{is}$ ($\hat{c}_{js'}$) is the electron creation (annihilation) operator with spin state $s(s')$ ($s, s' = \{\uparrow,\downarrow\}$) on site $i(j)$. The first term accounts for the probability for an electron to tunnel from site i to site j ($\boldsymbol{d}_{ij}$ is the distance between the sites), in the presence of a magnetic field, which introduces the Peierls phase factor Φ_{ij}/Φ_0 (see bellow, Φ_0 denotes the magnetic flux quantum). The second term is the Bychkov–Rashba interaction (λ_R denotes the strength of the field, $\boldsymbol{\delta}_{ij}$ is the unit vector pointing from site j to i and $\hat{\boldsymbol{s}}$ is the vector of Pauli matrices). The third term describes an uniform exchange field (with strength Δ_{ex}). The fourth term denotes the Ising type of an impurity with an opposite sign for the two spins (Δ_{is} is the strength of the impurity potential, $\Delta_{is} = -\Delta_{is'}$), and the last term is the on-site potential V_i, which can account for the effect of the electric field or certain types of charge disorder.

Distance dependent hopping

The distance dependent hopping amplitudes $t(\boldsymbol{d}_{ij})$ account for the change of the hopping probabilities due to, for example, the rotation between the layers, as underlined in Sec. 3.2.2. For the sake of completeness, the TB parametrisation from Refs. [139] and [138], that served in modelling the twisted bilayer graphene, once again reads

$$-t(\boldsymbol{r}_i, \boldsymbol{r}_j) = V_{pp\pi}\left[1 - \left(\frac{\boldsymbol{d_{ij}}\cdot\boldsymbol{e}_z}{d}\right)^2\right] + V_{pp\sigma}\left(\frac{\boldsymbol{d_{ij}}\cdot\boldsymbol{e}_z}{d}\right)^2, \tag{A.2}$$

$$\begin{aligned} V_{pp\pi} &= V^0_{pp\pi} e^{-\frac{d-a_0}{\delta}}, \\ V_{pp\sigma} &= V^0_{pp\sigma} e^{-\frac{d-d_0}{\delta}}, \end{aligned} \tag{A.3}$$

with $V^0_{pp\pi} = -2.7$ eV and $V^0_{pp\sigma} = 0.48$ eV are intralayer and interlayer hopping integrals, $a_0 \approx 0.142$ nm and $d_0 \approx 0.335$ nm are carbon-carbon distance in graphene and interlayer distance in bilayer graphene, respectively. $\boldsymbol{d}_{ij}$ is the vector connecting two sites, $d = |\boldsymbol{d_{ij}}|$ is the distance between them, and $\delta = 0.3187 a_0$ is chosen in order to fit the next-nearest intra-layer hopping to $0.1 V^0_{pp\pi}$. Through the scalar product between the distance vector $\boldsymbol{d}_{ij}$ and the local surface normal $\boldsymbol{e}_z$ the effects of the corrugation are taken into account. Furthermore, the distance modification of the hopping amplitude accounts for the effects of the strain. Due to the strain induced lattice distortions, the positions of the atomic orbitals will alter and in such a way change the values of the hopping terms.

Peierls substitution

Starting from the Schrödinger equation, the effect of the magnetic field on a charged particle can be accounted through the introduction of a canonical momentum

$$\hbar\boldsymbol{k} \to \hbar\boldsymbol{k} + q\boldsymbol{A}, \tag{A.4}$$

where q represents the electric charge of a particle, and $\boldsymbol{A}$ is the magnetic vector potential that can be related to the magnetic field

$$\boldsymbol{B} = \nabla \times \boldsymbol{A}. \tag{A.5}$$

Following the derivation of a TB model in Sec. 2.1, the canonical momentum adds only a phase factor, known as Peierls phase [158], to the hopping amplitude. The Peierls phase Φ_{ij} is defined as a path integral of the magnetic vector potential $\boldsymbol{A}$

$$\Phi_{ij} \equiv \Phi(\boldsymbol{r}_i, \boldsymbol{r}_j) = \frac{1}{\Phi_0}\int_{\boldsymbol{r}_i}^{\boldsymbol{r}_j} \boldsymbol{A} d\boldsymbol{l}, \tag{A.6}$$

where $\boldsymbol{r}_{i(j)}$ is the position vector of the site $i(j)$ and $\Phi_0 = h/e$ denotes the magnetic flux quantum. For a constant magnetic field pointing in the z direction ($\boldsymbol{B} = B\boldsymbol{i}_z$) and with the choice of the Landau gauge ($\boldsymbol{A} = By\boldsymbol{i}_x$), the Peierls phase reads

$$\Phi_{ij} = \frac{1}{2}B(y_j + y_i)(x_j - x_i), \tag{A.7}$$

where $\boldsymbol{r}_{i(j)} = [x_{i(j)}, y_{i(j)}]$.

Bychkov–Rashba spin-orbit coupling

The term that introduces Bychkov–Rashba spin-orbit coupling, which is induced by a proximity effect due to the broken mirror inversion symmetry in the case of a graphene/TMDC heterostructure, is modelled as an opposite spin, opposite sublattice coupling term with strength λ_R. It is responsible for the spin splitting of the bands and spin precession around a BRSOC induced pseudo-magnetic field, that appears in the plane in which the electron motion occurs, and is orthogonal to the electron momentum $\boldsymbol{k}$.

Pseudo-magnetic field

In Ch. 5 a periodic PMF is included in the tight-binding Hamiltonian to model the effects of the atomic corrugation (strain) without explaining the justification for such an approach. Starting from the simplest TB Hamiltonian for graphene in the nearest neighbour approximation

$$\hat{H} = -\sum_{i,j} t_0 \hat{c}_i^\dagger \hat{c}_j, \tag{A.8}$$

the effect of strain is included in the tight-binding Hamiltonian through the modulation of the hopping energy that changes exponentially with respect to the relative displacement [194, 284]

$$t_{ij} = t_0 e^{-\beta(d_{ij}/d_{ij}^0 - 1)} = t_0(1 + \delta t_{ij}), \tag{A.9}$$

where $\beta \approx 3.37$ is a strain modulation parameter [285], d_{ij} and $d_{ij}^0 \equiv a_{cc} \approx 0.142$ nm are the lengths of the strained and the unstrained bonds, respectively. This approximation is valid in the limit of weak strain ($(d_{ij}/d_{ij}^0 - 1) \ll 1$) [3]. Following a derivation of the continuum graphene

Hamiltonian [56], a smooth strain enters the Dirac equation as an effective vector potential $\boldsymbol{A}_{PMF}$ that satisfies [284]

$$A_{PMF}(\boldsymbol{r}_i) \approx A_x(\boldsymbol{r}_i) - iA_y(\boldsymbol{r}_i) = \frac{1}{ev_F}\sum_{n=1}^{3}\delta t_n(\boldsymbol{r}_i)e^{-i\boldsymbol{K}\boldsymbol{\delta_n}}, \tag{A.10}$$

where n denotes the sum over the 3 nearest neighbours of a carbon atom at the position $\boldsymbol{r}_i$ in the graphene lattice, v_F and e are the electron Fermi velocity and charge, respectively. Non-deformed bond vectors δ_n (Eq. (2.8)) are considered in the sum over different bonds. The magnetic vector potential can be related to the strain components [194, 285]

$$A_x - iA_y = \frac{\hbar\beta}{2ea_c c}(\varepsilon_{xx} - \varepsilon_{yy} + 2i\varepsilon_{xy}). \tag{A.11}$$

ε_{xy} denotes the $y(x)$ strain component of the displacement vector $\boldsymbol{u}_{x(y)}$, $\varepsilon_{xy} = \partial\boldsymbol{u}_{x(y)}/\partial y(x)$ defined along each bond. Furthermore, expansion of Eq. (A.10) combined with Eq. (A.11) connects the change in the nearest neighbour hoppings terms with the components of the strain tensor [286]

$$\begin{aligned} A_x &= \frac{\hbar\beta}{2ea_{cc}}\left(2\delta t_1 - \delta t_2 - \delta t_3\right), \\ A_y &= \frac{\hbar\beta}{2ea_{cc}}\frac{1}{\sqrt{3}}\left(\delta t_2 - \delta t_3\right). \end{aligned} \tag{A.12}$$

PMF can be further defined as

$$\boldsymbol{B}_{PMF} = \nabla \times \boldsymbol{A}_{PMF} = \left(\frac{\partial A_y}{\partial_x} - \frac{\partial A_x}{\partial_y}\right)\boldsymbol{i}_z. \tag{A.13}$$

Although an equivalence between the real- and pseudo-magnetic field exists, in the case of the latter the time-reversal symmetry is preserved as the PMF acts with an opposite sign in the two valleys of graphene.

Periodic pseudo-magnetic field

We can go back to the periodic PMF introduced in Ch. 5

$$\boldsymbol{B}_{PMF}(x,y) = B\left(\cos(\boldsymbol{b_1 r}) + \cos(\boldsymbol{b_2 r}) + \cos(\boldsymbol{b_3 r})\right)\boldsymbol{i}_z, \tag{A.14}$$

where B is the PMF amplitude, $\boldsymbol{b_1} = 2\pi/a_B[1, -1/\sqrt{3}]$, $\boldsymbol{b_2} = 2\pi/a_B[0, 2/\sqrt{3}]$, $\boldsymbol{b_3} = \boldsymbol{b_1} + \boldsymbol{b_2}$, and a_B is the buckled superlattice period. If the gauge is chosen such that $A_y = 0$, the expression for the magnetic vector potential, as $A_x = \int B_{PMF}dy$ (Eq. (A.13)) reads

$$A_x = B_0\frac{a_B}{2\pi}\left[\frac{1}{b_{1y}}\sin(\boldsymbol{b_1 r}) + \frac{1}{b_{2y}}\sin(\boldsymbol{b_2 r}) + \frac{1}{b_{3y}}\sin(\boldsymbol{b_3 r})\right]. \tag{A.15}$$

The effect of a particular field profile can be taken into account as a modification of the hopping terms, even without changing the positions of the lattice sites [285]. From Eqs. (A.12) and (A.15), because of the choice of the gauge $\delta t_2 = \delta t_3 = \delta t$, and under the choice $\delta t_1 = -\delta t$, the change of hooping terms finally reads

$$\begin{aligned} t_1 &= t_0 \left(1 - \frac{3A_x e a_c c}{4\hbar}\right), \\ t_2 = t_3 &= t_0 \left(1 + \frac{3A_x e a_c c}{4\hbar}\right). \end{aligned} \tag{A.16}$$

B | Super-moiré in encapsulated graphene

B.1 Identifying the rotation angle

Using geometrical considerations explained in the main text we are able to relate the theoretical prediction of the super-moiré harmonics to real-space periods, reconstruction energies or densities. Different combinations of moiré vectors give more harmonics in addition to the harmonics already defined in Eq. (7.4). In Fig. B.1, panels (a-c) period, reconstruction energy, and density are shown for 11 different harmonics that appear in the low energy spectrum (lower than 0.4 eV). Experimental results are obtained mostly as a function of carrier density, so panel B.1(c) can be particularly important for extracting the expected values of the rotation angles, and the period of the underlying periodicities from the super-moiré features.

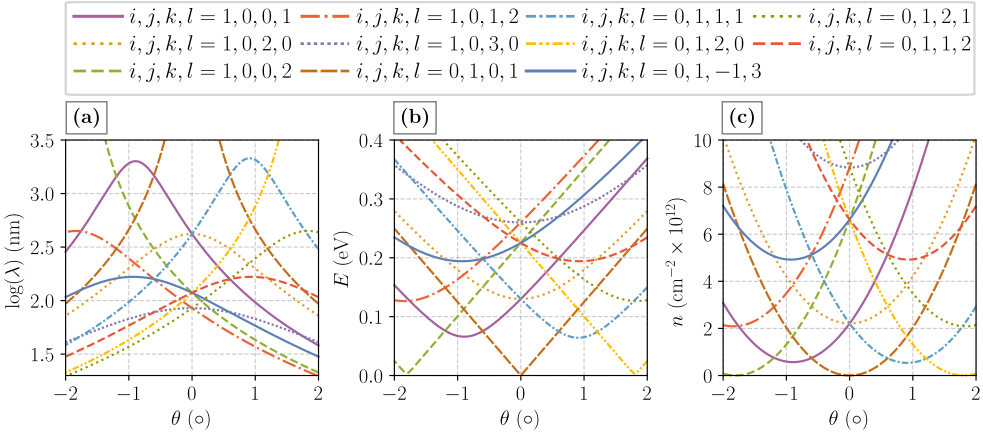

Figure B.1: Super-moiré (a) period, (b) energy and (c) the density corresponding to different harmonics as defined in Eq. (7.3).

B.2 Band structure - comparison with aligned bilayer

By solving the Diophantine equation from Eq. (7.5), commensurate structures that allow to define a unit cell can be obtained. One of the solutions is for rotations $\theta_1 = 0°$ (aligned hBN) and $\theta_2 \approx 0.6°$ (rotated hBN) resulting in the super-moiré period of $\approx$ 23.8 nm. Figure B.2 shows the band structure along the path $\Gamma - M - K - \Gamma$ in the SM mini-Brillouin zone and the DOS for a bilayer (aligned hBN/gr $\theta_1 = 0°$) and trilayer hBN/gr/hBN ($\theta_1 = 0°$ and $\theta_2 \approx 0.6°$), respectively.

In the bilayer case (Figs. B.2(a, b)), the hBN substrate induces a pair of secondary Dirac points at energies $\approx \pm 140$ meV, with large degree of electron-hole asymmetry which was discussed previously (at energies marked by black line), where E_{DP} is the (primary) Dirac point of graphene (marked by green line).The additional top hBN layer (Figs. B.2-(c, d)), as suggested from the other spectral calculations, results in additional Dirac-like points (marked by blue line in the DOS) at energies below the ones induced by aligned or rotated 2 layer moiré patterns ($\sim \pm 70$ meV). Additional secondary Dirac point due to the rotated hBN/gr appears as well (marked by red line).

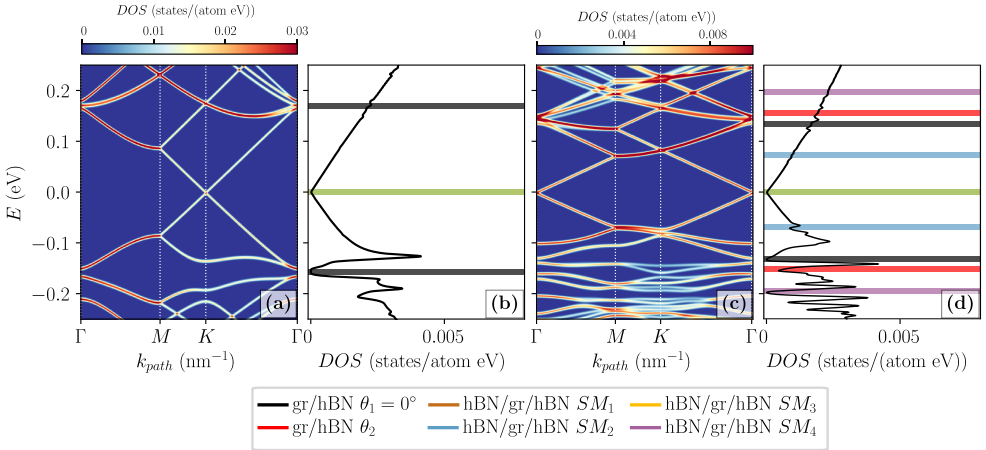

Figure B.2: Band structure and DOS of (a, b) bilayer hBN/gr $\theta_1 = 0°$ and (c, d) trilayer hBN/gr/hBN for $\theta_1 = 0°$ and $\theta_2 \approx 0.6°$.

The Dirac point in graphene is located at different points in the moiré or super-moiré mini-Brillouin zone, which is caused by different superlattice band folding [287].

B.3 Behaviour at higher rotation angles

To expand the discussion on the SM reconstruction effects, in Fig. 7.4 LDOS (at the same graphene site as in Fig. 7.4(b), panels B.3(a-c)), DOS (panels B.3(e-g)) and conductivity (panels B.3(h-j)) are shown in a system with rotation angles $\theta_1 = 0°$ and $\theta_2 = 0.3°$, $\theta_2 = 0.6°$, $\theta_2 = 0.9°$. The fits of the SM effects are marked with coloured stripes, where the different harmonics are labeled in the legend. Notice that the effects of the SM are more apparent in the LDOS when compared to global properties like DOS and conductivity, where the effects are averaged over different stacking regions. The SM features are almost completely wiped out at rotation $\theta_2 \approx 0.9°$, which confirms our findings about the necessity of close alignment of the layers in order to see the SM effects.

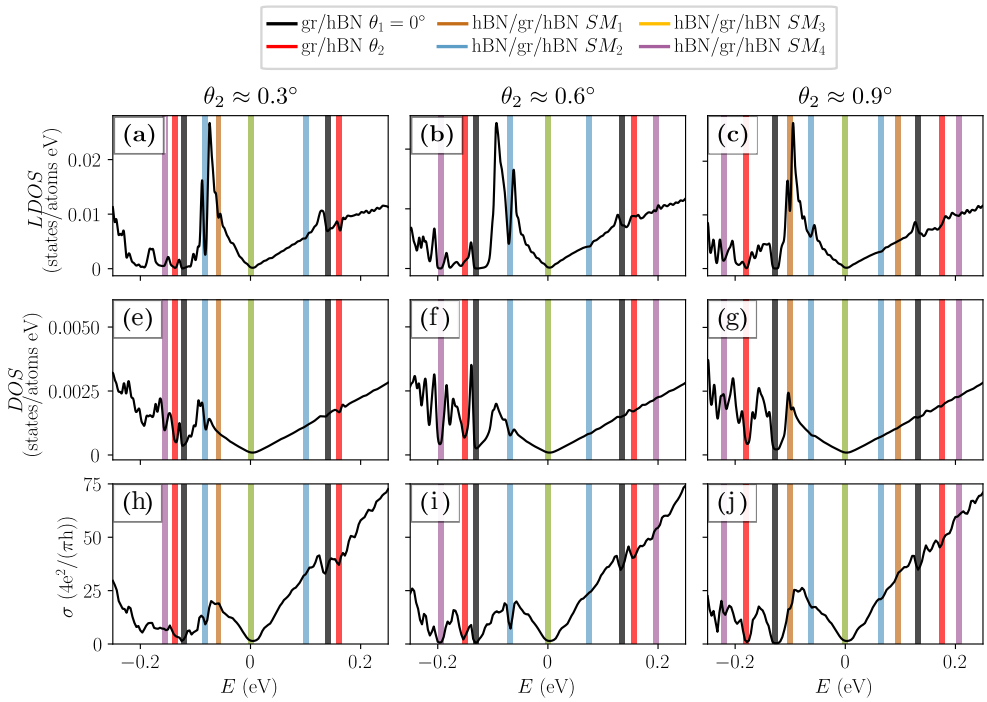

Figure B.3: Cuts of LDOS from Fig. 7.4(b) for $\theta_2 \approx 0.3$, $\theta_2 \approx 0.6$, $\theta_2 \approx 0.9$, panels (a-c), together with the conductivity (e-g) and the DOS plots in panels (h-j). Different coloured stripes in each figure correspond to fits of the harmonics defined in the legend.

C | Twisted heterostructure in Pybinding

Important part of the modelling of 2D heterostructures done in this work includes writing appropriate scripts in Pybinding [123] or KITE [134] codes. The simplicity of implementing a desired model is extensively covered in Pybinding documentation [123], while the specific functionalities in KITE code are presented in Sec. 3.2 and [133]. Still, the implementation of more complex structures is not discussed in details, which can appear to be a complex task. That is why in this Appendix a possible way of defining a twisted bilayer graphene model, at rotation angles that results in a commensurate system based on [235] as discussed in Ch. 6, is presented. The Hamiltonian defined in Sec. 3.2.2 is used. The script here is an example which discusses the important parts of the construction of a complex heterostructure, and the code tends to be lengthy. For reasons of keeping this section brief, not all of the parts and/or variables are defined/discussed. For a complete working example interested reader should visit [124], where additional scripts will become available.

To start with the lattice of tBLG will be created. In the following different constants are used

Listing C.1: Constants.

```
c0 = 0.3349              # [nm] graphene interlayer spacing
a = 0.1418               # [nm] graphene NNN spacing
a0 = sqrt(3) * 0.1418    # [nm] graphene NNN spacing
# Constants and hopping values
gamma0 = 2.7             # [eV] graphene NN intralayer hopping
gamma1 = 0.48            # [eV] graphene NN interlayer hopping
rc = 2.5 * a0            # [nm] hopping fitting parameter
lc = 0.0265              # [nm] hopping fitting parameter
q_sigma = c0 * 22.218    # [nm] hopping fitting parameter
q_pi = a * 22.218        # [nm] hopping fitting parameter
r0 = 0.184 * a           # [nm] hopping fitting parameter
```

One first chooses an angle of rotation for both layers `theta1` and `theta2`, after which the coefficient `w` and the commensurate angle (`angle`) are computed, from where the lattice vectors `l1` and `l2` can be defined.

For reasons of an automatic definition of the tBLG unit cell a model of monolayer graphene is first created with the shape of the desired unit cell, and an additional, second layer is created with the use of `@pb.site_generator`, which is available in the latest development version of Pybinding. After the model is created, the sites that form the tBLG lattice at a given rotation can be extracted.

Listing C.2: Creating the unit cell.

```
desired_angle = theta2 - theta1
desired_angle_rad = desired_angle / 180 * pi
coeff = [3. * (1. - cos(desired_angle_rad)),
         3. * (1. - np.cos(desired_angle_rad)),
         0.5 * (1. - 2. * np.cos(desired_angle_rad))]
[w1, w2] = np.roots(coeff)
w = np.round(w1) if w1 > w2 else np.round(w2)
angle = math.acos((3 * w ** 2 + 3 * w + 0.5) / (3 * w ** 2 + 3 * w + 1)
    ) * 180 / pi
# find moire unit cell vectors
l1 = w * a1 + (w + 1) * a2
l2 = - (w + 1) * a1 + (2 * w + 1) * a2
# the difference in rotation between the layers
theta_diff = angle * pi / 180
# make a unit cell shape from vectors l1 and l2
shape = unit_cell(l1, l2)
# rotation matrix for hBN layer
rotate = rotation_matrix(theta_diff)
# define a model starting from monolayer graphene with a shape of the
    unit cell
model = pb.Model(
    lattice_gr,
    shape,
    # add layers of B and N
    add_one_atomic_layer(name='C3',
                         position=[+ a_cc / 2 * math.sin(theta_diff), -
    a_cc / 2 * math.cos(theta_diff), -c0],
                         onsite_energy=0,
                         a1=rotate.dot(a1 / np.linalg.norm(a1) * a_cc *
     math.sqrt(3)),
                         a2=rotate.dot(a2 / np.linalg.norm(a2) * a_cc *
     math.sqrt(3)), shape=shape),
    add_one_atomic_layer(name='C4',
                         position=[- a_cc / 2 * math.sin(theta_diff), +
    a_cc / 2 * math.cos(theta_diff), -c0],
                         onsite_energy=0,
                         a1=rotate.dot(a1 / np.linalg.norm(a1) * a_cc *
     math.sqrt(3)),
                         a2=rotate.dot(a2 / np.linalg.norm(a2) * a_cc *
     math.sqrt(3)), shape=shape)
)

# get the positions and atom types
x, y, z = model.system.positions
atom_type = model.system.sublattices
```

The following function adds to the model a set of atomic sites of a given sublattice within the area defined by the shape.

Listing C.3: Add a single atomic layer.

```
def add_one_atomic_layer(name, position, onsite_energy, a1, a2, shape):
    """Add a layer made from single sublattice

    Parameters
    ----------
    name : str
        User friendly name for the sublattice.
    position : Tuple[float, float, float]
        Position in xyz coordinates.
    onsite_energy : float
        Onsite energy terms at the sublattice.
    a1, a2 : Tuple[float, float, float]
        Unit cell vectors.
    shape:
        Shape of the structure (unit cell).
    Returns
    -------

    Lattice site positions. Named tuple with x, y, z fields, each a 1D
    array.
    """

    @pb.site_generator(name, onsite_energy)
    def define_layer():
        lat = pb.Lattice(a1=a1, a2=a2)
        lat.add_sublattices((name, position, onsite_energy))
        model = pb.Model(
            lat,
            shape,
        )
        return model.system.positions
    return define_layer
```

If we assume that we have an `*.xyz` file where the positions `x, y`, and `z`, and the lattice vectors `l1, l2` of tBLG are defined, the next step would include a neighbour search for the given system. This problem can divided into two parts, finding all the neighbours in the original unit cell (in terms of relative indexing it is cell $[0, 0]$), and computing all the periodic neighbours (neighbours from the unit cells $[0, 1]$, $[1, 0]$, $[1, 1]$, $[1, -1]$, and the conjugate parts). The first step can be done by making a *k-dimensional tree* or a KD Tree (`scipy.spatial.cKDTree`) for an efficient search. For each site in the KD Tree we are searching for all the neighbours within a predefined radius. For the second step, neighbours should be computed between the trees representing the original $[0, 0]$ and one of the mirror unit cells that are translated by multiples of the lattice vectors. Within each of the two steps it is convenient to split the search for interlayer and intralayer neighbours, due to a different choice of the search radius. Examples of the two scripts are shown bellow. In these scripts `Type_1` and `Type_2` denote all the sites in the top and the bottom layer, respectively.

Listing C.4: Finding intralayer neighbours.

```
def find_row_and_col_intra(positions, positions_to, atom_type,
    d_min_intra, d_max_intra):
    """ Find indexes for intralayer neighbours
    positions : np.ndarray
        Position of sites.
    positions_to : np.ndarray
        Position of sites that are being connected.
    atom_type : Type of the sublattice
    d_min_intra, d_max_intra : float, float
        Min and max distance for intralayer neighbour.

    Returns
    -------
    np.array, np.array
        Index of hopping from , index of hopping to.
    """
    def find_neigh_in_layer(layer):
        kdtree1 = cKDTree(data=positions[layer])
        kdtree2 = cKDTree(data=positions_to[layer])

        coo = kdtree1.sparse_distance_matrix(kdtree2, d_max_intra,
    output_type='coo_matrix')
        abs_idx = np.flatnonzero(layer)
        idx = coo.data > d_min_intra
        row, col = abs_idx[coo.row[idx]], abs_idx[coo.col[idx]]
        return row, col

    z = positions[:, 2]
    layer1 = atom_type == 'Type_1'
    layer2 = atom_type == 'Type_2'
    row1, col1, row2, col2 = [], [], [], []
    if np.any(layer1):
        row1, col1 = find_neigh_in_layer(layer1)
    if np.any(layer2):
        row2, col2 = find_neigh_in_layer(layer2)
    row = np.concatenate((row1, row2))
    col = np.concatenate((col1, col2))

    return row.astype(np.int64), col.astype(np.int64)
```

Listing C.5: Finding interlayer neighbours.

```
def find_row_and_col_inter(positions, positions_to, atom_type,
    d_min_inter, d_max_inter):
    """ Find indexes for interlayer neighbours
    positions : np.ndarray
        Position of sites.
    positions_to : np.ndarray
        Position of sites that are being connected.
    l1, l2 : np.array, np.array
        Unit cell vectors.
    d_min_intra, d_max_intra : float, float
        Min and max distance for interlayer neighbour.

    Returns
    -------
    np.array, np.array
        Index of hopping from , index of hopping to.
    """
    # z = positions[:, 2]
```

```
    layer1 = atom_type == 'Type_1'
    layer2 = atom_type == 'Type_2'
    row, col = [], []
    if np.logical_and(np.any(layer1), np.any(layer2)):
        kdtree1 = cKDTree(positions[layer1])
        kdtree2 = cKDTree(positions_to[layer2])
        abs_idx1 = np.flatnonzero(layer1)
        abs_idx2 = np.flatnonzero(layer2)
        coo = kdtree1.sparse_distance_matrix(kdtree2, d_max_inter,
    output_type='coo_matrix')
        idx = coo.data > d_min_inter
        row, col = abs_idx1[coo.row[idx]], abs_idx2[coo.col[idx]]
    return np.array(row).astype(np.int64), np.array(col).astype(np.
    int64)
```

In this approach lattice is defined only with the atomic sites without any of the hopping terms. After all the neighbours are found (intralayer and interlayer) we can proceed in adding the hopping terms, now to the model, based on the indexes defined in the previous two functions and using a `@pb.hopping_generator`. Once the hoppings are generated, we can their values based on the distance vectors (in this case the system is assumed flat and the local normal is not computed for reasons of keeping the following function brief). For changing the default hopping value defined in the `@pb.hopping_generator` function `@pb.hopping_energy_modifier` can be used.

Listing C.6: Computing and adding hopping terms to the model.

```
def generate_hopping(intra_neighbors, inter_neighbors):
    """Generate hoppings based on the indexes"""

    @pb.hopping_generator('intralayer', energy=0.0)  # eV
    def intralayer_generator():
        intra = copy.deepcopy(intra_neighbors)
        return zip(*intra)

    @pb.hopping_generator('interlayer', energy=0.0)  # eV
    def interlayer_generator():
        inter = copy.deepcopy(inter_neighbors)
        return zip(*inter)

    @pb.hopping_energy_modifier
    def hopping_value(x1, y1, z1, x2, y2, z2, hop_id):
        """Set the value of the newly generated hoppings as a function
    of distance"""

        dx, dy, dz = x1 - x2, y1 - y2, z1 - z2
        d = np.sqrt(np.square(dx) + np.square(dy) + np.square(dz))

        v_pi = -gamma0 * np.exp(q_pi * (1.0 - r / a))
        v_sigma = gamma1 * np.exp(q_sigma * (1.0 - r / c0))

        return v_pi * (1 - r_ez ** 2) + v_sigma * r_ez ** 2
    return intralayer_generator, interlayer_generator, hopping_value
```

Final function that we would need creates a lattice out of the lists (vectors) of atomic positions and species (types), onsite energies, and, most

importantly, lattice vectors. Such a lattice can be created with

Listing C.7: Creating a lattice.

```
    def make_lattice(a1, a2, atom_type, positions, different_atoms,
    onsite_potential):
    """Import the loaded atoms to the lattice

    Parameters
    ----------

    a1, a2 : Tuple[float, float, float]
        Unit cell vectors
    atom_type : np.ndarray
        Sublattice labels.
    positions : np.ndarray
        Position of sites.
    different_atoms : list[str]
        Atom types loaded from XYZ
    onsite_potential : list[float]
        Onsite energy at each sublattice.

    Return
    ----------
        pb.Lattice lattice defined without the hopping terms

    """
    lat = pb.Lattice(a1=a1, a2=a2)
    list_atoms_sublattice = []

    count = np.zeros(len(different_atoms), dtype=int)
    sublattice_added = []
    for [i, atom] in enumerate(positions):
        if atom_type[i] in different_atoms:
            j = different_atoms.index(atom_type[i])
            list_atoms_sublattice.append((different_atoms[j] + str(
    count[j]), atom, onsite_potential[j]))
            sublattice_added.append(atom_type[i])
            count[j] += 1
    lat.add_sublattices(*list_atoms_sublattice)

    return lat
```

Because we created a tBLG system with either `C1-4` or `Type_1` and `Type_2` labels, and the lattice object requires unique name for each site, the atoms in the above function are labelled based on their type and the number of atoms already added.

Finally, a desired tBLG model can created by writing

Listing C.8: Creating a model.

```
model = pb.Model(make_lattice(a1, a2, atom_type, positions,
    different_atoms, onsite_potential),
                 generate_hopping(intra, inter)
                 )
```

from where the desired quantities can be computed by calling the appropriate functions.

Bibliography

[1] Alex Zunger. "Beware of plausible predictions of fantasy materials". In: *Nature* 566, 7745 (2019), pp. 447–449. DOI: 10.1038/d41586-019-00676-y.

[2] K. S. Novoselov. "Electric Field Effect in Atomically Thin Carbon Films". In: *Science* 306, 5696 (2004), pp. 666–669. DOI: 10.1126/science.1102896.

[3] M.I. Katsnelson. *Graphene: Carbon in Two Dimensions*. Cambridge University Press, 2012.

[4] Yuan Cao et al. "Unconventional superconductivity in magic-angle graphene superlattices". In: *Nature* 556, 7699 (2018), pp. 43–50. DOI: 10.1038/nature26160.

[5] Xiaoxiang Xi et al. "Strongly enhanced charge-density-wave order in monolayer NbSe2". In: *Nature Nanotechnology* 10, 9 (2015), pp. 765–769. DOI: 10.1038/nnano.2015.143.

[6] Sajedeh Manzeli et al. "2D transition metal dichalcogenides". In: *Nature Reviews Materials* 2, 8 (2017), p. 17033. DOI: 10.1038/natrevmats.2017.33.

[7] Kha Tran et al. "Evidence for moiré excitons in van der Waals heterostructures". In: *Nature* 567, 7746 (2019), p. 71. DOI: 10.1038/s41586-019-0975-z.

[8] Wenzhong Bao et al. "Controlled ripple texturing of suspended graphene and ultrathin graphite membranes". In: *Nature Nanotechnology* 4, 9 (2009), pp. 562–566. DOI: 10.1038/nnano.2009.191.

[9] C. R. Woods et al. "Commensurate–incommensurate transition in graphene on hexagonal boron nitride". In: *Nature Physics* 10, 6 (2014), pp. 451–456. DOI: 10.1038/nphys2954.

[10] Di Xiao et al. "Coupled Spin and Valley Physics in Monolayers of MoS_2 and Other Group-VI Dichalcogenides". In: *Physical Review Letters* 108, 19 (2012), p. 196802. DOI: 10.1103/PhysRevLett.108.196802.

[11] Andre K Geim and Irina V Grigorieva. "Van der Waals heterostructures". In: *Nature* 499, 7459 (2013), pp. 419–425. DOI: 10.1038/nature12385.

[12] K. S. Novoselov et al. "2D materials and van der Waals heterostructures". In: *Science* 353, 6298 (2016), aac9439. DOI: 10.1126/science.aac9439.

[13] Matthew Yankowitz et al. "van der Waals heterostructures combining graphene and hexagonal boron nitride". In: *Nature Reviews Physics* 1, 2 (2019), pp. 112–125. DOI: 10.1038/s42254-018-0016-0.

[14] Matthew Yankowitz et al. "Emergence of superlattice Dirac points in graphene on hexagonal boron nitride". In: *Nature Physics* 8, 5 (2012), pp. 382–386. DOI: 10.1038/nphys2272.

[15] L. A. Ponomarenko et al. "Cloning of Dirac fermions in graphene superlattices". In: *Nature* 497, 7451 (2013), pp. 594–597. DOI: 10.1038/nature12187.

[16] B. Hunt et al. "Massive Dirac Fermions and Hofstadter Butterfly in a van der Waals Heterostructure". In: *Science* 340, 6139 (2013), pp. 1427–1430. DOI: 10.1126/science.1237240.

[17] Zhi-Guo Chen et al. "Observation of an intrinsic bandgap and Landau level renormalization in graphene/boron-nitride heterostructures". In: *Nature Communications* 5, 1 (2014), p. 4461. DOI: 10.1038/ncomms5461.

[18] C. R. Dean et al. "Hofstadter's butterfly and the fractal quantum Hall effect in moiré superlattices". In: *Nature* 497, 7451 (2013), pp. 598–602. DOI: 10.1038/nature12186.

[19] A. Luican et al. "Single-Layer Behavior and Its Breakdown in Twisted Graphene Layers". In: *Physical Review Letters* 106, 12 (2011), p. 126802. DOI: 10.1103/PhysRevLett.106.126802.

[20] Guohong Li et al. "Observation of Van Hove Singularities in Twisted Graphene Layers". In: *Nature Physics* 6, 2 (2009), pp. 109–113. DOI: 10.1038/nphys1463.

[21] Wei Yan et al. "Angle-Dependent van Hove Singularities in a Slightly Twisted Graphene Bilayer". In: *Physical Review Letters* 109, 12 (2012), p. 126801. DOI: 10.1103/PhysRevLett.109.126801.

[22] Kyounghwan Kim et al. "Tunable Moiré Bands and Strong Correlations in Small-Twist-Angle Bilayer Graphene". In: *Proceedings of the National Academy of Sciences* 114, 13 (2017), pp. 3364–3369. DOI: 10.1073/pnas.1620140114.

[23] Yuan Cao et al. "Correlated insulator behaviour at half-filling in magic-angle graphene superlattices". In: *Nature* 556, 7699 (2018), pp. 80–84. DOI: 10.1038/nature26154.

[24] Shengqiang Huang et al. "Topologically Protected Helical States in Minimally Twisted Bilayer Graphene". In: *Physical Review Letters* 121, 3 (2018), p. 037702. DOI: 10.1103/PhysRevLett.121.037702.

[25] Hideo Aoki and Mildred S. Dresselhaus, eds. *Physics of Graphene*. Springer International Publishing, 2014.

[26] J.-H. Chen et al. "Charged-impurity scattering in graphene". In: *Nature Physics* 4, 5 (2008), pp. 377–381. DOI: 10.1038/nphys935.

[27] Yuanbo Zhang et al. "Experimental observation of the quantum Hall effect and Berry's phase in graphene". In: *Nature* 438, 7065 (2005), pp. 201–204. DOI: 10.1038/nature04235.

[28] K. S. Novoselov et al. "Room-Temperature Quantum Hall Effect in Graphene". In: *Science* 315, 5817 (2007), pp. 1379–1379. DOI: 10.1126/science.1137201.

[29] K. S. Novoselov et al. "Two-dimensional gas of massless Dirac fermions in graphene". In: *Nature* 438, 7065 (2005), pp. 197–200. DOI: 10.1038/nature04233.

[30] A. C. Ferrari et al. "Raman Spectrum of Graphene and Graphene Layers". In: *Physical Review Letters* 97, 18 (2006), p. 187401. DOI: 10.1103/PhysRevLett.97.187401.

[31] Fabio Pulizzi et al. "Graphene in the making". In: *Nature Nanotechnology* 14, 10 (2019), pp. 914–918. DOI: 10.1038/s41565-019-0552-5.

[32] C. R. Dean et al. "Boron nitride substrates for high-quality graphene electronics". In: *Nature Nanotechnology* 5, 10 (2010), pp. 722–726. DOI: 10.1038/nnano.2010.172.

[33] Alexander S. Mayorov et al. “Micrometer-Scale Ballistic Transport in Encapsulated Graphene at Room Temperature”. In: *Nano Letters* 11, 6 (2011), pp. 2396–2399. DOI: 10.1021/nl200758b.

[34] C. Lee et al. “Measurement of the Elastic Properties and Intrinsic Strength of Monolayer Graphene”. In: *Science* 321, 5887 (2008), pp. 385–388. DOI: 10.1126/science.1157996.

[35] Per Joensen, R.F. Frindt, and S.Roy Morrison. “Single-layer MoS2”. In: *Materials Research Bulletin* 21, 4 (1986), pp. 457–461. DOI: 10.1016/0025-5408(86)90011-5.

[36] Branimir Radisavljevic et al. “Single-layer MoS 2 transistors”. In: *Nature nanotechnology* 6, 3 (2011), p. 147. DOI: 10.1038/nnano.2010.279.

[37] Li Lin, Hailin Peng, and Zhongfan Liu. “Synthesis challenges for graphene industry”. In: *Nature Materials* 18, 6 (2019), pp. 520–524. DOI: 10.1038/s41563-019-0341-4.

[38] Daniel Rhodes et al. “Disorder in van der Waals heterostructures of 2D materials”. In: *Nature Materials* 18, 6 (2019), pp. 541–549. DOI: 10.1038/s41563-019-0366-8.

[39] Anubhav Jain et al. “The Materials Project: A materials genome approach to accelerating materials innovation”. In: *APL Materials* 1, 1 (2013), p. 011002. DOI: 10.1063/1.4812323.

[40] Lujun Wang et al. “New Generation of Moiré Superlattices in Doubly Aligned hBN/Graphene/hBN Heterostructures”. In: *Nano Letters* 19, 4 (2019), pp. 2371–2376. DOI: 10.1021/acs.nanolett.8b05061.

[41] Richard P Feynman. “Simulating physics with computers”. In: *International journal of theoretical physics* 21, 6 (1982), pp. 467–488. DOI: 10.1007/BF02650179.

[42] Neil W Ashcroft, N David Mermin, et al. *Solid state physics [by] Neil W. Ashcroft [and] N. David Mermin.* New York: Holt, Rinehart and Winston, 1976.

[43] J. C. Slater and G. F. Koster. “Simplified LCAO Method for the Periodic Potential Problem”. In: *Physical Review* 94, 6 (1954), pp. 1498–1524. DOI: 10.1103/physrev.94.1498.

[44] Sverre Froyen and Walter A. Harrison. “Elementary Prediction of Linear Combination of Atomic Orbitals Matrix Elements”. In: *Physical Review B* 20, 6 (1979), pp. 2420–2422. DOI: 10.1103/PhysRevB.20.2420.

[45] D A Papaconstantopoulos and M J Mehl. "The Slater Koster Tight-Binding Method: A Computationally Efficient and Accurate Approach". In: *Journal of Physics: Condensed Matter* 15, 10 (2003), R413–R440. DOI: 10.1088/0953-8984/15/10/201.

[46] M. Nakhaee, S. A. Ketabi, and F. M. Peeters. "Tight-Binding Studio: A Technical Software Package to Find the Parameters of Tight-Binding Hamiltonian". In: *arXiv* (2019). eprint: https://arxiv.org/abs/1910.02917.

[47] T. O. Wehling et al. "Resonant Scattering by Realistic Impurities in Graphene". In: *Physical Review Letters* 105, 5 (2010), p. 056802. DOI: 10.1103/PhysRevLett.105.056802.

[48] Aires Ferreira et al. "Unified description of the dc conductivity of monolayer and bilayer graphene at finite densities based on resonant scatterers". In: *Physical Review B* 83, 16 (2011), p. 165402. DOI: 10.1103/PhysRevB.83.165402.

[49] Jeil Jung et al. "*Ab Initio* Theory of Moiré Superlattice Bands in Layered Two-Dimensional Materials". In: *Physical Review B* 89, 20 (2014), p. 205414. DOI: 10.1103/PhysRevB.89.205414.

[50] M. Anđelković, L. Covaci, and F. M. Peeters. "DC conductivity of twisted bilayer graphene: Angle-dependent transport properties and effects of disorder". In: *Physical Review Materials* 2, 3 (2018), p. 034004. DOI: 10.1103/PhysRevMaterials.2.034004.

[51] Flaviano José dos Santos et al. "Impact of Complex Adatom-Induced Interactions on Quantum Spin Hall Phases". In: *Physical Review B* 98, 8 (2018), p. 081407. DOI: 10.1103/PhysRevB.98.081407.

[52] Luis M. Canonico, Tatiana G. Rappoport, and R. B. Muniz. "Spin and Charge Transport of Multiorbital Quantum Spin Hall Insulators". In: *Physical Review Letters* 122, 19 (2019), p. 196601. DOI: 10.1103/PhysRevLett.122.196601.

[53] T. P. Cysne et al. "Numerical Calculation of the Casimir-Polder Interaction between a Graphene Sheet with Vacancies and an Atom". In: *Physical Review B* 94, 23 (2016), p. 235405. DOI: 10.1103/PhysRevB.94.235405.

[54] Stefan Grimme, Christoph Bannwarth, and Philip Shushkov. "A Robust and Accurate Tight-Binding Quantum Chemical Method for Structures, Vibrational Frequencies, and Noncovalent Interactions of Large Molecular Systems Parametrized for All Spd-Block Elements ($Z = 1$–86)". In: *Journal of Chemical Theory and Computation* 13, 5 (2017), pp. 1989–2009. DOI: 10.1021/acs.jctc.7b00118.

[55] Philip Richard Wallace. "The band theory of graphite". In: *Physical Review* 71, 9 (1947), pp. 622–634. DOI: 10.1103/PhysRev.71.622.

[56] A. H. Castro Neto et al. "The electronic properties of graphene". In: *Reviews of Modern Physics* 81, 1 (2009), pp. 109–162. DOI: 10.1103/RevModPhys.81.109.

[57] S. Das Sarma et al. "Electronic transport in two-dimensional graphene". In: *Reviews of Modern Physics* 83, 2 (2011), pp. 407–470. DOI: 10.1103/RevModPhys.83.407.

[58] Edward McCann. "Asymmetry gap in the electronic band structure of bilayer graphene". In: *Physical Review B* 74, 16 (2006), p. 161403. DOI: 10.1103/physrevb.74.161403.

[59] M Mucha-Kruczyński, E McCann, and Vladimir I Fal'ko. "Electron-hole asymmetry and energy gaps in bilayer graphene". In: *Semiconductor Science and Technology* 25, 3 (2010), p. 033001. DOI: 10.1088/0268-1242/25/3/033001.

[60] A. H. Castro Neto et al. "The electronic properties of graphene". In: *Reviews of Modern Physics* 81, 1 (2009), pp. 109–162. DOI: 10.1103/revmodphys.81.109.

[61] L.E.F.F. Torres, S. Roche, and J.C. Charlier. *Introduction to Graphene-Based Nanomaterials: From Electronic Structure to - Quantum Transport*. Cambridge University Press, 2014.

[62] David Ferry and Stephen Marshall Goodnick. *Transport in nanostructures*. Cambridge university press, 1999.

[63] Thomas Ihn. *Semiconductor Nanostructures*. Oxford University Press, 2009.

[64] Henrik Bruus and Karsten Flensberg. *Many-body quantum theory in condensed matter physics: an introduction*. Oxford university press, 2004.

[65] A. Bastin et al. "Quantum Oscillations of the Hall Effect of a Fermion Gas with Random Impurity Scattering". In: *Journal of Physics and Chemistry of Solids* 32, 8 (1971), pp. 1811–1824. DOI: 10.1016/S0022-3697(71)80147-6.

[66] Supriyo Datta. *Electronic transport in mesoscopic systems*. Cambridge university press, 1997.

[67] Dmitry A Ryndyk et al. *Theory of Quantum Transport at Nanoscale*. Springer, 2016.

[68] John P. Boyd. *Chebyshev and Fourier Spectral Methods*. 2nd ed., rev. Dover Publications, 2001.

[69] Alexander Weiße et al. "The kernel polynomial method". In: *Reviews of Modern Physics* 78, 1 (2006), pp. 275–306. DOI: 10.1103/revmodphys.78.275.

[70] William Ford. *Numerical Linear Algebra with Applications*. Elsevier, 2015.

[71] Aires Ferreira and Eduardo R. Mucciolo. "Critical Delocalization of Chiral Zero Energy Modes in Graphene". In: *Physical Review Letters* 115, 10 (2015), p. 106601. DOI: 10.1103/PhysRevLett.115.106601.

[72] Eleftherios N Economou. *Green's Functions in Quantmn Physics*. Springer, 1979.

[73] H. Tal-Ezer and R. Kosloff. "An accurate and efficient scheme for propagating the time dependent Schrödinger equation". In: *The Journal of Chemical Physics* 81, 9 (1984), pp. 3967–3971. DOI: 10.1063/1.448136.

[74] Aires Ferreira and Eduardo R. Mucciolo. "Critical Delocalization of Chiral Zero Energy Modes in Graphene". In: *Physical Review Letters* 115, 10 (2015), p. 106601. DOI: 10.1103/physrevlett.115.106601.

[75] Simão M. João et al. "KITE: high-performance accurate modelling of electronic structure and response functions of large molecules, disordered crystals and heterostructures". In: *arXiv* (2019). eprint: https://arxiv.org/abs/1910.05194.

[76] Toshiaki Iitaka and Toshikazu Ebisuzaki. "Random phase vector for calculating the trace of a large matrix". In: *Physical Review E* 69, 5 (2004), p. 057701. DOI: 10.1103/PhysRevE.69.057701.

[77] J. H. García, L. Covaci, and T. G. Rappoport. "Real-Space Calculation of the Conductivity Tensor for Disordered Topological Matter". In: *Physical Review Letters* 114, 11 (2015), p. 116602. DOI: 10.1103/PhysRevLett.114.116602.

[78] N. Leconte, A. Ferreira, and J. Jung. "Efficient Multiscale Lattice Simulations of Strained and Disordered Graphene". In: *Semiconductors and Semimetals*. Elsevier, 2016, pp. 35–99.

[79] Hisashi Hiramoto and Shuji Abe. "Dynamics of an Electron in Quasiperiodic Systems. I. Fibonacci Model". In: *Journal of the Physical Society of Japan* 57, 1 (1988), pp. 230–240. DOI: 10.1143/JPSJ.57.230.

[80] S. Roche and D. Mayou. "Conductivity of Quasiperiodic Systems: A Numerical Study". In: *Physical Review Letters* 79, 13 (1997), pp. 2518–2521. DOI: 10.1103/PhysRevLett.79.2518.

[81] H. Tal-Ezer and R. Kosloff. "An accurate and efficient scheme for propagating the time dependent Schrödinger equation". In: *The Journal of Chemical Physics* 81, 9 (1984), pp. 3967–3971. DOI: 10.1063/1.448136.

[82] Stephan Roche. "Quantum transport by means of O(N) real-space methods". In: *Physical Review B* 59, 3 (1999), pp. 2284–2291. DOI: 10.1103/PhysRevB.59.2284.

[83] Zheyong Fan et al. "Linear Scaling Quantum Transport Methodologies". In: *arXiv* (2018). eprint: arXiv:1811.07387.

[84] W. A. Muñoz, L. Covaci, and F. M. Peeters. "Disordered Graphene Josephson Junctions". en. In: *Physical Review B* 91, 5 (2015), p. 054506. DOI: 10.1103/PhysRevB.91.054506.

[85] Tasko P. Grozdanov, Vladimir A. Mandelshtam, and Howard S. Taylor. "Recursion Polynomial Expansion of the Green's Function with Absorbing Boundary Conditions: Calculations of Resonances of HCO by Filter Diagonalization". In: *The Journal of Chemical Physics* 103, 18 (1995), pp. 7990–7995. DOI: 10.1063/1.470217.

[86] David E. Manolopoulos. "Derivation and Reflection Properties of a Transmission-Free Absorbing Potential". en. In: *The Journal of Chemical Physics* 117, 21 (2002), pp. 9552–9559. DOI: 10.1063/1.1517042.

[87] Tomas Gonzalez-Lezana, Edward J. Rackham, and David E. Manolopoulos. "Quantum Reactive Scattering with a Transmission-Free Absorbing Potential". In: *The Journal of Chemical Physics* 120, 5 (2004), p. 2247. DOI: 10.1063/1.1637584.

[88] Editorial. "Boosting materials modelling". In: *Nature Materials* 15, 4 (2016), pp. 365–365. DOI: 10.1038/nmat4619.

[89] Andrea Zen et al. "Fast and accurate quantum Monte Carlo for molecular crystals". In: *Proceedings of the National Academy of Sciences* 115, 8 (2018), pp. 1724–1729. DOI: 10.1073/pnas.1715434115.

[90] Giovanni Onida, Lucia Reining, and Angel Rubio. "Electronic excitations: density-functional versus many-body Green's-function approaches". In: *Reviews of Modern Physics* 74, 2 (2002), pp. 601–659. DOI: 10.1103/RevModPhys.74.601.

[91] M. Elstner et al. "Self-consistent-charge density-functional tight-binding method for simulations of complex materials properties". In: *Physical Review B* 58, 11 (1998), pp. 7260–7268. DOI: 10.1103/PhysRevB.58.7260.

[92] John C. Snyder et al. "Finding Density Functionals with Machine Learning". In: *Physical Review Letters* 108, 25 (2012), p. 253002. DOI: 10.1103/PhysRevLett.108.253002.

[93] Felix Brockherde et al. "Bypassing the Kohn-Sham equations with machine learning". In: *Nature Communications* 8, 1 (2017), p. 872. DOI: 10.1038/s41467-017-00839-3.

[94] M. Altarelli. "Electronic structure and semiconductor-semimetal transition in InAs-GaSb superlattices". In: *Physical Review B* 28, 2 (1983), pp. 842–845. DOI: 10.1103/PhysRevB.28.842.

[95] D. P. DiVincenzo and E. J. Mele. "Self-consistent effective-mass theory for intralayer screening in graphite intercalation compounds". In: *Physical Review B* 29, 4 (1984), pp. 1685–1694. DOI: 10.1103/PhysRevB.29.1685.

[96] M G Burt. "The justification for applying the effective-mass approximation to microstructures". In: *Journal of Physics: Condensed Matter* 4, 32 (1992), pp. 6651–6690. DOI: 10.1088/0953-8984/4/32/003.

[97] Garnett W. Bryant and W. Jaskólski. "Tight-binding theory of quantum-dot quantum wells: Single-particle effects and near-band-edge structure". In: *Physical Review B* 67, 20 (2003), p. 205320. DOI: 10.1103/PhysRevB.67.205320.

[98] P. Vogl, Harold P. Hjalmarson, and John D. Dow. "A Semi-empirical tight-binding theory of the electronic structure of semiconductors†". In: *Journal of Physics and Chemistry of Solids* 44, 5 (1983), pp. 365–378. DOI: https://doi.org/10.1016/0022-3697(83)90064-1.

[99] Jean-Marc Jancu et al. "Empirical spds* tight-binding calculation for cubic semiconductors: General method and material parameters". In: *Physical Review B* 57, 11 (1998), pp. 6493–6507. DOI: 10.1103/PhysRevB.57.6493.

[100] Huaxiang Fu, Lin-Wang Wang, and Alex Zunger. "Applicability of the $\mathbf{k} \cdot \mathbf{p}$ method to the electronic structure of quantum dots". In: *Physical Review B* 57, 16 (1998), pp. 9971–9987. DOI: 10.1103/PhysRevB.57.9971.

[101] G. C. Osbourn. "Strained-layer superlattices from lattice mismatched materials". In: *Journal of Applied Physics* 53, 3 (1982), pp. 1586–1589. DOI: 10.1063/1.330615.

[102] D. L. Smith and C. Mailhiot. "Theory of semiconductor superlattice electronic structure". In: *Reviews of Modern Physics* 62, 1 (1990), pp. 173–234. DOI: 10.1103/RevModPhys.62.173.

[103] Stefan Goedecker. "Linear scaling electronic structure methods". In: *Reviews of Modern Physics* 71, 4 (1999), pp. 1085–1123. DOI: 10.1103/RevModPhys.71.1085.

[104] C M Goringe, D R Bowler, and E Hernández. "Tight-binding modelling of materials". In: *Reports on Progress in Physics* 60, 12 (1997), pp. 1447–1512. DOI: 10.1088/0034-4885/60/12/001.

[105] Dimitris A. Papaconstantopoulos. *Handbook of the Band Structure of Elemental Solids: From Z = 1 To Z = 112*. 2nd ed., rev. Springer US, 2015.

[106] W. Matthew C. Foulkes and Roger Haydock. "Tight-binding models and density-functional theory". In: *Physical Review B* 39, 17 (1989), pp. 12520–12536. DOI: 10.1103/PhysRevB.39.12520.

[107] T. B. Boykin et al. "Diagonal parameter shifts due to nearest-neighbor displacements in empirical tight-binding theory". In: *Physical Review B* 66, 12 (2002), p. 125207. DOI: 10.1103/PhysRevB.66.125207.

[108] L Goodwin, A. J Skinner, and D. G Pettifor. "Generating Transferable Tight-Binding Parameters: Application to Silicon". In: *Europhysics Letters (EPL)* 9, 7 (1989), pp. 701–706. DOI: 10.1209/0295-5075/9/7/015.

[109] I. Kwon et al. "Transferable tight-binding models for silicon". In: *Physical Review B* 49, 11 (1994), pp. 7242–7250. DOI: 10.1103/PhysRevB.49.7242.

[110] J.-M. Jancu et al. "Transferable tight-binding parametrization for the group-III nitrides". In: *Applied Physics Letters* 81, 25 (2002), pp. 4838–4840. DOI: 10.1063/1.1529312.

[111] Yaohua Tan et al. "Transferable tight-binding model for strained group IV and III-V materials and heterostructures". In: *Physical Review B* 94, 4 (2016), p. 045311. DOI: 10.1103/PhysRevB.94.045311.

[112] Shengjun Yuan, Hans De Raedt, and Mikhail I. Katsnelson. "Modeling electronic structure and transport properties of graphene with resonant scattering centers". In: *Physical Review B* 82, 11 (2010), p. 115448. DOI: 10.1103/PhysRevB.82.115448.

[113] G. Alvarez et al. "The Truncated Polynomial Expansion Monte Carlo Method for Fermion Systems Coupled to Classical Fields: A Model Independent Implementation". In: *Computer Physics Communications* 168, 1 (2005), pp. 32–45. DOI: https://doi.org/10.1016/j.cpc.2005.02.001.

[114] Alexander Weiße. "Green-Function-Based Monte Carlo Method for Classical Fields Coupled to Fermions". In: *Physical Review Letters* 102, 15 (2009), p. 150604. DOI: 10.1103/PhysRevLett.102.150604.

[115] Kipton Barros and Yasuyuki Kato. "Efficient Langevin simulation of coupled classical fields and fermions". In: *Physical Review B* 88, 23 (2013), p. 235101. DOI: 10.1103/PhysRevB.88.235101.

[116] A. Holzner et al. "Chebyshev matrix product state approach for spectral functions". In: *Physical Review B* 83, 19 (2011), p. 195115. DOI: 10.1103/PhysRevB.83.195115.

[117] A. Braun and P. Schmitteckert. "Numerical Evaluation of Green's Functions Based on the Chebyshev Expansion". In: *Physical Review B* 90, 16 (2014), p. 165112. DOI: 10.1103/PhysRevB.90.165112.

[118] Christoph W Groth et al. "Kwant: A Software Package for Quantum Transport". In: *New Journal of Physics* 16, 6 (2014), p. 063065. DOI: 10.1088/1367-2630/16/6/063065.

[119] *PythTB website*. http://physics.rutgers.edu/pythtb/. Accessed: 2019-07-25.

[120] Zheyong Fan, Ville Vierimaa, and Ari Harju. "GPUQT: An efficient linear-scaling quantum transport code fully implemented on graphics processing units". In: *Computer Physics Communications* 230 (2018), pp. 113–120. DOI: 10.1016/j.cpc.2018.04.013.

[121] Moritz Kreutzer et al. "GHOST: Building Blocks for High Performance Sparse Linear Algebra on Heterogeneous Systems". In: *International Journal of Parallel Programming* 45, 5 (2017), pp. 1046–1072. DOI: 10.1007/s10766-016-0464-z.

[122] Kristofer Björnson. "TBTK: A quantum mechanics software development kit". In: *SoftwareX* 9 (2019), pp. 205–210. DOI: https://doi.org/10.1016/j.softx.2019.02.005.

[123] D. Moldovan, M. Anđelković, and F. M. Peeters. *Pybinding V0.9.4: A Python Package For Tight-Binding Calculations*. 2017. DOI: 10.5281/zenodo.826942.

[124] *Github account*. https://github.com/MAndelkovic/. Accessed: 2019-10-28.

[125] G Stefanucci and R. van Leeuwen. *G. Stefanucci and R. van Leeuwen, Nonequilibrium Many-Body Theory of Quantum Systems: A Modern Introduction*. Cambridge University Press, 2013.

[126] Aurélien Lherbier et al. "Charge Transport in Chemically Doped 2D Graphene". In: *Physical Review Letters* 101, 3 (2008), p. 036808. DOI: 10.1103/PhysRevLett.101.036808.

[127] V. Häfner et al. "Density of States in Graphene with Vacancies: Midgap Power Law and Frozen Multifractality". In: *Physical Review Letters* 113, 18 (2014), p. 186802. DOI: 10.1103/PhysRevLett.113.186802.

[128] Mirco Milletarì et al. "Covariant Conservation Laws and the Spin Hall Effect in Dirac-Rashba Systems". In: *Physical Review Letters* 119, 24 (2017), p. 246801. DOI: 10.1103/PhysRevLett.119.246801.

[129] A. Ferreira. "Large-scale spectral expansions: the Green's Function polynomial method and its efficient implementation". In: *(unpublished notes)* (2014).

[130] S. M. João and J. M. V. P. Lopes. "Non-Linear Optical Response of Non-Interacting Systems with Spectral Methods". In: *arXiv* (2018). eprint: http://arxiv.org/abs/1810.03732.

[131] Barry F. Smith. "Domain Decomposition Methods for Partial Differential Equations". In: *ICASE/LaRC Interdisciplinary Series in Science and Engineering*. Springer Netherlands, 1997, pp. 225–243. DOI: 10.1007/978-94-011-5412-3_8.

[132] *HDF5 website*. http://support.hdfgroup.org. Accessed: 2019-06-12.

[133] *KITE website*. https://quantum-kite.com/. Accessed: 2019-09-30.

[134] Simão Meneses João et al. *KITE: high-performance quantum transport software, 10.5281/zenodo.3245011*. 2019. DOI: 10.5281/ZENODO.3245011.

[135] Rafi Bistritzer and Allan H MacDonald. "Moiré bands in twisted double-layer graphene". In: *Proceedings of the National Academy of Sciences* 108, 30 (2011), pp. 12233–12237. DOI: 10.1073/pnas.1108174108.

[136] A. Luican et al. "Single-Layer Behavior and Its Breakdown in Twisted Graphene Layers". In: *Physical Review Letters* 106, 12 (2011), p. 126802. DOI: 10.1103/PhysRevLett.106.126802.

[137] Zhenhua Ni et al. "Reduction of Fermi velocity in folded graphene observed by resonance Raman spectroscopy". In: *Physical Review B* 77, 23 (2008), p. 235403. DOI: 10.1103/PhysRevB.77.235403.

[138] G. Trambly de Laissardière, D. Mayou, and L. Magaud. "Numerical studies of confined states in rotated bilayers of graphene". In: *Physical Review B* 86, 12 (2012), p. 125413. DOI: 10.1103/PhysRevB.86.125413.

[139] Pilkyung Moon and Mikito Koshino. "Energy spectrum and quantum Hall effect in twisted bilayer graphene". In: *Physical Review B* 85, 19 (2012), p. 195458. DOI: 10.1103/PhysRevB.85.195458.

[140] A. N. Kolmogorov and V. H. Crespi. "Registry-dependent interlayer potential for graphitic systems". In: *Physical Review B* 71, 23 (2005), p. 235415. DOI: 10.1103/PhysRevB.71.235415.

[141] Fernando Gargiulo and Oleg V Yazyev. "Structural and electronic transformation in low-angle twisted bilayer graphene". In: *2D Materials* 5, 1 (2017), p. 015019. DOI: 10.1088/2053-1583/aa9640.

[142] Nguyen N. T. Nam and Mikito Koshino. "Lattice relaxation and energy band modulation in twisted bilayer graphene". In: *Physical Review B* 96, 7 (2017), p. 075311. DOI: 10.1103/PhysRevB.96.075311.

[143] Procolo Lucignano et al. "Crucial role of atomic corrugation on the flat bands and energy gaps of twisted bilayer graphene at the magic angle $\theta \sim 1.08°$". In: *Physical Review B* 99, 19 (2019), p. 195419. DOI: 10.1103/PhysRevB.99.195419.

[144] Y Cao et al. "Superlattice-induced insulating states and valley-protected orbits in twisted bilayer graphene". In: *Physical Review Letters* 117, 11 (2016), p. 116804. DOI: 10.1103/PhysRevLett.117.116804.

[145] Zhenhua Qiao et al. "Quantum anomalous Hall effect in graphene from Rashba and exchange effects". In: *Physical Review B* 82, 16 (2010), p. 161414. DOI: 10.1103/PhysRevB.82.161414.

[146] Manuel Offidani and Aires Ferreira. "Anomalous Hall Effect in 2D Dirac Materials". In: *Physical Review Letters* 121, 12 (2018), p. 126802. DOI: 10.1103/PhysRevLett.121.126802.

[147] Zhenhua Qiao et al. "Two-Dimensional Topological Insulator State and Topological Phase Transition in Bilayer Graphene". In: *Physical Review Letters* 107, 25 (2011), p. 256801. DOI: 10.1103/PhysRevLett.107.256801.

[148] B. Amorim. "General theoretical description of angle-resolved photoemission spectroscopy of van der Waals structures". In: *Physical Review B* 97, 16 (2018), p. 165414. DOI: 10.1103/PhysRevB.97.165414.

[149] Ralph van Gelderen and C. Morais Smith. "Rashba and intrinsic spin-orbit interactions in biased bilayer graphene". In: *Physical Review B* 81, 12 (2010), p. 125435. DOI: 10.1103/PhysRevB.81.125435.

[150] Denis Kochan, Susanne Irmer, and Jaroslav Fabian. "Model spin-orbit coupling Hamiltonians for graphene systems". In: *Physical Review B* 95, 16 (2017), p. 165415. DOI: 10.1103/PhysRevB.95.165415.

[151] T. P. Cysne, A. Ferreira, and T. G. Rappoport. "Crystal-field effects in graphene with interface-induced spin-orbit coupling". In: *Physical Review B* 98, 4 (2018), p. 045407. DOI: 10.1103/PhysRevB.98.045407.

[152] M. Gmitra et al. "Trivial and inverted Dirac bands and the emergence of quantum spin Hall states in graphene on transition-metal dichalcogenides". In: *Physical Review B* 93, 15 (2016), p. 155104. DOI: 10.1103/PhysRevB.93.155104.

[153] Luyi Yang et al. "Long-lived nanosecond spin relaxation and spin coherence of electrons in monolayer MoS2 and WS2". In: *Nature Physics* 11, 10 (2015), pp. 830–834. DOI: 10.1038/nphys3419.

[154] Aron W. Cummings et al. "Giant Spin Lifetime Anisotropy in Graphene Induced by Proximity Effects". In: *Physical Review Letters* 119, 20 (2017), p. 206601. DOI: 10.1103/PhysRevLett.119.206601.

[155] Manuel Offidani and Aires Ferreira. "Microscopic theory of spin relaxation anisotropy in graphene with proximity-induced spin-orbit coupling". In: *Physical Review B* 98, 24 (2018), p. 245408. DOI: 10.1103/PhysRevB.98.245408.

[156] L. Antonio Benítez et al. "Strongly anisotropic spin relaxation in graphene–transition metal dichalcogenide heterostructures at room temperature". In: *Nature Physics* 14, 3 (2017), pp. 303–308. DOI: 10.1038/s41567-017-0019-2.

[157] Talieh S. Ghiasi et al. "Large Proximity-Induced Spin Lifetime Anisotropy in Transition-Metal Dichalcogenide/Graphene Heterostructures". In: *Nano Letters* 17, 12 (2017), pp. 7528–7532. DOI: 10.1021/acs.nanolett.7b03460.

[158] D. R. Hofstadter. "Energy levels and wave functions of Bloch electrons in rational and irrational magnetic fields". In: *Physical Review B* 14 (1976), pp. 2239–2249. DOI: 10.1103/PhysRevB.14.2239.

[159] X. Y. Zhou et al. "Landau levels and magneto-transport property of monolayer phosphorene". In: *Scientific Reports* 5, 1 (2015), p. 12295. DOI: 10.1038/srep12295.

[160] J. M. Pereira and M. I. Katsnelson. "Landau levels of single-layer and bilayer phosphorene". In: *Physical Review B* 92, 7 (2015), p. 075437. DOI: 10.1103/PhysRevB.92.075437.

[161] Motohiko Ezawa. "Highly anisotropic physics in phosphorene". In: *Journal of Physics: Conference Series* 603 (2015), p. 012006. DOI: 10.1088/1742-6596/603/1/012006.

[162] Shengjun Yuan et al. "Quantum Hall effect and semiconductor-to-semimetal transition in biased black phosphorus". In: *Physical Review B* 93, 24 (2016), p. 245433. DOI: 10.1103/PhysRevB.93.245433.

[163] Richard Korytár et al. "Signature of the Dirac cone in the properties of linear oligoacenes". In: *Nature Communications* 5, 1 (2014), p. 5000. DOI: 10.1038/ncomms6000.

[164] Daniel Faltermeier et al. "Optical properties of pentacene thin films and single crystals". In: *Physical Review B* 74, 12 (2006), p. 125416. DOI: 10.1103/PhysRevB.74.125416.

[165] Jose H. Garcia, Aron W. Cummings, and Stephan Roche. "Spin Hall Effect and Weak Antilocalization in Graphene/Transition Metal Dichalcogenide Heterostructures". In: *Nano Letters* 17, 8 (2017), pp. 5078–5083. DOI: 10.1021/acs.nanolett.7b02364.

[166] Vadim V. Cheianov and Vladimir I. Fal'ko. "Selective transmission of Dirac electrons and ballistic magnetoresistance of n-p junctions in graphene". In: *Physical Review B* 74, 4 (2006), p. 041403. DOI: 10.1103/physrevb.74.041403.

[167] E. McCann and V. I. Fal'ko. "Landau-Level Degeneracy and Quantum Hall Effect in a Graphite Bilayer". In: *Physical Review Letters* 96, 8 (2006), p. 086805. DOI: 10.1103/physrevlett.96.086805.

[168] Eduardo V. Castro et al. "Biased Bilayer Graphene: Semiconductor with a Gap Tunable by the Electric Field Effect". In: *Physical Review Letters* 99, 21 (2007), p. 216802. DOI: 10.1103/physrevlett.99.216802.

[169] Seon-Myeong Choi, Seung-Hoon Jhi, and Young-Woo Son. "Effects of strain on electronic properties of graphene". In: *Physical Review B* 81, 8 (2010), p. 081407. DOI: 10.1103/physrevb.81.081407.

[170] Ivar Martin, Ya. M. Blanter, and A. F. Morpurgo. "Topological Confinement in Bilayer Graphene". In: *Physical Review Letters* 100, 3 (2008), p. 036804. DOI: 10.1103/physrevlett.100.036804.

[171] M. Zarenia et al. "Chiral states in bilayer graphene: Magnetic field dependence and gap opening". In: *Physical Review B* 84, 12 (2011), p. 125451. DOI: 10.1103/physrevb.84.125451.

[172] D. R. da Costa et al. "Valley filtering using electrostatic potentials in bilayer graphene". In: *Physical Review B* 92, 4 (2015), p. 045417. DOI: 10.1103/physrevb.92.045417.

[173] Diana A. Cosma and Vladimir I. Fal'ko. "Trigonal warping effect on velocity and transverse confinement length of topologically confined states in bilayer graphene". In: *Physical Review B* 92, 16 (2015), p. 165412. DOI: 10.1103/physrevb.92.165412.

[174] Jing Li et al. "Gate-controlled topological conducting channels in bilayer graphene". In: *Nature Nanotechnology* 11, 12 (2016), pp. 1060–1065. DOI: 10.1038/nnano.2016.158.

[175] Zhenhua Qiao et al. "Electronic Highways in Bilayer Graphene". In: *Nano Letters* 11, 8 (2011), pp. 3453–3459. DOI: 10.1021/nl201941f.

[176] Ke Wang et al. "Gate-tunable current partition in graphene-based topological zero lines". In: *Physical Review B* 95, 24 (2017), p. 245420. DOI: 10.1103/physrevb.95.245420.

[177] M. Pelc et al. "Topologically confined states at corrugations of gated bilayer graphene". In: *Physical Review B* 92, 8 (2015), p. 085433. DOI: 10.1103/physrevb.92.085433.

[178] H. M. Abdullah et al. "Gate tunable layer selectivity of transport in bilayer graphene nanostructures". In: *EPL (Europhysics Letters)* 113, 1 (2016), p. 17006. DOI: 10.1209/0295-5075/113/17006.

[179] A. R. Akhmerov and C. W. J. Beenakker. "Boundary conditions for Dirac fermions on a terminated honeycomb lattice". In: *Physical Review B* 77, 8 (2008), p. 085423. DOI: 10.1103/physrevb.77.085423.

[180] Takeshi Nakanishi, Mikito Koshino, and Tsuneya Ando. "Transmission through a boundary between monolayer and bilayer graphene". In: *Physical Review B* 82, 12 (2010), p. 125428. DOI: 10.1103/physrevb.82.125428.

[181] Mikito Koshino. "Electronic transmission through AB-BA domain boundary in bilayer graphene". In: *Physical Review B* 88, 11 (2013), p. 115409. DOI: 10.1103/physrevb.88.115409.

[182] Edward McCann and Vladimir I Fal'ko. "Symmetry of boundary conditions of the Dirac equation for electrons in carbon nanotubes". In: *Journal of Physics: Condensed Matter* 16, 13 (2004), pp. 2371–2379. DOI: 10.1088/0953-8984/16/13/016.

[183] S. Slizovskiy and V. Fal'ko. "Cooling of chiral heat transport in the quantum Hall effect regime of graphene". In: *Physical Review B* 96, 7 (2017), p. 075434. DOI: 10.1103/physrevb.96.075434.

[184] Due to the finite nature of the BLG leads in the TB model, additional bands are shown above the bilayer band edge that would not otherwise be present. This leads to a high density of bands along the bilayer band edge, hence the dark region beneath the 'mexican hat' dispersion.

[185] Long-Jing Yin et al. "Direct imaging of topological edge states at a bilayer graphene domain wall". In: *Nature Communications* 7, 1 (2016), p. 11760. DOI: 10.1038/ncomms11760.

[186] T. L. M. Lane et al. "Ballistic electron channels including weakly protected topological states in delaminated bilayer graphene". In: *Physical Review B* 97, 4 (2018), p. 045301. DOI: 10.1103/PhysRevB.97.045301.

[187] Long Ju et al. "Topological valley transport at bilayer graphene domain walls". In: *Nature* 520, 7549 (2015), pp. 650–655. DOI: 10.1038/nature14364.

[188] Zheng Liu et al. "In-plane heterostructures of graphene and hexagonal boron nitride with controlled domain sizes". In: *Nature Nanotechnology* 8, 2 (2013), pp. 119–124. DOI: 10.1038/nnano.2012.256.

[189] C. Stampfer et al. "Energy Gaps in Etched Graphene Nanoribbons". In: *Physical Review Letters* 102, 5 (2009), p. 056403. DOI: 10.1103/PhysRevLett.102.056403.

[190] Andreas Sandner et al. "Ballistic Transport in Graphene Antidot Lattices". In: *Nano Letters* 15, 12 (2015), pp. 8402–8406. DOI: 10.1021/acs.nanolett.5b04414.

[191] S. Cai et al. "Periodic patterns and energy states of buckled films on compliant substrates". In: *Journal of the Mechanics and Physics of Solids* 59, 5 (2011), pp. 1094–1114. DOI: 10.1016/j.jmps.2011.02.001.

[192] E. Cerda and L. Mahadevan. "Geometry and Physics of Wrinkling". In: *Physical Review Letters* 90, 7 (2003), p. 074302. DOI: 10.1103/physrevlett.90.074302.

[193] T. Low, F. Guinea, and M. I. Katsnelson. "Gaps tunable by electrostatic gates in strained graphene". In: *Physical Review B* 83, 19 (2011), p. 195436. DOI: 10.1103/physrevb.83.195436.

[194] M. Ramezani Masir, D. Moldovan, and F.M. Peeters. "Pseudo magnetic field in strained graphene: Revisited". In: *Solid State Communications* 175-176 (2013), pp. 76–82. DOI: 10.1016/j.ssc.2013.04.001.

[195] M. Schneider et al. "Local sublattice symmetry breaking for graphene with a centrosymmetric deformation". In: *Physical Review B* 91, 16 (2015), p. 161407. DOI: 10.1103/physrevb.91.161407.

[196] B. Amorim et al. "Novel effects of strains in graphene and other two dimensional materials". In: *Physics Reports* 617 (2016), pp. 1–54. DOI: 10.1016/j.physrep.2015.12.006.

[197] N. Levy et al. "Strain-Induced Pseudo-Magnetic Fields Greater Than 300 Tesla in Graphene Nanobubbles". In: *Science* 329, 5991 (2010), pp. 544–547. DOI: 10.1126/science.1191700.

[198] Jiong Lu, A.H. Castro Neto, and Kian Ping Loh. "Transforming moiré blisters into geometric graphene nano-bubbles". In: *Nature Communications* 3, 1 (2012), p. 823. DOI: 10.1038/ncomms1818.

[199] Yuhang Jiang et al. "Visualizing Strain-Induced Pseudomagnetic Fields in Graphene through an hBN Magnifying Glass". In: *Nano Letters* 17, 5 (2017), pp. 2839–2843. DOI: 10.1021/acs.nanolett.6b05228.

[200] N. B. Kopnin, T. T. Heikkilä, and G. E. Volovik. "High-temperature surface superconductivity in topological flat-band systems". In: *Physical Review B* 83, 22 (2011), p. 220503. DOI: 10.1103/physrevb.83.220503.

[201] V. J. Kauppila, F. Aikebaier, and T. T. Heikkilä. "Flat-band superconductivity in strained Dirac materials". In: *Physical Review B* 93, 21 (2016), p. 214505. DOI: 10.1103/physrevb.93.214505.

[202] Evelyn Tang and Liang Fu. "Strain-induced partially flat band, helical snake states and interface superconductivity in topological crystalline insulators". In: *Nature Physics* 10, 12 (2014), pp. 964–969. DOI: 10.1038/nphys3109.

[203] D. C. Tsui, H. L. Stormer, and A. C. Gossard. "Two-Dimensional Magnetotransport in the Extreme Quantum Limit". In: *Physical Review Letters* 48, 22 (1982), pp. 1559–1562. DOI: 10.1103/physrevlett.48.1559.

[204] Xu Du et al. "Fractional quantum Hall effect and insulating phase of Dirac electrons in graphene". In: *Nature* 462, 7270 (2009), pp. 192–195. DOI: 10.1038/nature08522.

[205] Kirill I. Bolotin et al. "Observation of the fractional quantum Hall effect in graphene". In: *Nature* 462, 7270 (2009), pp. 196–199. DOI: 10.1038/nature08582.

[206] I. Skachko et al. "Fractional quantum Hall effect in suspended graphene probed with two-terminal measurements". In: *Philosophical Transactions of the Royal Society A: Mathematical, Physical and Engineering Sciences* 368, 1932 (2010), pp. 5403–5416. DOI: 10.1098/rsta.2010.0226.

[207] E. Y. Andrei et al. "Observation of a Magnetically Induced Wigner Solid". In: *Physical Review Letters* 60, 26 (1988), pp. 2765–2768. DOI: 10.1103/physrevlett.60.2765.

[208] Guohong Li et al. "Observation of Van Hove singularities in twisted graphene layers". In: *Nature Physics* 6, 2 (2009), pp. 109–113. DOI: 10.1038/nphys1463.

[209] A. Luican et al. "Single-Layer Behavior and Its Breakdown in Twisted Graphene Layers". In: *Physical Review Letters* 106, 12 (2011), p. 126802. DOI: 10.1103/physrevlett.106.126802.

[210] Matthew Yankowitz et al. "Emergence of superlattice Dirac points in graphene on hexagonal boron nitride". In: *Nature Physics* 8, 5 (2012), pp. 382–386. DOI: 10.1038/nphys2272.

[211] G. Giovannetti et al. "Doping Graphene with Metal Contacts". In: *Physical Review Letters* 101, 2 (2008), p. 026803. DOI: 10.1103/physrevlett.101.026803.

[212] Eva Y Andrei, Guohong Li, and Xu Du. "Electronic properties of graphene: a perspective from scanning tunneling microscopy and magnetotransport". In: *Reports on Progress in Physics* 75, 5 (2012), p. 056501. DOI: 10.1088/0034-4885/75/5/056501.

[213] Adina Luican, Guohong Li, and Eva Y. Andrei. "Scanning tunneling microscopy and spectroscopy of graphene layers on graphite". In: *Solid State Communications* 149, 27-28 (2009), pp. 1151–1156. DOI: 10.1016/j.ssc.2009.02.059.

[214] Kenjiro K. Gomes et al. "Designer Dirac fermions and topological phases in molecular graphene". In: *Nature* 483, 7389 (2012), pp. 306–310. DOI: 10.1038/nature10941.

[215] D. Moldovan, M. Ramezani Masir, and F. M. Peeters. "Electronic states in a graphene flake strained by a Gaussian bump". In: *Physical Review B* 88, 3 (2013), p. 035446. DOI: 10.1103/physrevb.88.035446.

[216] M. Neek-Amal et al. "Electronic structure of a hexagonal graphene flake subjected to triaxial stress". In: *Physical Review B* 88, 11 (2013), p. 115428. DOI: 10.1103/physrevb.88.115428.

[217] Mikkel Settnes, Stephen R. Power, and Antti-Pekka Jauho. "Pseudomagnetic fields and triaxial strain in graphene". In: *Physical Review B* 93, 3 (2016), p. 035456. DOI: 10.1103/physrevb.93.035456.

[218] Alexander Georgi et al. "Tuning the Pseudospin Polarization of Graphene by a Pseudomagnetic Field". In: *Nano Letters* 17, 4 (2017), pp. 2240–2245. DOI: 10.1021/acs.nanolett.6b04870.

[219] Z. Z. Zhang, Kai Chang, and F. M. Peeters. "Tuning of energy levels and optical properties of graphene quantum dots". In: *Physical Review B* 77, 23 (2008), p. 235411. DOI: 10.1103/physrevb.77.235411.

[220] Carmen Palacios-Berraquero et al. "Large-scale quantum-emitter arrays in atomically thin semiconductors". In: *Nature Communications* 8, 1 (2017), p. 15093. DOI: 10.1038/ncomms15093.

[221] Edward McCann and Mikito Koshino. "The Electronic Properties of Bilayer Graphene". In: *Reports on Progress in Physics* 76, 5 (2013), p. 056503. DOI: 10.1088/0034-4885/76/5/056503.

[222] A.V. Rozhkov et al. "Electronic Properties of Graphene-Based Bilayer Systems". In: *Physics Reports* 648 (2016), pp. 1–104. DOI: 10.1016/j.physrep.2016.07.003.

[223] J Hass, W A de Heer, and E H Conrad. "The Growth and Morphology of Epitaxial Multilayer Graphene". In: *Journal of Physics: Condensed Matter* 20, 32 (2008), p. 323202. DOI: 10.1088/0953-8984/20/32/323202.

[224] M. Sprinkle et al. "First Direct Observation of a Nearly Ideal Graphene Band Structure". In: *Physical Review Letters* 103, 22 (2009), p. 226803. DOI: 10.1103/PhysRevLett.103.226803.

[225] J. Hass et al. "Why Multilayer Graphene on $4H-\mathrm{SiC}(000\bar{1})$ Behaves Like a Single Sheet of Graphene". In: *Physical Review Letters* 100, 12 (2008), p. 125504. DOI: 10.1103/PhysRevLett.100.125504.

[226] P. Poncharal et al. "Raman Spectra of Misoriented Bilayer Graphene". In: *Physical Review B* 78, 11 (2008), p. 113407. DOI: 10.1103/PhysRevB.78.113407.

[227] Zhenhua Ni et al. "Reduction of Fermi Velocity in Folded Graphene Observed by Resonance Raman Spectroscopy". In: *Physical Review B* 77, 23 (2008), p. 235403. DOI: 10.1103/PhysRevB.77.235403.

[228] Long-Jing Yin et al. "Experimental Evidence for Non-Abelian Gauge Potentials in Twisted Graphene Bilayers". In: *Physical Review B* 92, 8 (2015), p. 081406. DOI: 10.1103/PhysRevB.92.081406.

[229] Elad Koren et al. "Coherent Commensurate Electronic States at the Interface between Misoriented Graphene Layers". In: *Nat. Nanotechnol.* 11 (2016), pp. 752–757. DOI: 10.1038/nnano.2016.85.

[230] Tarun Chari et al. "Resistivity of Rotated Graphite–Graphene Contacts". In: *Nano Letters* 16, 7 (2016), pp. 4477–4482. DOI: 10.1021/acs.nanolett.6b01657.

[231] Pablo San-Jose and Elsa Prada. "Helical Networks in Twisted Bilayer Graphene under Interlayer Bias". In: *Physical Review B* 88, 12 (2013), p. 121408. DOI: 10.1103/PhysRevB.88.121408.

[232] Kanchan Ulman and Shobhana Narasimhan. "Point Defects in Twisted Bilayer Graphene: A Density Functional Theory Study". In: *Physical Review B* 89, 24 (2014), p. 245429. DOI: 10.1103/PhysRevB.89.245429.

[233] G. Trambly de Laissardière, D. Mayou, and L. Magaud. "Localization of Dirac Electrons in Rotated Graphene Bilayers". In: *Nano Letters* 10, 3 (2010), pp. 804–808. DOI: 10.1021/nl902948m.

[234] M Van der Donck et al. "Piezoelectricity in Asymmetrically Strained Bilayer Graphene". In: *2D Materials* 3, 3 (2016), p. 035015. DOI: 10.1088/2053-1583/3/3/035015.

[235] J. M. B. Lopes dos Santos, N. M. R. Peres, and A. H. Castro Neto. "Graphene Bilayer with a Twist: Electronic Structure". In: *Physical Review Letters* 99, 25 (2007), p. 256802. DOI: 10.1103/PhysRevLett.99.256802.

[236] Noa Marom et al. "Stacking and Registry Effects in Layered Materials: The Case of Hexagonal Boron Nitride". In: *Physical Review Letters* 105, 4 (2010), p. 046801. DOI: 10.1103/PhysRevLett.105.046801.

[237] Oded Hod. "The Registry Index: A Quantitative Measure of Materials' Interfacial Commensurability". In: *ChemPhysChem* 14, 11 (2013), pp. 2376–2391. DOI: 10.1002/cphc.201300259.

[238] Fernando Gargiulo and Oleg V Yazyev. "Structural and electronic transformation in low-angle twisted bilayer graphene". In: *2D Materials* 5, 1 (2018), p. 015019. DOI: 10.1088/2053-1583/aa9640.

[239] M M van Wijk et al. "Relaxation of Moiré Patterns for Slightly Misaligned Identical Lattices: Graphene on Graphite". In: *2D Materials* 2, 3 (2015), p. 034010. DOI: 10.1088/2053-1583/2/3/034010.

[240] G. Trambly de Laissardière, D. Mayou, and L. Magaud. "Numerical Studies of Confined States in Rotated Bilayers of Graphene". In: *Physical Review B* 86, 12 (2012), p. 125413. DOI: 10.1103/PhysRevB.86.125413.

[241] R. Bistritzer and A. H. MacDonald. "Moire Bands in Twisted Double-Layer Graphene". In: *Proceedings of the National Academy of Sciences* 108, 30 (2011), pp. 12233–12237. DOI: 10.1073/pnas.1108174108.

[242] Yuanbo Zhang et al. "Direct Observation of a Widely Tunable Bandgap in Bilayer Graphene". In: *Nature (London)* 459, 7248 (2009), pp. 820–823. DOI: 10.1038/nature08105.

[243] Ivar Martin, Ya. M. Blanter, and A. F. Morpurgo. "Topological Confinement in Bilayer Graphene". In: *Physical Review Letters* 100, 3 (2008), p. 036804. DOI: 10.1103/PhysRevLett.100.036804.

[244] F. Zhang, A. H. MacDonald, and E. J. Mele. "Valley Chern Numbers and Boundary Modes in Gapped Bilayer Graphene". In: *Proceedings of the National Academy of Sciences* 110, 26 (2013), pp. 10546–10551. DOI: 10.1073/pnas.1308853110.

[245] Abolhassan Vaezi et al. "Topological Edge States at a Tilt Boundary in Gated Multilayer Graphene". In: *Physical Review X* 3, 2 (2013), p. 021018. DOI: 10.1103/PhysRevX.3.021018.

[246] Long Ju et al. "Topological Valley Transport at Bilayer Graphene Domain Walls". In: *Nature (London)* 520, 7549 (2015), pp. 650–655. DOI: 10.1038/nature14364.

[247] Long-Jing Yin et al. "Direct Imaging of Topological Edge States at a Bilayer Graphene Domain Wall". In: *Nat. Commun.* 7 (2016), p. 11760. DOI: 10.1038/ncomms11760.

[248] J. M. B. Lopes dos Santos, N. M. R. Peres, and A. H. Castro Neto. "Continuum model of the twisted graphene bilayer". In: *Physical Review B* 86, 15 (2012), p. 155449. DOI: 10.1103/PhysRevB.86.155449.

[249] C. J. Tabert and E. J. Nicol. "Dynamical Conductivity of AA-Stacked Bilayer Graphene". In: *Physical Review B* 86, 7 (2012), p. 075439. DOI: 10.1103/PhysRevB.86.075439.

[250] József Cserti, András Csordás, and Gyula Dávid. "Role of the Trigonal Warping on the Minimal Conductivity of Bilayer Graphene". In: *Physical Review Letters* 99, 6 (2007), p. 066802. DOI: 10.1103/PhysRevLett.99.066802.

[251] Mikito Koshino and Tsuneya Ando. "Transport in bilayer graphene: Calculations within a self-consistent Born approximation". In: *Physical Review B* 73, 24 (2006), p. 245403. DOI: 10.1103/PhysRevB.73.245403.

[252] T. M. R. Wolf et al. In: *Physical Review Letters* 123 (9 2019), p. 096802. DOI: 10.1103/PhysRevLett.123.096802.

[253] Yan-Yang Zhang et al. "Localization and the Kosterlitz-Thouless Transition in Disordered Graphene". In: *Physical Review Letters* 102, 10 (2009), p. 106401. DOI: 10.1103/PhysRevLett.102.106401.

[254] Yanyang Zhang et al. "Quantum blockade and loop currents in graphene with topological defects". In: *Physical Review B* 78, 15 (2008), p. 155413. DOI: 10.1103/PhysRevB.78.155413.

[255] Vitor M. Pereira, J. M. B. Lopes dos Santos, and A. H. Castro Neto. "Modeling Disorder in Graphene". In: *Physical Review B* 77, 11 (2008), p. 115109. DOI: 10.1103/PhysRevB.77.115109.

[256] E R Mucciolo and C H Lewenkopf. "Disorder and Electronic Transport in Graphene". In: *Journal of Physics: Condensed Matter* 22, 27 (2010), p. 273201. DOI: 10.1088/0953-8984/22/27/273201.

[257] N. M. R. Peres. "*Colloquium* : The Transport Properties of Graphene: An Introduction". In: *Reviews of Modern Physics* 82, 3 (2010), pp. 2673–2700. DOI: 10.1103/RevModPhys.82.2673.

[258] M. I. Katsnelson. "Zitterbewegung, Chirality, and Minimal Conductivity in Graphene". In: *EPJ B* 51, 2 (2006), pp. 157–160. DOI: 10.1140/epjb/e2006-00203-1.

[259] Vitor M. Pereira et al. "Disorder Induced Localized States in Graphene". In: *Physical Review Letters* 96, 3 (2006), p. 036801. DOI: 10.1103/PhysRevLett.96.036801.

[260] Hong-Shuai Tao et al. "Layer Anti-Ferromagnetism on Bilayer Honeycomb Lattice". In: *Scientific Reports* 4, 1 (2014), p. 5367. DOI: 10.1038/srep05367.

[261] Shengjun Yuan, Hans De Raedt, and Mikhail I. Katsnelson. "Modeling electronic structure and transport properties of graphene with resonant scattering centers". In: *Physical Review B* 82, 11 (2010), p. 115448. DOI: 10.1103/PhysRevB.82.115448.

[262] Daniela Dombrowski et al. "Energy-Dependent Chirality Effects in Quasifree-Standing Graphene". In: *Physical Review Letters* 118, 11 (2017), p. 116401. DOI: 10.1103/PhysRevLett.118.116401.

[263] Zihao Wang et al. "Composite super-moiré lattices in double aligned graphene heterostructures". English. In: *To appear in Science Advances* (2019).

[264] A. V. Kretinin et al. "Electronic Properties of Graphene Encapsulated with Different Two-Dimensional Atomic Crystals". In: *Nano Letters* 14, 6 (2014), pp. 3270–3276. DOI: 10.1021/nl5006542.

[265] Guorui Chen et al. "Signatures of tunable superconductivity in a trilayer graphene moiré superlattice". In: *Nature* 572, 7768 (2019), pp. 215–219. DOI: 10.1038/s41586-019-1393-y.

[266] Guorui Chen et al. "Evidence of a gate-tunable Mott insulator in a trilayer graphene moiré superlattice". In: *Nature Physics* 15, 3 (2019), pp. 237–241. DOI: 10.1038/s41567-018-0387-2.

[267] Kyounghwan Kim et al. "Tunable moiré bands and strong correlations in small-twist-angle bilayer graphene". In: *Proceedings of the National Academy of Sciences* 114, 13 (2017), pp. 3364–3369. DOI: 10.1073/pnas.1620140114.

[268] Rebeca Ribeiro-Palau et al. "Twistable electronics with dynamically rotatable heterostructures". In: *Science* 361, 6403 (2018), pp. 690–693. DOI: 10.1126/science.aat6981.

[269] Nathan R. Finney et al. "Tunable crystal symmetry in graphene-boron nitride heterostructures with coexisting moiré superlattices". In: *Nature Nanotechnology* 14, 11 (2019), pp. 1029–1034. DOI: 10.1038/s41565-019-0547-2.

[270] Pilkyung Moon and Mikito Koshino. "Electronic properties of graphene/hexagonal-boron-nitride moiré superlattice". In: *Physical Review B* 90, 15 (2014), p. 155406. DOI: 10.1103/physrevb.90.155406.

[271] M. Diez et al. "Emergence of Massless Dirac Fermions in Graphene's Hofstadter Butterfly at Switches of the Quantum Hall Phase Connectivity". In: *Physical Review Letters* 112, 19 (2014), p. 196602. DOI: 10.1103/physrevlett.112.196602.

[272] Patrick Zeller and Sebastian Günther. "What are the possible moiré patterns of graphene on hexagonally packed surfaces? Universal solution for hexagonal coincidence lattices, derived by a geometric construction". In: *New Journal of Physics* 16, 8 (2014), p. 083028. DOI: 10.1088/1367-2630/16/8/083028.

[273] Giacomo Argentero et al. "Unraveling the 3D Atomic Structure of a Suspended Graphene/hBN van Der Waals Heterostructure". In: *Nano Letters* 17, 3 (2017), pp. 1409–1416. DOI: 10.1021/acs.nanolett.6b04360.

[274] Steve Plimpton. "Fast Parallel Algorithms for Short-Range Molecular Dynamics". In: *Journal of Computational Physics* 117, 1 (1995), pp. 1–19. DOI: 10.1006/jcph.1995.1039.

[275] Steven J. Plimpton and Aidan P. Thompson. "Computational Aspects of Many-Body Potentials". In: *MRS Bulletin* 37, 5 (2012), pp. 513–521. DOI: 10.1557/mrs.2012.96.

[276] J. R. Wallbank et al. "Generic miniband structure of graphene on a hexagonal substrate". In: *Physical Review B* 87, 24 (2013), p. 245408. DOI: 10.1103/physrevb.87.245408.

[277] Ashley M. DaSilva et al. "Transport and particle-hole asymmetry in graphene on boron nitride". In: *Physical Review B* 91, 24 (2015), p. 245422. DOI: 10.1103/physrevb.91.245422.

[278] Jeil Jung et al. "Origin of band gaps in graphene on hexagonal boron nitride". In: *Nature Communications* 6, 1 (2015), p. 6308. DOI: 10.1038/ncomms7308.

[279] Hakseong Kim et al. "Accurate Gap Determination in Monolayer and Bilayer Graphene/h-BN Moiré Superlattices". In: *Nano Letters* 18, 12 (2018), pp. 7732–7741. DOI: 10.1021/acs.nanolett.8b03423.

[280] Wei Yang et al. "Epitaxial growth of single-domain graphene on hexagonal boron nitride". In: *Nature Materials* 12, 9 (2013), pp. 792–797. DOI: 10.1038/nmat3695.

[281] Matthew Yankowitz et al. "Dynamic band-structure tuning of graphene moiré superlattices with pressure". In: *Nature* 557, 7705 (2018), pp. 404–408. DOI: 10.1038/s41586-018-0107-1.

[282] Jeil Jung et al. "Moiré band model and band gaps of graphene on hexagonal boron nitride". In: *Physical Review B* 96, 8 (2017), p. 085442. DOI: 10.1103/physrevb.96.085442.

[283] Arash A. Mostofi et al. "An updated version of wannier90: A tool for obtaining maximally-localised Wannier functions". In: *Computer Physics Communications* 185, 8 (2014), pp. 2309–2310. DOI: 10.1016/j.cpc.2014.05.003.

[284] Vitor M. Pereira and A. H. Castro Neto. "Strain Engineering of Graphene's Electronic Structure". In: *Phys. Rev. Lett.* 103 (4 2009), p. 046801. DOI: 10.1103/PhysRevLett.103.046801.

[285] Gareth W Jones and Vitor M Pereira. "Designing electronic properties of two-dimensional crystals through optimization of deformations". In: *New Journal of Physics* 16, 9 (2014), p. 093044. DOI: 10.1088/1367-2630/16/9/093044.

[286] S. P. Milovanović et al. "Periodically strained graphene lattice: flat bands". In: *arXiv* (2019). eprint: https://arxiv.org/abs/1910.11752.

[287] Ye-Cheng Zhou, Hao-Li Zhang, and Wei-Qiao Deng. "A 3Nrule for the electronic properties of doped graphene". In: *Nanotechnology* 24, 22 (2013), p. 225705. DOI: 10.1088/0957-4484/24/22/225705.

Miša Anđelković

Curriculum Vitae

Heistraat 52
2610 Antwerpen
Belgium
(+32) 488 91 62 46
misa.s.andelkovic@gmail.com
MAndelkovic
MAndelkovic

Education

Dec. 2015–Current — **PhD studies in Physics**, *CMT group, Faculty of Science, University of Antwerp*, Antwerp, Belgium.

Research project — *Numerical methods based on Chebyshev polynomial expansions for investigating electronic transport of 2D materials and their heterostructures*

2014–2015 — **Master studies in Electrical Engineering and Computing**, *School of Electrical Engineering, University of Belgrade*, Belgrade, Serbia, GPA: 10/10.
Module: Nanoelectronics and Photonics.

Research project — *The modelling of electronic structure of wurtzite nanodots*

2010–2014 — **Bachelor of Science in Electrical Engineering and Computing**, *School of Electrical Engineering, University of Belgrade*, Belgrade, Serbia, GPA: 9.18/10.
Module: Physical Electronics, Section: Nanoelectronics, Optoelectronics and Laser Techniques.

Research project — *Strain modelling of semiconductor core-shell nanowires*

Fields of interest

- Electrical, optical and structural properties of 2D materials.
- Computational physics, polynomial expansions, high performance computing (HPC), tight binding method.
- Device engineering, modelling and manufacturing processes, micro- and nano-electro-mechanical systems (MEMS/NEMS).

Coding projects

KITE package Collaboration on developing package for atomistic modelling of electronic structure and response functions of large molecules, crystals and hybrid materials, specialized for HPC.

Pybinding package Contribution to the development of the python based package for numerical tight-binding calculations in solid state physics.

Publications

- *DC conductivity of twisted bilayer graphene: Angle-dependent transport properties and effects of disorder*, M. Anđelković, L. Covaci, and F. M. Peeters, Phys. Rev. Materials 2, 034004, 2018.
- *Ballistic electron channels including weakly protected topological states in delaminated bilayer graphene*, T. L. M. Lane, M. Anđelković, J. R. Wallbank, L. Covaci, F. M. Peeters, and V. I. Fal'ko, Phys. Rev. B 97, 045301, 2018.
- *Flat Bands in Buckled Graphene Superlattices*, Y. Jiang, M. Anđelković, S. P. Milovanović, L. Covaci, X. Lai, Y. Cao, K. Watanabe, T. Taniguchi, F. M. Peeters, A. K. Geim, E. Y. Andrei, arXiv:1904.10147, 2019.
- *KITE: high-performance accurate modelling of electronic structure and response functions of large molecules, disordered crystals and heterostructures*, S. M. João, M. Anđelković, L. Covaci, T. Rappoport, J. M. V. P. Lopes and A. Ferreira, arXiv:1910.05194, 2019.
- *Composite super-moiré lattices in double aligned graphene heterostructures*, Z. Wang, Y. B. Wang, J. Yin, E. Tóvári, Y. Yang, L. Lin, M. Holwill, J. Birkbeck, D. J. Perello, S. Xu, J. Zultak, R. V. Gorbachev, A. V. Kretinin, T. Taniguchi, K. Watanabe, S. V. Morozov, M. Anđelković, S. P. Milovanović, L. Covaci, F. M. Peeters, A. Mishchenko, A. K. Geim, K. S. Novoselov, V. I. Fal'ko, A. Knothe, C. R. Woods, To appear in Science Advances, 2019.
- *Double moiré with a twist: super-moiré in encapsulated graphene*, M. Anđelković, S. P. Milovanović, L. Covaci, F. M. Peeters, arxiv:1910.00345, 2019.
- *Periodically strained graphene lattice: flat bands*, S. P. Milovanović, M. Anđelković, L. Covaci, F. M. Peeters, arxiv:1910.11752, 2019.

Talks and poster presentations

11 Jul. 2018 *Effects of disorder and resonant scattering in twisted bilayer graphene*, contributed talk, Quantum Mechanics Meet Topology, Trieste, Italy.

11 Apr. 2018 *Ballistic electron channels in (twisted) bilayer graphene*, contributed talk, Belgian Physical Society meeting, Antwerp, Belgium.

29 Aug. 2017 *Disorder and field induced effects on the DC conductivity of twisted bilayer graphene*, poster presentation, Lausanne, Switzerland.

26 Jun. 2017 *Disorder and field induced effects on the DC conductivity of twisted bilayer graphene*, poster presentation, Graphene Study, Gothenburg, Sweden.

8 Dec. 2016 *Large-scale conductivity calculations of (twisted) bilayer graphene*, contributed talk, Euro-TMCS II, Cork, Ireland.

14 Jun. 2016 *The conductivity tensor of disordered (twisted) bilayer graphene*, poster presentation, Graphene week, Warsaw, Poland.

Work experience

2018–Current **Teaching assistant for the course Numeric Methods**, *Faculty of Science, University of Antwerp*, Antwerp, Belgium, Computer Practicum.

Nov./Dec., 2014 **Java application development, internship**, *MD & Profy*, Belgrade, Serbia.

Jul., 2014 **Work in cleanroom and in the laboratory for photolithography, internship**, *Institute for chemistry, technology, and metallurgy, center for microelectronic technologies*, Belgrade, Serbia.

Language proficiency

Serbian *native language*

English *professional proficiency*

Dutch *basic proficiency*